Chemical fingerprints of star forming regions and active galaxies

Pérez-Beaupuits, Juan-Pablo

rijksuniversiteit
groningen

Chemical fingerprints of star forming regions and active galaxies

Proefschrift

ter verkrijging van het doctoraat in de
Wiskunde en Natuurwetenschappen
aan de Rijksuniversiteit Groningen
op gezag van de
Rector Magnificus, dr. F. Zwarts,
in het openbaar te verdedigen op
vrijdag 8 oktober 2010
om 14.45 uur

door

Juan Pablo Pérez Beaupuits

geboren op 16 mei 1975
te Santiago, Chile

Promotor:	Prof. dr. M. C. Spaans
Beoordelingscommissie:	Prof. dr. W. A. Baan Prof. dr. K. M. Menten Prof. dr. K. Wada

ISBN 978-90-367-4544-4
ISBN 978-90-367-4545-1 (electronic version)

The scientist is not a person who gives the right answers, he is one who asks the right questions.

– Clause Levi-Strauss (French Philosopher, 1908 – 2009)

We have to abandon the idea that schooling is something restricted to youth. How can it be, in a world where half the things a man knows at 20 are no longer true at 40 – and half the things he knows at 40 had not been discovered when he was 20?.

– Arthur C. Clarke (English Writer of science fiction, 1917 – 2008)

The secret of success in life is for a man to be ready for his opportunity when it comes.

– Benjamin Disraeli (England's prime minister, 1804 – 1881)

Some men give up their designs when they have almost reached the goal; while others, on the contrary, obtain a victory by exerting, at the last moment, more vigorous efforts than ever before.

– Herodotus (Greek Historian, 484 BC – ca. 425 BC)

A mis padres

Front cover: photography of the Milky Way in the southern hemisphere, taken by Alexandru Tudorica, merged with a photography of a sunset at the Submillimeter Array in Mauna Kea, Hawaii, taken by J.P. Pérez-Beaupuits.

Back cover: photography of the Moon taken by Alexandru Tudorica, merged with a photography of J.P in the shore of the Vulcanoes National park, Hilo, Hawaii, taken by Raquel Monje.

Digital composition of the cover images designed by J.P. Pérez-Beaupuits.

Printed by: Ipskamp Drukkers B.V., Enschede, the Netherlands.

Contents

1 Introduction

On a typical clear night in the north of Chile, like the one captured in Fig. 1.1, it is possible to see in the sky above the Atacama desert an elongated dark cloud covering a bright kind of bulge, surrounded by countless stars. This white and fuzzy bulge, simply appreciated with the naked eye, is the center of our Galaxy, the Milky Way (translation of the Latin *Via Lactea*). As described in the original picture*, taken by Stéphane Guisard (in his work *Los Cielos de Chile*), Fig. 1.1 shows the Southern Cross and Coal bag in the far top right corner, and the Galactic Center, Scorpius and Sagittarius constellations in the middle of the picture. The dark lane obscuring the Galactic center is formed by numerous clouds of interstellar gas and dust found in the spiral arms and bar of the Galaxy (e.g., Churchwell et al., 2009).

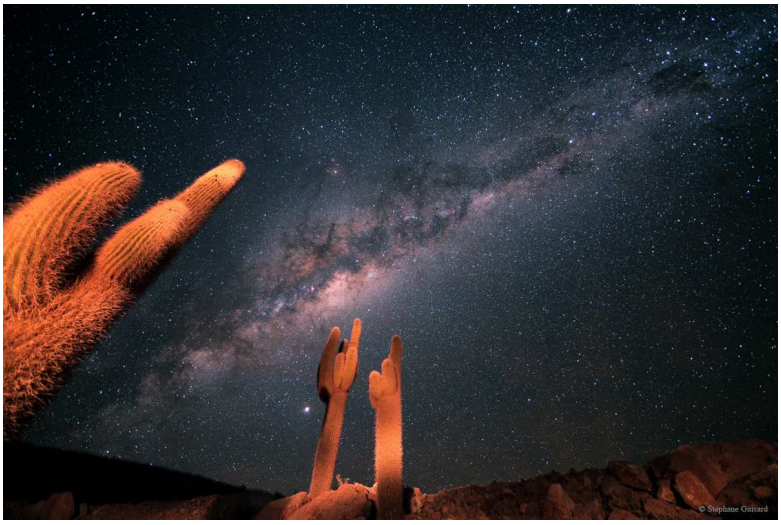

Figure 1.1: The Southern Hemisphere Milky Way and Echinopsis Atacamensis (cactus specie) with the rich Galactic center in the middle of the picture, as seen in the sky above San Pedro de Atacama, in the north of Chile. This is a 2 minute one-shot image taken with a digital camera by Stéphane Guisard, for his work *Los Cielos de Chile*.

* http://www.astrosurf.com/sguisard/Pagim/Milky-Way-Echinopsis-Atacamensis.html

The center of the Milky Way (MW) is seen nearly edge-on from the Earth, since the Galactic plane is inclined by about 60 degrees to the ecliptic (the plane of the Earth's orbit). Therefore, all the interstellar medium that fills the Galactic disk, obscures the bright Galactic center and the light emitted from stars that lie within the Galactic plane. Indirect methods, and observations at other wavelengths than the visible region of the spectrum (e.g., mm and sub-mm wavelengths, infrared, and X-rays), are required to study the center of the Galaxy.

Estimates of the motions of material around the Galactic center suggest the presence of a compact object of very large mass at the center of the MW (e.g., Jones & Lambourne, 2004, and references therein). The Galactic center is commonly considered to be demarked by the radio source Sagitarious A* (Nord et al., 2003). This source has recently been confirmed to be a supermassive black hole using X-ray observations (e.g., Aharonian et al., 2008, and references therein).

Most galaxies are believed to have a supermassive black hole at their center (e.g., Blandford, 1999), and they show different levels of brightness, star formation activity and accretion rates of matter into their black holes. However, the MW is less bright and active than many other galaxies undergoing strong star formation activity and emitting large amount of non-thermal radiation from their nuclear regions (e.g., Robson, 2004; Carroll & Ostlie, 2006). This can be interpreted as either the MW has already gone through an episode of strong star formation and accretion activity, and that nowadays is in a rather quiet state, or that it will eventually become more active in the future. Intense star formation, black hole accretion and the coalescence of active galactic nuclei are crucial phases in galaxy evolution. Different types of active galaxies and their connection with star formation activity are briefly described in Sec. 1.4.

The irradiation by UV and X-ray photons, as well as other thermodynamical processes (e.g. turbulence and shocks) occurring in the star forming regions and near the center of active galaxies, drive the excitation of atomic species, as well as the formation of several molecules (cf., Maloney et al., 1996; Martin-Pintado et al., 1997; Hollenbach & Tielens, 1999). Studies of atomic and molecular emission triggered by these processes can advance our understanding of the interaction (and feedback) of these processes in galaxy centers, and the impact that they have on the (mostly dense, molecular) interstellar medium and star forming gas.

Most interstellar molecules are detected by spectroscopic analysis (see Secs. 1.1 and 1.2) that measures absorption or emission at radio, (sub-)millimeter and micrometer (IR) wavelengths, rather than those corresponding to visual light. Single-dish and interferometer, (sub-)millimeter and IR facilities, both ground- and space-based, provide a wealth of new data. These observations reveal a wide range of physical conditions ranging from the cold, pre-collapse stage, where key molecules are depleted onto grains, to warmer, more evolved phases where ices evaporate and drive a rich chemistry (see Sec. 1.3).

High spatial resolution observations of Galactic star-forming regions (e.g., Orion Nebula, M17, S140) and the Galactic center are particularly important since molecular clouds of the size of maps ($\sim 3 \times 3$ pc^2) recently reported (e.g., Kramer et al.,

2004; Pérez-Beaupuits et al., 2010) will be resolved spatially by ALMA*, at the distance of nearby galaxies like the prototypical Seyfert NGC 1068 (~ 14 Mpc away). As such, star-forming regions in our own Milky Way can serve as a direct comparison for such regions in active galaxies that will become observable with ALMA in the coming years.

The following sections describe the main theoretical tools applied in the studies presented in this thesis. They are meant to give the casual reader the basic knowledge needed to understand the purpose of the observations performed, and for the interpretation, analysis and modelling of the data reported. A comprehensive introduction to each particular study is given in the respective chapters.

1.1 Spectroscopy: a powerful diagnostic tool

Atomic and molecular line observations are of great importance in astrophysics. They show the existence of certain chemical compounds in the interstellar medium (ISM). Several reaction chains have been proposed as the origin for the observed molecular species like [N II],[C I],^{12}CO, and HCN (e.g., Turner & Ziurys, 1988; Herbst, 2005, and references therein). Atomic and molecular lines can be used to probe the physical conditions of the ISM.

The density and the temperature of the interstellar gas are quantities that must be known for any succesful modelling. These two parameters influence differently the chemistry of molecular clouds, which introduces uncertainties in the interpretation of the measurements. These uncertainties can be reduced by observing several species or several transitions of a single species.

The intensities of the emission lines obtained with a spectrometer correspond to a measure of the number of molecules in, say, each rotational state (level population). By seeing how the molecules are distributed among the rotational energy states, so the relative intensity of the different emission lines, the temperature and density of the gas can be deduced. The sum of all the level populations, which can often be deduced from observations of just a few lines, gives the total number of molecules along the line of sight (the column density). Using observations of several emission lines, the temperature, density and column density of the gas can be estimated with radiative transfer algorithms (e.g., Hogerheijde & van der Tak, 2000; Poelman & Spaans, 2005, 2006; Elitzur & Asensio Ramos, 2006; van der Tak et al., 2007). The Doppler shift and shape of spectral lines yield information about the motions of the gas.

1.2 Radiative transfer

The essential physical ideas behind radiative transfer can be showen through the problems related multi-level line formation. The formulation discussed here follows the prescription given by Rybicki (1984), with some additional contributions

* http://www.almaobservatory.org/

inspired by Rybicki & Lightman (1986) and Kutner (1984). Further information and treatment of more complicated cases can be found in, e.g., Chandrasekhar (1950); Kourganoff (1952); Sobolev (1963); Rybicki (1972); Mihalas (1978); Kalkofen (1984); Rohlfs & Wilson (2004), and references therein.

Solutions of the multi-level line formation problem allows one to infer the number of molecules in the levels involved in the transitions of interest (i.e., the level populations). In general the excitation and radiative transfer are strongly coupled and special methods are needed in order to solve the system of coupled equations (e.g., Stutzki & Winnewisser, 1985; Hogerheijde & van der Tak, 2000; Juvela et al., 2001; Poelman & Spaans, 2005, 2006; Elitzur & Asensio Ramos, 2006; van der Tak et al., 2007; Hegmann et al., 2007).

In the excitation calculations it is assumed that the level populations respond mainly to the temperature and density in the ISM. Generally two sources of excitation are considered: (1) the kinetic energy of the gas, to which the molecules are coupled by collisions, and (2) a radiation field like line emission (photon trapping) and background continuum (IR pumping), to which the molecules are coupled by the emission and absorption of photons. The level of excitation of a particular species is determined by the relative coupling to these sources.

1.2.1 Equations of statistical equilibrium

In the multi-level line formation it is assumed that the net transition rate out of each level is balanced by the net transition rate into that level. This leads to the equations of statistical equilibrium for a multi-level molecule. For each bound level i, with population n_i, and energy E_i, there is an equation of the form

$$n_i \sum_j R_{ij} = \sum_j n_j R_{ji}, \tag{1.1}$$

where the sums are over all other bound levels j. The rate coefficients R_{ij} from level i to level j are given by

$$R_{ij} = \begin{cases} C_{ij} + B_{ij}\overline{J}^t_{ij} + A_{ij}, & E_i > E_j, \\ C_{ij} + B_{ij}\overline{J}^t_{ij}, & E_i < E_j. \end{cases} \tag{1.2}$$

The total collision rate coefficient C_{ij} (per molecule in state i) is usually assumed to be governed by H_2, the most abundant interstellar molecule. This coefficient settle the coupling between the excitation and the kinetic energy of the gas, and is defined as $C_{ij} = n_0\langle v\sigma_{ij}(v)\rangle$, where n_0 is the number density (cm^{-3}) of the collision partner, v is the speed ($\mathrm{cm\ s}^{-1}$) of the colliding particle and $\sigma_{ij}(v)$ is the collision cross section (cm^2) for a transition from the state i to the state j. These cross sections are very important for the excitation calculation, but theoretical and empirical values are available only for the simpler interstellar molecules. The $\langle\rangle$ indicates an average over the velocity distribution of the colliding particles, thus introducing the dependence of the excitations on the kinetic temperature (T_k) of the gas. The

product $\langle v\sigma_{ij}(v)\rangle$ is the parameter usually given in atomic and molecular databases (e.g., the LAMDA* database; Schöier et al. 2005).

1.2.2 The radiation field

The coupling to the radiation field is governed by the Einstein coefficients, A_{ij} and B_{ij}. The spontaneous emission rate is given by the A-coefficient while the rates of stimulated emission and absorption are given by the product between the corresponding B-coefficient and the *integrated mean intensity* $\overline{J}^t_{ij}$ defined by

$$\overline{J}^t_{ij} = \frac{1}{4\pi}\int d\Omega \int_0^\infty \varphi_{ij}(\nu) I^t_{ij}(\nu) d\nu, \tag{1.3}$$

where $I^t_{ij}(\nu) = I^t_{ji}(\nu)$ is the *total monochromatic specific intensity* or *brightness* and $\varphi_{ij}(\nu)$ is the *line profile function* at frequency ν for the line connecting levels i and j, Δ is the *characteristic width*, $\varphi(\nu) = \frac{1}{\Delta}\phi(x)$, where $\phi(x)$ is a dimensionless line profile function, and x is the dimensionless frequency variable $x = \frac{\nu-\nu_{ij}}{\Delta}$. Here ν_{ij} is the *line center frequency*, which is equal to the *rest* or *comoving frame* frequency.

The total monochromatic specific intensity for the ij line ($E_j > E_i$) is obtained from the equation of radiative transfer, which can be writen (in the fixed observer's frame) as

$$\frac{dI^t(\nu)}{d\ell} = -\kappa(\nu) I^t(\nu) + j(\nu), \tag{1.4}$$

where ℓ is the distance measured along the ray, with the line emission coefficient $j(\nu)$ and the absorption coefficient $\kappa(\nu)$. The absorption coefficient $\kappa(\nu)$ contains all the information about the intrinsic properties of the absorbing material the radiation must pass through.

1.2.3 The optical depth and source function

The dimensionless *monochromatic optical depth* τ_ν is defined by the absorption coefficient as $d\tau_\nu = -\kappa(\nu)d\ell$. A medium is said to be *optically thick* when τ_ν integrated along a path through the medium satisfies $\tau_\nu > 1$. When $\tau_\nu < 1$ the medium is said to be *optically thin*. In an optically thin medium a photon of frequency ν can traverse the medium without being absorbed. Whereas in an optically thick medium the average photon of frequency ν cannot traverse the entire medium without being absorbed.

Dividing the transfer equation (1.4) by $\kappa(\nu)$ we have

$$\frac{dI^t}{d\tau_\nu} = I^t - S. \tag{1.5}$$

where the *line source function* $S \equiv \frac{j(\nu)}{\kappa(\nu)} = \frac{n_j A_{ji}}{n_i B_{ij} - n_j B_{ji}}$ is defined as the ratio between the emission coefficient and the absorption coefficient.

* http://www.strw.leidenuniv.nl/ moldata/

1.2.4 Solving the radiative transfer equation

By expressing the intensity along a ray as a function of τ_ν, we can integrate equation (1.5) to give the formal solution for the total intensity I^t at a given point, in a given direction, and at a given frequency

$$I^t = I_b e^{-\tau_{\nu b}} + \int_0^{\tau_{\nu b}} e^{-\tau'_\nu} S(\tau'_\nu) d\tau'_\nu. \tag{1.6}$$

Here the optical depth scale is defined to be zero at the point where I^t is evaluated and to increase backwards along a ray to the boundary b of the medium, where it equals $\tau_{\nu b}$ and where there is an incident radiation field I_b.

As a reasonable first approximation, it is common to consider $S(\tau_\nu)$ independent of the position in the medium. That is, the source function S does not depend on τ_ν, so it can be taken out of the integral. This assumption leads to the simple form of equation (1.6)

$$I^t = I_b e^{-\tau_{\nu b}} + S(1 - e^{-\tau_{\nu b}}) = S + e^{-\tau_{\nu b}}(I_b - S), \tag{1.7}$$

which describes the specific intensity at any frequency. In radio and (sub)mm astronomy we are interested in the difference between a line intensity and the background continuum source (e.g. HII regions at centimeter wavelengths and the cosmic background radiation at millimeter wavelengths). Then, by substracting I_b in (1.7) we get the line intensity as

$$\Delta I = (S - I_b)(1 - e^{-\tau_{\nu b}}), \tag{1.8}$$

from where it is clear that if $S - I_b > 0$ we have an emission line, and if it is negative then we have an absorption line.

Equation (1.2) implies a system of L homogenous coupled linear equations, which in turn are coupled to the radiative transfer problem by the source function. The common numerical approach to solve this system of equations is an iteration scheme called *lambda-iteration*, in which one starts with an initial guess for the population densities (which give the corresponding source functions), obtained from some limiting case (e.g., thermal equilibrium), and then alternate between the statistical equilibrium equations (1.2) and the radiative transfer equations (1.6) until convergence is reached. The difficulty with these iterations lies in the coupled nature of the source function S.

1.3 Astrochemistry

Spectroscopy allows to determine the chemical composition of the ISM. Astrochemistry gives hints on how the chemical composition may vary, and how it may affect the evolution of the ISM. The chemical composition depends mostly on the density, the temperature, the radiation field and the elemental abundances of the gas. Since the chemical composition varies on astrophysical time scales, astrochemistry can eventually be used to determine cloud ages.

Numerous atoms and molecules tracing different gas chemistry have been detected in nearby galaxies (e.g., Henkel et al., 1987; Nguyen-Q-Rieu et al., 1991; Martín et al., 2003; Usero et al., 2004; Baan et al., 2008). These studies have shown that chemical differentiation, usually observed within Galactic molecular clouds, is also seen at larger scales (~ 100 pc) in extra-galactic environments.

Besides density and temperature, the chemistry of the gas is driven mainly by the intensity (or energy) of the impinging radiation field, or by mechanical processes like turbulent dissipation and shocks (e.g., Loenen et al., 2008). The ISM irradiated by Far-UV photons ($6 - 13.6$ eV) emitted by O and B stars is characterized by emission of atomic and molecular lines typical of a photon-dominated region (PDR) (e.g., Hollenbach & Tielens, 1999; Kaufman et al., 1999; Meijerink & Spaans, 2005). PDRs are commonly found in Galactic molecular clouds (e.g. Orion, M17SW, S140) and in galaxies with strong star formation activity (starbursts; see Sec. 1.4.1).

On the other hand, the chemistry driven by hard X-ray photons (> 1 keV) emitted during the accretion proccess in the proximity of active galactic nuclei (AGNs; see Sec. 1.4), corresponds to that of an X-ray Dominated Region (XDR) (e.g., Maloney et al., 1996; Lepp & Dalgarno, 1996; Meijerink & Spaans, 2005). These high energy photons can also be emitted by X-ray binaries (e.g., Barnard et al., 2008, and references therein), and other stellar sources of X-rays where XDRs can be expected as well (see Chap. 7).

Depending on the radiation field and density of the gas, the abundance of some species can be enhanced or suppressed (e.g., Meijerink & Spaans, 2005; Meijerink et al., 2007). Different atomic and molecular lines, and their role as diagnostic tools, are discussed in the next sections.

1.3.1 Atomic lines

Since the gas phase cools mainly via the atomic fine structure lines of [O I], [C II], [C I], as well as the many ^{12}CO rotational lines, (e.g., Kaufman et al., 1999; Meijerink & Spaans, 2005), these species are very important diagnostics for the cooling of the ISM in Galactic star forming regions, the Milky Way as a galaxy, and external galaxies up to high redshifts (e.g., Fixsen et al., 1999; Weiß et al., 2003; Kramer et al., 2005; Bayet et al., 2006; Jakob et al., 2007).

PDRs are characterized by strong emission in the fine-structure lines of [C I] 609 μm, [C II] 158 μm and [O I] 63 μm; rotational lines of ^{12}CO; ro-vibrational and pure rotational lines of H_2; many H_2O lines, as well as many broad mid-IR features associated with Polycylic Aromatic Hydrocarbons (PAHs) (e.g., Tielens & Hollenbach, 1985; Hollenbach & Tielens, 1999; Kaufman et al., 1999; Meijerink & Spaans, 2005; Poelman & Spaans, 2005, 2006). On the other hand, the fine-structure lines [Si II] 35 μm, the [Fe II] 1.26, 1.64 μm, as well as the 2 μm ro-vibrational H_2 transitions are also bright in XDRs (e.g., Lepp & Dalgarno, 1996; Maloney et al., 1996; Meijerink & Spaans, 2005; Meijerink et al., 2007).

The atomic lines Hα, Hβ, [N II] [O I], [O III], [Ne II], [Ne V], [S II], and [S III], and flux ratios between them, have been used to characterize different kinds of active

galaxies and sources of excitation (e.g., Veilleux & Osterbrock, 1987; Moorwood et al., 1996a; Spoon et al., 2000; Armus et al., 2006; Brandl et al., 2006; Farrah et al., 2007, and references therein). A brief description of active galaxies, in particular Seyferts and starbursts, is given in Sec. 1.4.

Galaxies with an AGN have typical [Ne V]/[Ne II] line flux ratios of $0.8 - 2$, and a [O IV]/[Ne II] flux ratios of $1 - 5$ (e.g., Sturm et al., 2002; Armus et al., 2004). On the other hand, starburst galaxies have a strict upper limit < 0.01 for the [Ne V]/[Ne II] flux ratios, and $0.01 - 0.2$ for the [O IV]/[N II] flux ratios (e.g., Sturm et al., 2002; Verma et al., 2003).

Low ionization lines (e.g., [Ne II] or [Si II]) tend to be enhanced in shocks (Voit, 1992). A line flux ratio [Ne II]/[Ne III] ≥ 10 is expected to be found in shocks as well (Binette et al., 1985).

1.3.2 Molecular lines

In astrophysics it is considered that molecules can form, under nonequilibrium conditions, in four separate schemes: shock-front chemistry, surface chemistry on dust grains, circumstellar chemistry, and gas-phase chemistry (which involves radiative association, ion-molecule reactions, dissociative recombination and neutral-neutral reactions). A detailed description of molecules in space, and the four basic schemes of interstellar chemistry, can be found in (e.g., Turner & Ziurys, 1988; Herbst, 1999, 2005, and references therein). Molecules can be rotationally and vibrationally excited, besides the electronic excitation common to atoms. Since excited rotational states have typical energy levels of $1 - 100$ K, vibrational states several 10^3 K and electronic states $5 \times 10^3 - 10^5$ K, observation of molecules opens the possibility to probe a wider range of interstellar excitation conditions than using atoms.

The most abundant molecule in the universe after H_2 is ^{12}CO (carbon monoxide). It has a non-zero dipole moment and its different transitions are triggered mainly by collisions with H_2. Therefore, it has extensively been used as a tracer of molecular gas and mass in Galactic and extra galactic sources (e.g., Scoville & Sanders, 1987; Tennyson, 2005). Other molecular tracers like ^{13}CO and C^{18}O are usually optically thin, and have been used to estimate the total ^{12}CO and H_2 column densities in Galactic molecular clouds, assuming typical [^{12}CO]/[^{13}CO] or [^{12}CO]/[C^{18}O] abundance ratios (e.g., Stutzki & Guesten, 1990; Kramer et al., 2004).

Since cold and dense gas is turned into stars under the influence of gravity, tracing the dense regions of molecular clouds and galaxies is one of the most important tasks in modern astronomy. Rotational transitions of molecules (observed at mm and sub-mm wavelengths) are especially important when studying cold and dense molecular clouds (Kutner, 1984). Molecular tracers, usually excited by collisions with H_2, He and electrons, are used to probe temperatures, densities, velocity fields and other insterstellar physical parameters in dense interstellar regions as described above. In this, elemental abundances can be quite different compared to Galactic molecular clouds, e.g., larger than $2 - 4$ solar in Quasars, or sub-solar in the Large and Small Magallanic clouds.

Some of the most common high density tracers are CN, CS, HC_3N, HCO^+, HCN and HNC, and each of them traces somewhat different dense regions due to their different critical densities and energy levels. This work gives special attention to HCN, HNC, CN, and HCO^+, to study the dense regions in the centers of active galaxies. They are thought to be good tracers of AGN-driven interstellar clouds, according to, e.g., Phillips & Lazio (1995); Kohno et al. (2001); Aalto (2004); García-Burillo et al. (2004); Usero et al. (2004); Aalto et al. (2007b), and references therein.

Other molecules can be used as thermometers (e.g., NH_3, CH_3CN, CH_3C_2H, and mid- and high-J ^{12}CO lines). However, these often give discrepant temperatures for the same cloud due to their chemistry being affected by different temperatures and density conditions (i.e., gradients). This means that they likely do not sample the same regions inside the cloud. For instance, CH_3CN is often found in the warm and dense core of a cloud, while CH_3C_2H is found in the cooler and less dense halo surrounding the core.

High speed shocks ($> 20\ \mathrm{km\,s^{-1}}$) can be traced through emissions of the SiO molecule from sputtered grains (e.g., Lada et al., 1978; Martin-Pintado et al., 1997; Usero et al., 2006), while the NS/CS, SO/CS and HCO/H_2CO line ratios are expected to be good tracers of low speed shocks ($10-20\ \mathrm{km\,s^{-1}}$) in hot cores (Viti et al., 2001).

1.4 Active galaxies and active galactic nuclei

A galaxy is considered ordinary if it shows a spectrum dominated by thermal emission and a spectral shape corresponding to a composite of black-body radiation (with a maximum usually in the visible or near-IR region of the spectrum) emitted by billions of stars, interstellar gas and dust. Active galaxies instead show significant contribution to its overall luminosity (or energy output) by some process other than thermal emission, which is mainly associated with synchrotron radiation (Carroll & Ostlie, 2006). Usually they exhibit higher luminosities ($\gtrsim 10 \times L_{\mathrm{MW}}{}^*$) than a normal galaxy, emitted mainly from their central regions. Depending on the type of active galaxy, its emitted energy can be observed in the infrared, radio, UV, X-ray and gamma-ray regions of the electromagnetic spectrum. Due to this particular feature, simultaneous observations in a multi-wavelength manner are useful to follow the behaviour of active galaxies, as it changes on short (from weeks to months) timescales.

There are several different, and often overlapping, classes of active galaxies: e.g., Seyferts, Markarians, Radio Galaxies, Quasi-Stellar Radio Sources (Quasars), Quasi-Stellar Objects (QSOs), Starbursts (SBs), and Radio-Loud Quasars. A detailed description of these, and other type of active galaxies, can be found in, e.g., Robson (2004); Carroll & Ostlie (2006).

What most active galaxies have in common is an Active Galactic Nucleus (AGN). The generally accepted model of an AGN (Fig. 1.2) assumes the presence of a supermassive black hole of between 10^6 and 10^9 $M_\odot$ located at the center of the

* where L_{MW} is the luminosity of the Milky Way $\sim 2 \times 10^{10}\ L_\odot$

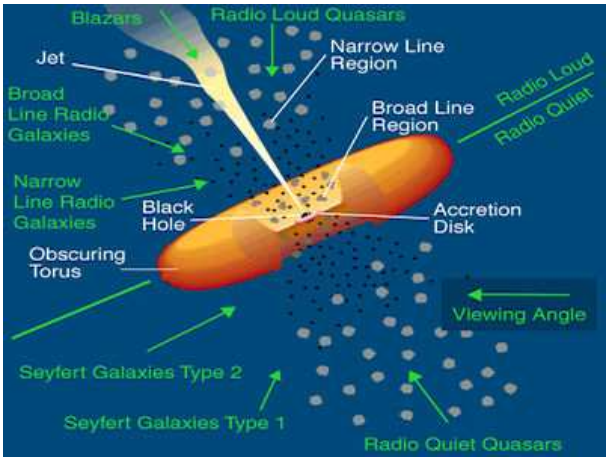

Figure 1.2: Schematic of an Active Galactic Nucleus and the interpretation of the unification theory. source: http://cassfos02.ucsd.edu/public/tutorial/AGN.html

galaxy. A torus of gas and dust, obscuring the central part of the galaxy, feeds the black hole through a flat accretion disk of dense material. Large amounts of gravitational energy are frequently released from the accretion disk in the form of powerful outflowing jets of hot plasma. This model of galaxy nuclei suggests that the differences observed between different types of active galaxies are simply a consequence of different viewing angles and different accretion rates – this is the *unification theory* of active galaxies. In contrast to the widely accepted view of a homogenous obscuring torus, recent high resolution observations and hydrodynamical simulations suggest that the nuclear obscuration may be due to a rather clumpy and filamentary molecular/dusty structure (e.g., Sánchez et al., 2009; Wada et al., 2009).

Many Seyfert galaxies (e.g. the prototypical Seyfert 2 galaxy NGC 1068) have circumnuclear starburst and hidden nuclear (within a few hundred parsecs from the center) starburst activity (e.g., Imanishi, 2002, 2003; Rodríguez-Ardila & Viegas, 2003). On the other hand, deeply buried AGNs have been found in many originally classified as starburst galaxies, like the exotic NGC 4945 (e.g., Marconi et al., 2000; Brusa et al., 2010). It has been argued that the AGN type could be discriminated not only by the viewing angles but also by the evolution and morphology of the circumnuclear starbursts (e.g., Umemura et al., 1999; Hunt & Malkan, 2004). However, it is not clear whether a specific relationship exists between AGN mass accretion and starbursts at various scales. What is understood is that intense star formation, black hole accretion and the coalescence of active galactic nuclei, like Arp 220, are crucial phases in galaxy evolution. Therefore, a brief description of Seyfert galaxies and starbursts is given in the next section.

1.4.1 Seyfert galaxies and Starbursts

Seyfert galaxies are mostly spiral galaxies with a tiny core that is about ten times more luminous than the whole Milky Way. Their brightness can fluctuate on time scales of about one month, and their spectra show broad forbidden emission lines (e.g., [O II], [O III], [N II], [Ne III], [S II], [S III]) corresponding to highly ionized gas. Seyfert galaxies also show strong emission in the infrared, ultraviolet, and X-ray spectral regions, whereas only less than 5% are radio loud (e.g., Seyfert, 1943; Osterbrock & Ferland, 2006).

Seyfert galaxies are first classified only on the spectral shape of the emission lines. Type 1 Seyferts are viewed mostly face-on and show both narrow and broad emission lines. Detailed descriptions of a subclassification of type 1 Seyferts can be found in Robson (2004) and Osterbrock & Ferland (2006). Instead, type 2 Seyferts exhibit only narrow lines since the broad line region (accretion disk and jets) is obscured by the surrounding molecular and dusty structure due to their mostly edge-on viewing angle (Khachikian & Weedman, 1974). Because the obscuring material is heated by the absorbed emission, type 2 Seyfert galaxies are also powerful infrared sources.

Several studies of the circumnuclear ionized regions of Seyferts indicate that many Seyfert galaxies have circumnuclear starburst regions (e.g., Wilson, 1988; Taniguchi et al., 1990; Cid Fernandes et al., 2001; Watabe & Umemura, 2005; Davies et al., 2005; Sani et al., 2010). Other observational studies indicate that circumnuclear starbursts actually obscure some AGNs (Levenson et al. 2001, 2007; Ballantyne 2008, and references therein).

Estimates of the age of the most recent episode of star formation in the circumnuclear region of the prototypical Seyfert galaxy NGC 1068 (the most luminous nearby type 2 Seyfert) suggest that its starburst is no longer active (Davies et al., 2007). This result agrees with an early study of a sample of type 2 Seyferts which indicates that their near and far-infrared luminosity is dominated by post-starburst emission (Dultzin-Hacyan & Benitez, 1994).

While ordinary galaxies only produce stars on the order of 1 $M_{\odot}$ per year, starburst galaxies exhibit an exceptionally high star formation rate (between 10 and 300 $M_{\odot}$ of stars per year) in their central kpc. A galaxy will maintain the undergoing starburst for $10^8 - 10^9$ years, which is much shorter than the evolutionary timescale of a galaxy (e.g., Carroll & Ostlie, 2006). Since only dense clouds can provide enough material to form stars, the star-forming regions are deeply obscured by gas and dust absorbing the UV radiation emmitted by the newly formed stars. Hence, starburst galaxies show strong emission mainly in the infrared region due to the re-radiation from the heated obscuring dust. The far-IR properties of Seyfert galaxies, in particular type 2s, were found to be similar to those of starburst galaxies (e.g., Rodriguez-Espinosa et al., 1987). All this observational evidence suggests a causal and/or physical relationship between AGN and circumnuclear starburst activity, which is discussed in the next section.

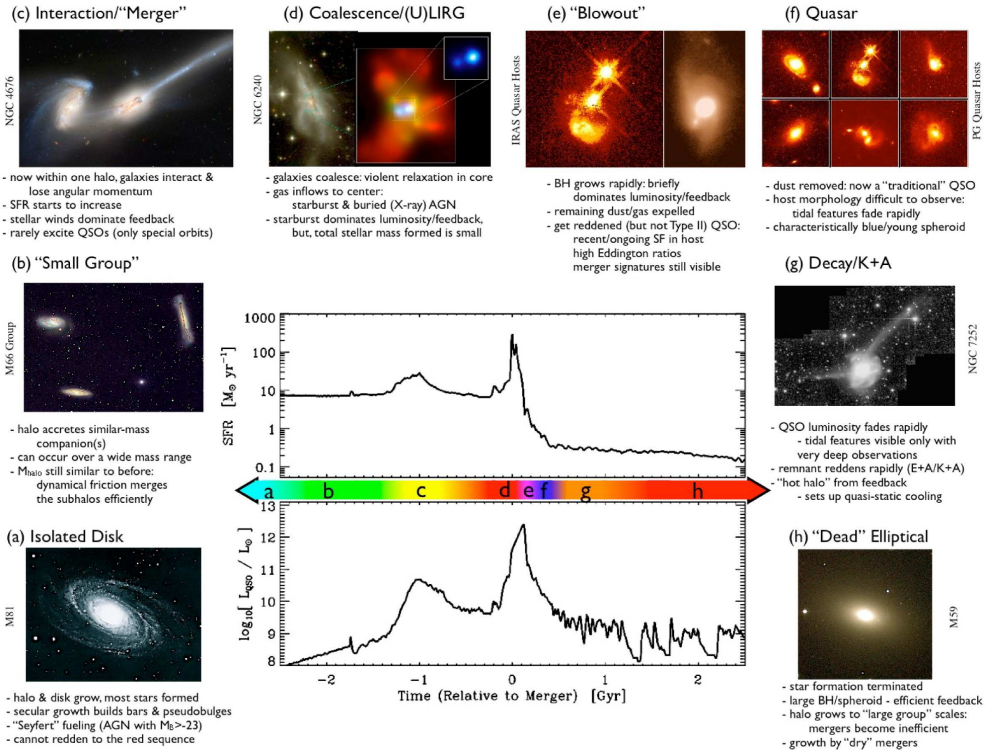

Figure 1.3: Schematic sequence of starbursts, active galactic nuclei, quasars, and spiral galaxies; formation and evolution from a merging event between gas-rich galaxies (from Hopkins et al. 2008). Note that the co-existence and interaction between the (X-ray producing) AGNs and starbursts (phase d and e) occurs in a relatively short period of time ($\lesssim 0.5$ Gyr) in this scenario.

1.4.2 The AGN-starburst connection

An early study by van Breugel et al. (1985) suggests that some starbursts may be triggered by radio jets from AGNs. Conversely, Norman & Scoville (1988) showed in later calculations that a compact central mass can be formed (and grow to a massive black hole) as a result of mass loss during post-main-sequence stellar evolution in a starburst galaxy. It was also proposed by Norman & Scoville (1988) that galactic interactions and mergers can form massive central star clusters. This model follows the generally accepted view, founded by Larson & Tinsley (1978), that interactions and mergers can trigger starbursts.

Subsequent observations showed that a merger event appears to be a more efficient mechanism to generate starbursts than interactions between galaxies (Bergvall et al., 2003). Although mergers seem to be needed to create starburst, it is not a sufficient condition. Dark matter, angular momentum flow and star formation processes in general may play an important role as well. Recent simulations by Martig & Bournaud (2008) indicate that the large-scale tidal field can enhance the merger-driven star formation activity of galaxies, and is particularly efficient at high ($z > 1$)

redshifts. Similarly, many AGN galaxies have interacting companions that can be the source of fuel for their central black hole (e.g., Carroll & Ostlie, 2006; Ivison et al., 2008; Koss et al., 2010; Smith et al., 2010, and references therein). Although, estimates from extinction-corrected [O III] luminosities of a sample of AGNs suggest that the accretion rate onto the black hole does not depend on the presence or absence of companions (Li et al., 2008).

All these models, as well as several other observations (e.g., Soltan, 1982; Magorrian et al., 1998; Ferrarese & Merritt, 2000; Graham et al., 2001; Häring & Rix, 2004), indicate that most AGNs and intense starbursts must originate from a common physical process. A plausible scenario considers that starbursts, supermassive black hole growth, and the formation of red elliptical and sub-millimeter galaxies (SMGs), are connected through an evolutionary sequence caused by mergers between gas-rich galaxies (e.g., Hopkins et al., 2006, 2008; Tacconi et al., 2008; Narayanan et al., 2009, 2010). Figure 1.3 shows a schematic sequence of events and phases in the evolution and formation of SBs, SMGs, QSOs and AGNs. In this scenario, galactic disks grow mainly in quiescence, with the possibility of secular-driven bar or pseudo-bulge formation, until the onset of a major merger. A significant fraction of Seyferts and low-luminosity quasars is expected to arise from this secular evolution (Hopkins et al., 2008).

Thus, the SBs and AGNs, producing strong UV and X-ray radiation, seem to be co-eval. The interaction processes (phase d and e in Fig. 1.3) between these two sources of energy and activity that dominate the formation and emission of molecular gas, is one of the long-standing issues concerning active galaxies. Galaxies that show the characteristic properties of both SBs and AGNs seem to be more luminous than normal AGN galaxies (Cid Fernandes et al., 2001). And several efforts have been made to determine whether the atomic and molecular emission is driven mainly by the SB or AGN (e.g., Cid Fernandes et al., 2001; Farrah et al., 2003; Sanders et al., 2004; Sanders & Ishida, 2004; Aalto et al., 2007b,a; Albrecht et al., 2007; Farrah et al., 2007; Aalto, 2008; Krips et al., 2008).

In order to contribute to these efforts, studies of high density tracers (HCN, HNC, CN, and HCO^+) in a group of Seyfert galaxies (NGC 1068, NGC 1365, NGC 3079, NGC 7469, NGC 2623), and spectral maps of IR fine-structure lines ([Ne II], [Ne V], [S II], [S III]) in the nucleus of NGC 4945 are presented in this thesis as well. Additionally, diffuse and warm gas ([C I], and mid-J ^{12}CO and ^{13}CO lines), as well as dense gas (HCN and HCO^+ $J = 4 \rightarrow 3$ lines) is studied in the Galactic star forming region M17 SW with high resolution maps. These maps will be useful to compare to future maps of molecular clouds in the nuclear region of Seyfert galaxies that will be resolved with ALMA. An spectroscopy analysis of high resolution hydrodynamical simulations of an AGN torus is also included in this thesis, and the basic formalism of the simulations is presented in the next section.

1.5 Hydrodynamic simulations of an AGN

The above sections indicate the interplay between star formation and black hole growth in galaxy centers from an observational perspective. Three-dimensional radiative magneto-hydrodynamic calculations with high resolution (sub–parsec) and large dynamic range (e.g., from 100 Schwarzschild radii to 100 pc) are necessary to construct physical models of the ISM influenced by star formation activity and the proximity of a supermassive black hole (SMBH). Only a few hydrodynamic studies of the central tens of parsecs of galaxies have been done so far (Wada & Norman 2002; Wada & Tomisaka 2005; Yamada et al. 2007; Schartmann et al. 2009; Wada et al. 2009). In this section we present the numerical method (set equations) used, as background for Chapter 5.

Simulations of the three-dimensional evolution of a rotating gas disk in a fixed spherical gravitational potential have been performed using a numerical scheme based on Eulerian hydrodynamics with a uniform grid. This scheme is the same as that described in Wada & Norman (2001), Wada (2001) and Wada et al. (2009). These studies of the evolution of the ISM in the inner 100 pc region around a SMBH take into account self-gravity of the gas, radiative cooling and heating due to supernovae (SNe) and due to a uniform FUV radiation field. All these features are summarized in the following equations, which are solved numerically

$$\partial\rho/\partial t + \nabla\cdot(\rho v) = 0, \tag{1.9}$$

$$\partial v/\partial t + (v\cdot\nabla)\,v + \nabla p/\rho = -\nabla\Phi_{ext} - \nabla\Phi_{BH} - \nabla\Phi_{sg}, \tag{1.10}$$

$$\partial E/\partial t + \nabla\cdot\left[(\rho E + p)\,v\right]/\rho = \Gamma_{\rm UV}\left(G_0\right) + \Gamma_{\rm SN} + v\cdot\nabla\Phi - \rho\Lambda\left(T_g, f_{\rm H_2}, G_0\right), \tag{1.11}$$

$$\nabla^2\Phi_{sg} = 4\pi G\rho, \tag{1.12}$$

where Φ is gravitational potential ($\Phi \equiv \Phi_{ext} + \Phi_{BH} + \Phi_{sg}$) and the specific total energy E is defined as

$$E \equiv |v|^2/2 + p/\left(\gamma-1\right)\rho, \tag{1.13}$$

with $\gamma = 5/3$. A time-independent external potential Φ_{ext} is assumed and defined as

$$\Phi_{ext} \equiv -\sqrt{(27/4)}\left[v_1^2/\left(r^2+a_1^2\right)^{1/2} + v_2^2/\left(r^2+a_2^2\right)^{1/2}\right], \tag{1.14}$$

where $a_1 = 100$ pc, $a_2 = 2.5$ kpc, $v_1 = v_2 = 147\ \mathrm{km\,s^{-1}}$. The potential $\Phi_{\rm BH}$ associated with the central black hole is defined as $\Phi_{\rm BH} \equiv -GM_{\rm BH}/\left(r^2+b^2\right)^{1/2}$, where $M_{\rm BH} = 1.3\times10^7\ M_\odot$ and $b = 1$ pc. A rotation curve based on the external potentials Φ_{ext} and $\Phi_{\rm BH}$, and the adopted mass distribution with a core radius a_1 of 100 pc is shown in Wada et al. (2009). This estimated curve is roughly consistent with rotation curves derived from VLTI/Keck observations of nearby Seyfert nuclei (Hicks et al., 2009).

The hydrodynamic part of the equations is solved by a second-order advection upstream splitting method (AUSM) based on Liou & Steffen (1993). The Poisson equation, Eq.(1.12), is solved to calculate the self-gravity of the gas using the Fast Fourier Transform (FFT) and the convolution method. A grid of $1024^2 \times 512$ points, and a periodic Green's function, are used to calculate the potential of an isolated system (Hockney & Eastwood, 1981).

The cooling function $\Lambda\left(T_g, f_{\mathrm{H}_2}, G_0\right)$ used in the energy equation, Eq.(1.11), is based on a radiative transfer model of photodissociation regions (PDRs; Meijerink & Spaans 2005). This cooling function depends on the molecular gas fraction f_{H_2}, the intensity of the FUV radiation field, G_0, and the gas temperature T_g which ranges between 20 K and 10^8 K. For a detailed description of this cooling function see Wada et al. (2009, their Appendix B).

The low resolution model of Wada et al. (2009), with $256^2 \times 128$ grid points, was used as input for the XDR chemical model and the 3-D radiative transfer calculations described in Chapter 5. This cartesian grid covers a $64^2 \times 32$ pc^3 region around the galactic center (giving a spatial resolution of 0.25 pc).

Using these simulations, predictions can be made for ALMA by incorporating X-ray chemistry (XDRs). Observables, like line maps of ^{12}CO, HCN, and [C I], are constructed through the use of a 3-D radiative transfer code. As specific application, focus is on the distinction between SBs and AGNs through HCN/HCO$^+$ ratios and very high-J ^{12}CO lines, as well as the X-factor.

1.6 Observatories

Several telescopes (listed below) were used during the last four years and many observational data were gathered after successful proposals and observing runs. Not all these data are presented here because some of them were affected by the bad weather conditions or by instrumental problems found at the time of the observations. Whereas other data are not conclusive enough to account for a publication and further observations are planned to complement those data. Nevertheless, the studies included in this thesis are the most representative ones of all the areas of astrophysics research I am interested, and that I managed to get involved in, during the course of my Ph.D. All the observatories I visited and/or managed to get data with are:

- the Onsala Space Observatory (OSO*) 20m telescope at ~ 23 m altitude in Onsala, Sweden.
- the Combined Array for Research in Millimeter-wave Astronomy (CARMA†) at $2,196$ m altitude in Cedar Flat, eastern California, U.S.A.
- the Very Large Telescope (VLT‡) at $2,635$ m altitude on the Paranal hill, south of Antofagasta, Chile.

* http://www.chalmers.se/rss/oso-en
† http://www.mmarray.org/
‡ http://www.eso.org/public/teles-instr/vlt/

- the Institut de Radioastronomie Millimétrique (IRAM*) 30m telescope at $2,850\ \mathrm{m}$ altitude in Pico Veleta, Granada, Spain.
- the Submillimeter Array (SMA†) at $4,080\ \mathrm{m}$ altitude at the foot of Pu'u Poli'ahu, Mauna Kea, Hawaii.
- the James Clerk Maxwell Telescope (JCMT‡) at $4,092\ \mathrm{m}$ altitude at the foot of Pu'u Poli'ahu, Mauna Kea, Hawaii.
- the Atacama Pathfinder EXperiment (APEX§) telescope at $5,105\ \mathrm{m}$ altitude on the Chajnantor plateau, Atacama desert, Chile.
- the Spitzer¶ space telescope, in Earth-trailing Heliocentric orbit, at about $124,078,174\ \mathrm{km}$ from Earth.

1.7 This thesis

In this thesis, several mm and IR spectral observations are used to assess the dominant source of excitation in the nuclear regions of starburst and Seyfert galaxies, as well as in a Galactic star-forming region. A 3-D hydrodynamical model of an AGN is studied in order to provide different diagnostics for future high resolution observations of nearby and high redshift active galaxies.

Outline of the thesis

In Chapter 2 , we estimate and discuss the excitation conditions of HCN and HNC in a sample of five Seyfert galaxies, based on single dish observations of the $J = 3 \rightarrow 2$ and $J = 1 \rightarrow 0$ transitions, and the line intensity ratios between them. We also observed CN $J = 1 \rightarrow 0$ and $J = 2 \rightarrow 1$ emission and discuss its role in photon and X-ray dominated regions.

In Chapter 3 , we use single dish observations of the $J = 4 \rightarrow 3$ transition of HCN, HNC, and HCO^+, as well as the CN $N_J = 2_{5/2} \rightarrow 1_{3/2}$ and $N_J = 3_{5/2} \rightarrow 2_{5/2}$, to constrain the physical conditions of the dense gas in the central region of the Seyfert 2 galaxy NGC 1068 and to determine signatures of the AGN or the starburst contribution. We estimate the excitation conditions of HCN, HNC, CN, and HCO^+ based on the line intensity ratios and radiative transfer models. We discuss the results in the context of models of irradiation of the molecular gas by UV light and X-rays.

* http://www.iram-institute.org/EN/30-meter-telescope.php
† http://www.cfa.harvard.edu/sma/
‡ http://www.jach.hawaii.edu/JCMT/
§ http://www.apex-telescope.org/
¶ http://www.spitzer.caltech.edu/

In Chapter 4 , we map of the central region of NGC 4945 using three of the four Spitzer-IRS modules (SH, SL and LL). We produce maps of the flux distribution of the starburst tracers [Ne II], [Ne III], [S III], and [S IV] at 12.81, 15.56, 18.71, and 10.51 μm, respectively, and a map of the AGN narrow-line region tracer [Ne V] at 14.32 μm. We determine the spatial distribution of ISM emission and absorption features, which allow to characterize the physical conditions in the frosty exotic ISM exposed to the hostile radiation from the circumnuclear starburst and the deeply buried AGN.

In Chapter 5 , we estimate the effects (in terms of chemical abundances and excitation) of X-ray irradiation from an AGN, in the atomic and molecular gas of a three-dimensional hydrodynamic model of an AGN torus. A three-dimensional radiative transfer code that uses Monte-Carlo techniques with fixed directions is adapted to use the 3D hydrodynamical model (temperature, density and velocity field) as input. A line tracing approach is used to compute line intensities and profiles for arbitrary viewing angles. Several atomic and molecular diagnostic lines can be tested.

In Chapter 6 , we used the dual color multiple pixel receiver CHAMP$^+$ on the APEX telescope to obtain a $5'.3 \times 4'.7$ map of the $J = 6 \rightarrow 5$ and $J = 7 \rightarrow 6$ transitions of ^{12}CO, the ^{13}CO $J = 6 \rightarrow 5$ line, and the $^3P_2 \rightarrow {}^3P_1$ 370 μm fine-structure transition of [C I] in the nearly edge-on M17 SW nebula. With these high resolution ($7''-9''$) maps ($\sim 3\times3$ pc^2) we constrain the ambient conditions (using LTE and non-LTE radiative transfer models) and spatial distribution of the warm (50 to several hundred K) and dense gas ($n(\mathrm{H_2}) > 10^5$ cm^{-3}) across the interface region of M17 SW.

In Chapter 7 , we probe the ambient conditions and spatial distribution, as well as the influence of UV and (hard) X-rays, of the difuse ($n(\mathrm{H_2}) \sim 10^3$ cm^{-3}) and dense gas ($n(\mathrm{H_2}) > 10^5$ cm^{-3}) towards the core of M17 SW. The dual color single pixel receiver FLASH on the APEX telescope was used to map a 4.1 pc $\times$ 4.7 pc region in emission from the $^3P_1 \rightarrow {}^3P_0$ 609 μm fine-structure transition of [C I], and the APEX-2 SIS receiver was used to map the emission from the $J = 4 \rightarrow 3$ transition of HCN and HCO$^+$ in a smaller region of 2.6 pc $\times$ 1.3 pc.

2

HNC, HCN and CN in Seyfert galaxies

– J.P. Pérez-Beaupuits, S. Aalto and H. Gerebro –

Bright HNC 1–0 emission, rivalling that of HCN 1–0, has been found towards several Seyfert galaxies. This is unexpected since traditionally HNC is a tracer of cold (10 K) gas, and the molecular gas of luminous galaxies like Seyferts is thought to have bulk kinetic temperatures surpassing 50 K. There are four possible explanations for the bright HNC: (a) Large masses of hidden cold gas; (b) chemistry dominated by ion-neutral reactions; (c) chemistry dominated by X-ray radiation; and (d) HNC enhanced through mid-IR pumping. In this work we aim to distinguish the cause of the bright HNC and to model the physical conditions of the HNC and HCN emitting gas. We have used SEST, JCMT and IRAM 30m telescopes to observe HNC 3–2 and HCN 3–2 line emission in a selection of 5 HNC-luminous Seyfert galaxies. We estimate and discuss the excitation conditions of HCN and HNC in NGC 1068, NGC 3079, NGC 2623 and NGC 7469, based on the observed 3–2/1–0 line intensity ratios. We also observed CN 1–0 and 2–1 emission and discuss its role in photon and X-ray dominated regions. HNC 3–2 was detected in 3 galaxies (NGC 3079, NGC 1068 and NGC 2623). Not detected in NGC 7469. HCN 3–2 was detected in NGC 3079, NGC 1068 and NGC 1365, it was not detected in NGC 2623. The HCN 3–2/1–0 ratio is lower than 0.3 only in NGC 3079, whereas the HNC 3–2/1–0 ratio is larger than 0.3 only in NGC 2623. The HCN/HNC 1–0 and 3–2 line ratios are larger than unity in all the galaxies. The HCN/HNC 3–2 line ratio is lower than unity only in NGC 2623, which makes it comparable to galaxies like Arp 220, Mrk 231 and NGC 4418. We conclude that in three of the galaxies the HNC emissions emerge from gas of densities $n \lesssim 10^5$ cm^{-3}, where the chemistry is dominated by ion-neutral reactions. In NGC 1068 the emission of HNC emerges from lower ($< 10^5$ cm^{-3}) density gas than HCN ($> 10^5$ cm^{-3}). Instead, we conclude that the emissions of HNC and HCN emerge from the same gas in NGC 3079. The observed HCN/HNC and CN/HCN line ratios favor a PDR scenario, rather than an XDR one, which is consistent with previous indications of a starburst component in the central regions of these galaxies. However, the $N(\mathrm{HNC})/N(\mathrm{HCN})$ column density ratios obtained for NGC 3079 can be found only in XDR environments.

Originally published in *Astronomy & Astrophysics*, Vol. 476, pp 177–192 (2007)

2.1 Introduction

The hydrogene cyanide, HCN molecule, is commonly used as an extragalactic tracer of molecular gas with densities $n(H_2)$ larger than 10^4 cm^{-3} (e.g. Solomon et al., 1992; Curran et al., 2000; Kohno, 2005). The HCN to CO intensity ratio varies significantly, from 1/3 to 1/40 in starburst galaxies, and it has not been determined whether this variation depends on the dense molecular gas content or on the abundance and/or excitation conditions. In addition, recent results seems to indicate that HCN may not be an unbiased tracer of the dense molecular gas content in LIRGs and ULIRGs (Graciá-Carpio et al., 2006). It is essential, therefore, to use other molecular tracers than HCN, in order to understand the physical conditions in the dense gas.

A molecule of particular interest, for comparison with HCN, is its isomer HNC. The detection of interstellar HNC supports the theory of dominant ion-molecule chemistry in dark molecular clouds. Both species are thought to be created by the same dissociative recombination of $HCNH^+$. This ion can produce HCN and HNC, with approximately equal abundances. Models based only on this scheme would predict then an HNC/HCN ratio ≈ 1. However, the observed HNC/HCN abundance ratios vary significantly between different kinds of molecular clouds - the ratio ranges from 0.03 to 0.4 in warm cores ($T_k > 15$ K), and can be as high as 4.4 in cold cores ($T_k < 15$ K).

The CN (cyanogen radical) molecule is another tracer of dense gas, with a lower (by a factor of 5) critical density than HCN. CN is also chemically linked to HCN and HNC by photodissociations (e.g. Hirota et al., 1999). Surveys of the 1–0 transition of CN and HNC have been done in order to trace a cold, dense phase of the gas in luminous galaxies (Aalto et al., 2002). It was found that the HNC 1–0 luminosities often rivalled those of HCN 1–0. These results seem to contradict the idea of warm ($T_k \gtrsim 50$ K) gas in the centers of luminous galaxies (e.g. Wild et al., 1992; Wall et al., 1993) whose IR luminosities were suggested to originate from star formation rather than AGN activity (Solomon et al., 1992).

According to observations in the vicinity of the hot core of Orion KL, experimental data, chemical steady state and shock models, the HNC/HCN ratio decreases as the temperature and density increase (e.g. Schilke et al., 1992; Talbi et al., 1996; Tachikawa et al., 2003). If a bright HNC 1–0 transition line is nevertheless detected under these conditions, it could be due to the following possible explanations: (a) the presence of large masses of hidden cold gas and dust at high densities ($n > 10^5$ cm^{-3}); (b) chemistry dominated by ion-molecule reactions with $HCNH^+$ at low density ($n \approx 10^4$ cm^{-3}) in regions where the temperature dependence of the HNC abundance becomes weaker; (c) enhancement by mid-IR pumping, also in low density regions where the lines would not be collisionally excited; and (d) the influence of UV-rays in Photon Dominated Regions (PDRs) and/or X-rays in X-ray Dominated Regions (XDRs) at densities $n \gtrsim 10^4$ cm^{-3} and at total column densities $N_{\rm H} > 3 \times 10^{21}$ cm^{-2} (Meijerink & Spaans, 2005).

In the case of CN, observations of its emission towards the Orion A molecular complex (Rodriguez-Franco et al., 1998) suggest that this molecule is also en-

Table 2.1: Sample of galaxies [a].

Galaxy	Seyfert	RA [hh mm ss]	DEC [° ′ ″]	v_{sys} [km s^{-1}]	Distance [b] [Mpc]	Ω_S(CO) [c] [″ ^{2}]	Ω_S(HCN) [d] [″ ^{2}]
NGC 3079	2	10 01 57.805	+55 40 47.20	1116±1	15.0±1.1	15×7.5	5×5
NGC 1068	2	02 42 40.711	-00 00 47.81	1137±3	15.3±1.1	30×30	10×10
NGC 2623	2	08 38 24.090	+25 45 16.80	5549±1	74.6±5.4	8×8	2.6×2.6
NGC 1365	1.8	03 33 36.371	-36 08 25.45	1636±1	22.0±1.6	50×50	16.5×16.5
NGC 7469	1.2	23 03 15.623	+08 52 26.39	4892±2	65.8±4.8	8×8	4×6

a) The Seyfert classification, positions (in equatorial J2000 coordinates) and heliocentric radial velocities were taken from NED.

b) The distances were calculated using the Hubble constant ($H_0 \approx 74.37$ km s^{-1} Mpc^{-1}) estimated by Ngeow & Kanbur (2006).

c) The source sizes of the CO 1–0 transition line were estimated from the maps presented in (Koda et al., 2002) for NGC 3079, (Schinnerer et al., 2000) for NGC 1068, (Bryant & Scoville, 1999) for NGC 2623, (Sandqvist, 1999) for NGC 1365, and (Papadopoulos & Allen, 2000) for NGC 7469. The source sizes for the $J = 2 - 1$ transition line were assumed equal to that of the $J = 1 - 0$ line. For NGC 7469, the source size of the CO 2–1 emission estimated from the corresponding map presented by (Davies et al., 2004) agrees well with the source size estimated for the CO 1–0 line.

d) Source sizes of HCN 1–0 were estimated from the corresponding maps published in Kohno et al. (2000) for NGC 3079, Kohno et al. (2001) and Helfer & Blitz (1995) for NGC 1068, and Davies et al. (2004) for NGC 7469. The source sizes of NGC 2623 and NGC 1365 were estimated using proportions found in NGC 1068 (read text in §3.5). Because of their chemical link, the source sizes of the CN and HNC molecules were assumed the same as that of HCN. Due to the lack of high resolution maps, the source sizes corresponding to the emission of the higher transition lines were assumed equal to that of the $J = 1 - 0$ line.

hanced in PDRs, but particularly in XDRs, where a CN/HCN abundance ratio larger than unity is expected (e.g. Lepp & Dalgarno, 1996; Meijerink et al., 2007).

We have observed low and high transition lines of the HCN, HNC and CN molecules in a group of Seyfert galaxies, which are supposed to host both sources of power, AGN and starburst activity, in their central region. Our interest is to assess the excitation conditions of HCN and HNC, distinguish between the above possible causes of the bright HNC, and to explore the relation between the CN emission, XDRs and dense PDRs in these sources.

In Sec. 2.2 we describe the observations. The results (spectral lines, line intensities and line ratios) are presented in Sec. 2.3. The interpretation of line shapes and gas distribution in the most relevant cases, as well as the possible explanations for the bright HNC and the modelling of the excitation conditions of HCN and HNC are discussed in Sec. 2.4. The conclusions and final remarks of this work are presented in Sec. 2.5.

2.2 Observations

We have used the James Clerk Maxwell Telescope (JCMT) in 2005 to observe the HNC J=3–2 (271 GHz) and the HCN J=3–2 (267 GHz) lines towards a sample of Seyfert galaxies. The sample consists of five Seyfert galaxies of which two are Seyfert 1 type and three are considered mainly Seyfert 2. Table 2.1 lists the coordi-

Table 2.2: Beamsizes & efficiencies.

Transition	ν [GHz]	HPBW [a] [″]		$\eta_{\rm mb}$ [a]		Telescope [a]	
HCN 1-0	88.632	44	28	0.65	0.77	OSO	IRAM
HNC 1-0	90.663	55	27	0.74	0.77	SEST	IRAM
CN 1-0	113.491	45	22	0.71	0.74	SEST	IRAM
CO 1-0	115.271	44	21	0.70	0.74	SEST	IRAM
CN 2-1	226.875	23	11	0.51	0.53	SEST	IRAM
CO 2-1	230.538	20	11	0.66	0.52	JCMT	IRAM
HCN 3-2	265.886	18	9	0.60	0.45	JCMT	IRAM
HNC 3-2	271.981	18	9	0.60	0.44	JCMT	IRAM

a) The columns are divided in two sub-columns (*left*: OSO, SEST, JCMT, and *right* IRAM) indicating the telescope used to obtain the corresponding parameter. The IRAM 30m telescope was used to observe NGC 3079. The other sources were observed with the OSO 20m, SEST and JCMT telescopes.

nates of the center positions observed in these galaxies, their sub-classification as Seyfert galaxies and heliocentric radial velocities, according to the NASA/IPAC Extragalactic Database (NED) (http://nedwww.ipac.caltech.edu/). The distances were calculated assuming a Hubble constant of $H_0 = 74.37 \pm 2.27\ \mathrm{km\,s^{-1}}$ Mpc^{-1} (Ngeow & Kanbur, 2006)).

Observations of CN and HNC J=1–0 (90 GHz) were made in 2002 using the Swedish ESO Southern Telescope (SEST). HCN J=1–0 (88 GHz) data from literature were also used. The system temperatures ranged between 350 K and 430 K. In the case of CN J=1–0 (226 GHz) the weather conditions were not so good, making the system temperature range between 490 K and 760 K. Pointing was checked regularly on SiO masers and the rms was found to be about 3″.

For the SEST observations we alternated between a 500 MHz and 1 GHz backend, depending on weather. Simultaneous observations with the 1 and 3 mm receiver were taking place. In addition, the data of the Seyfert galaxy NGC 3079 obtained during the IRAM survey in 2006 is included in this work. We used the software package XS (written by P. Bergman) to reduce the data and fit the gaussians. Beamsizes and efficiencies are shown in Table 2.2.

2.3 Results

2.3.1 NGC 1068

The molecular line emissions observed in NGC 1068 are shown in Figure 2.1. A first-order polynomial was used in most cases to correct the baselines, with the exception of the HCN 3–2 and CN 2–1 spectra, for which a second-order polynomial was required. The velocity resolution was set to 15 $\mathrm{km\,s^{-1}}$ for CO and CN, whereas a 25 $\mathrm{km\,s^{-1}}$resolution was used for HNC and HCN. These velocity resolutions represent less than 10% of the line widths. The spectra are centered with respect to the heliocentric systemic velocity $\mathrm{v_{sys}} = 1137\ \mathrm{km\,s^{-1}}$ (from NED).

The J=1–0 and J=2–1 lines of CO show a triple structure where the peaks can

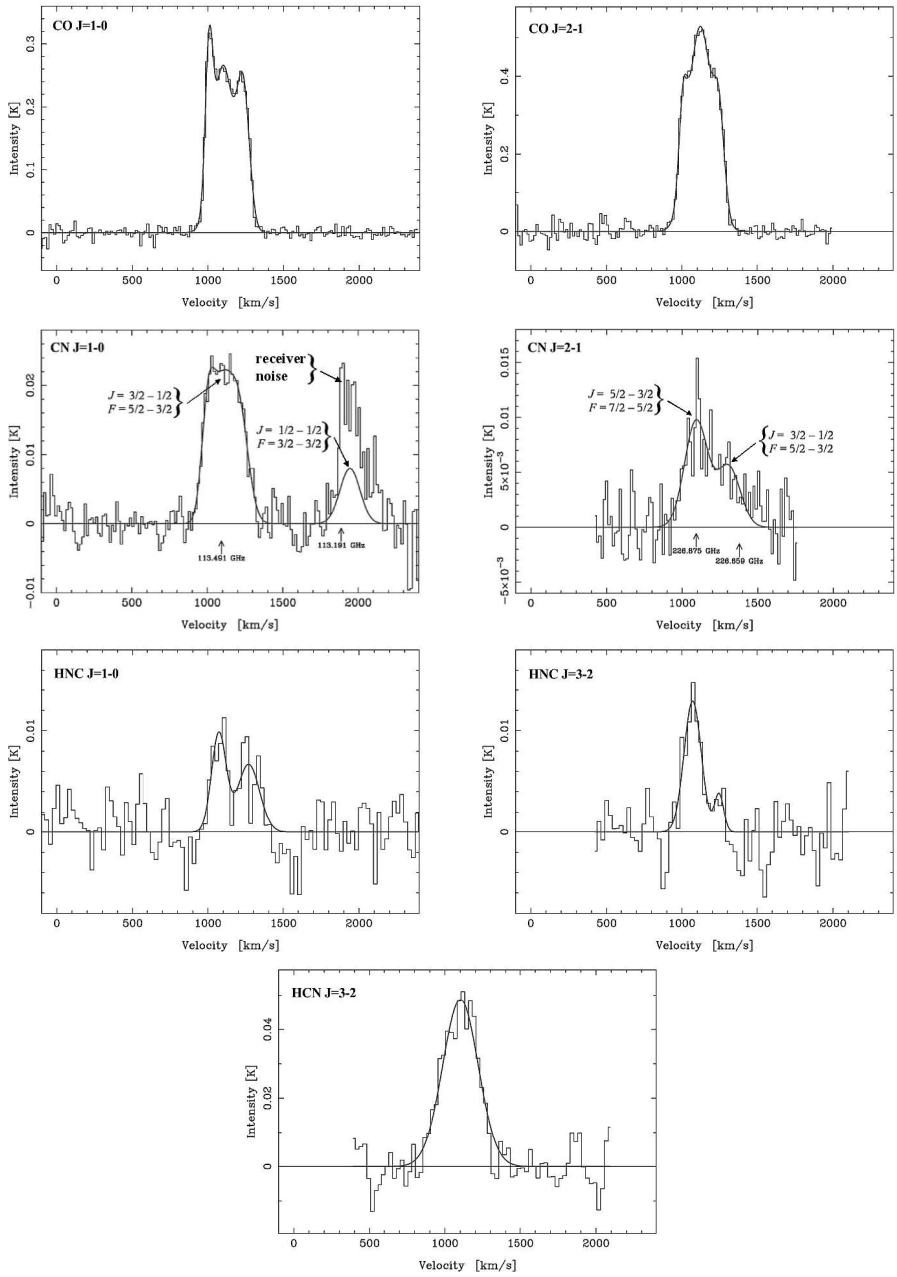

Figure 2.1: Molecular line emissions in **NGC 1068**. The velocity resolution was set to 25 $\mathrm{km\,s^{-1}}$for HNC and HCN, and to 15 $\mathrm{km\,s^{-1}}$for CO and CN. The spectra are centered with respect to the heliocentric systemic velocity $\mathrm{v_{sys}} = 1137\,\mathrm{km\,s^{-1}}$. Emission from the spiral arms are detected in the CO 1-0 line. The CO 2-1 line is dominated by the emission coming from the CND. The two main spingroups of CN are detected in both J=1–0 and J=2–1 transitions. In the CN 1–0 the second spingroup is corrupted by noise in the spectrum. The two spingroups are blended in the CN 2–1 line. The different line shapes (profiles) of the HCN and HNC spectra seem to indicate that their emissions emerge from different regions.

Table 2.3: NGC 1068 line parameters.

Transition	Gaussian Component	V [$\mathrm{km\,s^{-1}}$]	T_A^* [mK]	ΔV [$\mathrm{km\,s^{-1}}$]
CO 1-0	1	1007± 1	225.2±14.9	58± 3
	2	1100± 3	265.1± 3.8	156±11
	3	1234± 2	215.3±10.8	96± 4
CO 2-1	1	1007± 2	206.8±32.5	63± 9
	2	1121± 4	529.3± 8.8	179±16
	3	1245± 3	222.7±37.8	81±10
CN 1-0	1	1001±23	12.8±13.2	94±42
	2	1091±68	19.4± 4.7	154 [a]
	3	1213±32	15.6± 9.5	136±54
	4	1946±26	8.3 [b]	154 [a]
CN 2-1	1	1093± 9	10.4± 0.9	154±66
	2	1289±14	6.2± 0.9	154 [a]
HCN 3-2	1	1103± 7	48.7± 2.4	275±17
HNC 1-0	1	1073±13	9.7± 1.8	114±30
	2	1268±20	6.7± 1.5	170±62
HNC 3-2	1	1071± 9	12.9± 1.8	134±23
	2	1250±24	3.7± 2.5	70±58

[a] The line widths were set to the value found in the main component of the CN 2–1 line.

[b] In order to avoid the effect of the artefact in the backend, the intensity was locked to the value expected for this spingroup.

be attributed mainly to the bars and the spiral arms, as described by Helfer & Blitz (1995).

We detect two of the main spingroups of CN 1–0: the 1–0 (J = 3/2 – 1/2, F = 5/2 – 3/2) line at the center of the spectrum, and the 1-0 (J = 1/2 – 1/2, F = 3/2 – 3/2) line shifted 856 $\mathrm{km\,s^{-1}}$ to the right. This spectrum shows three components as well, however they are hard to distinguish due to the blending. In fact if we freely fit three gaussian components, the uncertainties of the center velocity, amplitude and line width are about 100% or larger. Instead, if we set the line width of the central component to 154 $\mathrm{km\,s^{-1}}$, which corresponds to the line width found for the CN J=2–1 line as described below, we get reasonable values. Only the first gaussian component shows high uncertainties in the amplitude and line width. Since the beam sizes of the CN and CO molecules are similar at the frequencies of the J=1–0 lines, we think that both beams pick up emission coming from the spiral arms and bars. Although, the nuclear region seems to be the predominant component in the case of CN.

Due to the second spingroup is corrupted by noise in the backend, we set the amplitude of the gaussian to 8.3 mK, which corresponds to the expected factor of about 0.43 times the amplitude of the main spingroup, according to the National Institute of Standards and Technology (NIST). The resulting central velocity of the

second component was 1946 $\mathrm{km\,s^{-1}}$($\sim$ 113.169 GHz), i.e., about 22 MHz shifted from the expected frequency for this spingroup.

In the CN 2–1 line, the two spingroups at 226.8746 GHz (2–1, J = 5/2 – 3/2, F = 7/2 – 5/2) and 226.6596 GHz (2–1, J = 3/2 – 1/2, F = 5/2 – 3/2) are severely blended since the shift is $\sim$300 $\mathrm{km\,s^{-1}}$. In order to identify the two spingroups we first fit two gaussian components to get the line width of the main spingroup, which is 154 ± 66. We then set this value to both gaussian components and fit again the other parameters. The second spingroup is, in the optically thin limit, a factor 0.54 weaker than the main spingroup. We get a factor ~ 0.6 between the intensities obtained from the gaussian fit. On the other hand, the resulting center velocity of the second component is 1289 $\mathrm{km\,s^{-1}}$, which corresponds to a shift of about 68 MHz with respect to the expected frequency of the second spingroup. Besides the noise in the data, this shift may also be produced by the influence of the unresolved spingroups, (2–1, J = 3/2 – 1/2, F = 1/2 – 1/2) and (2–1, J = 3/2 – 1/2, F = 3/2 – 1/2), located in between the two main spingroups. Together, these inter-spingroups would produce an intensity comparable to that of the second spingroup.

The line shape and intensity of the CN 2–1 spectrum differs from the one obtained by (Usero et al., 2004) (thereafter U04). Besides the lack of baseline coverage observed in the U04 spectrum, there is a substantial discrepancy between the estimated source sizes. In U04 the emission of most of the molecules was assumed to emerge from a $6''\times4''$ region, which corresponds to their estimate of the size of the circumnuclear disk (CND), based on the CO 2–1 high resolution map presented by (Schinnerer et al., 2000).

If we correct the peak antenna temperature ($T_A^* \approx 9.7$ mK) of our CN 2–1 spectrum, in order to obtain the main beam brightness temperature $T_{\rm mb}$ in the same way done in U04 ($T_{mb} = T_A^* \times \eta_{mb}^{-1} \times \Omega_{mb} \times \Omega_S^{-1}$), we get a peak $T_{\rm mb}$ of about 0.42 K, which is about 0.18 K (or a factor of $\sim$1.8) larger than the peak temperature obtained by U04.

Due to the chemical link between HCN and CN, here we rather estimate the source size based on the high resolution map of HCN 1–0, published in Helfer & Blitz (1995). We estimate that the emissions of HCN, CN (and very likely HNC as well) emerge from a more extended region of about $10''\times10''$. This source size can also be inferred from the HCN 1–0 map presented by Kohno et al. (2001).

By correcting the peak antenna temperature (as described in Sec. 2.3.5) we get a peak $T_{\rm mb}$ of about 0.12 K, which is a factor 2 smaller than what was found by U04.

The HCN 3–2 line has its center velocity at $V \approx 1103$ $\mathrm{km\,s^{-1}}$ which coincides with the main HCN emission shown in the position-velocity (*p-v*) map by Tacconi et al. (1994) (this is discussed in Sec. 2.4). The line width and line shape of this spectrum are consistent with HCN 1–0 spectra published in previous work (Nguyen et al., 1992; Curran et al., 2000).

The HNC spectra present a double peak profile in which the main peak has its center velocity at $V \approx 1070$ $\mathrm{km\,s^{-1}}$ in both the J=1–0 and J=3–2 transitions. However, the line shape and intensity of the HNC 1–0 spectrum differs from the

one obtained by Hüttemeister et al. (1995)). The HNC 3–2 spectrum seems to be affected by noise, since the amplitude and line width of the secondary component have uncertainties larger than 50%. The different line shapes observed between the HNC and HCN spectra would indicate that they emerge from regions of different kinematics. The line parameters are summarized in Table 2.3.

2.3.2 NGC 1365

Figure 2.2 shows the molecular line emissions observed in NGC 1365. Without considering the second spingroups of CN, all the molecular spectra of NGC 1365 present a double peak structure, irrespective of the beam size or line transition.

This double peak structure can also be seen in the CO 2–1 and CO 3–2 spectra showed in Sandqvist et al. (1995) and in Sandqvist (1999), respectively.

The two strongest spingroups of the CN 1–0 line are also detected in this galaxy, with a double peak structure at the nuclear region. The strongest peak was used as reference for the main spingroup. We first fit two gaussian components to the main group and then we set the line width of the second spingroup, observed at around 2400 $\mathrm{km\,s^{-1}}$, to the value found for the main spingroup. The proportion found between the amplitude of the spingroups is about 0.3 instead of the expected value of 0.43, according to NIST. The data around the second spingroup are strongly affected by noise, so its central velocity is shifted by about 50 $\mathrm{km\,s^{-1}}$ from the expected value of about 800 $\mathrm{km\,s^{-1}}$.

In the CN 2–1 line, the second spingroup overlaps with the double structure itself. The line widths of the two spingroups are set according to the value found for the CN 1–0 line. Given their combined intrinsic line strengths, the integrated line intensity ratio of the two spingroups is expected to be about 1.85 (assuming optically thin emission). If we also set the line width of the second peak of the double structure at 212 $\mathrm{km\,s^{-1}}$, as found for CN 1–0, we get a proportion of about 0.4 between the two spingroups. Instead, if we set the amplitude of the second spingroup to 5.7 mK (the expected proportion) and we fit the line width of the double peak structure, we get a value of 181 $\mathrm{km\,s^{-1}}$, which is about 30 $\mathrm{km\,s^{-1}}$less than the width found in the CN 1–0 line. In any case, the center velocity of the second spingroup is shifted by about 30 $\mathrm{km\,s^{-1}}$ more than the expected velocity.

The HNC 1–0 and HCN 3–2 spectra have a structure similar to that of the CN 1–0 spectrum. Note that in CO 1–0 the double-peak is more pronounced than in the CN, HCN or HNC spectra, where the low velocity peak dominates. The line parameters are summarized in Table 2.4.

2.3.3 NGC 3079

The molecular line emissions observed in NGC 3079 are shown in Figure 2.3. The spectra are centered with respect to the heliocentric systemic velocity $\mathrm{v_{sys}} = 1116$ $\mathrm{km\,s^{-1}}$. The velocity resolution was set to 20 $\mathrm{km\,s^{-1}}$ for HNC and HCN, and to 10 $\mathrm{km\,s^{-1}}$ for CO and CN. Four structures are observed in the CO lines, which are not present in the other spectra. The CO lines are picking up extended lower density

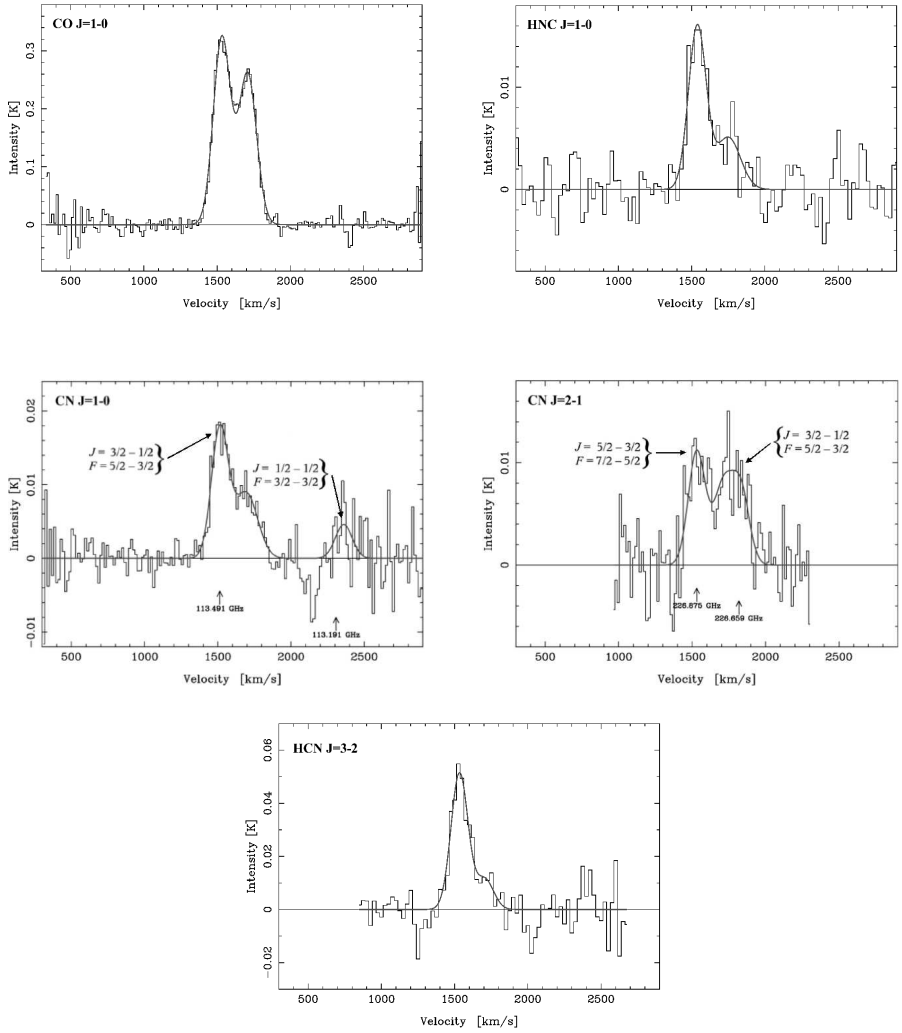

Figure 2.2: Molecular line emissions in **NGC 1365**. The spectra are centered with respect to the heliocentric systemic velocity $v_{sys} = 1636\ km\,s^{-1}$. The velocity resolution was set to 25 $km\,s^{-1}$for HNC and HCN, and to 15 $km\,s^{-1}$for CO and CN. A double peak line shape is observed in all the spectra. This structure is related with the double peak emission coming from the center of the galaxy. In the CN spectra both spingroups are detected. The second spingroup of the CN 2–1 line overlaps the double structure itself.

Table 2.4: NGC 1365 line parameters.

Transition	Gaussian Component	V [$\mathrm{km\,s^{-1}}$]	T_A^* [mK]	ΔV [$\mathrm{km\,s^{-1}}$]
CO 1-0	1	1532± 2	322.7±5.2	136±4
	2	1709± 3	260.3±5.0	142±5
CN 1-0	1	1511±13	16.8±3.5	130±25
	2	1685±33	8.9±1.4	212±92
	3	2356±18	4.7±1.2	130 [a]
CN 2-1	1	1526±11	10.4±1.5	130 [a]
	2	1727±35	8.4±1.9	212 [b]
	3	1846±35	4.11±3.5	130 [a]
HCN 3-2	1	1534± 5	51.4±3.4	136±13
	2	1706±25	11.4±3.3	142 [c]
HNC 1-0	1	1539±11	16.0±1.7	142±23
	2	1750±34	5.1±1.4	195±98

[a] The two spingroups are supposed to have the same line width, so these were set according to the value found for the main spingroup of the CN 1–0 line.

[b] The line width of the second component of the double peak structure was set to the corresponding value found in the CN 1–0 line.

[c] The second component of HCN 3–2 seems to be affected by noise, so its line width was locked at $\Delta V = 142$ $\mathrm{km\,s^{-1}}$, i.e., the corresponding line width of the CO 1–0 line.

gas, compared to the CN lines (which have similar beam size). Hence the difference in line shape.

The CN 1-0 line present a double peak structure. Only the main spingroup (J = 3/2 - 1/2, F = 5/2 - 3/2) of the CN 1-0 line is observed since the second spingroup falls beyond the bandwidth of the backend. In the CN 2-1 line, the two main spingroups, (J = 5/2 - 3/2, F = 7/2 - 5/2) and (J = 3/2 - 1/2, F = 5/2 - 3/2), are detected. But they are severely blended and merged with the double peak structure. In this case, only two gaussians were fitted because a third (middle) component presented large uncertainties in both the amplitude and line width, due to the noise in the spectrum. The two components are separated by only 254 $\mathrm{km\,s^{-1}}$, and the proportion between their amplitudes is about 0.65. The difference between these and the expected values is attributed to the noise and the blending of the emission of the second spingroup.

The HCN spectrum of the J=1–0 and J=3–2 transitions agree with the HCN 1–0 spectrum obtained by Nguyen et al. (1992).

The HNC 1–0 spectrum is different from the tentative detection presented by Hüttemeister et al. (1995), which is broader and more intense than the spectrum showed here. Besides the similar line shapes, our HCN and HNC spectra extends from 900 $\mathrm{km\,s^{-1}}$ to 1300 $\mathrm{km\,s^{-1}}$. Instead, the HNC spectrum showed in Hüttemeister et al. (1995) peaks at around 1300 $\mathrm{km\,s^{-1}}$. Hence, we believe that our HNC detections are correct. In this case, because of the similar line shapes and widths

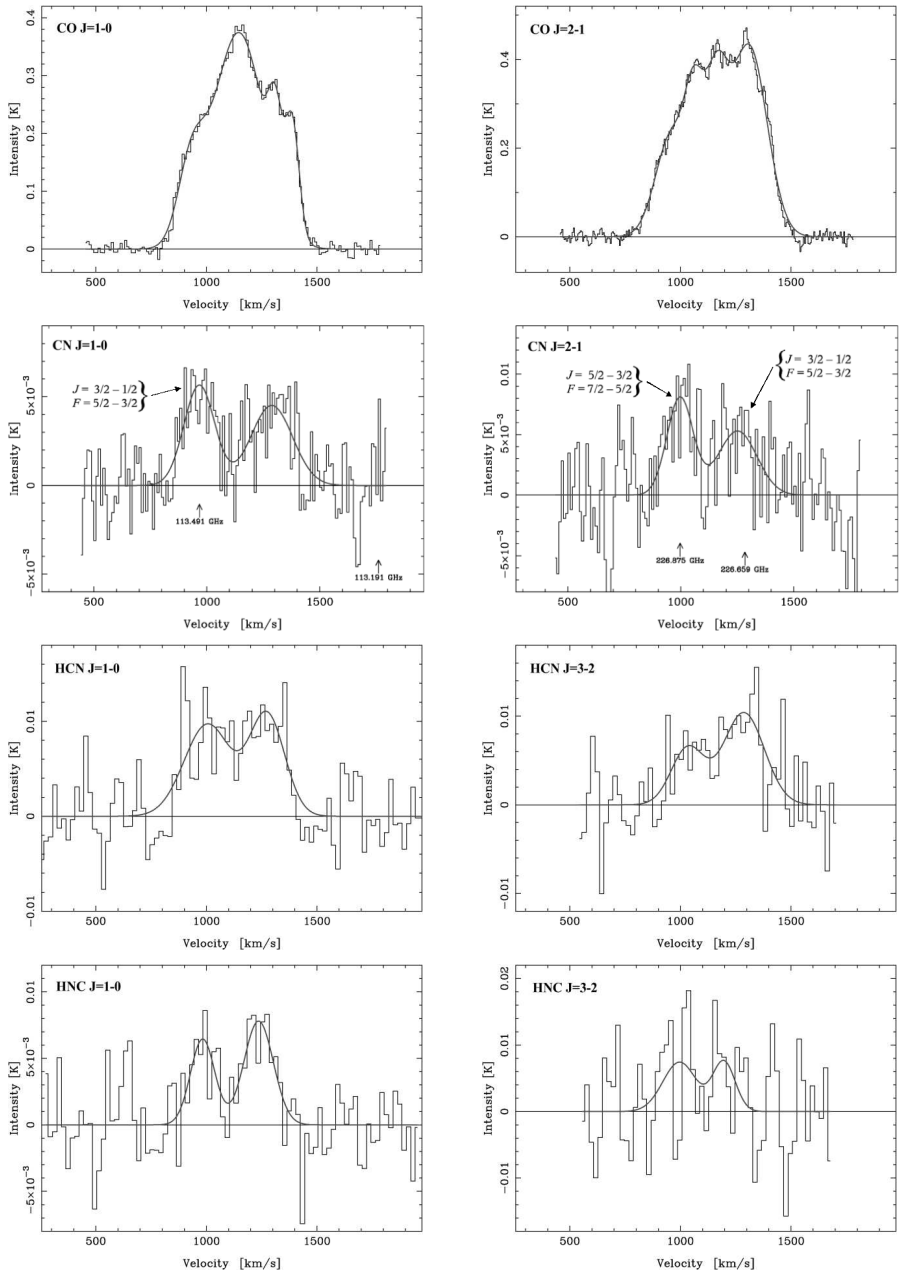

Figure 2.3: Molecular line emissions in **NGC 3079**. The velocity resolution was set to 20 $\mathrm{km\,s^{-1}}$for HNC and HCN, and to 10 $\mathrm{km\,s^{-1}}$for CO and CN. The spectra are centered with respect to the heliocentric systemic velocity $\mathrm{v_{sys}} = 1116\ \mathrm{km\,s^{-1}}$. Emission from four structures are observed in the CO lines. Only the main spingroup is observed in the CN 1–0 line. The second spingroup is on the right edge of the spectrum, out of the bandwidth. Instead, both spingroups are observed in the CN 2–1 line, although the second spingroup overlaps the double structure of the CN emission. The both transitions of HCN and HNC have similar line shapes, which indicates that their emissions emerge from the same region.

Table 2.5: NGC 3079 line parameters.

Transition	Gaussian Component	V [$\mathrm{km\,s^{-1}}$]	T_A^* [mK]	ΔV [$\mathrm{km\,s^{-1}}$]
CO 1-0	1	932± 4	129.4±11.8	143± 9
	2	1146± 3	374.3± 3.3	269±13
	3	1312± 6	145.1±13.1	74± 9
	4	1389± 5	186.3± 9.1	72± 5
CO 2-1	1	964±15	233.3±18.9	175±18
	2	1062±18	224.3±84.9	98±18
	3	1160±20	321.7±35.3	126±20
	4	1311±14	428.3± 9.4	190± 7
CN 1-0	1	967± 9	5.6± 0.6	162±23
	2	1287±15	4.5± 0.6	215±33
CN 2-1	1	997±14	8.1± 1.5	137±34
	2	1251±25	5.3± 1.3	203±69
HCN 1-0	1	1005±30	9.7± 1.4	249±73
	2	1274±21	10.7± 1.7	188±49
HCN 3-2	1	1033±42	6.4± 2.1	176±93
	2	1287±32	10.4± 1.8	219±70
HNC 1-0	1	983±17	6.5± 1.7	129±41
	2	1236±21	7.8± 1.5	157±38
HNC 3-2	1	996±48	7.4± 3.2	178±124
	2	1197±43	7.5± 3.8	120±90

(although the HNC 3–2 line is strongly affected by noise, and its peak intensities have uncertainties between 40% and 50%.), the HCN and HNC emissions are likely emerging from the same gas. The line parameters are summarized in Table 2.5.

2.3.4 NGC 2623 and NGC 7469

The HNC 3–2 line emission observed in NGC 2623 is shown in the *top left panel* of Figure 2.4. The velocity resolution was set to 25 $\mathrm{km\,s^{-1}}$. The spectrum is centered with respect to the heliocentric systemic velocity $\mathrm{v_{sys}} = 5535\ \mathrm{km\,s^{-1}}$(NED). After a total integration time of 2 hours we do not detect HCN 3–2 emission in this galaxy.

The *top right panel* of Figure 2.4 shows the CO 2-1 spectrum observed in NGC 7469. The velocity resolution was set to 15 $\mathrm{km\,s^{-1}}$. The spectrum is centered with respect to the systemic velocity $\mathrm{v_{sys}} = 4892\ \mathrm{km\,s^{-1}}$. The CO spectrum shows a double peak structure, like the one observed in NGC 1365. We observed the HNC 3–2 line for about 1 hour of integration time, but we do not detect any emission. The *bottom panels* show the spectra of the not detected lines. The line parameters of the detected transition lines are summarized in Table 2.6.

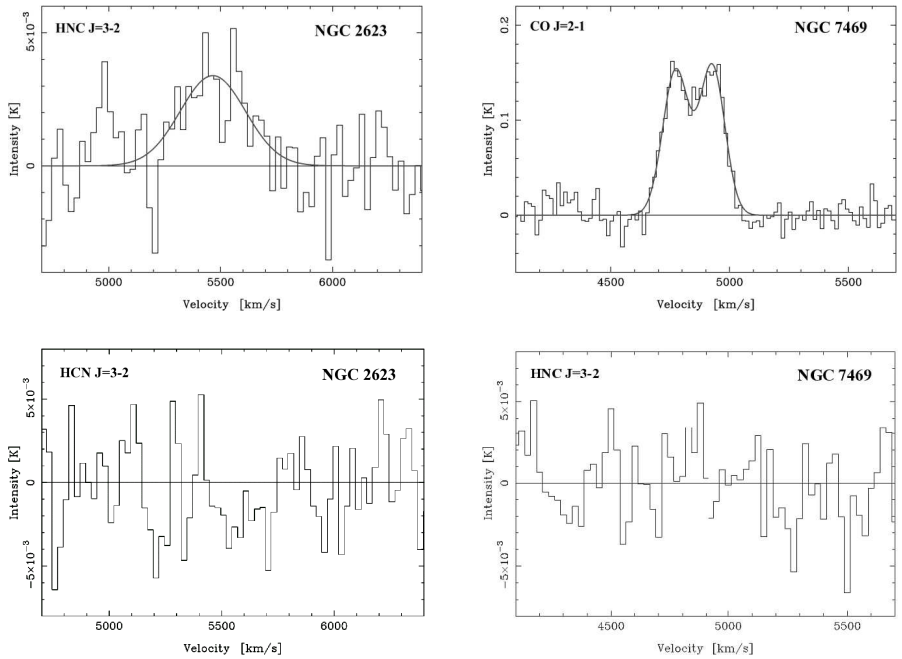

Figure 2.4: Molecular line emissions in **NGC 2623** (*left*) and **NGC 7469** (*right*). The velocity resolution was set to 25 $\mathrm{km\,s^{-1}}$for HNC and to 15 $\mathrm{km\,s^{-1}}$for CO. The spectra are centered with respect to the heliocentric systemic velocities $\mathrm{v_{sys}} = 5535$ and $\mathrm{v_{sys}} = 4892\ \mathrm{km\,s^{-1}}$for NGC 2623 and NGC 7469, respectively. We do not detect HCN 3-2 emission in NGC 2623 nor HNC 3-2 in NGC 7469. Their observed intensities were less than 2σ.

Table 2.6: Line parameters of NGC 2623 and NGC 7469. The third column indicate the gaussian components (G.C.) used to fit the spectral lines.

Source	Transition	G.C.	V [$\mathrm{km\,s^{-1}}$]	T_A^* [mK]	ΔV [$\mathrm{km\,s^{-1}}$]
N2623	HNC 3-2	1	5465±34	3.4± 0.7	337±88
N7469	CO 2-1	1	4773±0	0.15± 0	126±0
		2	4927±0	0.16± 0	123±0

2.3.5 Line intensities and ratios

The velocity integrated intensities are showed in Table 2.7. In order to compute the line intensity ratios were corrected for the different beam sizes obtained with different frequencies and telescopes, according to the correction factors defined for compact sources in Rohlfs & Wilson (2004). In the case of extended sources ($\Omega_S > \Omega_{mb}$) the ratios were corrected for the main beam filling factor, which was approximated as $f_{mb} = \Omega_S/(\Omega_S+\Omega_{mb})$. The beams, as well as the source structures, were assumed to be gaussians.

Table 2.7: Velocity-integrated intensities [a].

Galaxy	I(CO) 1-0	I(CO) 2-1	I(CN) 1-0	I(CN) 2-1	I(HCN) 1-0 [b]	I(HCN) 3-2	I(HNC) 1-0	I(HNC) 3-2
NGC 3079	205.8±20.6	375.4±37.6	2.7±0.4	4.5±0.7	5.7±0.8	8.0±1.4	2.9±0.5	5.0±1.9
NGC 1068	113.7±11.4	203.6±20.5	9.4±1.0	6.1±0.7	10.0±1.7	22.7±2.5	3.2±0.5	3.5±0.6
NGC 2623	30.2±3.2 [c]	-	$\lesssim$1.3 [c]	-	-	$\lesssim$0.5	0.9±0.3 [c]	1.8±0.4
NGC 1365	122.3±12.3	181.0±18.1 [d]	5.9±0.7	7.5±0.9	6.0±0.1	15.0±2.0	4.7±0.6	-
NGC 7469	25.6±3.8 [e]	61.5±6.4	1.8±0.3 [c]	-	1.5±0.3	-	1.1±0.2 [c]	$\lesssim$0.8

a) The values refer to the main-beam brightness temperature, $I_{\rm mb}$, in [K km s^{-1}]. The errors and upper limits correspond to 1σ (defined by the r.m.s. in the spectra) and added in quadrature to the 10% of error considered for the main beam efficiencies, $\eta_{\rm mb}$, reported in Table 2.2 and by the Onsala Space Observatory (OSO).

b) HCN 1–0 integrated intensities reported by Curran et al. (2000) corrected for a main-beam efficiency of 0.65, according to the on-line values reported by OSO. Our own data are reported for NGC 3079.

c) Integrated intensities reported by Aalto et al. (2002). The values were rounded to one decimal figure and corrected by the main beam efficiencies reported by OSO, 0.64, 0.45 and 0.43, of the J=1–0 transition of HNC, CN and CO, respectively.

d) CO 2–1 integrated intensity obtained by Sandqvist et al. (1995). A 10% of error was assumed for the reported intensity.

e) CO 1–0 integrated intensity derived from Curran et al. (2000) considering a main beam efficiency of 0.43 according to the values reported by OSO.

The source sizes reported in Table 2.1 were estimated from high resolution maps available in the literature. For NGC 3079 a source size of $15'' \times 7.5''$ was estimated for the CO 1–0 emission, considering only intensities above 15% of the peak integrated intensity of the contour map presented by Koda et al. (2002). In NGC 1068 most of the CO 1–0 emission emerges from the two spiral arms, with the largest extension of $\sim$40" (e.g. Helfer & Blitz, 1995; Schinnerer et al., 2000). Considering intensities above 20% of the peak emission of the high resolution map by Schinnerer et al. (2000) the source size of the CO 1-0 emission in NGC 1068 was estimated as $30'' \times 30''$. For NGC 2623 a source size of $8'' \times 8''$ was estimated from the CO 1–0 map presented in Bryant & Scoville (1999), which agrees well with the estimate made by Casoli et al. (1988).

In the case of NGC 1365 the CO emission is concentrated in the nuclear and bar regions (Sandqvist et al., 1995). Hence the source size of the CO emission was estimated as $50'' \times 50''$, corresponding to intensities above 20% of the peak emission in the CO 3–2 map by (Sandqvist, 1999).

From Papadopoulos & Allen (2000) and Davies et al. (2004) the source size of the CO emission in NGC 7469 was estimated as $8'' \times 8''$, which correspond to intensities above 40% of the peak emission in the high resolution map by Davies et al. (2004). The criteria of selection of the source size of CO varies depending on the gradient of the emission observed in the different sources.

The source size of the high density tracers CN, HCN and HNC were estimated

Table 2.8: Line intensity ratios.

Galaxy	CO $\frac{2-1}{1-0}$	CN $\frac{2-1}{1-0}$	HCN $\frac{3-2}{1-0}$	HNC $\frac{3-2}{1-0}$
NGC 3079	0.77±0.20	0.48±0.15	0.18±0.06	0.25±0.12
NGC 1068	0.81±0.21[a]	0.19±0.05	0.47±0.14	0.15±0.05
NGC 2623	[b]	-	-	0.36±0.15
NGC 1365	0.84±0.12[c]	0.44±0.12	0.42±0.12	-
NGC 7469	0.97±0.28	-	-	$\lesssim 0.20$

a) For NGC 1068 we corrected the JCMT CO J=2–1 observations to the beam size of the SEST CO J=1–0 line, applying the factor 20/44, the ratio between the respective beams. With this, the beam dilution effect is cancelled in both transition lines.

b) See Casoli et al. (1988).

c) For NGC 1365 we also corrected the CO J=2–1 observations to the beam size of the CO J=1–0 line, applying the factor 25/44 between the respective SEST beams. The ratio given above is slightly higher than the one reported by Sandqvist et al. (1995).

through HCN maps available in the literature. In all these maps, we observed that the HCN 1–0 emissions emerge mainly from the nuclear region of the galaxies. Since there are no published maps of CN nor HNC emissions for the galaxies studied here, the corresponding source sizes were considered equal to that of the HCN emission, due to their chemical link. Since there are no HCN maps for NGC 1365 and NGC 2623, the factor $\sqrt{\Omega_S(\mathrm{HCN})}/\sqrt{\Omega_S(\mathrm{CO})} \approx 0.33$ found in NGC 1068 was used to estimate the source size of the HCN 1–0 emission, based on their corresponding $\Omega_S(\mathrm{CO})$. The estimated $\Omega_S(\mathrm{HCN})$ are shown in Table 2.1.

The line ratios were computed assuming an error of 10% in the reported beam efficiencies η_{mb}, 5% of error in the main beam θ_{mb} (Table 2.2), and a 10% error in the estimated source sizes θ_S (Table 2.1). The obtained ratios are shown in Table 2.8. From these ratios we can conclude that CO, as well as the high density tracers - CN, HCN and HNC - are subthermally excited.

2.4 Discussion

2.4.1 The distribution of dense gas

We compare the spectral shape of the high density tracers with HCN and CO position-velocity maps available in the literature in order to address the location of the dense gas.

NGC 1068

In NGC 1068 the two outer peaks of the CO 1–0 spectrum (Figure 2.1) coincide with the maximum double peak emission seen in the CO position-velocity (p-v) map obtained by Helfer & Blitz (1995), so they can be attributed to the emission emerging from the spiral arms. The center is attributed to the emission emerging from the CND, as can be inferred from the CO 2–1 spectrum (Figure 2.1). This center

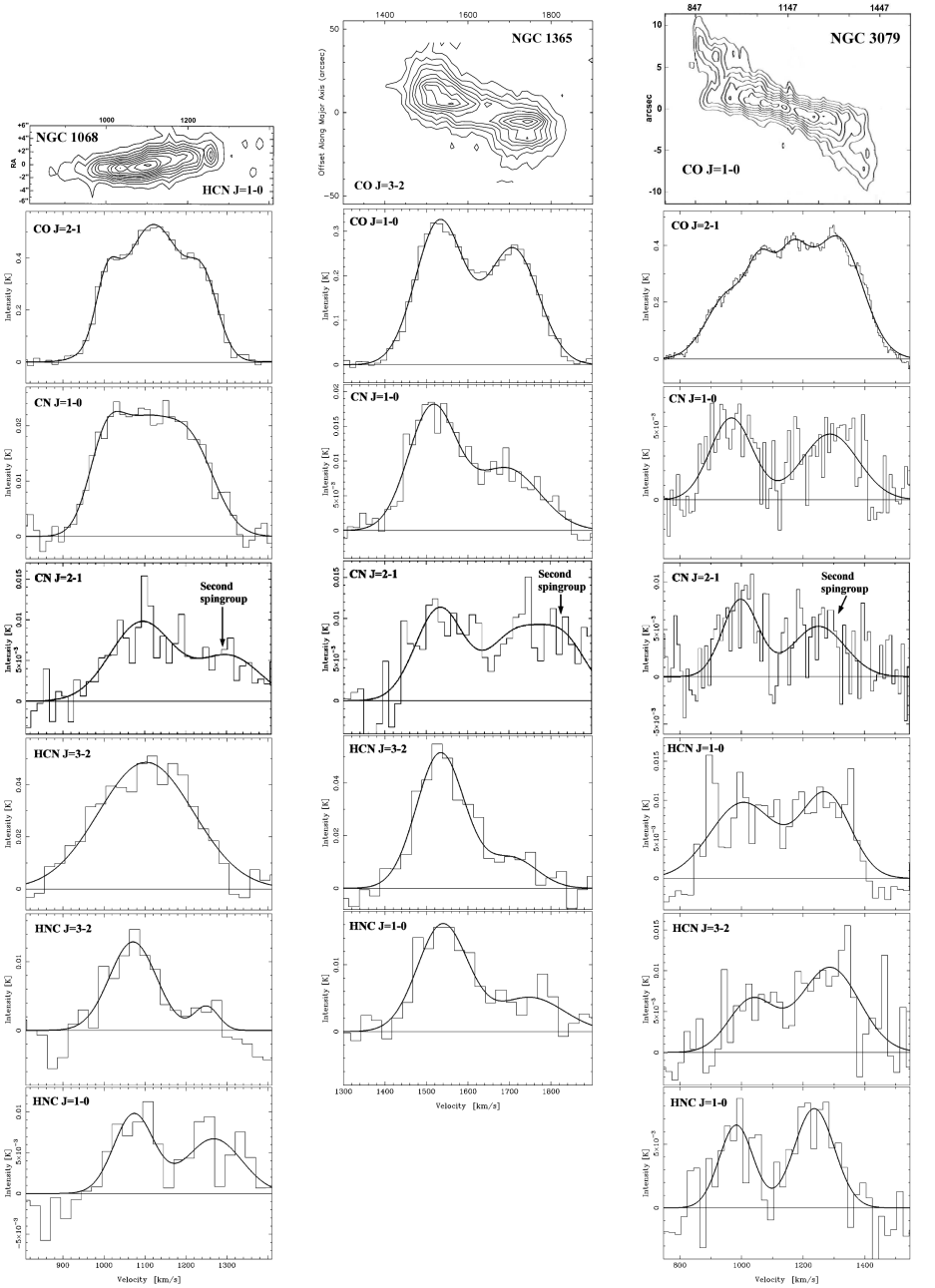

Figure 2.5: (*Top-left panel*) Position-velocity (*p-v*) map of HCN 1–0 emission in **NGC 1068**, adapted from Tacconi et al. (1994). The spectra below are the respective emission lines of Figure 2.1, re-rescaled to fit the velocity scale of the HCN *p-v* map. (*Top-middle panel*) Position-velocity map of CO 3–2 emission in **NGC 1365**, adapted from Sandqvist (1999). The spectra below are the re-scaled versions of the ones shown in Figure 2.2. (*Top-right panel*) Position-velocity map of CO 1–0 emission in **NGC 3079**, adapted from Koda et al. (2002). The spectra below are the re-scaled versions of the ones shown in Figure 2.3.

peak coincides with the maximum HCN emission at 1100 $\mathrm{km\,s^{-1}}$seen in the HCN p-v map obtained by Tacconi et al. (1994). This *p-v* map is shown in the *left panel* of Figure 2.5 for comparison, along with the corresponding scaled spectra observed in NGC 1068.

The main spingroup of the CN 1–0 line (Figure 2.1) shows a shape similar to that of the CO 1–0 line. So contributions of emission coming from the CND, as well as from the spiral arms, can also be inferred. The main spingroup of the CN 2–1 spectrum also coincides with the maximum HCN emission around 1100 $\mathrm{km\,s^{-1}}$.

The HCN spectra seem to contain two components, although we fit only one gaussian to the spectrum. The main component fits the region in the *p-v* where the strongest HCN emission is coming from. The secondary component might be attributed to the secondary peak emission of HCN, observed around 1035 $\mathrm{km\,s^{-1}}$. Another smaller peak is seen in the *p-v* map around 1255 $\mathrm{km\,s^{-1}}$, but this component is not detected in the HCN spectra.

In the HNC spectra, instead, two clear components are observed. The main component has a center velocity of 1073 $\mathrm{km\,s^{-1}}$ which lies in between the two main peaks of the HCN emission observed in the corresponding *p-v* map. With respect to the CO *p-v* map (Helfer & Blitz, 1995), the main HNC component comes from a region where the CO emission is faint. Instead, the secondary component of HNC seems to emerge from a region around 1250 $\mathrm{km\,s^{-1}}$, which corresponds to the secondary peak emission in the CO *p-v* map, and roughly to the third peak of the HCN emission in the respective map. Although, the latter is uncertain due to the noise in the spectra.

NGC 1365

On top of the *middle panel* of Figure 2.5 we show the CO 3–2 *p-v* map of the central region of NGC 1365, from (Sandqvist, 1999). The spectra below correspond to the re-scaled spectra shown in Figure 2.2. The double peak structure of the spectra coincides fairly well with the double peak emission observed in the *p-v* map. The left components of the spectra seem to emerge from a region around 1530 $\mathrm{km\,s^{-1}}$.

The right components of most of the spectra could emerge from the region around 1710 $\mathrm{km\,s^{-1}}$, with the exception of the CN 1–0 line. The right component of CN 1–0 seems to emerge from around 1750 $\mathrm{km\,s^{-1}}$which, in turn, coincides with the maximum emission level of the right peak in the CO 3–2 *p-v* map.

The two peaks in the CO 3–2 *p-v* map are of about the same intensity, which is reflected in the ^{12}CO 1–0 spectrum, where both components have intensities $T_A^* \sim 0.3$ K. The ^{12}CO 3–2 and ^{13}CO 1–0 data obtained by (Sandqvist, 1999) also have this feature. However, the CN, HCN and HNC spectra, exhibit a gradient between the intensities of their high and low velocity components. This can also be seen in the HCN 1–0 and HCO^+ 1–0 spectra obtained by (Sandqvist, 1999). This intensity gradient could be due to either a larger abundance of the species, or to a higher excitation in the corresponding region of the lower velocities.

Since the observed double peak structure does not change with the beam size (one single feature), we think that the observed nucleus of NGC 1365 lacks a fore-

ground circumnuclear disk, i.e., it is consistent with a Seyfert 1 nucleus.

NGC 3079

The four-peak structure observed in NGC 3079 can be identified in the CO 1–0 *p-v* map of Koda et al. (2002). The *top-right* panel of Figure 2.5 shows an adaptation of the Fig.10 in Koda et al. (2002) with 0" offset along the minor axis of NGC 3079. Since this galaxy is almost edge-on, most of the CO emission is probably coming from the spiral arms, besides the nuclear region. Instead, the high density tracers are expected to be mostly nuclear, as in the case of NGC 1068. This can explain the double-peak structure of the line shape of the CN, HCN and HNC molecules, in contrast to the CO lines.

Note that in this case the CN spectra are slightly dominated by the lower-velocity peak, as in the case of NGC 1068 and NGC 1365, whereas the HCN and HNC spectra of NGC 3079 are dominated by the higher-velocity peaks. The lower and higher velocity peaks are not perfectly aligned. The maximum separation between the peaks is $\sim 80\ \mathrm{km\,s^{-1}}$for the lower-velocity peaks and $\sim 60\ \mathrm{km\,s^{-1}}$for the higher-velocity peaks. The lower-velocity peaks are centered around 1000 $\mathrm{km\,s^{-1}}$and the higher-velocity peaks around 1270 $\mathrm{km\,s^{-1}}$, which means the high density tracers tend to avoid the peaks of the CO 2–1 emission.

Since the line shapes of CN, HCN and HNC are similar, and they do not change with the beam size, their emissions likely emerge from the nuclear region in this galaxy, in contrast to the case of NGC 1068, where the line shape of the HCN emission changes with the beam size.

2.4.2 The HCN/HNC line ratios

The line intensity ratios between HCN and the other high density tracers (HNC and CN) are shown in Table 2.9. Below we discuss the implicances of the HCN/HNC ratios.

NGC 1068: The HCN/HNC 3–2 & 1–0 line intensity ratios increase towards the CND. The ratio varies from ∼2.0 for the lower transition lines, to ∼6.5 for the higher transition. The large J=1–0 beam picks up emission from both the CND and the starburst ring, whereas the J=3–2 beam picks up emission coming mainly from the CND. This could be interpreted either as that the abundance ratio differs between the starburst ring and the CND, or that the abundance is actually the same but the physical conditions are different in these two regions. On the other hand, there could also be optical depth effects since the difference in the ratios is consistent with a larger optical depth in the J=1–0 transition line of HNC. In Sec. 2.4.3 we estimate the excitation conditions of HCN and HNC, from which we can derive the corresponding optical depths. As described in Figure 2.6, the optical depth of the J=1–0 line of HNC is larger (starting from τ=0.01) than that of the J=3–2 line (which starts from τ=0.003) in almost all the possible excitation conditions. In the case of HCN, the situation is the opposite. The lowest optical depth of the HCN J=1–0 line is 0.03, whereas in the J=3–2 line is 0.32. In any case, X[HCN]/X[HNC]

Table 2.9: Intensity ratios between the high density tracers.

Galaxy	$\frac{\text{HCN}}{\text{HNC}}$ 1-0	$\frac{\text{HCN}}{\text{HNC}}$ 3-2	$\frac{\text{CN}}{\text{HNC}}$ 1-0	$\frac{\text{CN } 2-1}{\text{HNC } 3-2}$	$\frac{\text{CN}}{\text{HCN}}$ 1-0	$\frac{\text{CN } 2-1}{\text{HCN } 3-2}$
NGC 3079	2.15±0.67	1.60±0.75	0.64±0.20	1.25±0.58	0.30±0.09	0.78±0.25
NGC 1068	2.01±0.65	6.48±1.95	1.98±0.58	2.58±0.78	0.98±0.29	0.40±0.29
NGC 2623	1.4[a]	$\lesssim$0.26	$\lesssim$0.77[a]	-	$\lesssim$0.5[a]	-
NGC 1365	1.35±0.37	-	0.87±0.25	-	0.64±0.17	0.67±0.19
NGC 7469[b]	1.50±0.57	-	0.85±0.28	-	0.57±0.21	-

a) Ratios reported by Aalto et al. (2002).

b) New ratios computed using the HCN 1-0 source size estimated from (Davies et al., 2004).

is at least 6.5 in the CND. According to Meijerink et al. (2007), this ratio can be found in gas of density $n_{\rm H} \sim 10^5 {\rm cm}^{-3}$ and with PDR conditions, at a distance from the source of $\sim 10^{16}$ cm, if the Habing flux G_0 is about 10^4, or at a slightly larger distance of 2×10^{16} cm, if $G_0 = 10^5$. On the other hand, in an XDR environment, this ratio would be found at a distance of 7×10^{16} cm, if the radiation flux F_{FUV} is 16 erg ${\rm cm}^{-2}$ ${\rm s}^{-1}$, or at a much larger distance of about 2×10^{18} cm, if $F_{FUV} = 160$ erg ${\rm cm}^{-2}$ ${\rm s}^{-1}$.

NGC 3079: The HCN/HNC ratio decreases for the higher transitions. The HNC 3–2 emission rivals that of HCN, making the HCN/HNC 3–2 line ratio only 1.6. As described above, a similar analysis of the expected distribution of these ratios and molecules, in a PDR and XDR environments, can be done based on Meijerink et al. (2007).

NGC 2623: In this galaxy we do not detect HCN 3–2. We estimate an upper limit of 0.26 for the HCN/HNC ratio of the J=3–2 line. We observe that the ratio does not only decreases for the higher transitions, but also this is the only galaxy in our sample where $I({\rm HCN}) < I({\rm HNC})$ in the J=3–2 line, which makes it comparable to galaxies like Arp 220, Mrk 231 and NGC 4418, according to the recent work by Aalto et al. (2007b). They propose that the overluminous HNC can be explained by a pumping effect due to mid-IR background radiation with brightness temperatures $T_{\rm B} \gtrsim 50$ K and densities below critical, or due to the ISM chemistry being affected by X-rays. According to Schilke et al. (1992), shocks are also possible sources of explanation.

The HCN/HNC 1–0 ratio is about 2.0 in NGC 1068 and NGC 3079, and ∼1.4 in the others. This indicates a brighter HNC emission in NGC 2623, NGC 1365 and NGC 7469. Luminous HNC in galaxies may have the following plausible explanations:

a) **Large masses of hidden cold gas and dust**.
If the HCN and HNC emission is emerging from gas of densities $n({\rm H}_2) > 10^5$ ${\rm cm}^{-3}$ then the HNC chemistry would be dominated by reactions like ${\rm HNC} + {\rm O} \rightarrow {\rm CO} + {\rm NH}$ which would destroy HNC at higher temperatures. Thus, at

high gas densities, a bright HNC line would imply a considerable amount of cold ($T_k < 24$ K) dense gas.

b) **Chemistry dominated by ion-neutral reactions.**
If, however, the bulk of the HCN and HNC emission is emerging from gas of densities $\sim 10^4$ cm^{-3} then the relative HNC abundance may be substantial, despite the high temperature. The reason for this is that, at lower densities, reactions with $HCNH^+$ (HCN and HNC reacts with H_3^+ to form $HCNH^+$) become more important. The ion abundance is higher and once HCN and HNC become protonated, $HCNH^+$ will recombine to produce either HCN or HNC with 50% probability. This scenario is interesting since the electron and ion abundance is likely higher in PDRs Photon Dominated Regions (PDRs) (e.g. Tielens & Hollenbach, 1985; Hollenbach & Tielens, 1999). Therefore, in a PDR chemistry, the connection between HNC and kinetic temperature may be weak since we expect the $HCNH^+$ reactions to be important.

c) **Chemistry dominated by hard X-rays.**
The X-ray irradiation of molecular gas leads to a so called X-ray dominated region (XDR) (e.g. Maloney et al., 1996) similar to PDRs associated with bright UV sources. The more energetic (1-100 keV) X-ray photons penetrate large columns ($10^{22} - 10^{24}$ cm^{-2}) of gas and lead to a different ion-molecule chemistry. Models of XDRs by Meijerink & Spaans (2005) and Meijerink et al. (2007) indicate that the HNC/HCN column density ratio is elevated (and larger than unity) compared to PDRs and quiescent cloud regions for gas densities around 10^5 cm^{-3}.

d) **HNC enhanced through mid-IR pumping.**
Both HCN and HNC may be pumped by an intense mid-IR radiation field boosting the emission also from low density regions where the lines would not be collisionally excited. For HNC the coupling to the field is even stronger than for HCN, thus increasing the probability for IR pumping in extreme galaxies, such as Mrk 231. Ultraluminous galaxies, such as Mrk 231 and Arp 220, have central mid-IR sources with optically thick radiation temperatures well in excess of those necessary to pump the HNC molecule (Soifer et al., 1999). Even if the HNC abundance is lower than HCN, the HNC emission may have a higher filling factor due to the IR pumping (i.e. IR pumped emission from gas clouds otherwise at too low density to excite the HNC molecule) (Aalto et al., 2002).

The study carried out so far allows us to distinguish between the above scenarios in some of the sources presented here. The number density $n(H_2)$ required for alternative (b) is too low to efficiently excite the HNC (or HCN) 1–0 and 3–2 lines, and we should therefore expect subthermal HCN and HNC excitation in this case. An HNC 3–2/1–0 line ratio of 0.3 or less is an indication that the gas densities are below 10^5 cm^{-3}, depending on temperature and column density, as it is discussed in Sec. 2.4.3. A HNC 3–2/1–0 ratio lower than 0.3 is observed in NGC 3079, NGC 1068 and NGC 7469 (Table 2.8).

The ratio ∼0.4 found in NGC 2623 is in the limit between case (a) and (b). On the other hand, case (c) and (d) cannot easily be ruled out. More information is required in order to distinguish between the proposed scenarios, as suggested by Aalto et al. (2007b).

The HCN 3–2/1–0 line ratio is below 0.3 only in NGC 3079, whereas it is larger than 0.4 in NGC 1068 and NGC 1365. This result is interesting since it implies that in NGC 3079 both HCN and HNC emission emerge from the same gas, whereas in NGC 1068 the HNC emission has to emerge from a lower ($< 10^5$ cm^{-3}) density gas than HCN. It would be interesting to see if this result holds for NGC 1365. We expect to obtain the HNC 3–2 data for this galaxy in a future project.

The pumping scenario (c) should lead to a HNC 3–2/1–0 line ratio close to unity. This is not observed either in the HNC or in the HCN data we have. However, it is not possible to rule out this scenario since low excitation may be the result of mid-IR pumping of low density gas. Detailed modelling is needed in this case.

2.4.3 Excitation conditions of HCN and HNC

We used the radiative transfer code RADEX* (van der Tak et al., 2007) to explore a wide range of possible excitation conditions that can lead to the observed line ratios. This code is sensible to the column density of a molecule per line width, and uses a constant temperature and density of the collision partner, which in this case is H_2. Another limitation of RADEX is that it cannot handle large optical depths ($\tau < 100$). Our analysis is not depth dependent and we assume a homogeneous sphere for the escape probability approach. Hence, our models aim to reproduce a sort of average cloud that represent the physical conditions of the emitting gas, which is a well fitted starting model for single dish observations, where all the emissions detected are convolved with the telescope beams.

The grid consists of densities between 10^4 and 10^7 cm^{-3}, temperatures between 4 and 200 K, and column densities per line width between 10^{10} and 10^{18} cm^{-2} km^{-1} s. Excitation maps were generated in order to obtain the total column density per line width ($N/\Delta\upsilon$ cm^{-2} km^{-1} s) as function of the kinetic temperature (T_k K) and the number density of molecular hydrogen ($n(\mathrm{H_2})$ cm^{-3}). The countour lines of the maps describe the dichotomy between temperature and density. This means that, for a given column density, the observed 3–2/1–0 line ratio can be obtained with high temperatures and low densities, or low temperatures and high densities.

The hyperfine structure of the HCN J=1–0 transition line is not included in this study. The extrapolated HCN data of the LAMDA† database were used instead (Schöier et al., 2005). Note that the hyperfine components may be overlapping and may interact radiatively in AGN-like environments. This process requires further analysis and modelling that is not included in RADEX. We are not able to generate an excitation map of CN due to the lack of collision data for this molecule. An study to extrapolate the collision data for CN from, e.g. CS, is ongoing.

* http://www.sron.rug.nl/∼vdtak/radex/index.shtml
† http://www.strw.leidenuniv.nl/∼moldata/

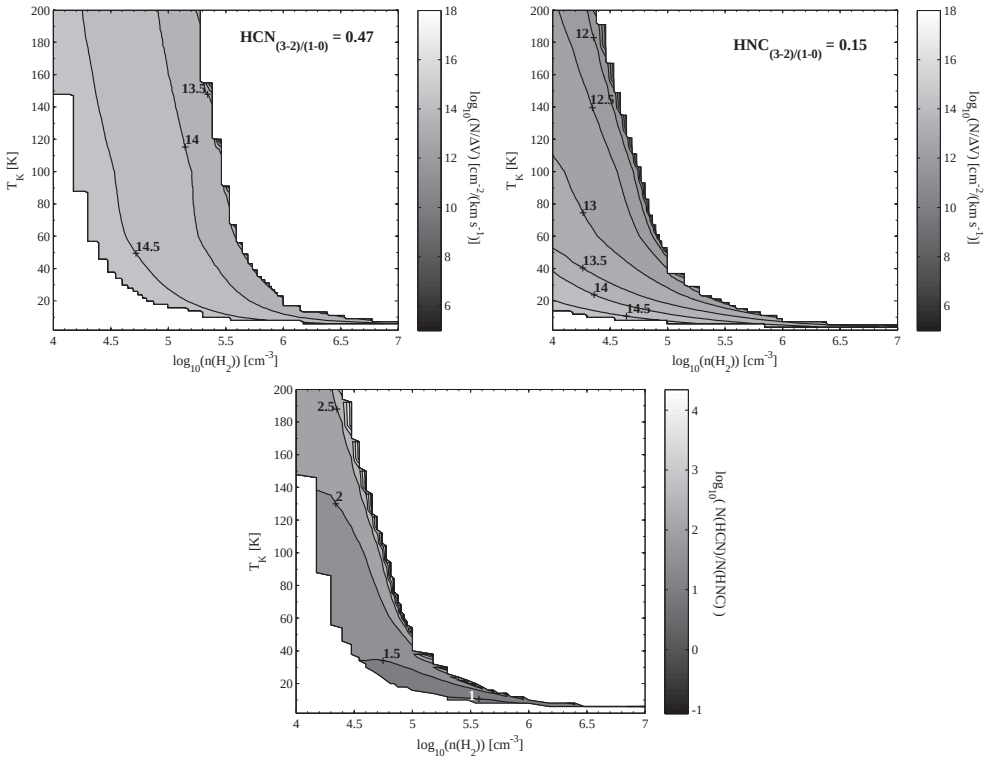

Figure 2.6: Excitation conditions modelled for the 3–2/1–0 line ratios of HCN (*top left*) and HNC (*top right*) observed in **NGC 1068**. The conditions required for the HCN and HNC molecules overlap in a narrow region. The relative column densities in the overlap zone of the excitation conditions of these molecules is shown in the *bottom* plot. The optical depth in the whole region explored for HCN ranges between 0.03 and 10 in the J=1–0 line, and between 0.32 and 30 in the J=3–2 line. In the case of HNC the optical depth ranges between 0.01 and 30 in the J=1–0 line, and between 0.003 and 30 in the the J=3–2 line. The optically thin limit of both molecules and lines is depicted by the right edge of the excitation conditions, whereas the optically thick limit correspond to the left edge of the figures above.

NGC 1068

Figure 2.6 shows the excitation condition maps for the HCN and HNC molecules, modeled from the average ratios observed in NGC 1068. These maps show that HCN (*top left*) requires higher density gas and higher column density than HNC (*top right*) in order to obtain the observed 3–2/1–0 line ratios.

Considering a kinetic temperature $T_k = 80$ K and a density $n(\mathrm{H_2}) \sim 10^5\ \mathrm{cm^{-3}}$, as estimated by Tacconi et al. (1994), we found that $N(\mathrm{HCN})/\Delta\upsilon \sim 1.5{\times}10^{14}\ \mathrm{cm^{-2}\,km^{-1}\,s}$, which agrees with the respective value found by Tacconi et al.

According to the recent PDR and XDR models by Meijerink & Spaans (2005) and Meijerink et al. (2007), under PDR conditions a temperature $T_k = 80$ K can be reached at a total column density of $N_{\mathrm{H}} \approx 3 \times 10^{21}\ \mathrm{cm^{-2}}$, if the Habing flux is $G_0 \sim 10^3$ (a Habing flux $G_0 = 1$ corresponds to a far UV flux $F_{FUV} = 1.6 \times$

10^{-3} erg cm^{-2} s^{-1}), or at $N_{\rm H} \approx 8 \times 10^{21}$ cm^{-2} if $G_0 \sim 10^5$. At those depths the density $n({\rm H_2})$ would be slightly higher than 10^5 cm^{-3}, though. On the other hand, in an XDR environment a temperature of 80 K and a density of 10^5 cm^{-3} can be reached at a slightly larger column density of $N_{\rm H} \approx 10^{22}$ cm^{-2}, if the impinging radiation field is $F_{FUV} \sim 1.6$ erg cm^{-2} s^{-1}, or at a much larger depth equivalent to $N_{\rm H} \approx 2 \times 10^{24}$ cm^{-2} if the radiation flux is $F_{FUV} \sim 160$ erg cm^{-2} s^{-1}.

However, at a temperature of 80 K and density of 10^5 cm^{-3} there is no solution for HNC. This means that either the HNC emission arises from a gas with different physical conditions than HCN, or that both molecules trace a cooler ($T_k < 80$ K) and lower density gas ($n({\rm H_2}) < 10^5$ cm^{-3}), if the emission of both molecules arise from the same gas.

If the HCN and HNC emissions actually trace the same gas, the range of possible excitation conditions can be constrained to the zone where the conditions for HCN and HNC overlap. The *bottom* plot of Figure 2.6 shows the average overlap zone, where the contours correspond to the ratio between the total column densities of HCN and HNC. The overlap zone is defined by the optically thin limit (right edge of the excitation maps) of the HNC transition lines and the optically thick limit (left edge of the excitation maps) of the HCN lines. The models show that $N({\rm HCN})$ is larger than $N({\rm HNC})$ in all the overlap zone. According to Figure 10 in Meijerink & Spaans (2005), $N({\rm HNC})/{\rm N(HCN)}$ column density ratios lower than unity can be found mostly in PDRs, but also in XDR environments if the total column density $N({\rm H})$ is lower than 10^{24} cm^{-2}. If we still assume the same temperature (80 K) proposed by Tacconi et al. (1994), and we consider the contour line where $N({\rm HCN})$ is about 2.5 orders of magnitude larger than $N({\rm HNC})$, we find that the gas density should be $n({\rm H_2}) \sim 6 \times 10^4$ cm^{-3}, which agrees with the observed HNC 3–2/1–0 line ratio discussed in Sec. 2.4.2. However, this density would not be consistent with the result found by Tacconi et al. (1994) nor with the observed HCN 3–2/1–0 line ratio, which implies that the HNC emissions arise from a more diffuse gas than HCN.

NGC 3079

The excitation conditions modelled for the HCN and HNC line ratios observed in NGC 3079 overlap in most of the range explored (Figure 2.7). This suggest that the emission from both molecules likely arise from the same gas. The spectral line shapes of HCN and HNC, showed in Figure 2.3, also hint that their distribution may be the same, although their line centers and widths are affected by noise. The *bottom* plot of Figure 2.7 shows the overlap zone of the excitation conditions, where $N({\rm HNC})$ is mostly between 0.5 and 1 order of magnitude larger than $N({\rm HCN})$.

According with the PDR and XDR models by Meijerink & Spaans (2005), a column density ratio $N({\rm HNC})/{\rm N(HCN)}$ larger than unity can be found only in XDR environments at a total column density $N({\rm H}) > 10^{24}$ cm^{-2}, with radiation fields $F_x \sim 1.6$ erg cm^{-2} s^{-1} (or equivalent Habing flux $G_0 \sim 10^3$) and total density $n({\rm H}) \sim 10^3$ cm^{-3}. $N({\rm HNC})/{\rm N(HCN)}$ column density ratios larger than unity at $N({\rm H}) > 10^{24}$ cm^{-2} can also be found with stronger radiation fields ($F_x \sim 160$ erg cm^{-2} s^{-1})

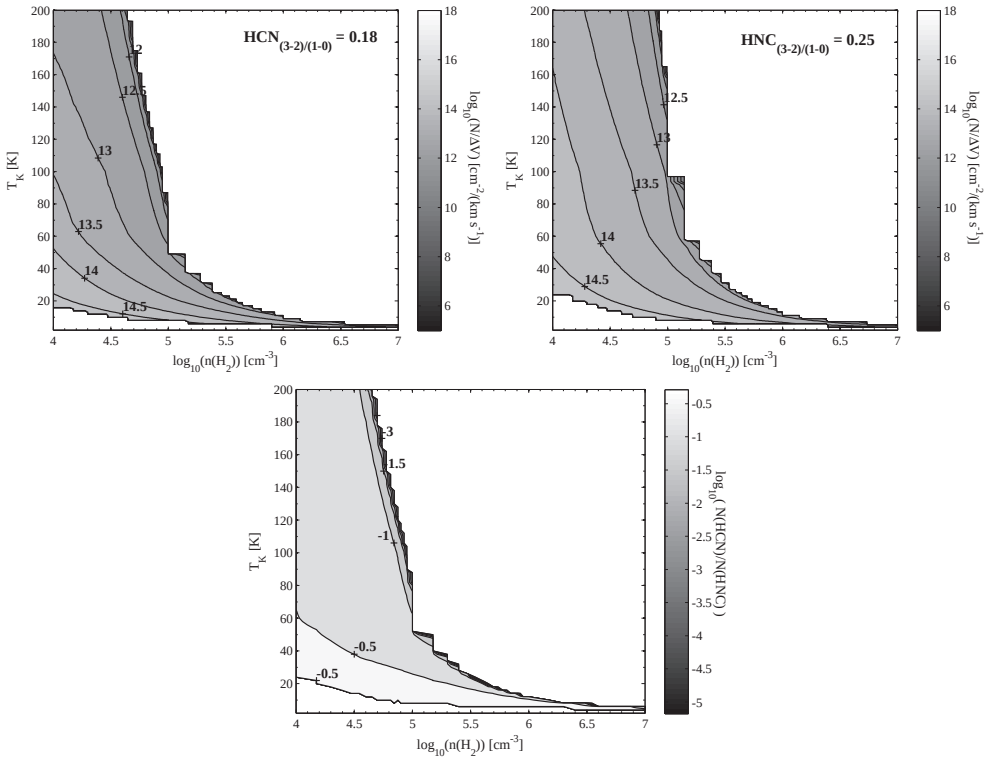

Figure 2.7: Excitation conditions modelled for the 3–2/1–0 line ratios of HCN (*top left*) and HNC (*top right*) observed in **NGC 3079**. The excitation conditions required for these molecules overlap in most of the range explored. This suggest that their emissions emerge from gas with the same physical conditions. The *bottom* plot shows the overlap zone. There is a large zone of excitation conditions where the column density of HNC is between 3 and 10 times larger than that of HCN. The contour lines of -0.5 depict the zone of the physical conditions for which the column density of HNC is about 3 times larger than that of HCN. For both molecules and transition lines the optical depth ranges between 0.001 and 30. The optically thick limit is basically defined by the limit of convergence of RADEX ($\tau_{\rm max} \sim 100$).

and higher densities (n(H) $\sim 3 \times 10^5$ cm^{-3}). On the other hand, N(HNC)/N(HCN) can be larger than unity at N(H) $< 10^{23}$ cm^{-2} if the radiation fields are on the order of 1.6 erg cm^{-2} s^{-1} and the total density is about 3×10^5 cm^{-3}.

We did not explore densities lower than 10^4 cm^{-3} since the HCN and HNC molecules are expected to trace higher densities. If we assume $T_k \approx 80$ K, as in the case of NGC 1068, and a density $n(\mathrm{H_2}) \sim 10^5$ cm^{-3}, the column densities per line width would be about 10^{12} and 10^{13} cm^{-2} km^{-1} s for HCN and HNC, respectively. In the case of HNC both lines are equally thick (optically) at 80 K in the whole range of densities, whereas HCN is more optically thin. At a density of 10^5 cm^{-3} the optical depth of HNC is $\sim$1 in both lines, whereas τ is $\sim$0.3 and $\sim$0.1 in the J=1–0 and J=3–2 lines of HCN, respectively. A density lower than 10^5 cm^{-3} is more likely to be the right case in order to be consistent with the line ratios observed and discussed in Sec. 2.4.2.

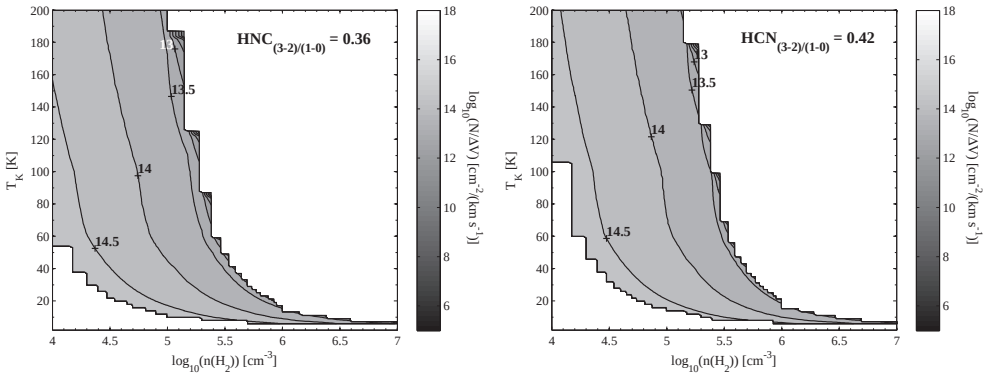

Figure 2.8: Excitation conditions modelled for the 3–2/1–0 line ratio of HNC (*left*) and HCN (*right*) observed in **NGC 2623** and **NGC 1365**, respectively. For NGC 2623 the optical depth of HNC 3–2 ranges between 0.003 and 10 in the J=1–0 line, and between 0.32 and 30 in the J=3–2 line. In the case of NGC 1365 the optical depth in the HCN 3–2 line ranges between 0.1 and 30, and between 0.01 and 10 in the J=1–0 line.

NGC 2623 and NGC 1365

Figure 2.8 shows that both NGC 2623 and NGC 1365 have similar excitation conditions for HNC and HCN, respectively. As in the case of HCN in NGC 1068, both molecules could be embedded in gas with densities larger than 10^5 cm^{-3} at 80 K, which is consistent with line ratios larger than 0.3, as discussed in Sec. 2.4.2. The column densities per line width of these molecules would be about 6×10^{13} cm^{-2} km^{-1} s for HNC and about 10^{14} cm^{-2} km^{-1} s for HCN, if the gas density is 10^5 cm^{-3}.

2.4.4 The CN/HNC and CN/HCN line ratios

The CN/HNC ratio increases towards the CND in both galaxies, NGC 1068 and NGC 3079. The CN/HNC 1–0 ratio is lower than unity in all the galaxies, with the exception of NGC 1068. This can be interpreted as that HNC is more abundant than CN, assuming the same excitation conditions and that the emission emerge from the same gas and distribution in the galaxy. However, since we do not really know the source size of CN (and basically neither that of HNC) the beam dilution effects could be more (or less) severe than estimated here.

Although the beam dilution uncertainty of CN also applies to the CN/HCN ratio, this case is more interesting because none of the galaxies where we do have data show ratios larger than one, neither for the global ratio (J=1–0) nor for the nuclear part of the galaxies (higher transitions). All of these galaxies are considered active galaxies, so the presence of an AGN increases the chances of finding an X-ray dominated region (XDR) in their nuclear regions, as it seems to be the case of NGC 1068, according to Usero et al. (2004).

In an XDR the CN molecule is expected to be more abundant than HCN (e.g.

Lepp & Dalgarno, 1996; Meijerink & Spaans, 2005; Meijerink et al., 2007), and hence the CN/HCN intensity ratio could also be larger than unity, especially for the higher transition lines - CN 2–1 and HCN 3–2 - where the beam dilution is less important than for the J=1–0 line. However, this is not seen in any of the sources presented here, nor in the sample of galaxies shown by Aalto et al. (2002), where results for AGN are presented along with starburst galaxies.

According to Meijerink et al. (2007), in a PDR environment the $N(\mathrm{CN})/N(\mathrm{HCN})$ column density ratio ranges between 2.0 and 0.5 for densities between 10^4 and 10^6 cm^{-3}, respectively, whereas in an XDR this ratio varies from over a 1000 (at $n(\mathrm{H_2}) \sim 10^4$ cm^{-3}) to 40 (at $n(\mathrm{H_2}) \sim 10^6$ cm^{-3}). If the CN intensity lines are proportional to the column density, and the estimate of the beam dilution is accurate enough, our results would favor a PDR scenario, rather than an XDR, with densities $< 10^6$ cm^{-3} in the central regions of all these galaxies. However, if the CN molecule is indeed more abundant than HCN, then the weaker intensity lines could be also due to a stronger optical depth effect (in the escape probability sense) for CN. A rigorous modeling and analysis of the CN molecule would be required in order to understand and predict the intensities of this molecule.

On the other hand, the PDR scenario would also be consistent with the results found for the HNC and HCN molecules described above. HCN/HNC line intensity ratios larger than unity are usually found in PDR environments at total column densities $N(\mathrm{H})$ lower than 10^{22} cm^{-2}, while this ratio is larger for strong (> 10 erg s^{-1} cm^{-2}) radiation fields and low ($\sim 10^4$ cm^{-3}) densities in an XDR environment (Meijerink et al., 2007). The lower densities required to observe this ratios in an XDR environment tend to dismiss this alternative since our simulations in Sec. 2.4.3 favor densities $\sim 10^5$ cm^{-3} for the HNC and HCN molecules, as in the case of NGC 1068. In particular, there is evidence of recent starburst in the dense nuclear disk of NGC 1068 (Davies et al., 2006). These results are consistent with a model considering both, AGN and starburst components, required for modelling the UV to FIR atomic spectrum of NGC 1068 (Spinoglio et al., 2005).

2.5 Conclusions

We have used the SEST and JCMT telescopes to carry out a survey of CN 2–1, HCN 3–2 and HNC 3–2 line emission in a sample of 4 Seyfert galaxies, plus NGC 3079 which was observed with the IRAM 30m telescope. The conclusions we draw are as follows:

1) We detected HNC 3–2 emission in 3 of the 5 galaxies, while we obtain an upper limit for one of them (NGC 7469). HCN 3–2 was also detected in 3 galaxies (NGC 3079, NGC 1068 and NGC 1365), while it was not detected in NGC 2623. CN 2–1, along with the spingroups (J = 5/2 – 3/2, F = 7/2 – 5/2) and (J = 3/2 – 1/2, F = 5/2 – 3/2) was also detected in NGC 3079, NGC 1068 and NGC 1365.

2) We find that in 3 of the galaxies the HNC 3–2/1–0 line ratios suggest that the

HNC emissions emerge from gas of densities $n \lesssim 10^5$ cm^{-3}, where the chemistry is dominated by ion-neutral reactions. In NGC 2623 a model of large masses of hidden cold (10 K) gas and dust, as well as a chemistry dominated by ion-neutral reactions, are yet to be distinguished as the correct interpretation for the bright HNC observed in this galaxy.

3) The 3–2/1–0 line ratios and the modelled excitation conditions imply that the HNC emission emerges from a more diffuse ($n < 10^5$ cm^{-3}) gas region than the HCN emission ($n > 10^5$ cm^{-3}) in NGC 1068, whereas they emerge from the same lower density ($n \lesssim 10^5$ cm^{-3}) gas in NGC 3079.

4) The HCN/HNC and CN/HCN line ratios tentatively favor a PDR scenario, rather than an XDR one, in the 3 Seyfert galaxies where we have CN, HNC and HCN data. The $N(\mathrm{HNC})/N(\mathrm{HCN})$ column density ratios obtained for NGC 3079 can be found only in XDR environments.

In order to complete the sample, we plan to observe HCN 3–2 and CN 2–1 in NGC 7469, CN 2–1 in NGC 2623 and HNC 3–2 in NGC 1365. We plan to perform high resolution observations to further study the distribution and source sizes of CN and HNC.

Modeling the collision data for CN would be useful to compute the column density ratio between CN and HCN, which would complement the $N(\mathrm{HNC})/N(\mathrm{HCN})$ ratio in order to have a more sophisticated tool to estimate and distinguish the prevalent environment conditions of the dense gas in the nuclear region of Seyfert galaxies.

The AGN contribution (through XDR effects) is typically of a small angular scale and can be seriously affected by beam dilution at the transition lines studied in this work. On the other hand, the starburst contribution is of a larger angular scale than the AGN, and it effects can be contaminating our observations, and hence leading to the favored PDR scenario found with our models. Hence, our suggested interpretations could change if we zoom in on these sources. Therefore, high resolution maps of HNC and CN molecules are necessary to complement those of HCN, and to do a more accurate estimate of molecular abundances and line intensity ratios, which take source size into account. Observations of the higher transition lines (e.g. J=4–3) can also aid to disentangle the effects of the AGN and the starburst ring, due to the smaller beam size obtained at higher frequencies.

Acknowledgements

We are grateful to the SEST staff for their help during the observing run and to S. Curran and A. Polatidis for helping with some of the SEST observations. The authors thanks to S. Hüttemeister, M. Spaans, and R. Meijerink for useful discussions of the data and modeling. We also thank F. van der Tak and J. Black for their help and discussions about RADEX. Molecular databases that have been helpful include LAMBDA and NIST.

3

Dense molecular gas in NGC 1068

– J.P. Pérez-Beaupuits, M. Spaans, F.S.S. van der Tak, S. Aalto, S. García-Burillo, A. Fuente and A. Usero –

Single-dish observations of molecular tracers have suggested that both star formation and an AGN can drive the gas chemistry of the central ∼kpc of active galaxies. The irradiation by UV photons from an starburst or by X-rays from an AGN is expected to produce different signatures in molecular chemistry, which existing data on low-J lines cannot distinguish, as they do not trace gas at high temperature and density. Depending on the angular scale of a galaxy, the observed low-J lines can be dominated by the emission coming from the starburst ring rather than from the central region. With the incorporation of high-J molecular lines, we aim to constrain the physical conditions of the dense gas in the central region of the Seyfert 2 galaxy NGC 1068 and to determine signatures of the AGN or the starburst contribution. We used the James Clerk Maxwell Telescope to observe the J=4–3 transition of HCN, HNC, and HCO^+, as well as the CN $N_J = 2_{5/2} - 1_{3/2}$ and $N_J = 3_{5/2} - 2_{5/2}$, in NGC 1068. We estimate the excitation conditions of HCN, HNC, and CN, based on the line intensity ratios and radiative transfer models. We discuss the results in the context of models of irradiation of the molecular gas by UV light and X-rays. A first-order estimate leads to starburst contribution factors of 0.58 and 0.56 for the CN and HCN J=1–0 lines, respectively. We find that the bulk emission of HCN, HNC, CN, and the high-J HCO^+ emerge from dense gas ($n(\mathrm{H_2}) \geq 10^5\ \mathrm{cm^{-3}}$). However, the low-$J$ HCO^+ lines (dominating the HCO^+ column density) trace less dense ($n(\mathrm{H_2}) < 10^5\ \mathrm{cm^{-3}}$) and colder ($T_K \leq 20$ K) gas, whereas the high-J HCO^+ emerges from warmer (> 30 K) gas than the other molecules. We also find that the HNC/HCN and CN/HCN line intensity ratios decrease with increasing rotational quantum number J. The HCO^+ J=4–3 line intensity, compared with the lower transition lines and with the HCN J=4–3 line, support the influence of a local XDR environment. The estimated $N(\mathrm{CN})/N(\mathrm{HCN}) \sim 1-4$ column density ratios are indicative of an XDR/AGN environment with a possible contribution of grain-surface chemistry induced by X-rays or shocks.

Adapted from the original publication in *Astronomy & Astrophysics*, Vol. 503, pp 459–466 (2009)

3.1 Introduction

Active galaxies often have high concentrations of molecular gas in their central (<kpc) region, which may be feeding a central active galactic nucleus (AGN) or an starburst (e.g. Sanders & Mirabel, 1996; Gao & Solomon, 1997, 1999). Molecular gas irradiation by hard X-ray photons ($>$ 1 keV) emitted during the accretion process in the proximity of AGNs, leads to an X-ray dominated region (XDR) (e.g. Maloney et al., 1996; Lepp & Dalgarno, 1996; Meijerink & Spaans, 2005). In an starburst region, the formation/destruction of molecules is instead driven by far-UV photons (6 – 13.6 eV) emitted by O and B stars, which leave the fingerprint of a photon-dominated region (PDR) (c.f. Hollenbach & Tielens, 1999, and references therein). An increased X-ray ionization of molecular clouds can enhance the abundance of several molecules (e.g. CN, HNC, HCN and HCO^+) with respect to their abundances found in PDRs (e.g. Lepp & Dalgarno, 1996; Meijerink & Spaans, 2005; Meijerink et al., 2007). Conversely, the chemical state of the molecular gas is a tracer of the dominant energy source of AGNs.

The prototypical Seyfert 2 galaxy NGC 1068 (located at a distance ~ 14.4 Mpc and with a bolometric luminosity of $\sim 10^{11} L_{\odot}$) is a known source where the star formation and/or AGN activity can be debated as the main driving mechanism of its gas chemistry. It hosts a circumnuclear starburst ring of about $2.5 - 3$ kpc in diameter (Schinnerer et al., 2000), which delimits a ~ 2.3 kpc stellar bar (Scoville et al., 1988). The detection of strong CO emission coming from the starburst ring indicates that its massive star formation activity is being fed by vast amounts of molecular gas (e.g. Planesas et al., 1989, 1991; Helfer & Blitz, 1995; Schinnerer et al., 2000). However, significant CO emission also arises from a circumnuclear disk (CND) of about 200 pc in diameter (Solomon & Barrett, 1991; Schinnerer et al., 2000). Earlier observations of high HCN/CO luminosity ratios, measured in the CND of NGC 1068, suggested an abnormal (by Galactic standards) chemistry of molecular gas (Tacconi et al., 1994; Sternberg et al., 1994). Later observations of HCN, HCO^+ and HCO, among other molecules (Usero et al., 2004), suggest that the chemistry in the CND of NGC 1068 corresponds to that of an XDR. On the other hand, single-dish observations of other high-density tracers (HNC and CN) in the CND of NGC 1068 show that the HNC/HCN and CN/HCN line ratios favor a PDR, rather than an XDR scenario (Pérez-Beaupuits et al., 2007). This independent observational evidence for both PDR and XDR scenarios is consistent with a model that considers an AGN and starburst component to be present in NGC 1068 (Spinoglio et al., 2005). However, a later estimate indicates that the age of the most recent episode of star formation, within the central 10–100 pc, is about 250 ± 50 Myr (Davies et al., 2007). This result suggests a recent, although no longer active, starburst activity in the CND of NGC 1068.

Nevertheless, it was noted in Pérez-Beaupuits et al. (2007) that the result of a favored PDR scenario in the CND of NGC 1068 may be misleading, since the AGN contribution (through XDR effects) is typical of an smaller angular scale than the starburst contribution (PDR). X-rays are known to penetrate deeper than UV photons into a single molecular cloud. But its effects are rather local, since the

energy flux of the radiation decreases with radial distance from the source. On the other hand, an starburst region is more spread, and several O/B stars will typically be closer to a molecular cloud than a single X-ray source. Thus the PDR effects will dominate the bulk of the gas. Hence, the smaller angular size of the action zone of an X-ray source (the region around an X-ray source that dominates over UV driven chemical effects) will be affected by beam dilution, and the radiation emerging from the starburst component can dominate the overall emission collected by a single dish beam. This is a known drawback of single dish observations of extragalactic sources that, depending on the diameter of the telescope used, complicates the efforts to disentangle the AGN activity from that of the starburst ring, when considering the intensities of the lower transitions of molecular lines. Given that the starburst contribution is likely dominant at radii $R \sim 14''$ in NGC 1068, but not in the CND at $R \sim 2''$, the low-J lines observed with single dish telescopes (with beam $> 25''$) can be dominated by the contribution from the starburst ring, and if uncorrected, can be misleading.

In this paper we present observations of high-J lines of HCN, HNC, CN and HCO^+ on NGC 1068. Due to the smaller beam size, these lines are less affected by the contribution from the starburst ring, than the J=1–0 lines. We also present a first order estimate of the starburst contribution, based on independent observations of the J=1–0 lines, and correct the intensities of these lines accordingly. Since HNC is the isomer of HCN, the radiation of these molecules is expected to arise from gas with the same physical conditions. However, radiative transfer models based on the $\frac{3-2}{1-0}$ line ratios of these molecules showed that the HNC emissions arise from less dense gas than HCN, when considering a kinetic temperature of about 80 K (Pérez-Beaupuits et al., 2007). We compare these previous results with those obtained from the new $\frac{4-3}{3-2}$ line ratios. The molecular abundances estimated from the radiative transfer models are subsequently compared to those obtained with our PDR and XDR models.

In Sec. 3.2 we describe the observations. The results (spectral lines and line intensities) are presented in Sec. 3.3. The modelling and analysis of the excitation conditions and abundances of HCN, HNC, HCO^+ and CN are presented in Sec. 3.4. The conclusions and final remarks of this work are presented in Sec. 3.7.

3.2 Observations and data reduction

We have used the 16-pixel receiver HARP (Heterodyne Array Receiver Programme) on JCMT*, during December 2006, to observe the J=4–3 lines of HNC (363 GHz), HCN (355 GHz) and HCO^+ (357 GHz), as well as the CN $N_J = 3_{5/2} - 2_{5/2}$ (339 GHz), toward the center of the Seyfert galaxy NGC 1068 (r.a. $= 02^{\rm h}42^{\rm m}40.7^{\rm s}$, dec. $= -00^\circ 00' 48''$). Beamsizes and efficiencies are shown in Table 3.1. We used HARP as a single pixel in staring mode, since it was the only receiver available to cover

* The JCMT is operated by the Joint Astronomy Center on behalf of the Science and Technology Facilities Council of the United Kingdom, the Netherlands Organization for Scientific Research, and the National Research Council of Canada.

Table 3.1: Beam sizes & efficiencies.

Molecule	Transition J/N_J	ν [GHz]	HPBW [$''$]	$\eta_{\rm mb}$
CN	$2_{5/2} - 1_{3/2}$	226.875	21	0.67
CN	$3_{5/2} - 2_{5/2}$	339.517	15	0.63
HCN	$4 - 3$	354.505	14	0.63
HCO^+	$4 - 3$	356.734	14	0.63
HNC	$4 - 3$	362.630	14	0.63

the high frequencies. The $10^{\rm th}$ pixel was used to point the telescope at the nuclear region of NGC 1068. Detection in the other pixels was negligible and beyond the scope of this work, since they point outside the circumnuclear disk. Pointing was checked regularly on SiO masers and the RMS was found to be lower than $2''$. Since HARP was not fully commissioned at the time of the observations, we regularly checked the calibration of the receiver observing the CO J=3–2 line in the reference source CRL168 and we compared it with the representative spectrum obtained with the former receiver B3. It was found that the calibration CO J=3–2 line observed with HARP was fainter than the reference spectrum, and our data was corrected according to the variations of the calibration observed during the run. We also used the receiver A3 to observe the CN $N_J = 2_{5/2} - 1_{3/2}$ (226 GHz) line. The backend was the ACSIS correlator, and when observing with HARP we used a bandwidth of 1 GHz since the 1.8 GHz bandwidth was showing some anomalies in the overlap area and a higher system temperature. Unfortunately, this limited our baseline coverage. Nevertheless, we used 2048 spectral channels which gives a resolution of about 0.4 $\rm km\,s^{-1}$ in the original spectra. We obtained different numbers of scans (on-source observations) for all the observed lines, with integration times between 5 and 10 minutes each, to allow for calibration observations between the scans.

After a weighted (by system temperature and integration time) average of the scans, a baseline was removed from the average spectra and the resolution was lowered to reduce the level of noise. A first-order polynomial was used in most of the spectra to fit the baselines. Only for CN $N_J = 3_{5/2} - 2_{5/2}$ a second order polynomial was needed. The velocity resolution was reduced to 20 $\rm km\,s^{-1}$, which represents less than 10% of the line widths. Small variations in the channels chosen to define the baselines in the original averaged spectra, lead to variations of $< 6\%$ in the integrated intensities of the final spectra shown in the next section. The average system temperature was about 300 K for total on-source integration times between 35 minutes and 4.1 hours. The S/N levels (the peak antenna temperatures, obtained from the gaussian fit, with respect to the r.m.s. of the baselines) ranged between 3 and 7. The software package XS (written by P. Bergman, Onsala Space Observatory) was used to reduce the data and fit the Gaussians.

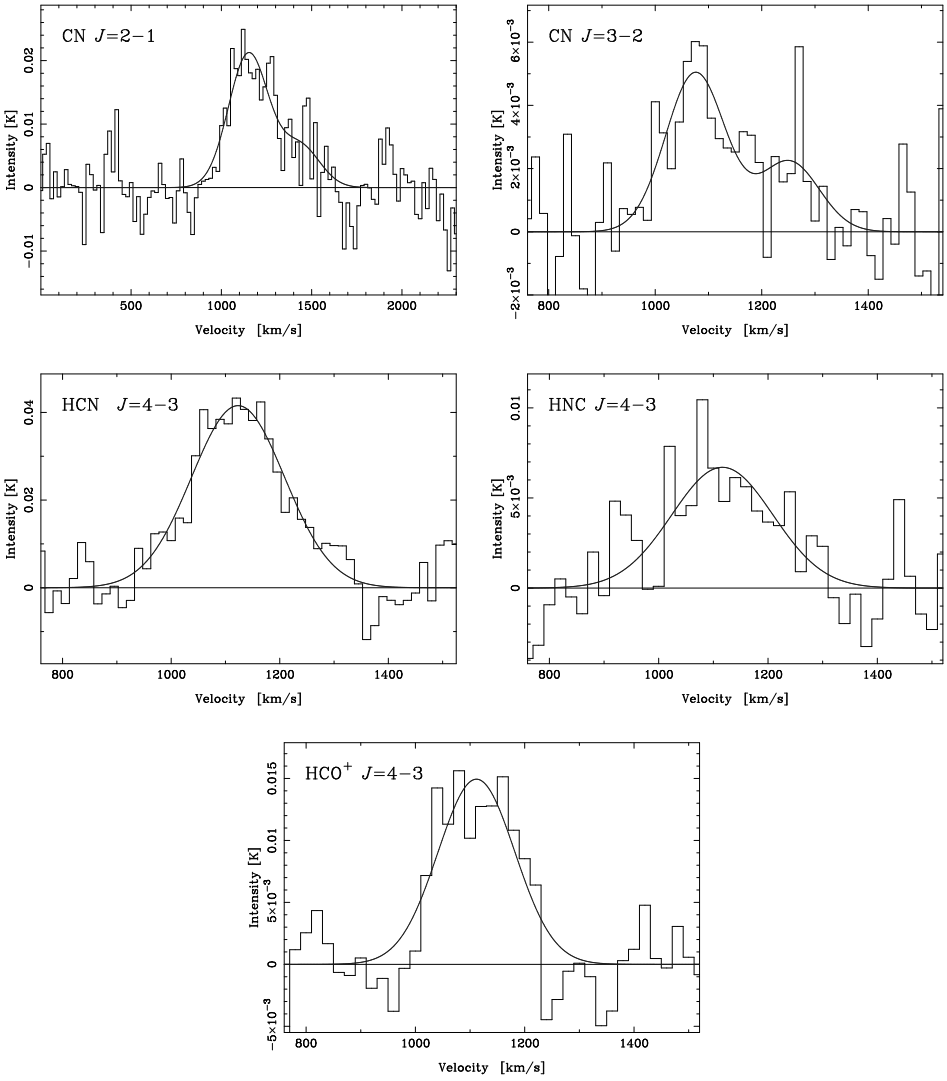

Figure 3.1: Molecular line emissions in NGC 1068. The velocity resolution was reduced to 20 $\mathrm{km\,s^{-1}}$for all the lines. The spectra are centered with respect to the heliocentric systemic velocity $\mathrm{v_{sys}} = 1137\ \mathrm{km\,s^{-1}}$.

Table 3.2: NGC 1068 line parameters.

Molecule–J	V [km s^{-1}]	T_A^* [mK]	ΔV [km s^{-1}]
CN $N_J = 2_{5/2} - 1_{3/2}$	1151±15 1444±42	21.4± 1.7 7.1± 2.1	265±35 265 [a]
CN $N_J = 3_{5/2} - 2_{5/2}$	1076±14 1252±33	5.0± 0.9 2.2± 0.8	132±34 132 [a]
HCN J=4–3	1123± 6	41.5± 2.4	202±14
HNC J=4–3	1116±18	6.7± 1.1	218±47
HCO$^+$ J=4–3	1112± 8	14.9± 1.4	166±19

[a] The uncertainty of this parameter was larger than 100%, if let free. So we set its value to the one found for the main gaussian component.

Table 3.3: Velocity-integrated intensities. [a]

Molecule	Transition J/N_J	Intensity [K km s^{-1}]
CN	$2_{5/2} - 1_{3/2}$	11.7± 1.4
CN	$3_{5/2} - 2_{5/2}$	1.6± 0.3
HCN	$4 - 3$	13.9± 1.6
HNC	$4 - 3$	2.7± 0.3
HCO$^+$	$4 - 3$	3.8± 0.5

a) Total velocity integrated temperature considering all the components of each spectral line. The values correspond to the main-beam brightness intensity, $I_{mb} = \int T_A^*/\eta_{\rm mb}\delta v$, in [K km s^{-1}].

3.3 Results

The observed molecular line emissions are shown in Figure 3.1 and the line parameters of the gaussian fits are summarized in Table 3.2. The spectra are centered with respect to the heliocentric systemic velocity $\rm v_{sys} = 1137\ km\,s^{-1}$, taken from the NASA/IPAC Extragalactic Database (NED). The velocity-integrated intensities are shown in Table 3.3.

The HCN J=4–3 spectrum shows the same single peak structure as the lower-J transitions reported by Pérez-Beaupuits et al. (2007) and Curran et al. (2000). The average line width is about 25% ($\sim 70\ \rm km\,s^{-1}$) narrower than the average width observed in the lower J-transitions.

The double peak structure seen in the HNC J=1–0 and J=3–2 spectral lines by Pérez-Beaupuits et al. (2007) is not present in the J=4–3 line. This may be due to the smaller beam size and to the lower signal to noise ratio of our data. The center velocity of the gaussian fit is just about 10 $\rm km\,s^{-1}$ away from the center velocities of the main component in the lower transition lines (within $\sim 1\sigma$). Since this is

a single component line, its average width is about 50 $\mathrm{km\,s^{-1}}$ wider than the line widths of the lower transition lines reported by Pérez-Beaupuits et al. (2007), but similar to the line width of the HNC J=1–0 line reported by Hüttemeister et al. (1995).

The HCO^+ spectrum shows a single peak structure, and appears to be narrower than the J=1–0 and J=3–2 lines reported by Krips et al. (2008). Our J=4–3 line has an average line width of about 166 km/s, while the lines reported by Krips et al. have average line widths of about 240 km/s. This may be an indication that the J=4–3 line traces a different gas than the lower transitions. But due to the relatively low S/N~ 6, deeper observations are needed.

Using receiver A3, the two CN spingroups at 226.8746 GHz (N = 2–1, J = 5/2 – 3/2, F = 7/2 – 5/2) and 226.6596 GHz (N = 2–1, J = 3/2 – 1/2, F = 5/2 – 3/2) were detected. The central velocity of the second spingroup is about 17 $\mathrm{km\,s^{-1}}$ away from the expected velocity, which is within the 1σ error. In the optically thin limit, the second spingroup is expected to be a factor ≤ 0.56 weaker than the main spingroup. The factor we obtained from the gaussian fit in Figure 3.1 is $\sim 0.33 \pm 0.1$, which means that this line is close to optically thin.

Observing CN with HARP at ~ 339.5 GHz, we also detected a double peak structure. However, the two spingroups at 339.517 GHz (N = 3–2, J = 5/2 – 5/2, F = 7/2 – 7/2) and 339.476 GHz (F = 5/2 – 5/2) are severely blended. The separation between the two peaks is 176 ± 36 $\mathrm{km\,s^{-1}}$, whereas the separation between the farthest spingroup (at 339.447 GHz, F = 3/2 – 3/2) that we could detect in our bandwidth is expected to be at just about 62 $\mathrm{km\,s^{-1}}$ towards the higher velocities. So we do not think the double peak structure is due to another spingroup. Nevertheless, two gaussian components are needed to fit the line profile. Given the noise in the spectrum, the line width of the second component was set to the line width found for the main component.

3.4 Discussion

3.4.1 Structure of the CND and limitations of the model

Millimeter/sub-millimeter and mid-IR high spatial resolution observations of the nuclear region of NGC 1068 support the classical picture of a rotating torus (e.g. Tacconi et al., 1994; Schinnerer et al., 2000; Galliano et al., 2005; Poncelet et al., 2007). However, in some previous works (e.g., Schinnerer et al. 2000) it was speculated that the classical (large-scale) molecular torus is not always needed to explain the occultation of the nuclear regions. Recent mid-IR observations have shown the existence of two molecular streamers feeding the galactic nucleus of NGC 1068 (Tomono et al., 2006; Sánchez et al., 2009). These observations suggest that the occultation of the nuclear region can also be associated with a nuclear concentration of molecular gas and dust that forms an optically thick amorphous clumpy structure (Sánchez et al., 2009). Although it is very likely that this structure encloses smaller infalling clouds, they are not resolved at the 0.075” (scale size ~ 5

pc at a distance of 14.4 Mpc) resolution of the Very Large Telescope (VLT).

In the case of millimeter and sub-millimeter interferometer maps of high density tracers (e.g. Tacconi et al., 1994; García-Burillo et al., 2008), not even the streamers are resolved. This represents a limitation of the current millimeter and sub-millimeter observations in comparison with visual and IR wavelength ranges, with which the morphology and dynamics of the gas can be studied in more detail. This limitation is even more severe in single dish observations for which, depending on the lines observed, the emitting regions (or clouds) can be of a much smaller scale ($\sim$ 1 order of magnitude) than the beam size of the telescope. In particular, our single dish observations of HCN, HNC, CN and HCO^+ are sensitive to the high density ($\sim 10^5$ cm^{-3}) clouds that can be embedded even inside the feeding streamers observed by Sánchez et al. (2009). The size of these dense clumps is expected to be from < 1 pc up to a few pc, embedded in large molecular clouds of the order of tens of parsecs. In the near future, only the Atacama Large Millimeter Array (ALMA) is expected to resolve these smaller clouds at millimeter and sub-millimeter wavelengths with resolutions (at 1mm) between 0.1" and 0.01" (scale size $7 - 0.7$ pc at the distance of NGC 1068).

Ideally, we would like to be able to observe and to model the physical environment in extra-galactic sources, just like it has been done for the Milky Way. Relatively complex radiative transfer codes like, for instance, RATRAN (Hogerheijde & van der Tak, 2000) and $\beta 3D$ (Poelman & Spaans, 2005), can be used to model the internal dynamics, temperature and density structure of individual molecular clouds. However, the detailed structure and signatures of the individual clouds are convolved and smeared out with a large ($> 10''$) beam in single dish extra-galactic observations. Therefore, we do not have the information needed to constrain the parameters related to the detailed internal structure of the clouds. What we have is the convolved intensity and line profile of the emission emerging from all the clumps that fall within the telescope beam. Therefore, all modeling efforts are limited to estimate only the bulk of the gas properties. For this purpose, the less complex radiative transfer code RADEX* (van der Tak et al., 2007) is a sensitive model for estimating these average physical conditions of the high density gas from single dish observations towards extra-galactic sources. However, due to the lack of spatial resolution in our data, and the limitations of our model, the following discussion and the conclusions derived from them should be taken as qualitative orders of magnitude. Higher spatial resolution, such as the resolutions that ALMA will provide, are necessary to reach definitive conclusions.

3.4.2 Line ratios and starburst contribution

The observed line ratios of molecular transitions have been largely used as a tool for estimating the physical conditions of the molecular gas. However, the conversion from $T_{\rm mb}$ to T_R is uncertain through the source size of the emitting region and, hence, the derived physical conditions (T_K, $n(\rm H_2)$ and N) depend strongly on this

* http://www.sron.rug.nl/∼vdtak/radex/radex_manual.pdf

conversion. Special care regarding this issue has been taken in previous work (e.g. Tacconi et al., 1994; Usero et al., 2004; Pérez-Beaupuits et al., 2007; Krips et al., 2008).

The high resolution map of the CO J=1–0 line in NGC 1068 reported by Schinnerer et al. (2000) shows that the morphology of this galaxy consists mostly of a nuclear region (circumnuclear disk) and spiral arms (starburst ring). Since our aim is to use the HCN, CN, HNC and HCO^+ data as a diagnostic tool for AGN-like environments, we are interested only in the emission emerging from the CND of NGC 1068. However, the starburst ring could potentially be contributing to the observed emission and, hence, influence the results of the radiative transfer models, as noted by Pérez-Beaupuits et al. (2007). This is particularly relevant for the J=1–0 lines of all the molecules because of the larger beam size. Therefore, the line intensity ratios, involving the J=1–0 transitions, could be misleading.

A priori, the most straightforward way to estimate the contribution from the starburst ring would be to use interferometer data, for instance, from the HCN J=1–0 map reported by Tacconi et al. (1994). Although this is possible, using interferometer data is somewhat delicate due to the missing flux. Even though the zero spacing problem can be resolved through spectra observed with a single-dish telescope in the direction of the interferometer phase center, only part of the short spacing information can be recovered. Besides, high quality interferometer and single-dish data are required in order to minimize the artifacts in the final combined data. Because the uncertainties in this technique are higher, and because high quality data are not available for all the lines needed, we derive below a first-order estimate of the starburst contribution, based on single-dish data only. We use the available J=1–0 lines of HCN, HNC and CN observed with different telescopes (SEST, OSO, IRAM 30m).

The total flux or intensity $F_{\rm TOTAL}$, measured with a beam of FWHM=$\theta_{\rm mb}$ that includes emission from the starburst ring ($F_{\rm SB}$), of average radius $r \sim 14''$, and from the CND ($F_{\rm CND}$, with an smaller radius of about 1"), can be decomposed as follows:

$$F_{\rm TOTAL} = F_{\rm CND} * w_{\rm CND} + F_{\rm SB} * w_{\rm SB}, \tag{3.1}$$

where $w_{\rm CND}$ and $w_{\rm SB}$ are weighting functions that can be estimated as $w_{\rm CND} \sim 1$, because the size of the CND is small compared to the beams of any of the available single dish data, and

$$w_{\rm SB} \sim exp\left[-4 * ln(2) * \left(\frac{14''}{\theta_{\rm mb}}\right)^2\right]. \tag{3.2}$$

In eq. (3.2) we assume that the contribution comes *only* from an axisymmetric ring-like distribution of radius $r = 14''$, neglecting the contribution from the bar or any other feature at intermediate radii. Since we have at least two *independent* observations of the J=1–0 line, with different telescopes of beams $\theta_{\rm mb1}$ and $\theta_{\rm mb2}$, we can have a first-order estimate of the starburst contribution as:

$$F_{\rm SB} \sim \frac{F_{\rm TOTAL1} - F_{\rm TOTAL2}}{w_{\rm SB1} - w_{\rm SB2}}. \tag{3.3}$$

Hence, from eq. (3.1), the starburst contribution factor $f_{\rm SB}$ of a line observed with any telescope can be estimated as:

$$f_{\rm SB} \sim \frac{F_{\rm SB} * w_{\rm SB}}{F_{\rm TOTAL}}. \tag{3.4}$$

So we can estimate the intensity that emerges from the CND from the observed total intensity as $F_{\rm CND} \sim F_{\rm TOTAL} * (1 - f_{\rm SB})$. This means that, the larger $f_{\rm SB}$, the larger will be the $\frac{3-2}{1-0}$ ratios. Note that, from equation (3.2), $f_{\rm SB}$ depends on the beam size $\theta_{\rm mb}$ of the telescope used for the observations. Using the peak intensities from Pérez-Beaupuits et al. (2007) and from available IRAM 30m data for the same CN, HCN and HNC J=1–0 lines (Usero et al., in preparation) and the corresponding telescope beams, we estimate the $f_{\rm SB}$ factors as $0.58{\pm}0.25$ for CN (SEST, $\theta_{\rm mb} = 45''$), 0.56 ± 0.32 for HCN (OSO, $\theta_{\rm mb} = 44''$) and 0.99 ± 0.50, for HNC (SEST, $\theta_{\rm mb} = 55''$).

The similar (within ~ 4%) starburst contribution factors found for CN and HCN, as observed with SEST and OSO, respectively, are as expected since the respective beam sizes are also similar (within $\sim$ 2%). Instead, the high contribution factor estimated for HNC would indicate that only 1% of the observed emission emerges from the nuclear region, in contrast to the 42% and 44% found for CN and HCN. If this was real, we would expect to see a pronounced double peak structure, with the proper velocity centers, in the HNC J=1–0 line profile. Since this is not the case, we think that the substantial difference between the starburst contribution factors of HNC and the other molecules might be due to some problems (e.g., pointing or calibration errors) in the spectral line reported in Pérez-Beaupuits et al. (2007), which was noted to be different than the one previously reported by Hüttemeister et al. (1995). Thus, we use the HNC J=1–0 line from Hüttemeister et al. for the following analysis. However, this line, as well as the low-J HCO^+ lines reported by Krips et al. (2008), was observed with the IRAM 30m telescope only. Therefore, we cannot estimate the corresponding starburst contribution factor, due to the lack of independent observations. Hence, for HNC and HCO^+ J=1–0 lines we adopt the value $f_{\rm SB} = 0.45 \pm 0.31$ estimated from the HCN observations done with the 30m telescope ($\theta_{\rm mb} = 28''$). The starburst contribution factors for the higher-J transitions are expected to be negligible because of the smaller beams at higher frequencies, so we can assume these to be zero.

After correcting the J=1–0 lines for the starburst contribution, we correct the peak intensities for beam dilution as $T_R = \frac{T_A^*}{\eta_{\rm mb}} \times \frac{\theta_{\rm S}^2 + \theta_{\rm mb}^2}{\theta_{\rm S}^2}$. The ratios between the line intensities are shown in Table 3.4. We use the ratios between the peak intensities of the *main components* in the Gaussian fit shown in Table 3.2. The peak intensity corresponds to the emission emerging from regions with velocities close to the systemic velocity of NGC 1068, and the ratios obtained from these values should be similar to those obtained from the velocity-integrated intensities, if the line widths of the corresponding components of the different transitions are also similar. The

Table 3.4: Line intensity ratios between the peak antenna temperatures, assuming a source size of 1.5".

Molecule	Transitions	Ratio [a]
CN	$\frac{^2 5/2 - ^1 3/2}{^1 3/2 - ^0 1/2}$	0.61±0.39
CN	$\frac{^3 5/2 - ^2 5/2}{^2 5/2 - ^1 3/2}$	0.13±0.04
HCN	$\frac{3-2}{1-0}$	1.01±0.53
HCN	$\frac{4-3}{3-2}$	0.49±0.14
HNC	$\frac{3-2}{1-0}$	0.38±0.18
HNC	$\frac{4-3}{3-2}$	0.30±0.10
HCO^+	$\frac{3-2}{1-0}$	0.12±0.04 [b]
HCO^+	$\frac{4-3}{3-2}$	1.37±0.46

a) See (Pérez-Beaupuits et al., 2007) for the J=1–0 and J=3–2 transitions. The low-J lines of HCO^+ were obtained from (Krips et al., 2008).

b) This ratio slightly differs from that found by (Krips et al., 2008) because we use the ratio between the peak main beam temperatures and we corrected the HCO^+ J=1–0 line for the starburst contribution factor.

peak intensities of the low-J transitions of HCN and CN were taken from Pérez-Beaupuits et al. (2007). The peak main beam temperatures of the lower transitions of HCO^+ were provided by M. Krips (private communication; Krips et al. 2008).

The line ratios were computed considering uncertainties of 10% in the reported beam efficiencies η_{mb}, 5% in the main beam θ_{mb}, and 10% in the estimated source size θ_S. As described in the next section, θ_S was assumed to be 1.5" and the same for all the lines. Note that the high uncertainties given in Table 3.4 should be considered lower limits, since comparison of data observed with different telescopes may introduce additional uncertainties due to the presence of different unknown systematics between the telescopes.

3.4.3 Modeling the excitation conditions

We explore a wide range of possible excitation conditions that can lead to the observed line intensities and line ratios, in a similar way as described in Pérez-Beaupuits et al. (2007). In the radiative transfer models, the kinetic temperature T_K and the hydrogen density $n(H_2)$ can be constrained from the *line ratios* (Table 3.4), whereas the column density (per line width) is mostly constrained by the *line intensities*. We used the intensity of the J=3–2 line of HCN, HNC, and HCO^+, and the $N_J = 2_{5/2} - 1_{3/2}$ line of CN, since these are common in the ratios between the low-J and high-J lines. The intensity of these lines was corrected by beam dilution as described below. We use the radiative transfer code RADEX to build a cube of kinetic temperature T_K, number density $n(H_2)$ and column density per line width $N/\Delta V$ for each molecule.

For most of the molecules we explored collisions only with H_2, since this is

considered to be the most important astrophysical process. Other collision partners can be H and He. Although their collision cross sections are comparable, H_2 is about 5 times more abundant than He, and H is at least one order of magnitude less abundant than H_2 in the dense cores of molecular clouds (e.g. Meijerink & Spaans, 2005). Hence, the effects of collisions with these other partners can be neglected. Nevertheless, in contrast with HCN, HNC and HCO^+, the open shell molecular structure of the CN radical makes it more interactive with electrons. Therefore, we also explore the CN–e^- collision as an additional process that could aid the excitation of CN, since the electron abundance can be enhanced by a high ionization degree in PDRs and XDRs.

The volume density explored ranges between $10^4\ \mathrm{cm}^{-3}$ and $10^7\ \mathrm{cm}^{-3}$, the kinetic temperature varies from 4 K to 200 K, and the column density per line width lies between $10^{10}\ \mathrm{cm}^{-2}\,\mathrm{km}^{-1}\,\mathrm{s}$ and $10^{18}\ \mathrm{cm}^{-2}\,\mathrm{km}^{-1}\,\mathrm{s}$. In order to get the actual column density and optical depth, the values that will be reported here must be multiplied by a line width. According to (Schinnerer et al., 2000), the velocity dispersion at the nuclear region of NGC 1068 is about 23 $\mathrm{km\,s}^{-1}$. So, we could expect local velocity dispersions (line widths) ranging between 3 $\mathrm{km\,s}^{-1}$and 10 $\mathrm{km\,s}^{-1}$.

The original RADEX code was modified in order to include dust background emission as a diluted blackbody radiation field, in the same way as done by (Poelman & Spaans, 2005). We consider the emission component at 34 K described in (Spinoglio et al., 2005), scaled by the continuum optical depth $\tau_c(\nu)$ at a particular frequency. Since in our models we consider up to ten transitions, we estimated $\tau_c(\nu)$ as increasing linearly with the frequency of the transition (from Fig.4c in (Spinoglio et al., 2005). We modeled the total background radiation as a composite between the Cosmic Background Radiation (CMB), as a blackbody function at 2.73 K, and the diluted dust radiation, which was estimated as $\tau_c \times B(T_{dust})$, where $B(T_{dust})$ is the Planck function at $T_{dust} = 34$ K and $\tau_c(\nu) = \tau_{100\mu\mathrm{m}}(100\mu\mathrm{m}/\lambda)$. From Hollenbach et al. (1991) we adopted the value $\tau_{100\mu\mathrm{m}} = 10^{-3}$, hence the continuum optical depth becomes $\tau_c(\nu) = 10^{-5}[\mathrm{cm}]\nu/c$, where ν is the rest frequency of the transition in [Hz], and c is the speed of light in [cm/s].

The inclusion of the diluted continuum emission does not affect the results found for HCO^+ but decreases (from $10^{4.7}\mathrm{cm}^{-3}$ to $10^{5.2}\mathrm{cm}^{-3}$) the minimum density at which solutions are found for CN, and it increases (by $\sim 10 - 20$ K) the minimum temperatures found for HCN and HNC, at the lowest densities, in comparison with a model that considers only the CMB as background radiation. The lower limits of the column densities per line width increases as well.

The physical conditions of HCN, HCO^+, and HNC were modeled using the collisional data available in the LAMDA* database Schöier et al. (2005). In the case of CN, we used the collision rates estimated by Fuente et al. (1995). We do not consider hyperfine splitting of CN, HNC and HCN, since they are not resolved in extragalactic systems.

In Pérez-Beaupuits et al. (2007) the excitation conditions of HCN and HNC overlapped, assuming that their emission emerges from the same region. Since we

* http://www.strw.leidenuniv.nl/∼moldata/

Table 3.5: Physical conditions estimated from line ratios[a] and line intensities.

Molecule/ratio	$n(\mathrm{H_2})$ $[\mathrm{cm^{-3}}]$	T_K [K]	$N/\Delta v$[b] $[\mathrm{cm^{-2}\,km^{-1}\,s}]$	τ[b]
HCN	$10^4 - 10^7$	> 20	$10^{13.2} - 10^{15.2}$	$10^{-3.0} < \tau_{1-0} < 10^{2.4}$ $10^{0.2} < \tau_{3-2} < 10^{2.8}$ $10^{0.2} < \tau_{4-3} < 10^{2.8}$
HNC	$10^4 - 10^7$	$10 - 90$	$10^{12.8} - 10^{15.0}$	$10^{-1.0} < \tau_{1-0} < 10^{2.6}$ $1 < \tau_{3-2} < 10^{2.8}$ $10^{-0.6} < \tau_{4-3} < 10^{2.4}$
CN	$10^{5.2} - 10^7$	$10 - 20$	$10^{14} - 10^{15.2}$	$10^{-2.0} < \tau_{1_{3/2}-0_{1/2}} < 10^{2.4}$ $1 < \tau_{2_{5/2}-1_{3/2}} < 10^{2.8}$ $10^{-0.4} < \tau_{3_{5/2}-2_{5/2}} < 10^{1.4}$
$\mathrm{HCO^+}$ $\frac{4-3}{3-2}$	$10^{5.9} - 10^7$	> 30	$10^{11.9} - 10^{12.2}$	$10^{-4.0} < \tau_{3-2} < 10^{-1.2}$ $10^{-2.2} < \tau_{4-3} < 10^{-1.2}$

a) Results from the single-phase model with a source size $\theta_\mathrm{S} = 1.5''$.

b) In order to get the actual column density and optical depth, the values reported here must be multiplied by a pertinent line width, i.e. thermal plus turbulent width (FWHM) of the lines. According to Schinnerer et al. (2000), the velocity dispersion at the nuclear region of NGC 1068 is about 23 $\mathrm{km\,s^{-1}}$.

now have more transitions, we can constrain the temperature and density for each molecule separately, and then see if they agree or not.

Once the starburst contribution to the low-J lines is removed, the bulk of the emission for all the dense gas tracers mostly arises from the CND. There should not be a significant difference in the sizes of the CND as seen in HCN, $\mathrm{HCO^+}$, HNC and CN, if all the lines can be modeled by a single phase. So we assume the same source size for all the J lines to correct them for beam dilution. From the interferometer maps of CN, HCN and $\mathrm{HCO^+}$ available in the literature for NGC 1068 (e.g. Tacconi et al., 1994; Kohno et al., 2001; García-Burillo et al., 2008), we estimate that the source size (FWHM) of these molecules ranges between about 1 and 2 arcseconds.

We can model the physical conditions for most of the line ratios of most of the molecules, considering an average source size $\theta_\mathrm{S} = 1.5''$. The estimated physical conditions are summarized in Table 3.5. A summary of the main results is presented below. Details of the modeling and analysis of the uncertainties are given in the subsequent sections.

3.4.4 The physical environment of HCN

The *left panel* of Figure 3.2 shows the mean $N(\mathrm{HCN})/\Delta v$ $\mathrm{cm^{-2}\,km^{-1}\,s}$ (the mean between the maximum and minimum $N/\Delta v$ that yield valid solutions), for all the explored densities $n(\mathrm{H_2})$ and temperatures T_K that can reproduce, within 1σ, the observed HCN $\frac{3-2}{1-0}$ and HCN $\frac{4-3}{3-2}$ line ratios and the intensity of the HCN J=3–2 line. The *right panel* of Figure 3.2 shows how $N(\mathrm{HCN})/\Delta v$ changes with $n(\mathrm{H_2})$ at different temperatures. These curves are easier to compare with the output of

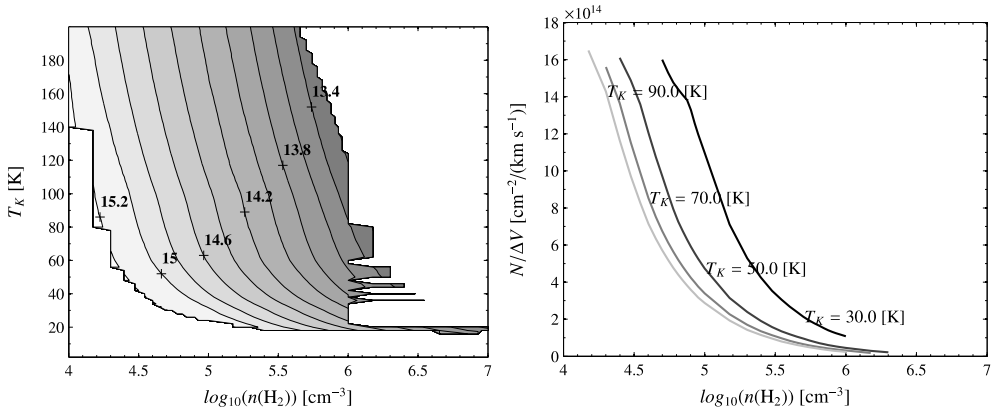

Figure 3.2: *Left* - Excitation conditions modeled for the $\frac{3-2}{1-0}$ and $\frac{4-3}{3-2}$ line ratios of HCN. The contour lines correspond to the mean column density of HCN per line width ($N(\mathrm{HCN})/\Delta\upsilon$ cm^{-2} km^{-1} s), in the region where the estimated line ratios and the J=3–2 line intensity reproduce, within 1σ, the observed values. *Right* - Transversal cuts of the column density per line width at different temperatures modeled above. The column densities are of the order of 10^{14} cm^{-2} km^{-1} s, in linear scale.

Large Velocity Gradient (LVG) models (e.g. Goldreich & Scoville, 1976) commonly found in the literature. To make these curves more clear we do not show the error bars (or uncertainties) of $N(\mathrm{HCN})/\Delta\upsilon$ for each temperature in the plot. But they range between 25.0% – 48.8% at 30 K, 24.2% – 40.6% at 50 K, 18.4% – 38.0% at 70 K, and 21.2% – 36.4% at 90 K. Note that the uncertainties decrease towards the higher $n(\mathrm{H_2})$ densities.

The lower and upper limits of the HCN column density per line width are $10^{13.2}$ cm^{-2} km^{-1} s at the highest density of about 10^6 cm^{-3}, and $10^{15.4}$ cm^{-2} km^{-1} s at the lowest density explored of 10^4 cm^{-3}, respectively. There is also a narrower temperature region (around 20 K) with densities higher than 10^6 cm^{-3}, where solutions for the observed ratios and intensities are also possible. The optical depths τ of each line are summarized in Table 3.5.

All the solutions are found for temperatures higher than 20 K, with a clear degeneracy between the kinetic temperature and molecular hydrogen density. That is, a given column density can be obtained with either high T_K and low $n(\mathrm{H_2})$, or low T_K and high $n(\mathrm{H_2})$.

3.4.5 The physical environment of HNC

In the case of the double peak structure observed in the lower transition lines of HNC, only the main peak (at velocity $\sim 1073 \pm 13$ km s^{-1}) was considered in the analysis, since this is the component that is closer to the central velocity observed in the HNC J=4–3 line.

The *left panel* of Figure 3.3 shows all the excitation conditions for which the observed HNC $\frac{3-2}{1-0}$ and HNC $\frac{4-3}{3-2}$ line ratios and the intensity of the HNC J=3–

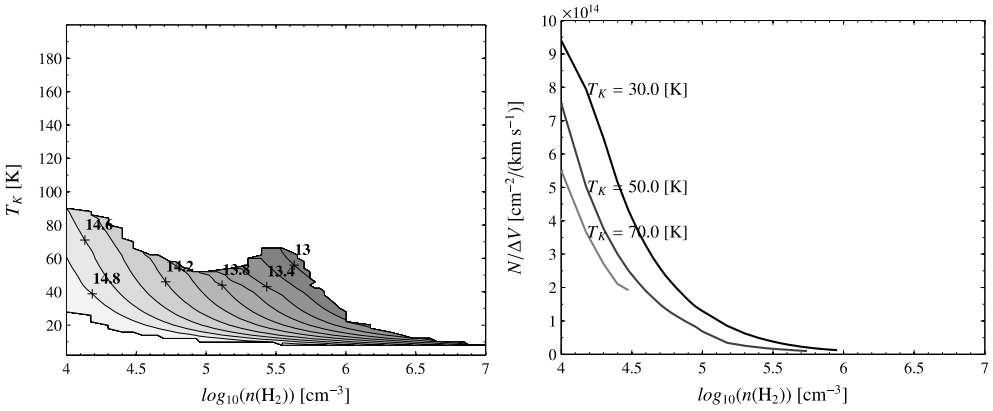

Figure 3.3: *Left* - Excitation conditions modeled for the $\frac{3-2}{1-0}$ and $\frac{4-3}{3-2}$ line ratios of HNC. The contour lines correspond to the mean column density of HNC per line width ($N(\mathrm{HNC})/\Delta v$ cm^{-2} km^{-1} s), in the region where the estimated line ratios and the J=3–2 line intensity reproduce, within 1σ, the observed values. *Right* - Transversal cuts of the column density per line width at different temperatures modeled above. The column densities are of the order of 10^{14} cm^{-2} km^{-1} s, in linear scale.

2 line can be reproduced within 1σ. The mean column density of HNC per line width ($N(\mathrm{HNC})/\Delta v$ cm^{-2} km^{-1} s) is shown in the contour plot. The *right panel* of Figure 3.3 shows how the column density changes with $n(\mathrm{H_2})$ at different temperatures. The corresponding error bars ranges are 6.4% – 35.9% at 30 K, 7.6% – 32.3% at 50 K, and 8.3% – 26.0% at 70 K. The error bars decrease towards the higher $n(\mathrm{H_2})$ densities.

The estimated $N(\mathrm{HNC})/\Delta v$ cm^{-2} km^{-1} s column density per line width ranges between $10^{12.8}$ cm^{-2} km^{-1} s and $10^{15.4}$ cm^{-2} km^{-1} s. The $n(\mathrm{H_2})$ densities required to reproduce these ratios range from 10^4 cm^{-3} (and probably lower than that, when considering higher temperatures outside of our explored grid) and 10^7 cm^{-3} at temperatures of about 10 K. A summary of the corresponding optical depth τ can be found in Table 3.5.

In contrast with HCN, the temperatures at which solutions can be found for HNC are limited up to about 90 K, for the lowest densities explored. At a density of $10^{5.5}$ cm^{-3}, T_K ranges between 10 K and 70 K. But at densities $\geq 10^6$ cm^{-3} only temperatures lower than 30 K are allowed.

3.4.6 The physical environment of HCO$^+$

Using the common source size of 1.5” and the starburst contribution factor of 0.45 in the HCO$^+$ J=1–0 line, our model is not able to reproduce the observed HCO$^+$ $\frac{3-2}{1-0}$ line ratio and HCO$^+$ J=3–2 line intensity. The *left panel* of Figure 3.4 shows the mean column density of HCO$^+$per line width ($N(\mathrm{HCO^+})/\Delta v$ cm^{-2} km^{-1} s) modeled for the HCO$^+$ $\frac{4-3}{3-2}$ line ratio and HCO$^+$ J=3–2 line intensity. The *right panel* of Figure 3.4 shows how the column density changes with $n(\mathrm{H_2})$ at different tempera-

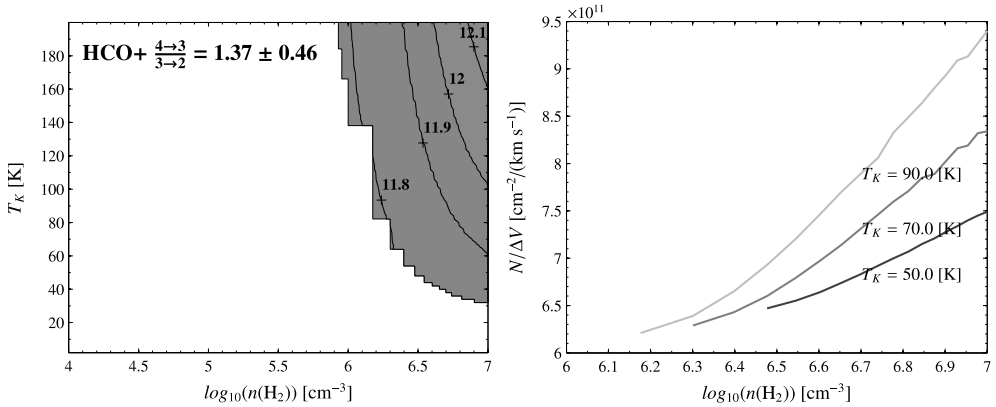

Figure 3.4: *Left* - Excitation conditions modeled for the $\frac{4-3}{3-2}$ line ratio of HCO^+. The contour lines correspond to the mean column density of HCO^+per line width ($N(HCO^+)/\Delta v$ cm^{-2} km^{-1} s), in the region where the estimated line ratios and the J=3–2 line intensity reproduce, within 1σ, the observed values. *Right* - Transversal cuts at different temperatures of the column density per line width modeled above. The column densities are of the order of 10^{11} cm^{-2} km^{-1} s, in linear scale.

tures. The corresponding error bars ranges are 29.9% – 30.1% at 50 K, and 29.3% – 30.0% at 70 K, and 29.0% – 30.1% at 90 K. In this case the error bars decrease towards the lower $n(H_2)$ densities.

The model shows that the high-J lines trace gas with densities larger than $10^{5.9}$ cm^{-3} and temperatures larger than 30 K. Solutions with temperatures lower than 30 K could also be found at densities larger than those explored in this work ($n(H_2) > 10^7$ cm^{-3}). The columns range from $10^{11.9}$ cm^{-2} km^{-1} s to $10^{12.2}$ cm^{-2} km^{-1} s, and both lines are optically thin ($\tau \leq 10^{-1.2}$) over the whole range of columns (Table 3.5). The analysis of the uncertainties in the HCO^+ model is discussed in the sec. 3.5.2.

3.4.7 The physical environment of CN

Only the main spingroups of each transition were considered for modelling the physical conditions of CN. The hyperfine structure of CN is not included in the model. Hence, the radiative lines of CN are described just by the quantum numbers N and J. The collisional data are the same as used by (Fuente et al., 1995).

The excitation conditions derived from the two line ratios with the one-phase model (with a source size of 1.5") are shown in the *left panel* of Figure 3.5. In contrast with HCN and HNC, these conditions overlap just in an small region, with a narrow temperature range. At the lowest density for which solutions are found ($n(H_2) = 10^{5.2}$ cm^{-3}), the kinetic temperature of the gas T_K is between 14 K and 16 K. At higher densities ($n(H_2) \geq 10^7$ cm^{-3}) the gas can be as cold as 10 K.

The *right panel* of Figure 3.5 shows how the column density changes with $n(H_2)$ at $T_K = 14$ K. The dashed lines correspond to the upper and lower limits of

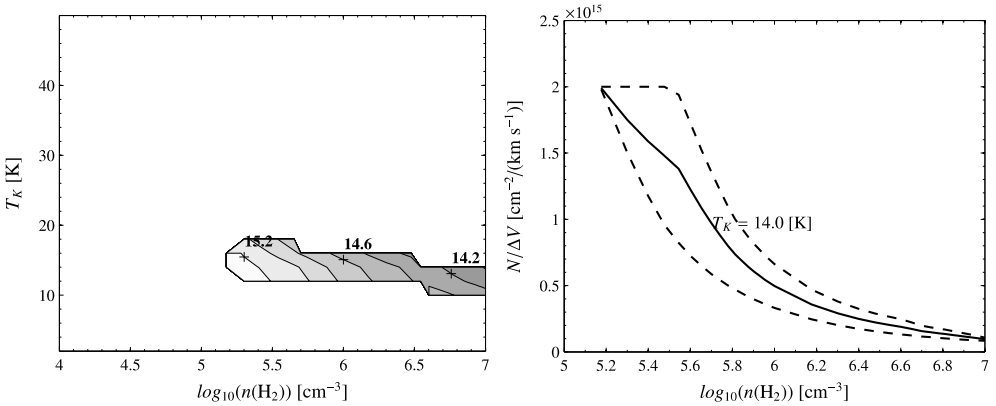

Figure 3.5: *Left* - Excitation conditions modeled for the $\frac{2_{5/2}-1_{3/2}}{1_{3/2}-0_{1/2}}$ and $\frac{3_{5/2}-2_{5/2}}{2_{5/2}-1_{3/2}}$ line ratios of CN. The contour lines correspond to the mean column density of CN per line width ($N(\mathrm{CN})/\Delta v$ cm^{-2} km^{-1} s) in the region where the estimated line ratios and the $N_J = 2_{5/2} - 1_{3/2}$ line intensity reproduce, within 1σ, the observed values. *Right* - Transversal cut at $T_K = 14$ K of the column density per line width modeled above. The values are of the order of 10^{15} cm^{-2} km^{-1} s, in linear scale. The dashed lines correspond to the upper and lower limits of $N(\mathrm{CN})/\Delta v$ cm^{-2} km^{-1} s.

$N(\mathrm{HCO^+})/\Delta v$ cm^{-2} km^{-1} s. Note that for $n(\mathrm{H_2}) = 10^{5.2}$ cm^{-3} and $n(\mathrm{H_2}) = 10^{7}$ cm^{-3} the limits converge, which means there is only one solution at $T_K = 14$ K for those densities.

The column densities per line width have a lower limit of about 10^{14} cm^{-2} km^{-1} s at $n(\mathrm{H_2}) = 10^{7}$ cm^{-3} and an upper limit of $10^{15.6}$ cm^{-2} km^{-1} s at a density of $10^{4.7}$ cm^{-3}. The corresponding optical depths of each line can be found in Table 3.5.

Besides molecular hydrogen, we also explore the effects of electrons as a second collision partner for CN. These could be significant both in PDR and XDR environments, due to enhancement of the ionization degree by radiation. The collision rates are the same as used in Black & van Dishoeck (1991), and were obtained from J.H. Black (private communication). These rates are available only for $T_K = 20$ K.

In a PDR environment, the CN emissivity peaks at a total hydrogen column density of about $10^{21.5} - 10^{22}$ cm^{-2}. At these depths the electron abundance is $\sim 10^{-5}$, and the CN column density is of the order of 10^{14} cm^{-2}. We found that for densities $n(\mathrm{H_2}) \geq 10^{4}$ cm^{-3} the effect of collisions between CN and electrons is negligible.

The only region where the electron abundance can be larger is at the edge of a PDR cloud, that is $N_{\mathrm{H}} \leq 10^{21.5}$ cm^{-2}. There the electron abundance is still about four orders of magnitude lower than the total hydrogen density, but it can be at least two orders of magnitude larger than the H_2 density (Meijerink & Spaans, 2005). At those shallow depths, however, the column of CN is not significant ($N(\mathrm{CN}) \leq 10^{10}$ cm^{-2}). In order to boost the electron abundance to higher levels, in the region where most of the CN emission originates, we would require a gas phase carbon abundance of about $3 - 4$ times Solar. However, these higher

abundances are not supported by other works (e.g. Kraemer et al., 1998).

In an XDR, the ambient conditions along the cloud are different than those found in a PDR, with larger ($10^{-2} - 10^{-4}$) relative electron abundances (Meijerink & Spaans, 2005). In the main emitting region ($N(\mathrm{H}) \geq 10^{22}$ cm^{-2}) the electron density $n(e^-)$ is expected to be about 10 cm^{-3} if $n(\mathrm{H_2}) \sim 10^5$ cm^{-3}. These densities produce changes of the order of 10% in the excitation temperatures T_{ex} of CN, with respect to those obtained when using only H_2 as collision partner, and the column density $N(\mathrm{CN})$ has to decrease with about 50% to get the same line strengths.

Hence, the effect of electrons as secondary collision partner of CN, is not important in a PDR environment. In an XDR environment, small effects can be expected.

3.5 Analysis of the uncertainties

We analyze here how the uncertainties in the input parameters of our models (4–3/3–2, 3–2/1–0 line ratios and the J=3–2 line intensities) propagates to the solutions we find. The two main uncertainties in our models are the estimated common source size ($\theta_S = 1.5''$) for all the molecules and transitions, and the first order estimate of the starburst contribution factor f_{SB} for the J=1–0 lines. The starburst contribution factor affects only the $\frac{3-2}{1-0}$ line ratios which in turn will modify, to some extent, the combination of temperatures (T_K), densities ($n(\mathrm{H_2})$) and column densities (N) for which solutions are found. On the other hand, the source size affects mostly the J=3–2 line intensities (used to constrain the radiative transfer models) which in turn affect mostly the range of temperature and column densities of the solutions. The source size is also present in the 4–3/3–2 and 3–2/1–0 line ratios, as we correct these lines for beam dilution. However, because the source size is about one order of magnitude smaller than the size of the respective beams, its effect in the line ratios is negligible.

The solutions for the HCN and HNC line ratios are less sensitive to these two parameters since the range of temperatures and densities for which solutions exist is large enough (which allows for more flexibility in the T_K vs $n(\mathrm{H_2})$ space) and because the $\frac{4-3}{3-2}$ line ratios, which basically define and constrain the overlap with the solutions found for the ratio between the lower-J lines, are independent of f_{SB}. The effect is reflected mostly in the column densities per line width due to changes in the source size.

3.5.1 Uncertainties in CN

The solutions for CN are particularly sensitive to the source size. As mentioned before, the starburst contribution factor affects only the ratio between the lower J-lines. The range of T_K and $n(\mathrm{H_2})$ for which we find solutions for the CN $\frac{3_{5/2}-2_{5/2}}{2_{5/2}-1_{3/2}}$ line ratio is smaller than that for the $\frac{2_{5/2}-1_{3/2}}{1_{3/2}-0_{1/2}}$ ratio. Hence, the final solutions for CN (given by the overlap between the solutions found separately for the ratios between the low-J lines and the high-J lines) is constrained by the solutions found

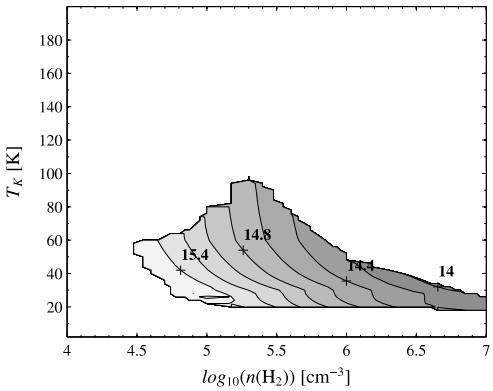

Figure 3.6: Excitation conditions modeled for the $\frac{2_{5/2}-1_{3/2}}{1_{3/2}-0_{1/2}}$ and $\frac{3_{5/2}-2_{5/2}}{2_{5/2}-1_{3/2}}$ line ratios of CN, using a source size of 1". The contour lines are as defined before. Considering this smaller source size, the range of temperatures where solutions are found can go up to 100 K, and densities can be as low as $10^{4.5}$ cm^{-3}.

for the $\frac{3_{5/2}-2_{5/2}}{2_{5/2}-1_{3/2}}$ line ratio.

Because the solutions found for the CN are already constrained, little changes in the source size have a larger impact than for HCN and HNC. If we assume a larger source size of 2", the solutions for CN are restricted to an small range of temperature around 10 ± 4 K and for densities between $10^{5.7}$ cm^{-3} and $10^{6.6}$ cm^{-3}. On the other hand, if we assume an smaller source size of 1", the solutions for CN line ratios can be found in a larger region of T_K and $n(\mathrm{H_2})$ than those found for a source size of 1.5", as shown in Figure 3.6. The smaller source size of 1" increases the estimated CN $N_J = 2_{5/2} - 1_{3/2}$ radiation temperature by a factor 2.25, which is reflected mostly in the range of kinetic temperatures at which we can find solutions for the observed line ratios. When using $\theta_S = 1.5''$ the maximum temperature where solutions can be found is 20 K, at a density of $10^{5.3}$ cm^{-3} (Figure 3.5). But when using an smaller source size (Figure 3.6) the temperature range can go *from* 20 K up to 100 K, at the same density.

3.5.2 Uncertainties in HCO$^+$

On the other hand, the HCO$^+$ $\frac{3-2}{1-0}$ is affected by both, θ_S and f_{SB}, and the fact that we do not find solutions for this ratio may be due to the uncertainties in these two parameters. We explored different alternatives and we found that our model can reproduce the observed ratio, and HCO$^+$ J=3–2 line intensity, if we assume either a larger source size ($\theta_S = 2''$), or a larger starburst contribution factor ($f_{\mathrm{SB}} = 0.60$). The results are shown in the *left* and *right* panels of Figure 3.7. A larger starburst contribution factor increases the HCO$^+$ $\frac{3-2}{1-0}$ line ratio, and allows for solutions at slightly higher temperatures than assuming a larger source size. Note that in both cases solutions for densities $< 10^4$ cm^{-3} are also possible. This result, however, rises a new question since these solutions do not overlap with the solutions found

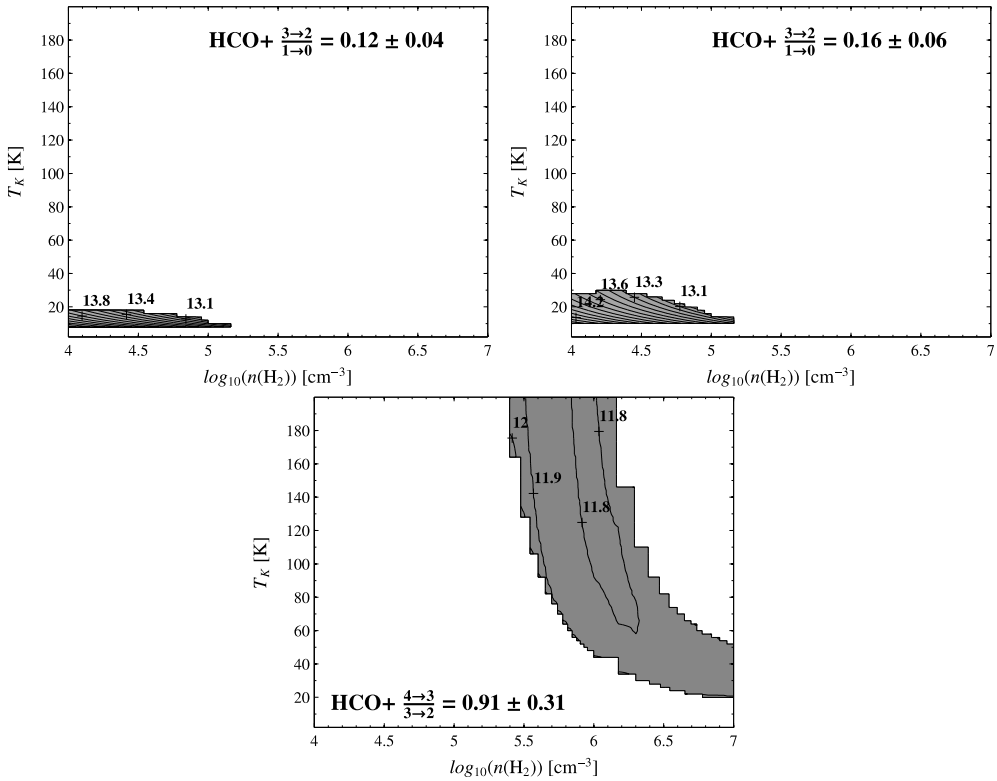

Figure 3.7: *Left* - Excitation conditions modeled for the $\frac{3-2}{1-0}$ line ratio of HCO^+, when considering the estimated starburst contribution factor $f_{SB} = 0.45$, but a larger source size $\theta_S = 2''$. *Right* - Excitation conditions modeled for the $\frac{3-2}{1-0}$ line ratio of HCO^+, when considering a larger starburst contribution factor $f_{SB} = 0.60$, and the common source size $\theta_S = 1.5''$. *Bottom* - Excitation conditions modeled for the $\frac{4-3}{3-2}$ line ratio of HCO^+, when reducing the HCO^+ J=4–3 line intensity by a factor 1.5. The higher transition J=4–3 still traces mostly the dense and warm gas ($n(\mathrm{H_2}) \geq 10^{5.4}$ cm^{-3}, $T_K \geq 20$ K), whereas the $\frac{3-2}{1-0}$ line ratio indicates that those lines would trace less dense ($n(\mathrm{H_2}) < 10^{5.2}$ cm^{-3}) and cold (10 K $< T_K <$ 30 K) gas.

for the HCO^+ $\frac{4-3}{3-2}$ ratio (Figure 3.4).

The fact that the ratio between the higher transition lines traces denser ($n(\mathrm{H_2}) > 10^{5.9}$ cm^{-3}) and warmer ($T_K > 30$ K) gas than what the lower transition lines would indicate, and that they do not overlap either with the solutions found for HCN, HNC or CN, may raise some skepticism about the HCO^+ J=4–3 line. So we also explored the results of our model, assuming that the HCO^+ J=4–3 line could be somehow overestimated (e.g., undetected calibration problems, or intrinsic instrumental differences, like sensitivities, between the JCMT and the IRAM 30m telescopes).

In Sec. 3.2 we mentioned that HARP observations of the calibration source showed less flux than the reference spectra observed with the former receiver B3. Those differences account for factors between 1.1 and 1.5, that where used to correct each of our scans before adding them up. So, if we reduce the final

HCO^+ J=4–3 line by a factor 1.5 (which would be the worst case scenario) the HCO^+ $\frac{4-3}{3-2}$ line ratio reduces to 0.91 ± 0.31 and the new solutions would be as shown in the *bottom* panel of Figure 3.7. It can be seen that, even in this worst case scenario, there would not be an overlap between the solutions found for the ratio between the lower J lines and those found for the higher J lines.

This result would imply that the lower and higher J-lines of HCO^+ trace different gas phases, and a single-phase model may not be the most appropriate to reproduce the observed HCO^+ ratios and intensities. Hence, a two-phase model, where different sizes of the emitting region could be seen by different J lines, may be a better approach for HCO^+. In fact, Krips et al. (2008) mentioned that the size of the emitting region decreases with increasing J line, according to recent SMA data. A multiple-phase model can also be applied to the HCN, HNC and CN molecules. Among molecules, those which are easily dissociated should have small sizes. Hence, a decreasing source size with increasing J line seems natural. However, the only way to constrain these models would be by using interferometer maps (fluxes, beam deconvolution, etc.) to accurately estimate the actual source size seen by the different J lines. Nevertheless, this is a task that is beyond the scope of this work.

3.6 Line intensity and abundance ratios

The line intensity ratios, with respect to HCN, are summarized in Table 3.6. The intensities used correspond to the peak antenna temperature of the main component of the gaussian fits, corrected for starburst contribution, beam efficiency, and beam dilution, assuming a source size of 1.5" for all the lines. We also find that most of the line intensity ratios (the HCO^+/HCNJ=4–3 ratio is the exception that is discussed below) decrease with increasing rotational quantum number J, similar to what was found by Krips et al. (2008) for the HCN/CO ratio. This was also noticed for the HNC/HCN J=1–0 and J=3–2 line ratios observed in NGC 1068, and other Seyfert galaxies, by Pérez-Beaupuits et al. (2007). Since the beam sizes are comparable, this could be an indication that the higher-J levels of CN and HNC are less populated than those of HCN.

This is what we would expect assuming collisional excitation of the molecules, where T_{ex} is proportional to $\tau \times n(\mathrm{H_2})$. From the excitation conditions modeled in Sec. 3.4.3, the HNC column densities, and hence τ_{HNC}, tend to be lower than that of HCN. On the other hand, even if the column densities that we find for CN are as high (or higher in some cases) than the columns found for HCN, the optical depth τ_{CN} tends to be lower than τ_{HCN} because of the higher (fine and hyperfine) splitting of the rotational levels of CN. Thus, the high energy levels of CN and HNC would be less populated than those of HCN.

In the following sections we address the relative abundance issue by estimating the abundance ratio as the ratio between the column densities estimated from the radiative transfer models described before.

Table 3.6: Line intensity ratios between molecules.

Molecules	Transition[a]		
	J=1–0	J=3–2	J=4–3
$\frac{\mathrm{HNC}}{\mathrm{HCN}}$	0.71±0.45	0.26±0.08	0.16±0.05
$\frac{\mathrm{CN}}{\mathrm{HCN}}$	0.89±0.69	0.54±0.15	0.14±0.04
$\frac{\mathrm{HCO^+}}{\mathrm{HCN}}$	1.10±0.59	0.13±0.04	0.36±0.10

a) The lines correspond to J=1–0, J=3–2 and J=4–3, for HCN, HNC and HCO^+. In the case of CN, the lines are actually $N_J = 1_{3/2} - 0_{1/2}$, $N_J = 2_{5/2} - 1_{3/2}$ and $N_J = 3_{5/2} - 2_{5/2}$, respectively.

3.6.1 HNC/HCN

The range of temperatures where we can analyze the HNC/HCN ratio is limited by the solutions found for HNC, which go up to ~ 90 K at the lowest density explored ($n(\mathrm{H_2}) = 10^4$ cm^{-3}). The *left panel* in Figure 3.8 shows the mean $N(\mathrm{HNC})/N(\mathrm{HCN})$ column density ratio for the temperatures and densities where the solutions found for each molecule (left panels of Figs. 3.3 & 3.2) overlap. The mean column density ratio ranges between 0.10 and 0.18, with errors that vary between 30% and 55% of the mean value. Note that similar ratios can be found at two different temperatures for a particular density. The *right panel* in Figure 3.8 shows the mean value, and corresponding upper and lower limits, of the $N(\mathrm{HNC})/N(\mathrm{HCN})$ ratio at 20 K and 50 K. At these temperatures the ratios are quite similar (within 15%) for the density range $n(\mathrm{H_2}) = 10^{5.3-5.7}$ cm^{-3}.

The fact that the line intensity ratios (Table 3.6) are also lower than unity, indicates that the bulk of the HNC and HCN emission emerges from warm gas ($T_K > 30$ K). This agrees with observations in the vicinity of the hot core of Orion KL, and experimental and theoretical data, where the HNC/HCN line ratio decreases as the temperature and density increase (e.g. Schilke et al., 1992; Talbi et al., 1996; Tachikawa et al., 2003).

On the other hand, the ratios $N(HNC)/N(HCN) < 1$ estimated with our models cannot be directly interpreted as a signature of a pure PDR or XDR environment in the CND of NGC 1068. The HNC abundance can be decreased due to temperatures higher than traditionally expected, produced deep inside a molecular cloud by mechanisms other than radiation, like turbulence and shocks (Loenen et al., 2008). If the temperature is higher than 100 K, the conversion of HNC into HCN is more efficient and HNC is suppressed (Schilke et al., 1992; Talbi et al., 1996). These high temperatures are not found in regions where the abundance of HCN and HNC is high enough to be detected, for traditional PDR or XDR models (Meijerink & Spaans, 2005). The high SiO abundance observed in the CND of NGC 1068 can be a direct evidence of the possible contributions from mechanical heating (shocks) and dust grain chemistry induced by X-rays (García-Burillo et al., 2008). Hence, a more elaborated PDR/XDR model that includes both mechanical heating and grain surface chemistry will be needed to further understand the results of our radiative

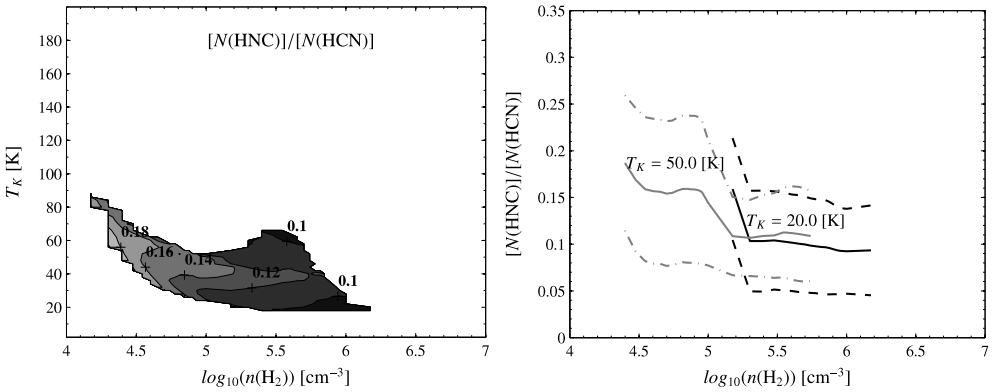

Figure 3.8: *Left* - Ratios between the mean column densities of HNC and HCN ($N(\mathrm{HNC})/\mathrm{N(HCN)}$). *Right* - Transversal cut of the ratios at different temperatures. The *dashed* and *dashed-dot* lines correspond to the upper and lower limits of the ratios at 20 K and 50 K, respectively.

transfer models.

3.6.2 CN/HCN

When using the one-phase model with a source size $\theta_S = 1.5''$, the physical conditions estimated for the CN and HCN molecules (left panel in Figs. 3.5 & 3.2) overlap *only* in an small region around $n(\mathrm{H_2}) \sim 10^{5.5}$ cm^{-3} and $T_K \sim 20$ K. The *left panel* in Figure 3.9 shows the mean $N(\mathrm{CN})/N(\mathrm{HCN})$ column density ratio and the corresponding upper and lower limits. The maximum ratio of 0.93 ± 0.07 is found at $n(\mathrm{H_2}) \sim 10^{5.4}$ cm^{-3}. The ratio decreases almost linearly with density (while the uncertainty increases), and it reaches the minimum ratio of 0.73 ± 0.2, with a larger uncertainty of $\sim 29\%$, at a density of $n(\mathrm{H_2}) \sim 10^{5.5}$ cm^{-3}. The ratio then increases slowly, with a constant uncertainty, up to 0.76 ± 0.2 at $n(\mathrm{H_2}) \sim 10^{5.7}$ cm^{-3}.

If we assume a larger source size $\theta_S = 2''$ for CN, the solutions obtained do not overlap with those found for HCN. However, when using an smaller source size $\theta_S = 1''$ for CN, there is a large overlap in the physical conditions found for these molecules (left panel in Figs. 3.6 & 3.2). The *right panel* in Figure 3.9 shows the mean $N(\mathrm{CN})/N(\mathrm{HCN})$ column density ratio for the new model. The new mean column density ratios now range between ~ 2 and ~ 4, with errors that vary between 20% and 50% of the mean value. The maximum mean ratios (≥ 3.6) are found at a density of $\sim 10^6$ cm^{-3} and temperatures between 40 K and 60 K, while the minimum mean ratios (< 2.3) can be found at a larger density range of $n(\mathrm{H_2}) \sim 10^{5-6}$ cm^{-3} but at lower temperatures ($T_K < 30$ K).

The *bottom panel* in Figure 3.9 shows the mean value, and corresponding upper and lower limits, of the $N(\mathrm{CN})/N(\mathrm{HCN})$ ratio at 18 K, 30 K and 50 K. At $T_K = 18$ K the new ratios (with uncertainties ranging from 23.6% to 26.5%) are larger (ranging between 3 and 4) and are found at a higher density range ($n(\mathrm{H_2}) > 10^{6.6}$ cm^{-3}) than in the 1.5" source size model. On the other hand, at densities between

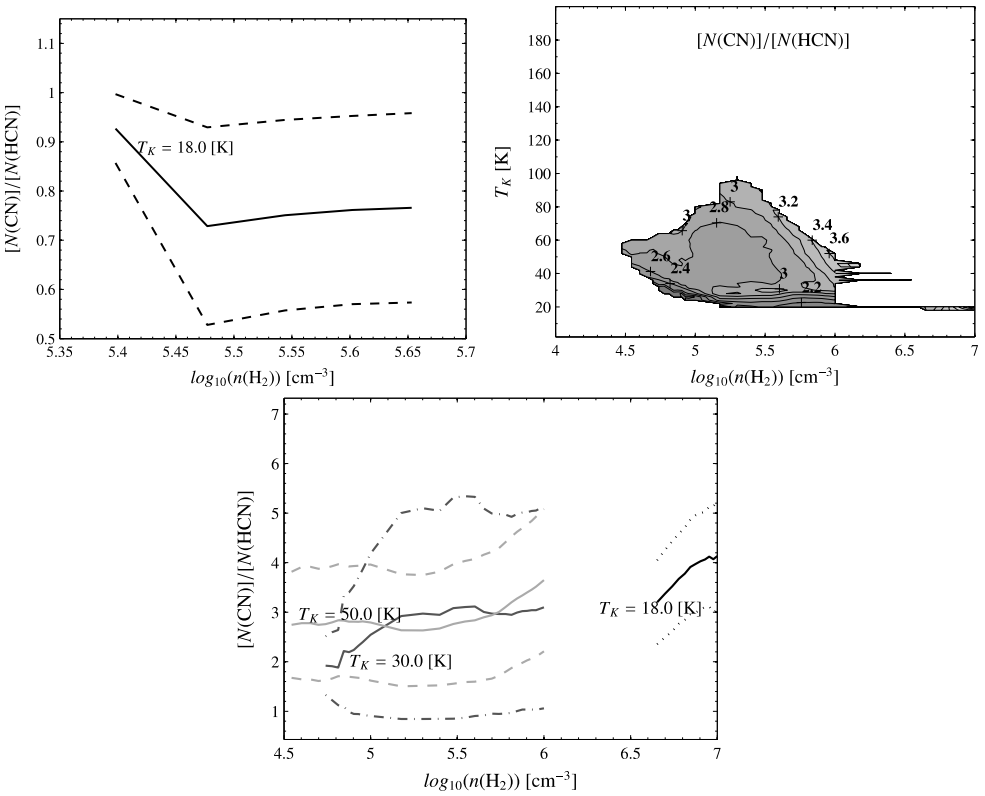

Figure 3.9: *Left* - The $N(\mathrm{CN})/N(\mathrm{HCN})$) column density ratios for the small range of density at $T_K = 18$ K, where the physical conditions found for CN and HCN overlap when using the one-phase model with $\theta_S = 1.5''$. *Right* - Ratios between the mean column densities of CN and HCN, when using a source size $\theta_S = 1''$ for CN. *Bottom* - Transversal cuts, at different temperatures, of the ratios showed in the middle panel. The *dotted*, *dashed-dotted* and *dashed* lines correspond to the upper and lower limits of the ratios at 18 K, 30 K and 50 K, respectively.

10^5 cm^{-3} and 10^6 cm^{-3} the ratios found for 30 K and 50 K are very similar (within 10%), but the uncertainties of the ratios at $T_K = 30$ K are larger (63.6%–72.4%) than those for $T_K = 50$ K (39.0%–43.7%). These larger uncertainties for the ratios at $T_K = 30$ K imply that the corresponding upper limits increase to values > 5 at a density $n(\mathrm{H_2}) \sim 10^{5.6}$ cm^{-3}. Note that the uncertainties at $T_K = 30K$, and hence the upper limits, decrease for densities $< 10^{5.1}$ cm^{-3}.

The mean column density ratios estimated with $\theta_S = 1.5''$ can be easily found in an XDR environment, but the predominance of this component cannot be concluded from the $N(\mathrm{CN})/N(\mathrm{HCN})$ ratio only, since ratios ~ 1.0 are also expected in a PDR component (Lepp & Dalgarno, 1996; Meijerink et al., 2007). The mean column density ratios $2 \lesssim N(\mathrm{CN})/N(\mathrm{HCN}) \lesssim 4$ estimated with $\theta_S = 1''$, are tentatively more consistent with an XDR/AGN environments (Lepp & Dalgarno, 1996; Meijerink et al., 2007). However, these and higher [CN]/[HCN] abundance ratios

have also been found in PDR/starburst scenarios (e.g. Fuente et al., 2005). The fact that we find a relatively low $N(\mathrm{CN})/N(\mathrm{HCN})$ column density ratio, with respect to what would be expected in a pure XDR scenario, could be explained by an over-abundance of HCN due to the grain-surface chemistry suggested by García-Burillo et al. (2008).

Nevertheless, assuming an smaller emitting region for CN than for HCN introduces a new question regarding the chemistry/physics driving the formation (or destruction) of these two molecules. If this is the case, then we would need to explain why CN is absent in the hypothetically more extended region covered by HCN. Perhaps this scenario could also be explained by the possible contributions from mechanical heating and dust grain chemistry suggested in Loenen et al. (2008) and García-Burillo et al. (2008). However, exploring this alternative would require high resolution maps of at least SiO, HCN, CN and HNC, in addition to a composite mechanical heating, X-rays and dust-grain chemistry model, to properly account for the different contributing scenarios. This is an study that can be addressed in a follow up work.

3.6.3 HCO^+/HCN

Figure 3.4 indicates that the emission from the high-J HCO^+ lines emerge from gas that does not co-exist with HCN, HNC and CN, in the nuclear region of NGC 1068. The column density ($10^{11.9} - 10^{12.2}\ \mathrm{cm^{-2}\,km^{-1}\,s}$) estimated from the $HCO^+\ \frac{4-3}{3-2}$ ratio, and the possible solutions found for the $HCO^+\ \frac{3-2}{1-0}$ ratio (left panels of Figure 3.7), also indicates that the warmer and denser gas traced by the high-J lines is only an small fraction (0.5% – 10%) of the total HCO^+ gas. Most of it is confined to the lower transitions.

The main reason for the lack of co-existence is the HCO^+ J=4–3 line. The possible solutions found for the $HCO^+\ \frac{3-2}{1-0}$ ratio, considering the uncertainties, would be consistent, in terms of density, with the HCN and HNC molecules, albeit at somewhat lower temperature. However, if we consider a larger source size of about 2" (as shown in Sec. 3.5.2), the HCO^+ J=3–2 line intensity will decrease, and solutions for temperatures up to 30 K (at densities of a few times $10^4\ \mathrm{cm^{-3}}$) will be possible, and the solutions for the high-J ratio will require just slightly lower ($N(\mathrm{HCO^+}) \sim 10^{11.7-12.0}\ \mathrm{cm^{-2}\,km^{-1}\,s}$) column densities per line width. Hence, the HCO^+ J=4–3 line seems to indicate a different gas phase.

Krips et al. (2008) found that the HCN/CO line intensity ratios decrease with increasing rotational quantum number J, for AGN dominated galaxies, including NGC 1068. We find the same trend in the HNC/HCN and CN/HCN line intensity ratios (Table 3.6). The HCO^+/HCN ratio, however, defies this trend. Interestingly, the higher-J levels of HCO^+ may be more populated than its lower levels due to a local X-ray source (Meijerink et al., 2007). This result is consistent with an XDR, given that in strongly irradiated dense XDRs the HCO^+ column builds up with depth to high values before the HCN does. Hence, the column weighted temperature of the HCO^+ molecule is higher, from which the HCO^+ J=4–3 line benefits. The HCN

behavior with depth is more gradual, avoiding the strong separation between the low and high-J lines (e.g. Meijerink & Spaans, 2005, their Fig. 9).

The J=4–3 line ratio between the peak intensities of HCN and HCO^+ (the inverse value is shown in Table 3.6) is about ~ 2.7, and is consistent with the ratio reported by Kohno et al. (2001). Instead, the velocity-integrated intensity ratio $\frac{I(HCN)}{I(\mathrm{HCO^+})} J = 4-3$ is ~ 3.7 (from Table 3), which is larger than the ratio between the peak intensities due to the smaller line width of the HCO^+ J=4–3 line. This number is right above the maximum value shown in Fig.3 of Kohno (2005). Interestingly, this places NGC 1068 in a distinguished position within the Kohno diagram, among their pure AGNs.

3.7 Conclusions

We have used HARP on JCMT to observe the J=4–3 line of HCN, HNC, HCO^+ , and the $N_J = 2_{5/2} - 1_{3/2}$ and $N_J = 3_{5/2} - 2_{5/2}$ transitions of CN, in the nuclear region of NGC 1068. We estimated the excitation conditions and abundance ratios of these molecules in the CND from radiative transfer models, assuming a single phase gas for all the molecules and lines. We compared column density ratios with predictions from PDR/starburst and XDR/AGN models.

We deduced a first-order estimate of the starburst contribution to the J=1–0 lines, out of independent observations with different telescopes. The starburst contribution of the higher-J lines should be negligible because of the smaller beam sizes at the higher observing frequencies.

We first expected, and assumed, that the source sizes, seen by the different molecules and transitions, should not be significantly different. We estimated the source sizes for HCN, CN and HCO^+ from the different interferometer maps available in the literature, and used a common value of 1.5" for all the observed lines. The results of our models showed that the HCN, HNC and partly CN, can co-exist in gas with similar kinetic temperature (10 – 20 K) and hydrogen density ($10^{5.3-5.7}$ $\mathrm{cm^{-3}}$).

However, the analysis of the uncertainties in source size, as well as in the starburst contribution factor, shows that the HCO^+ molecule seems to trace a totally different gas phase, both with respect to the other molecules and its own different transitions. The HCO^+ $\frac{4-3}{3-2}$ line ratio indicates that the emission of these lines emerges from gas with densities larger than $10^{5.9}$ $\mathrm{cm^{-3}}$ and temperatures higher than 30 K. Instead, the HCO^+ $\frac{3-2}{1-0}$ line ratio would traces less dense ($n(\mathrm{H_2}) \leq 10^5$ $\mathrm{cm^{-3}}$) and colder ($T_K \leq 20$ K) gas, when using models with either an smaller source size or a higher starburst contribution factor.

The physical conditions estimated from the line ratios are based on the assumption of a single-phase model with the same size of the emitting region. However, a single-phase scenario clearly does not hold for the HCO^+ molecule. The lack of an independent measurement of the HCO^+ J=1–0 line, and the assumption of the same starburst contamination factor for this line as the one found for HCN from the IRAM 30m data, introduces an additional uncertainty. Nevertheless, the fact

that the high-J lines of HCO^+ clearly trace higher densities and temperatures, with lower HCO^+ column densities, indicates that this gas is less extended throughout the CND, in terms of volume and maybe in surface as well.

The line intensity ratios of CN/HCN and HNC/HCN decrease with increasing rotational quantum number J. The HCO^+/HCN intensity ratios, instead, do not follow this trend. The HCO^+ J=4–3 line intensity, compared with the lower transition lines and with the HCN J=4–3 line, support the influence of a local XDR environment.

The $N(\mathrm{CN})/N(\mathrm{HCN}) \sim 1-4$ column density ratios estimated with the single-phase model are indicative of an XDR/AGN environment with a possible contribution of grain-surface chemistry induced by X-rays or shocks.

The single-phase model, with a common source size seen by all the molecules and transitions, works well for HCN and HNC. However, HCO^+ shows clear evidence that different lines can trace completely different gas phases. Besides, assuming an average source size for all the molecules and lines can be a good first approximation, but has the clear drawback that estimates derive mostly from the J=1–0 interferometer maps, which do not trace very warm and dense gas, and are sensitive to beam smearing effects. High resolution maps of the higher-J lines may show slight differences in source sizes that can be considered negligible, at a first glance. But, as was shown with CN and HCO^+, even an error of a fraction of an arcsecond in the estimated source size can make a big difference in the physical conditions derived from the radiative transfer models. High resolution maps of the different transitions used in the models would aid to reduce the uncertainties in the models. In addition, a more elaborated PDR/XDR model that includes mechanical heating and grain-surface chemistry, will be necessary to properly account for the different contributing factors.

The spatial extent and morphology of the emitting regions of different J lines, as well as the detailed dynamics and physical environment of the high density tracers, can be tested with the higher spatial resolution maps that ALMA will provide in the future.

Acknowledgements

Many thanks go to Kalle Torstensson for doing the observations, and to the JCMT staff for their support. We are grateful to J.H. Black for useful comments and M. Krips for providing HCO^+ data. We are grateful to the referee for the careful reading of the manuscript and constructive comments and suggestions. Molecular Databases that have been helpful include the NASA/JPL, LAMDA and NIST. This work has benefitted from research funding by the European Community's sixth Framework Programme under RadioNet R113CT 2003 5058187.

4

The deeply obscured AGN of NGC 4945

– J.P. Pérez-Beaupuits, H.W.W. Spoon, M. Spaans, J.D. Smith –

The nearly edge-on galaxy NGC 4945 is one of the closest galaxies where an AGN and starburst coexist, and is one of the brightest sources at $100\ \mathrm{keV}$. Near and mid-infrared spectroscopy have shown very strong obscuration of its central region, rivaled only in strength by some of the most deeply obscured ULIRGs. In contrast, at optical and infrared wavelengths the AGN has remained undetected until very recently. In order to determine the spatial distribution of ISM emission features, and to characterize the physical conditions in the ISM exposed to the radiation from the circumnuclear starburst and the deeply buried AGN, we map the central region of NGC 4945 in three of the four Spitzer-IRS modules (SH, SL and LL). In particular, we produce maps of the flux distribution of the starburst tracers [Ne II], [Ne III], [S III] and [S IV] at 12.81, 15.56, 18.71 and 10.51 μm, respectively, and a map of the AGN narrow-line region tracer [Ne V] at 14.32 μm. The first $\sim$2.3$''$ resolution maps of the [Ne V] 14.32 μm fine-structure line and the deep silicate absorption feature at 9.7 μm of the nucleus of NGC 4945 are presented. The [Ne V] emission flux was detected down to a level of $0.017 \times 10^{-21}\ \mathrm{W\ cm^{-2}}$, and shows an extended distribution rather than a point source-like distribution. We obtained an extinction map (A_V) based on the apparent strength of the 9.7 μm silicate absorption feature. The peak emission of most of the extinction corrected lines coincides (within $\sim 1''$) with the position of the H_2O maser. The [Ne V]/[Ne II] ratios obtained in all the region mapped are lower than the ratios typically observed in AGNs. Whereas the [Ne III]/[Ne II] ratios observed along the starburst ring are consistent with the ratios expected in shocks. This may be due to an excess [Ne II] emission driven by the starburst ring, or to the presence of many SN remnants. An extinction $A_\mathrm{V} \sim 5500\ \mathrm{mag}$ is needed to obtain typical AGN [Ne V]/[Ne II] line ratios of > 0.8, consistent with X-ray derived columns $N_\mathrm{H} > 10^{24}\ \mathrm{cm^{-2}}$ obscuring the AGN BLR of NGC 4945.

Paper in preparation. Based on observations obtained with the Spitzer Space Telescope, which is operated by the Jet Propulsion Laboratory, California Institute of Technology, under NASA contract 1407.

4.1 Introduction

The active galaxy NGC 4945 is one of the closest (at a distance of ~ 3.82 Mpc, adopted from the recent estimates by Karachentsev et al. 2007, which imply a spatial scale of ~ 18.5 pc/arcsec) galaxies that host both, an AGN and starburst. Earlier X-ray observations showed evidence for a hidden AGN (Iwasawa et al., 1993; Guainazzi et al., 2000). These observations revealed a Compton-thick spectrum with an absorbing column density of $N_{\rm H} = 5 \times 10^{24}$ cm^{-2} (Iwasawa et al., 1993). The nucleus of NGC 4945 is one of the brightest extragalactic sources at 100 keV (Done et al., 1996), and the brightest Seyfert 2 AGN at > 20 keV (Itoh et al., 2008).

Rather than a point source marking the presence of the AGN in optical and near-infrared images, the nearly edge-on ($i \sim 80^o$) line of sight to the central region reveals evidence for strong and patchy extinction, which is especially apparent in HST-NICMOS $H - K$ maps (Marconi et al., 2000). A dust lane aligned along the major axis of the galactic disk obscures parts of the central region just southeast of the K-band peak. The K-band peak itself lies $\sim 1''$ west (but, within the uncertainty) of the position of the H_2O maser (Greenhill et al., 1997), which we adopt as the location of the AGN.

Estimates from IRAS observations indicate that about 75% of the total infrared luminosity of the galaxy ($L_{\rm IR} = 2.4 \times 10^{10}\ L_\odot$) is generated within an elongated region of $12'' \times 9''$ (about 222×167 pc^2) centered on the nucleus (Brock et al., 1988). The structure of this region, as shown in high resolution HST-NICMOS observations of the Paα line, is consistent with a nearly edge-on starburst disk with a $4.5''$ (~ 83 pc) radius (Marconi et al., 2000).

Although the star formation and supernova rates in the nuclear region were originally estimated to be moderate ($\sim 0.4\ M_\odot$ yr^{-1} and ~ 0.05 yr^{-1}, respectively; Moorwood & Oliva 1994), more recent estimates based on high resolution (angular scale of 0.3 pc) radio observations and estimates of supernova remnant source counts, sizes and expansion rates, lead to a type II supernova rate of $> 0.1(v/10^4)$ yr^{-1}, and star formation rate limits of $2.4(v/10^4) < SFR(M \geq 5\ M_\odot) < 370\ M_\odot$ yr^{-1}, where v is the shell radial expansion velocity in km s^{-1} (Lenc & Tingay, 2009). These supernova and star formation rates are, within a factor two, similar to those estimated in NGC 253 and M82 (Pedlar et al., 2003; Lenc & Tingay, 2006), which are also nearly edge-on starburst galaxies, have similar distances close to 4 Mpc and all show similar infrared luminosities (Rice et al., 1988). The impact of the central starburst on the circumnuclear region is large, as revealed by the presence of a conical cavity evacuated by a supernova driven wind (Moorwood et al., 1996c; Marconi et al., 2000). The HST-NICMOS images of the H_2 1-0 S(1) line at 2.12 μm show that the edges of the cavity extend out to $5''$ ($\sim$93pc) north from the NGC 4945 nucleus (Marconi et al., 2000).

Near and mid-infrared spectroscopy indicate that the ISM in the central region of NGC 4945 is very different than that of other nearby starburst galaxies, such as M 82 and NGC 253, which present similar inclination angles. The strong absorption features of both volatile (CO and CO_2) and refractory (H_2O) ices observed in the 2.4–5 μm ISO-PHT-S spectrum indicate the presence of shielded cold molecular

clouds obscuring the NGC 4945 nucleus (Spoon et al., 2000, 2003). The detection of a strong absorption feature of XCN ice at 4.62 μm by Spoon et al. (2000, 2003) indicates that these molecular clouds have been processed in an energetic environment (Lacy et al., 1984), and processed ice is suggested to be a common characteristic of dense molecular material in star forming galactic nuclei (Spoon et al., 2003). A highly distorted PAH emission spectrum produced by a very deep 9.7 μm silicate absorption feature is more evidence for the unusually strongly obscured nuclear region (Spoon et al., 2000; Brandl et al., 2006). This makes NGC 4945 a unique nearby laboratory to study an environment that can be found only in distant ULIRGs.

Previous mid-infrared spectroscopic observations could not confirm the presence of an AGN in NGC 4945. Just an upper limit of the 14.32 μm [Ne v] emission, considered a tracer of AGN narrow-line regions (Moorwood et al., 1996b; Genzel et al., 1998, e.g.,), was obtained from ISO-SWS observations (Spoon et al., 2000). The VLT-ISAAC observation of the 3.93 μm [Si ix] line, commonly observed in the soft X-ray photoionized gas of many Seyfert galaxies (Oliva et al., 1994; Lutz et al., 2002), resulted in a non-detection (Spoon et al., 2003). Only recent observations with the more sensitive IRS-SH spectrograph on Spitzer allowed the detection (although at a very faint level) of the 14.32 μm [Ne v] line towards the NGC 4945 nucleus (Bernard-Salas et al., 2009). The [Ne v]14.3μm/[Ne ii]12.8μm flux ratio found in NGC 4945 is ~ 0.007, which indicates an AGN contribution of less than a few percent using the diagram by Farrah et al. (2007) (their Fig. 16). This detection of [Ne v] relative to [Ne ii] is about 10 times weaker than what was observed in other Seyfert galaxies like Mrk 266 and NGC 1365 (Bernard-Salas et al., 2009).

In this paper we study the mid-IR properties of the nuclear region of NGC 4945. Spitzer-IRS spectral mapping observations of a $20.7'' \times 20.7''$ (about 383×383 pc^2) region are presented. The mapping capabilities of Spitzer-IRS allow the study of a number of properties of the nuclear region in NGC 4945. For instance, the extent of the AGN coronal line region as traced by the [Ne v] line, the extent of the crystalline silicate absorbing region (and a search for the sources responsible for the presence of crystalline silicates), disentangling PAH emission and silicate absorption along the line of sight, and the excitation and age of the circum-nuclear starburst based on line ratios of forbidden lines. Although we actually used the Spitzer-IRS modules SH, SL and LL, in this work we present the most interesting results from the SH and SL spectral maps only, since in this work we focus on the analysis of the spatial distribution of ISM emission and absorption features. We present for the first time the maps of the starburst tracers [Ne ii] 12.81 μm, [Ne iii] 15.56 μm, [S iii] 18.71 μm, and [S iv] 10.51 μm, and a map of the AGN narrow-line region tracer [Ne v] at 14.32 μm, and analyze the ratios between some of these tracers as different diagnostics. The organization of this article is as follows. In Sect. 4.2 we describe the observations and the data reduction. The maps obtained are presented in Sect. 4.3. The analysis of the data is presented in Sect. 4.4. The conclusions and final remarks are presented in Sect. 4.5.

4.2 Observations and data reduction

We mapped the central region of NGC 4945 with the InfraRed Spectrograph* (IRS - Houck et al. 2004) on board of the Spitzer Space Telescope (Werner et al., 2004) through the guaranteed time observation (GTO) program P40479 (PI: H.W.W. Spoon). The spectral maps were done in moderate resolution (R$\sim$600) with the Short-High (SH; 9.9 – 19.6 μm) IRS† module, and at low resolution (R$\sim$60–120) using the Short-Low (SL1; 7.4 – 14.5 μm, SL2; 5.2 – 7.7 μm) and Long-Low (LL1; 19.5 – 38.0 μm, LL2; 14.0 – 21.3 μm) IRS modules.

The SH module was used to measure mainly the fine-structure emission lines (starburst tracers) [S IV] at 10.51 μm, [Ne II] at 12.81 μm, [Ne III] at 15.56 μm, [S III] at 18.71 μm, the AGN narrow-line region tracer [Ne V] at 14.32 μm, and the molecular hydrogen (pure rotational) lines, H_2 0-0 S(2) and H_2 0-0 S(1) at 12.3 μm and 17.0 μm, respectively. We also obtained a map of the CO_2 ice absorption feature at 11.0 μm from the SH module. With the SL module we obtained maps of the H_2 S(3), and the silicate absorption feature at 9.7 μm.

4.2.1 SH map

The IRS-SH map was obtained in July 2007 (at the beginning of the summer visibility window) when the SH slit was relatively aligned with the minor axis of NGC 4945. The area mapped was limited to a set of 3 parallel by 10 perpendicular pointings centered on the nucleus, and covering an area of $21'' \times 26''$. The *top panel* of Fig. 4.1 shows the orientation of the SH slit overlaid on the Spitzer-MIPS 24 μm map of the central region of NGC 4945 (by courtesy of Varoujian Gorjian, private communication).

A S/N>20 in the 14.5 μm continuum was reached in order to detect the 1 μm wide absorption band of CO_2 ice at 15.3 μm. The quality of the map was optimized by splitting up the mapping into 4 1-cycle maps of 120 sec, each of which was alternated with a staring mode off-source sky measurement to keep track of rogue pixels and to obtain an accurate measure of the sky background. The total time used for the SH map, including sky positions, was 6.5 hrs.

4.2.2 SL map

Due to a *Spitzer anomaly*‡ that began a few hours before the original schedule of the observations, the IRS-SL map of the nuclear region of NGC 4945 was delayed till August 2008, when the SL slit was no longer perfectly aligned with the galaxy major axis. A minimum S/N of 40 in the 6.7 μm continuum for SL2 and of 30 at 11.0 μm for SL1 was achieved. These sensitivities were obtained with 5 cycles of

* The IRS was a collaborative venture between Cornell University and Ball Aerospace Corporation funded by NASA through the Jet Propulsion Laboratory and the Ames Research Center.

† http://ssc.spitzer.caltech.edu/irs/highleveloverview

‡ http://www.spitzer.caltech.edu/news/856-feature06-25-Engineers-Studying-Spitzer-Anomaly

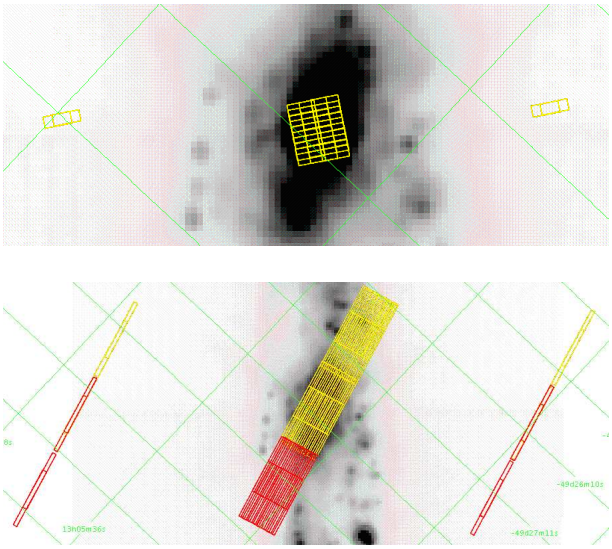

Figure 4.1: Spitzer-MIPS 24 μm map (Varoujian Gorjian, priv.comm.) of the central region of NGC 4945. The galaxy major axis runs vertical. North is toward the upper right, East toward the upper left. Along the declination axis the grid spacing is $\sim$1 arcminute, and about 12 seconds along the R.A. axis. The region mapped with the IRS-SH module (*top panel*) is about $21'' \times 26''$, while a larger region of $37'' \times 67''$ was mapped with the IRS-SL (*bottom panel*) module. The red and yellow grids correspond to the SL1 and SL2 spectral orders, respectively. The sky (off-source) positions observations are indicated by the grids to the left and right of the galaxy major axis. The images were produced with the Spitzer/Leopard software package used to query the archive and download the data.

14 sec ramps, which allowed to map a region of about $37'' \times 67''$ in 2 parallel by 19 perpendicular pointings centered on the nucleus of NGC 4945.

In order to sample the background continuum and to identify rogue pixels, we also obtained off-source spectra with the same integration times and number of cycles at two positions sufficiently above and below the galaxy disk. The off-source spectra were taken before and after the SL mapping. The total time used for the SL map, including sky positions, amounts to 3.1 hrs. The orientation of the SL slit, overlaid on the Spitzer-MIPS 24 μm map of NGC 4945, is shown in the *bottom panel* of Fig. 4.1.

4.2.3 Data reduction

The Basic Calibrated Data (BCD) were pre-processed with the Spitzer pipeline versions S16.1 for SH, and S18.1 for SL. Rogue pixels were cleaned, and maps were built, using the IRS mapping reduction package CUBISM*, designed by the SINGS† legacy team (Smith et al., 2007). With this tool we performed the flux calibration, background subtraction, and estimated the statistical uncertainty at each spectral

* http://ssc.spitzer.caltech.edu/dataanalysistools/tools/cubism/

† http://ssc.spitzer.caltech.edu/spitzermission/observingprograms/legacy/

wavelength. We create the first spectral cubes from the slit observations combined with CUBISM. After creating the first cubes, we further cleaned the data using the back-tracking procedure described in Smith et al. (2007). All the pixels with flux uncertainty larger than 50% were flagged, so they were not used in subsequent reconstructions of the spectral cubes. We iterate on the cleaning procedure by performing visual inspections throughout the maps, of small sections of the spectra around the emission lines, PAH and silicate features of interest, and we reconstructed the cubes after cleaning new pixels.

The spectral cubes obtained with CUBISM are in units of surface brightness, $\mathrm{MJy\ sr^{-1}}$, but we convert them to $\mathrm{W\ cm^{-2}\ \mu m^{-1}\ sr^{-1}}$ to work and present the spectra. We use the units of flux density $\mathrm{W\ cm^{-2}}$ to present the integrated line fluxes and maps. For this we use the conversion $1\ \mathrm{arcsec^2} = 2.3504 \times 10^{-11}\ \mathrm{steradian}$, knowing that the pixel size* of the IRS/SH map is $\sim$2.26 $\mathrm{arcsecs/pixel}$, which leads to $1.2005 \times 10^{-10}\ \mathrm{steradians}$ that we need to multiply by in order to get the maps in units of flux density. In the case of IRS/SL the pixel size is $\sim$1.85 $\mathrm{arcsecs/pixel}$, so we have slightly smaller $8.04424 \times 10^{-11}\ \mathrm{steradians}$ per pixel than in the SH map.

4.3 Analysis and results

During the data reduction and spectral analysis process we found that the SH spectral orders† are mismatched at levels that vary across the mapped region. This effect is smoothed (although not completely solved) by increasing the overlap between the orders (in the wavsamp calibration file) and by increasing the size of the aperture used to extract 1-D average spectra, as discussed below. We also observed module to module mismatches, which inhibit us from reliably combining the SH and SL modules to perform further analyses like, for instance, using the H_2 S(3) line as an extinction indicator. These mismatches in the SH orders and between modules have not been addressed before‡, probably because they are apparent only in high S/N data as those presented in this work. The IRS-SH/SL orders/modules mismatch problem seen in high S/N data is a new issue that we are still studying together with members of the SINGS team (J.D. Smith, private communication). Fortunately, most of the emission and absorption features we are interested in are found within the spectral orders, and those features observed near the edge of the orders are treated with extreme care or not addressed at all.

The average spectra, considering the whole field of view (FOV) of the SL and SH maps, are shown in the *top* and *bottom* panel of Fig. 4.2, respectively. The spectrum of the IRS/SL map corresponds to the average spectrum extracted from a similar FOV as that of the IRS/SH map. The most important fine-structure emission lines and PAH features are indicated in both spectra.

We developed our own IDL procedures to work on the 1-D spectra that were

* See http://coolwiki.ipac.caltech.edu/index.php/Units for a description of Spitzer units and conversions

† http://ssc.spitzer.caltech.edu/irs/irsinstrumenthandbook/

‡ http://ssc.spitzer.caltech.edu/irs/features/

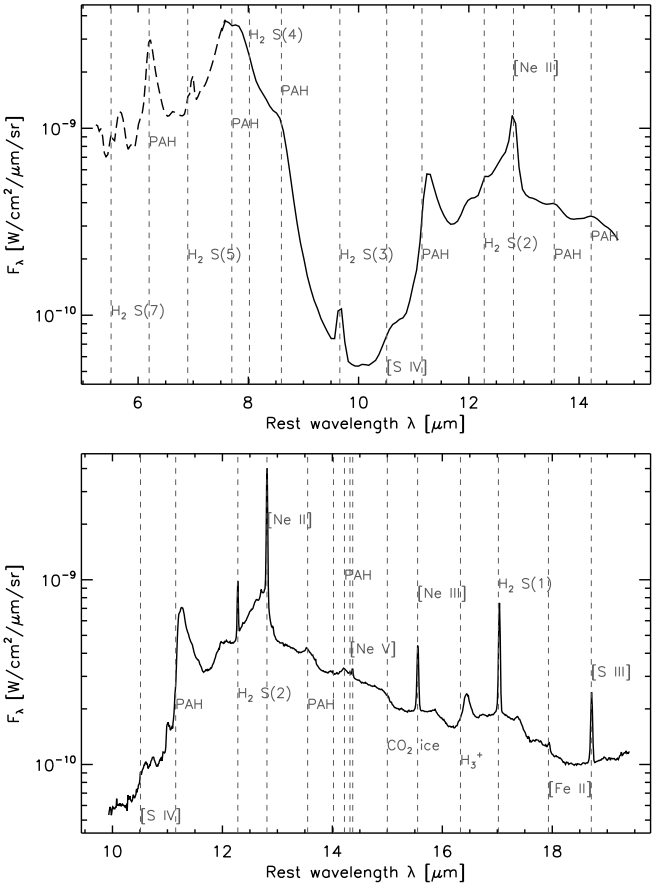

Figure 4.2: *Top panel* - Average spectrum of the equivalent field of view of the SH map of the nuclear region of NGC 4945, as seen in the SL map. The SL1 order is shown with a *dashed* line. The most significant fine structure emission lines and PAH features in the SL wave range are labelled, in particular the ones that overlap with the SH waverange. *Bottom panel* - Average spectrum of the whole field of view of the SH map. The higher spectral resolution of the IRS/SH module allows to distinguish emission lines like [Ne V]14.32μm and [Cl II]14.37μm, otherwise blended in the IRS/SL module. These spectra are not corrected for extinction.

used to build the final maps. In the SH cube, the map contains 11×11 pixels of $\sim 2.3''$ each. So the whole field of view covers a region of about 468×468 pc^2 ($1''$ corresponds to ≈ 18.5 pc at the distance of 3.82 Mpc). These 1-D spectra were extracted from the clean SH cubes by averaging the spectra over a moving 2×2 pixel aperture. The whole field of view was covered with a step size of 1 pixel, so the reduced map contains only 10×10 pixels but covering the same area as the original map. However, the last slit observation of the IRS/SH map covers just about one third of the spatial region associated with each pixel. Therefore, we conclude that the last column of the original 11×11 grid map produced by CUBISM is not representative of the actual spatial region associated with that slit

column, and we do not use it in our maps. So the final maps reduced with the 2×2 aperture correspond to 9×9 pixels, covering a slightly smaller region than the original maps. The coordinates assigned to each pixel of the resulting map are those of the center of the 2×2 aperture. Using the 2×2 pixel extraction box the S/N of the spectra is increased by a factor 2 (from the $\sqrt{4}$ pixels), and reduce the effect of the mismatch between orders mentioned above. This corresponds to a standard procedure recommended by J.D. Smith (private communication) to obtain IRS maps of extended sources.

The average Full Width Half maximum (FWHM) of the IRS/SH Point Spread Function (PSF) has been estimated to be $\sim 5.16''$ and $\sim 4.31''$ for the direction along the spectral dispersion axis and the spatial axis of the slit, respectively, while the corresponding average PSF FWHM values of the SL2 (mostly used in this work) are $\sim 3.76''$ and $3.27''$, respectively (Pereira-Santaella et al., 2010, their appendix A). According to Pereira-Santaella et al., the 1-σ deviation around the average centroid position in SL modules was found to be ~ 20 times smaller than the SL pixel size ($1.85''$). While the maximum 1-σ deviation in the SH module was found to be $\sim 0.6''$, which is considered small compared to the SH pixel size ($2.26''$). This indicates that the average 2×2 aperture maps can still be resolved. We test this for our maps in Sec. 4.3.4.

From the SH 2×2 aperture average spectra we obtained maps of the starburst tracers [S IV] at 10.51 μm, [Ne II] at 12.81 μm, [Cl II] at 14.37 μm, [Ne III] at 15.56 μm, [S III] at 18.71 μm, as well as the AGN tracer [Ne V] at 14.32 μm, and the pure rotational molecular hydrogen lines, H_2 S(2) and H_2 S(1) at 12.3 μm and 17.0 μm, respectively. For each line we first estimate a continuum level by fitting a second-order polynomial to the base of the emission line, or a cubic spline with selected anchor points (pivots) when the emission line was on top of a complex PAH or silicate feature. We applied the same aperture reduction procedure for the SL map, from where we obtained a map of the silicate absorption feature at 9.7 μm and the corresponding silicate strength as described in Sec. 4.3.4. We also obtained a map of the the molecular hydrogen line H_2 S(3) at 9.66 μm.

4.3.1 The spectral complex around [Ne V] 14.32 μm

The complexity of the spectral range around the [Ne V] 14.32 μm is shown in Fig. 4.3. A PAH feature at ∼13.95 μm seems to be present just next to where the first bending mode of HCN at 14.02 μm is expected to be found either in emission or in absorption. Depending on the temperature of the surrounding molecular gas, HCN can be vibrationally excited by absorbing the infrared photons at 14.0 μm. This will produce a subsequent cascade process that can enhance HCN rotational lines in the (sub-)millimeter range. This corresponds to the IR-pumping scenario proposed to explain the bright HCN $J = 1 \rightarrow 0$ (and higher) transition observed in some ULIRGs and Galactic star-forming regions (e.g., Aalto et al., 1995; García-Burillo et al., 2006; Guélin et al., 2007; Aalto et al., 2007b; Pérez-Beaupuits et al., 2010). Although, due to the order mismatch (mentioned in Sec. 4.3) observed between ~ 13.90 μm and ~ 14 μm, also seen by Pereira-Santaella et al. (2010), we are

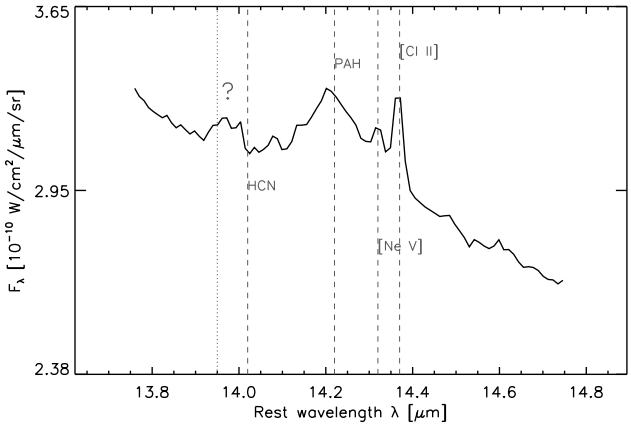

Figure 4.3: Zoom into the [Ne V] complex wavelength range from the average IRS/SH spectrum of Fig. 4.2. At these wavelengths we find the first bending mode of HCN at $14.02\ \mu$m, and the AGN tracer [Ne V] at $14.22\ \mu$m, almost blended with the fine-structure emission line [Cl II] at $14.37\ \mu$m, on the slope of the PAH feature around $14.22\ \mu$m. The dotted line shows the wavelength at which we found an order mismatch, probably producing the unknown feature observed next to the HCN $14.02\ \mu$m, which could be affected.

unable to conclude whether we detect or not the HCN $14.02\ \mu$m feature.

A larger PAH feature is observed around $\sim$14.22 μm, and on its rightmost (and less steep) slope the fine-structure emission lines of [Ne V] 14.32 μm and [Cl II] 14.37 μm are found. Chlorine, which has an ionization potential of $12.97\ \mathrm{eV}$, is known to play an important role in characterizing the neutral gas components in the ISM. When H_2 is abundant (optically thick in the FUV), it reacts (exothermically by $0.17\ \mathrm{eV}$) with [Cl II] to form HCl^+, which leads to the formation of [Cl I] and H I (Jura, 1974; Jura & York, 1978). This means, chlorine is predominantly ionized in H I regions while it is predominantly neutral when cold H_2 components are present (Sonnentrucker et al., 2002, 2003). The [Cl II] 14.37 μm fine-structure emission line was clearly detected ($>3\sigma$) in the whole region mapped with the IRS/SH module, and presents a similar (although more spreadout) distribution than that of the [Ne II] 12.81 μm line.

Because its high-ionization potential ($97.1\ \mathrm{eV}$) is too large to allow production by main-sequence stars, the fine-structure line [Ne V] 14.32 μm is commonly used to probe the narrow line region of AGNs (e.g., Moorwood et al., 1996b; Genzel et al., 1998; Armus et al., 2007; Alonso-Herrero et al., 2009; Baum et al., 2010; Willett et al., 2010, and references therein). It has recently been used as a diagnostic tool to unambiguously identify AGN galaxies that have not been identified as such using optical spectroscopy (Goulding & Alexander, 2009).

4.3.2 Estimating the line emission flux

The emission fluxes were estimated by fitting a Gaussian profile to the fine-structure lines and integrating the flux above a local continuum, which was estimated from a

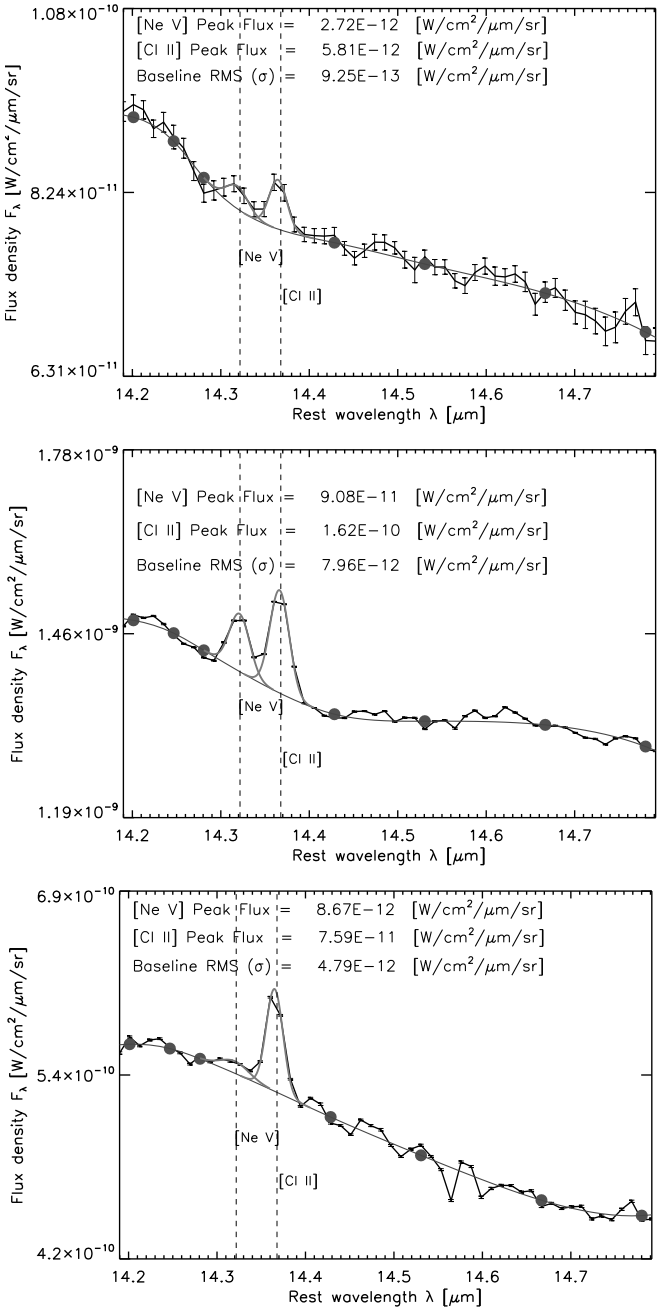

Figure 4.4: Gaussian fit of the [Ne V] 14.32 μm and [Cl II] 14.37 μm fine-structure emission lines at three different pixels of the IRS/SH map. The error bars indicate the uncertainties of the spectral data. The filled circles indicates the pivots used for the cubic spline interpolation of the baseline. The *top panel* shows less than 3σ detection for [Ne V] but a clear detection of the [Cl II] line. The spectrum of the *middle panel* shows clear detections of both lines. The *bottom panel* shows $<3\sigma$ detection for [Ne V], in spite of the low uncertainties in the data points.

cubic spline interpolation of selected anchor points (pivots). Since we we want to determine the actual spatial distribution of the emission lines in the nuclear region of NGC 4945, we set a strict 3σ level detection for all the fine-structure emission lines, and at least two data points (or a full width of $\sim$560 $\mathrm{km\,s^{-1}}$at 14.32 μm) in the profile to consider a feature as a real emission line in the spectrum. For a robust estimate of the local continuum we adopted an average flux of five points around each of the selected pivots used in the cubic spline interpolation. Figure 4.4 shows the Gaussian fit of the [Ne v] 14.32 μm and [Cl ii] 14.37 μm fine-structure emission lines at three different positions of the IRS/SH map. The uncertainty of each spectral data point is indicated by the error bars. The pivots used for the cubic spline interpolation of the local continuum (baseline) are shown with filled circles. These pivots are at the wavelengths 14.201 μm, 14.247 μm, 14.281 μm, 14.428 μm, 14.531 μm, 14.667 μm, and 14.780 μm.

The *top panel* of Fig. 4.4 shows the spectrum in a region of the map with relatively high uncertainties ($\sim$1.4% on average) in the spectral data and with high RMS (as computed from the baseline, and indicated in the legend of the plots) that leads to less than a 3σ detection for [Ne v], but a clear detection ($>3\sigma$) for the [Cl ii] line. The spectrum of the *middle panel* was extracted from the central 2$\times$2 pixel aperture of the map, which has a S/N ratio $\sim$9 in the line and $>$100 in the continuum, and is among the highest S/N in the whole IRS/SH map. This spectrum shows very low uncertainties ($\sim$0.06% on average) in the data, and clear detections of both lines. Although with low uncertainties in the data ($\sim$0.13%), the *bottom panel* of Fig. 4.4 shows less than a 3σ detection for [Ne v] (with a S/N$\sim$1.8), but a strong detection of [Cl ii] 14.37 μm. With this Gaussian fit procedure, we produced 9$\times$9 pixels maps (as described above) of several fine-structure lines, PAH features and the silicate absorption feature at 9.7 μm (discussed in Sec. 4.3.4), covering a region of $20.7'' \times 20.7''$ (about 383$\times$383 $\mathrm{pc^2}$). The SH maps are shown in Figs. 4.5 and 4.6, where the peak fluxes are shown with a white pixel. In the case of the [Ne v] 14.32 μm the pixels with flux density lower than 0.017×10^{-21} $\mathrm{W\,cm^{-2}}$ correspond to a detection level $< 3\sigma$.

4.3.3 Visual extinction

Lower limits on the reddening in the nuclear region of NGC 4945 were obtained from the HST-NICMOS $H-K$ color image (Marconi et al., 2000). An average color $H-K=1.1$, yielding an $A_{\mathrm{V}} \approx 11$ mag, was observed in the region of the Paα ring. This A_{V} is comparable with extinctions larger than 13 mag, as estimated from the Brα/Brβ and Paα/Hα ratios (Moorwood & Oliva, 1988; Marconi et al., 2000).

In order to compare with our data, we produced an image of A_V at the same resolution of the IRS/SH maps, using the HST-NICMOS $H-K$ colour image. First, we use the same definition of foreground screen extinction given in Marconi et al. (2000)

$$A_{\mathrm{V}}(H-K) = \frac{E(H-K)}{c(H)-c(K)}, \tag{4.1}$$

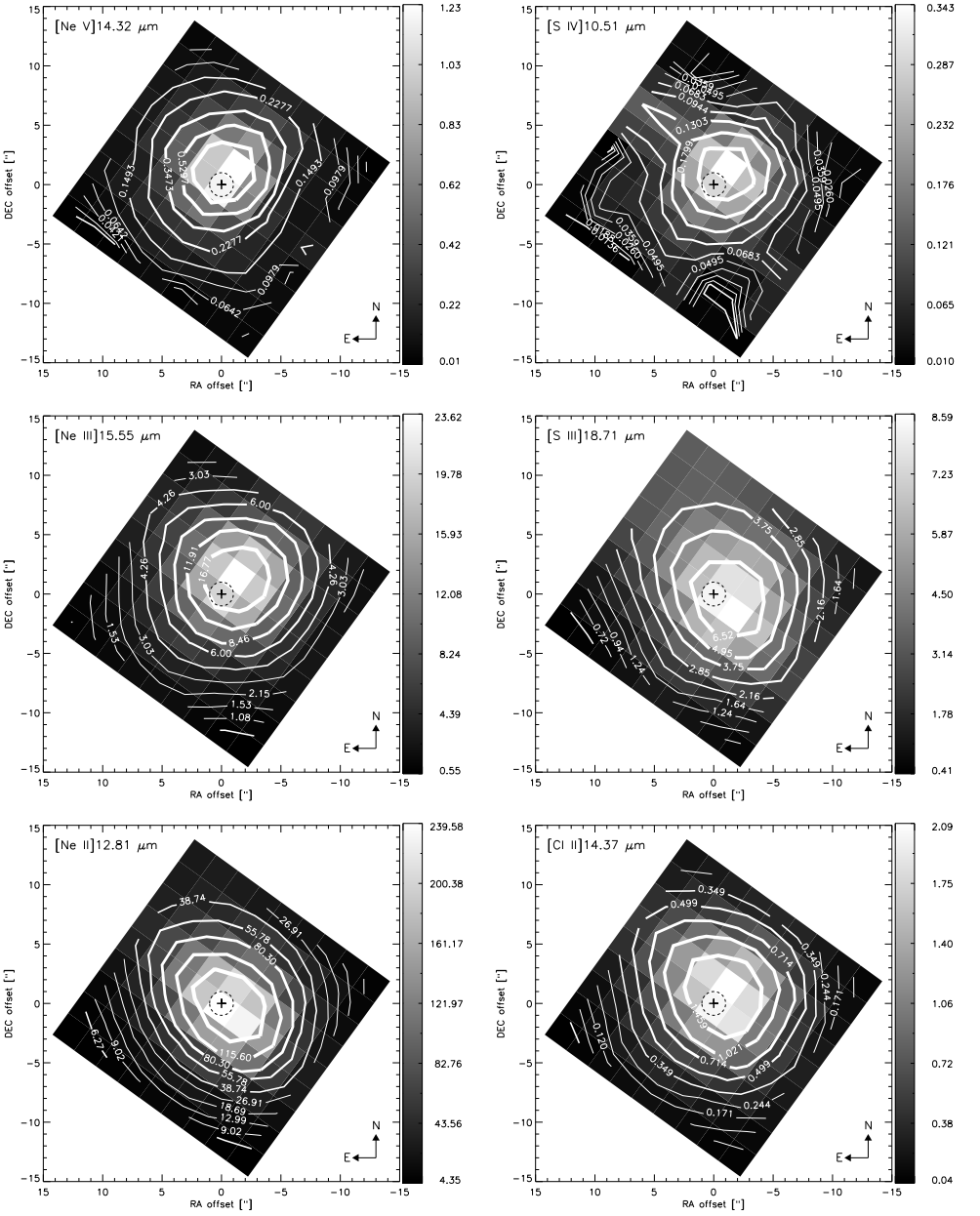

Figure 4.5: IRS/SH maps of the flux density (10^{-21} W cm^{-2}) of the fine-structure lines (*left panels*, from top to bottom) [Ne V] 14.32 μm, [Ne III] 15.55 μm, [Ne II] 12.81 μm, (*right panels*, from top to bottom) [S III] 18.71 μm, [S IV] 10.51 μm, and line [Cl II] 14.37 μm. The peak fluxes are shown with a white pixel. These flux density maps are not corrected for extinction. The dashed-line circle represents the $\pm 1''$ pointing accuracy of Spitzer, and the contour lines are labelled. The reference ($\Delta\alpha = 0, \Delta\delta = 0$) is marked with a cross and corresponds to the position R.A.(J2000)=13:05:27.477, Dec.(J2000)=-49:28:05.57 of the H_2O maser reported by Greenhill et al. (1997).

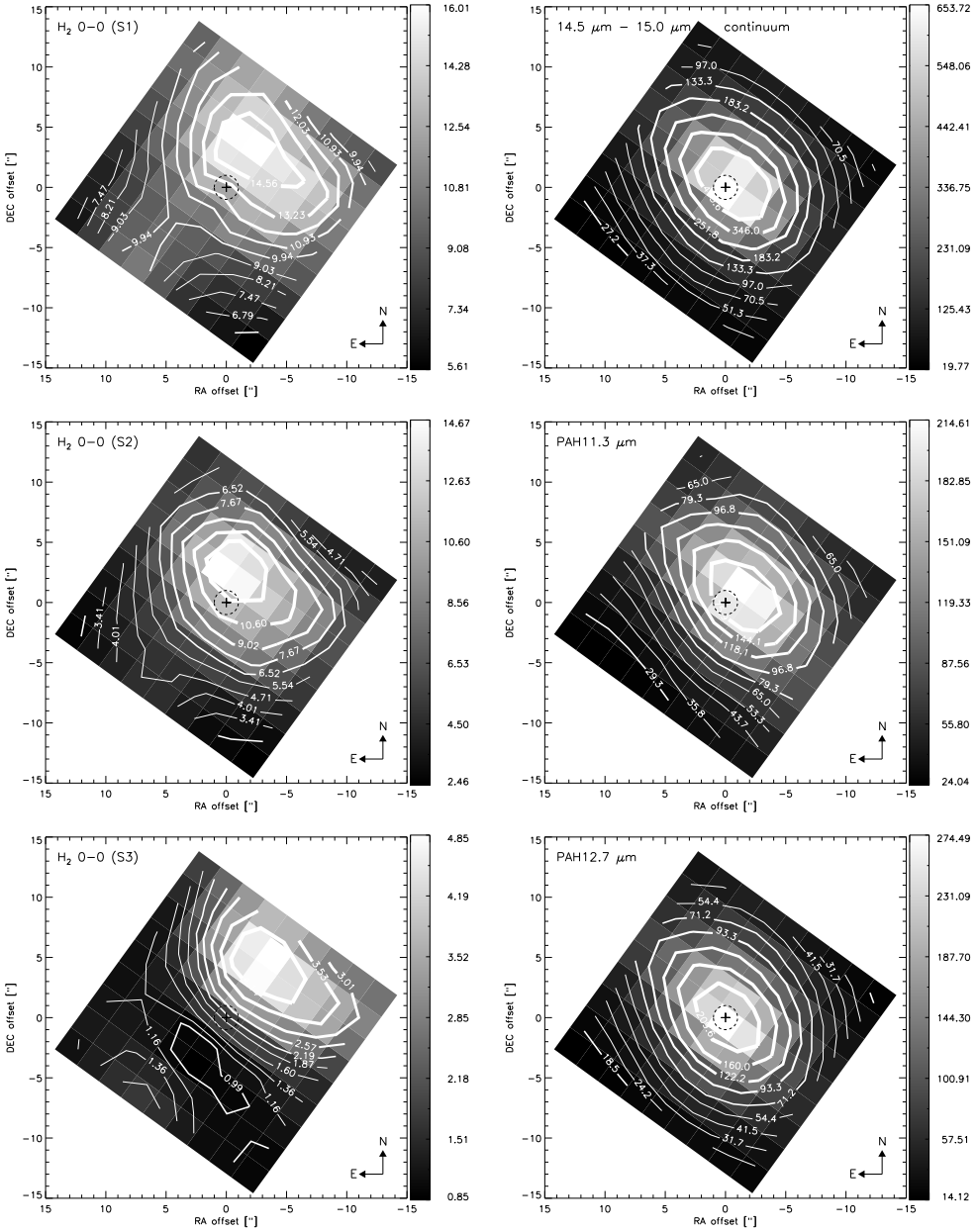

Figure 4.6: IRS/SH maps of the flux density (10^{-21} W cm^{-2}) of the molecular hydrogen lines (*left panels*, from top to bottom) H_2 S(1) and H_2 S(2) at 17.0 μm and 12.3 μm, respectively, and the H_2 S(3) line at 9.7 μm from the IRS/SL map. The *right panel* shows (from top to bottom) the average continuum between 14.5 μm and 15.0 μm, and the PAH features at 11.3 μm and 12.7 μm. The peak fluxes are shown with a white pixel. These flux density maps are not corrected for extinction. The dashed-line circle represents the $\pm 1''$ pointing accuracy of Spitzer, and the contour lines are labelled. The reference ($\Delta\alpha = 0, \Delta\delta = 0$) is marked with a cross and corresponds to the position R.A.(J2000)=13:05:27.477, Dec.(J2000)=-49:28:05.57 of the H_2O maser reported by Greenhill et al. (1997).

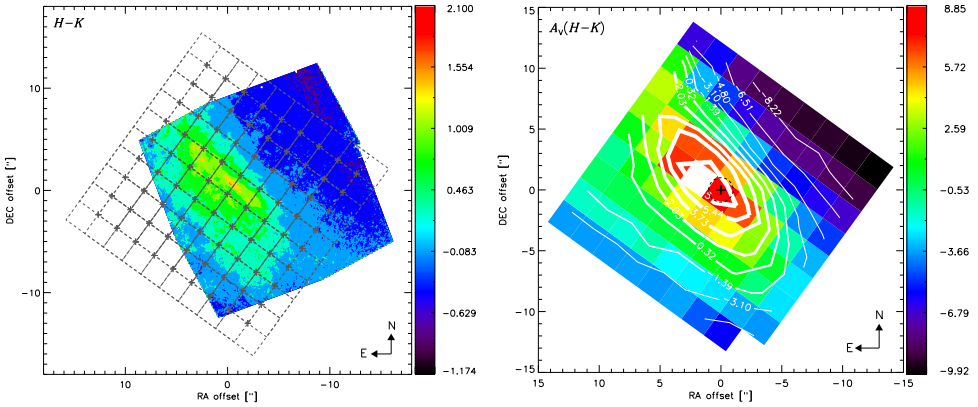

Figure 4.7: *Left panel* - HST-NICMOS $H-K$ colour image (mag) reported by Marconi et al. (2000). The Spitzer-IRS SH grid is overlaid to show the difference in resolution and the different orientation of the fields of view. *Right panel* - Foreground screen extinction $A_{\rm V}(H-K)$ estimated from the $H-K$ colour image at the resolution of the IRS/SH map.

where $E(H-K)$ is the colour excess that can be obtained from the difference between the observed and intrinsic colours, $E(H-K) = (H-K) - (H-K)_0$. We use the average intrinsic colour $(H-K)_0 \approx 0.22 \pm 0.1$ mag of spiral and elliptical galaxies reported by Hunt et al. (1997). The $c(H)$ and $c(K)$ coefficients are derived from the extinction law, $A_\lambda = c(\lambda)A_{\rm V}$. Instead of using the $A_\lambda \propto (\lambda/1\ \mu m)^{-1.75}$ law ($\lambda > 1\ \mu m$) assumed by Marconi et al. (2000), we used the extinction law for the local ISM reported by Chiar & Tielens (2006), which considers solid and porous spheres and a continuous distribution of ellipsoids in the extinction profiles used for the amorphous silicates in the $9.7\ \mu$m absorption feature. We interpolated the c coefficients at $\lambda = 1.606\ \mu m$ and $\lambda = 2.218\ \mu m$ of the HST-NICMOS H and K bands, respectively. In Chiar & Tielens (2006) the local ISM continuum extinction was found to be described by the expression

$$log(A_\lambda/A_K) = 0.65 - 2.4log(\lambda) + 1.34log(\lambda)^2, \tag{4.2}$$

using $A_K/A_{\rm V} = 0.09$ to normalize the extinction to the K band (Whittet, 2003). Beyond 8 μm the silicate profile of WR-98A is superimposed using $A_{\rm V}/\tau(9.7\ \mu m) = 18$ (Roche & Aitken, 1984). So we used eq.(4.2) and $A_K/A_{\rm V} = 0.09$ to estimate the $c(H)$ and $c(K)$ coefficients for the stellar light-based extinction $A_{\rm V}(H-K)$.

The *left panel* of Fig. 4.7 shows the HST-NICMOS $H-K$ mag image reported by Marconi et al. (2000) with the Spitzer-IRS SH grid overlaid. We took all the pixels of the $H-K$ image that fall into one single pixel of the SH grid, and computed the average $A_{\rm V}$ for each pixel. The resulting foreground extinction, at the resolution of the SH maps, is shown in the *top panel* of Fig. 4.7. Since the field of view of the SH map and the HST-NICMOS images are not aligned, the SH pixels that are off the $H-K$ image were adopted as the average of the nearest two pixels with actual estimates along the northeast-southwest axis, assuming that the foreground

extinction remains fairly constant along the plane of the galaxy below the conical cavity (Moorwood et al., 1996c; Marconi et al., 2000). The peak of this stellar light-derived extinction lies about $2.3''$ (~ 43 pc) northeast of the H_2O maser.

4.3.4 The deep silicate absorption around 9.7 μm

From the IRS/SL cubes we can study the amorphous silicate grains, which present a broad and deep absorption feature around 9.7 μm. The presence of PAH emission along the same line of sight as the silicate absorption makes it hard to measure the apparent silicate depth. If one assumes the PAH emission to be foreground to the silicate absorption a different apparent silicate depth is found than when it is assumed that they are mixed. Silicate absorption can also be foreground to the PAH emission. Here we use the method proposed by Spoon et al. (2007, their Fig.2) for absorption-dominated spectra to infer the apparent strength of this silicate feature. First, we extracted 1-D spectra from the SL map rebinned to the 2×2 pixel aperture of the SH map described in Sec. 4.3. For each spectrum, we adopted a local mid-infrared continuum by interpolating the feature-free continuum pivots at 5.3 μm and 13.55 μm.

Because the S/N is not uniform for all the pixels of the SL map, and the features around 5.3 μm change depending on the proximity to the nucleus of NGC 4945, we used a similar procedure as the one used for [Ne v] 14.32 μm (Sec. 4.3.1). The flux density assigned to the pivot at 5.3 μm was adopted as the minimum flux observed between 5.1 μm and 5.5 μm. In order to avoid contamination from the H_2 S(3) molecular line, the flux density estimated for the deepest point adopted at 9.85 μm was the median flux density between 9.7 μm and 10.0 μm. The flux estimated for the pivot at 13.55 μm was the median flux observed between 12.9 μm and 14.0 μm. Then we computed the ratio between the observed flux density ($f_{\rm obs}$) and the estimated continuum flux density ($f_{\rm cont}$) at 9.85 μm, and we obtained the apparent silicate strength $S_{\rm sil}$ as

$$S_{\rm sil} = ln\left[\frac{f_{\rm obs}(9.85\ \mu{\rm m})}{f_{\rm cont}(9.85\ \mu{\rm m})}\right]. \tag{4.3}$$

The $S_{\rm sil}$ is equivalent to the optical depth of the silicate absorption ($\tau_{9.7\ \mu{\rm m}}$) defined in Rieke & Lebofsky (1985). The *left panel* of Fig. 4.8 shows the IRS/SL map (rebinned to the 2×2 aperture of the IRS/SH map) of the apparent silicate strength at 9.85 μm. The silicate-based extinction $A_{\rm V}(9.85\ \mu{\rm m})$, shown in the *right panel* of Fig. 4.8, was estimated from the average visual extinction to silicate optical depth ratio $A_{\rm V}/\tau(9.7\ \mu{\rm m}) = 18$, which is appropriate for the local ISM (Roche & Aitken, 1984; Rieke & Lebofsky, 1985). The spatial distribution of the silicate-based extinction is similar to that of the stellar light-based extinction $A_{\rm V}(H-K)$ estimated in Sec.4.3.3. The peak extinction is found at the same relative position (Δ R.A. $= 2, \Delta$ Dec $= 1$), at about $2.3''$ (~ 43 pc) northeast of the H_2O maser (Greenhill et al., 1997). The estimated extinction strength of the pixels in the top and left corners of the $A_{\rm V}(H-K)$ map do not seem to be correlated with the corresponding pixels of

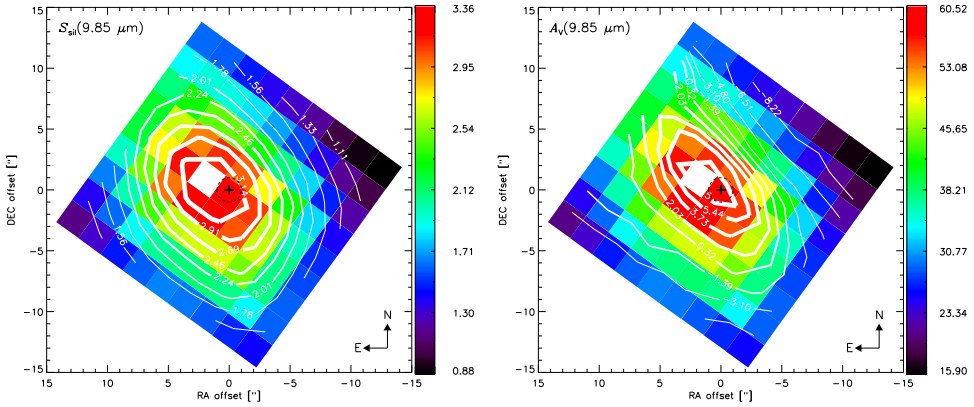

Figure 4.8: *Left panel* - IRS/SL map of the apparent silicate strength $S_{\rm sil}$ estimated at 9.85 μm. *Right panel* - Silicate-based extinction $A_{\rm V}(9.85\ \mu{\rm m})$ map estimated from the average visual extinction to silicate optical depth ratio $A_{\rm V}/\tau(9.7\ \mu m) = 18$ for the local ISM (Roche & Aitken, 1984; Rieke & Lebofsky, 1985) and assuming $\tau(9.7\ \mu m) \approx S_{\rm sil}(9.85\ \mu{\rm m})$. The contour lines of the stellar light-based extinction $A_{\rm V}(H-K)$ of Fig. 4.7 are overlaid on the $A_{\rm V}(9.85\ \mu{\rm m})$ map (colour pixels).

the $A_{\rm V}(9.85\ \mu{\rm m})$ map. Most likely this is due to the extrapolation method used in Sec. 4.3.3 to estimate $A_{\rm V}(H-K)$ on those pixels.

It is known that extinction estimated from optical or near-infrared observations generally underestimates the actual extinction if the environment probed is optically thick at the emission lines observed. If most of the emitting region is obscured, as in the case of the nucleus of NGC 4945, the visual extinction estimate is representative of the surface of the obscured region and not the region itself. This effect is reflected in the different extinctions derived from the $H-K$ optical image and the silicate-based estimate derived from our mid-IR observations, where the peak extinction is about 7 times stronger than that of the stellar light-based estimate. Our $A_{\rm V}(9.85\ \mu{\rm m})$ is also a factor $\sim$1.7 higher than the extinction ($A_{\rm V} = 36^{+18}_{-11}$ mag) previously inferred from ISO observations of the [S III] 18.7/33.5 μm line ratio (Spoon et al., 2000). This difference might be explained by the peaked nature of the silicate-based extinction map and because of the larger apertures ($\geq 14'' \times 20''$) of the ISO observations, which averages out the extinction to the lower value.

Figure 4.9 shows the contour lines of the IRS/SH flux density map of the molecular hydrogen line H_2 S(1) 17.0 μm (*left panel*) and the IRS/SL map of the H_2 S(3) 9.7 μm line (*right panel*), overlaid on the silicate-based extinction $A_{\rm V}(9.85\ \mu{\rm m})$ map. The molecular hydrogen emission avoids the obscured nucleus and peaks about 43 pc ($\sim 2.3''$) away from the highest obscuration. Although the H_2 S(2) 12.3 μm (Fig. 4.6) has a similar distribution as the H_2 S(1) line, its peak emission lies closer ($\sim 2.3''$, one pixel) to the peak obscuration and to the H_2O maser than the other H_2 lines.

Since the distribution of the silicate-based extinction $A_{\rm V}(9.85\ \mu{\rm m})$ is similar to that of the stellar light-based extinction $A_{\rm V}(H-K)$ we think that the near-IR de-

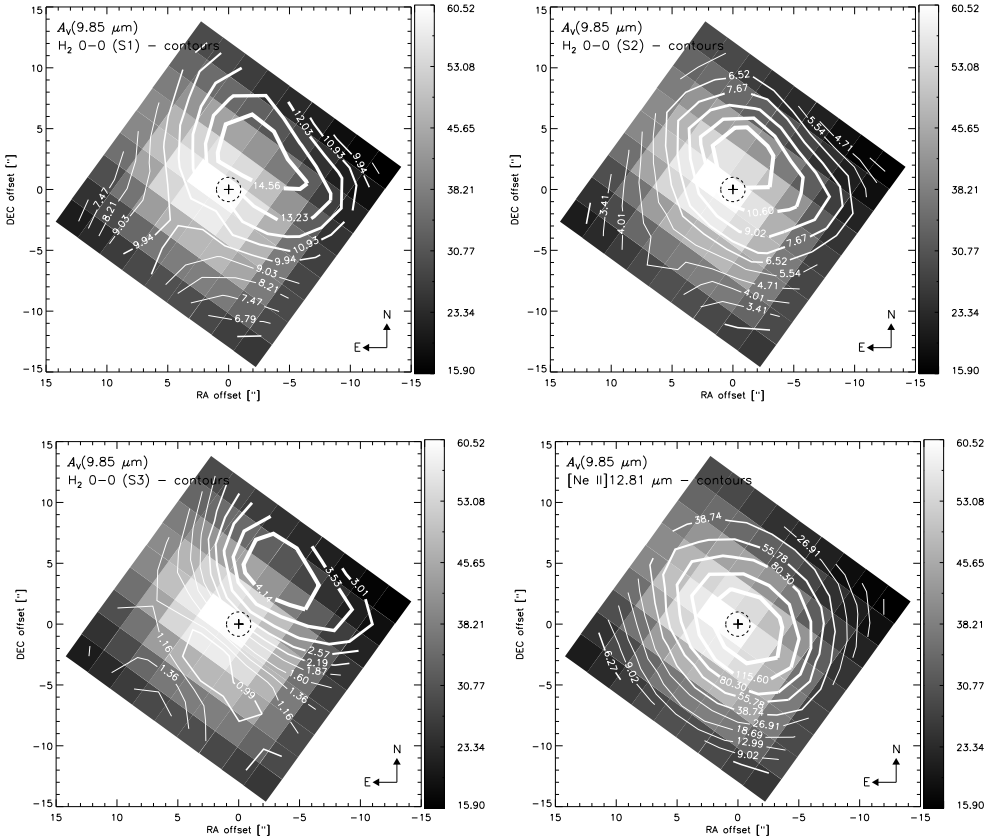

Figure 4.9: IRS/SL map of the silicate-based extinction $A_{\rm V}(9.85\ \mu{\rm m})$ with the contour lines of the IRS/SH map of the flux density (in units of 10^{-21} W cm^{-2}) of the molecular hydrogen line H_2 S(1) 17.0 μm (*top left panel*), the IRS/SH map of the H_2 S(2) 12.3 μm line (*top right panel*), the IRS/SL map of the H_2 S(3) 9.7 μm line (*bottom left panel*), and the IRS/SH map of the [Ne II] 12.81 μm (*bottom right panel*). The figures show that the H_2 emission is stronger in a region $\gtrsim$43 pc ($\gtrsim$2.3″) away from the peak obscuration, although the H_2 S(2) is the closest to the peak obscuration and to the H_2O maser, as well as the [Ne II], which peaks at the H_2O maser (within $\sim 1''$), as seen in Fig. 4.5.

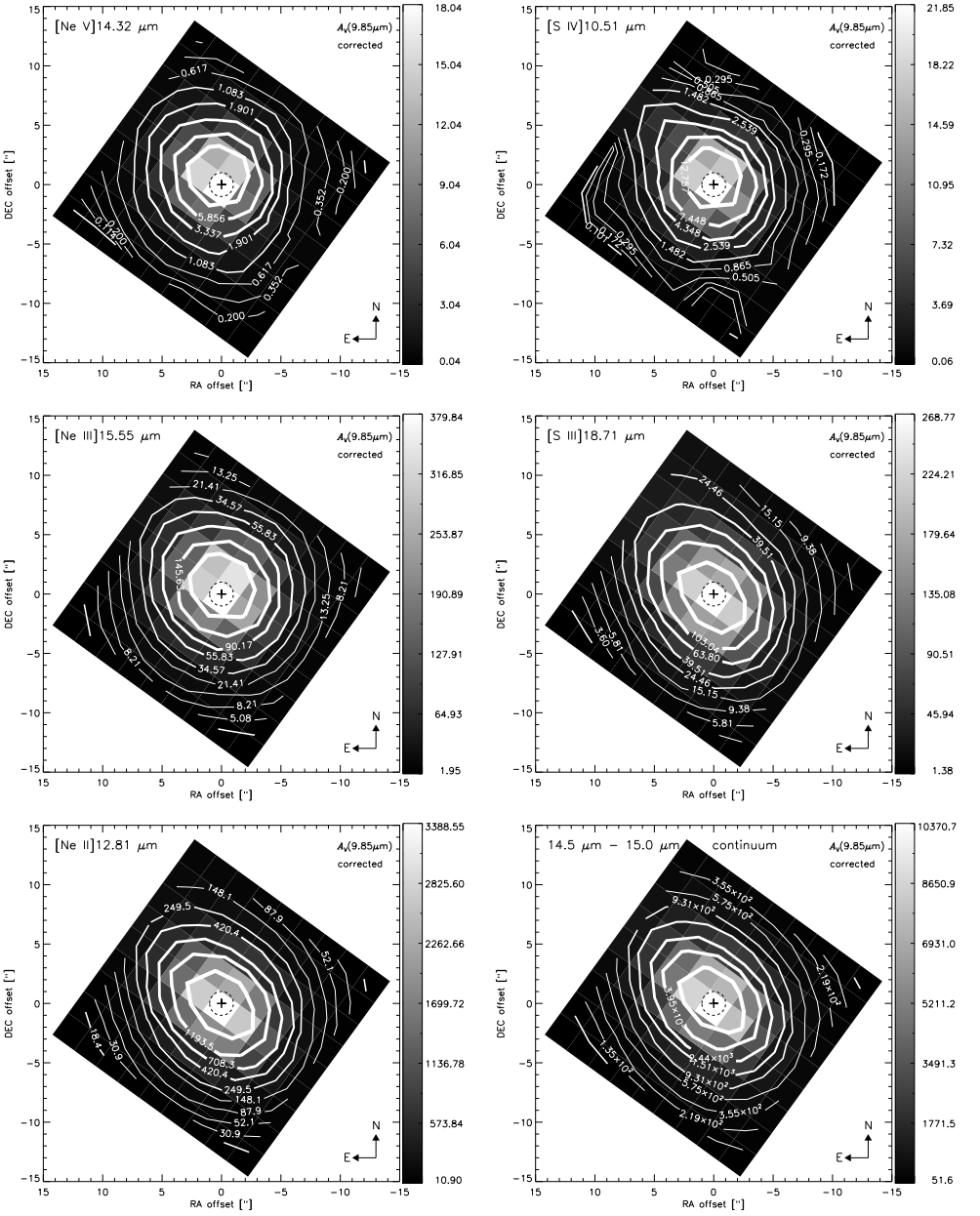

Figure 4.10: IRS/SH flux density (10^{-21} W cm^{-2}) maps, corrected for extinction using the extinction law for the local ISM from Chiar & Tielens (2006) and the silicate-based extinction $A_{\rm V}(9.85\ \mu{\rm m})$ (Figs.4.8 and 4.9). The *left panels* show (from top to bottom) the fine-structure lines [Ne V]14.32 μm, [Ne III]15.55 μm, and [Ne II]12.81 μm. The *right panels* show (from top to bottom) the [S III]18.71 μm, [S IV]10.51 μm lines, and the average continuum between 14.5 μm and 15.0 μm. The notations are as in Fig. 4.5. Note that after correcting for extinction, all these emission lines (and the average continuum) peak at about the same position of the H_2O maser.

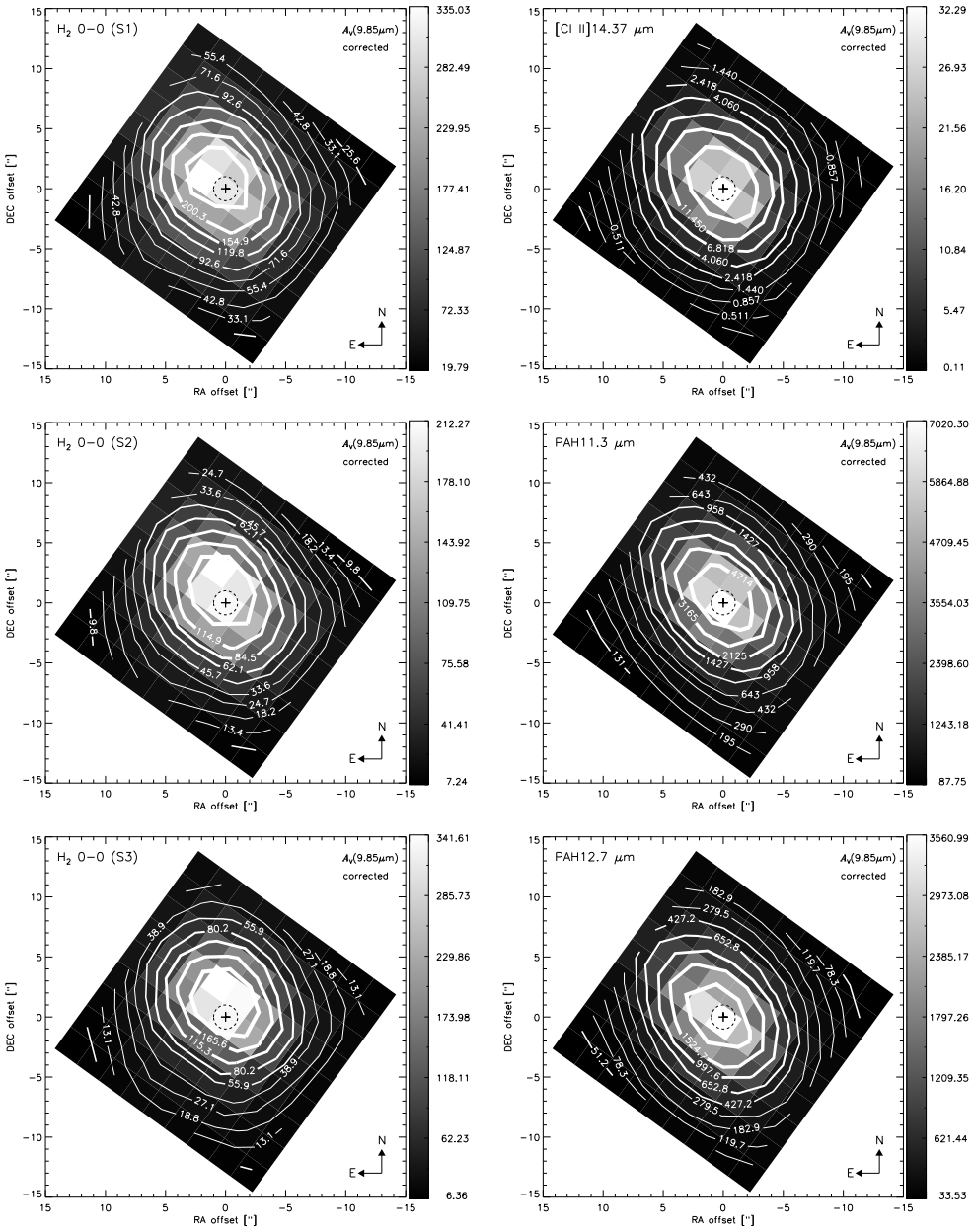

Figure 4.11: IRS/SH flux density (10^{-21} W cm^{-2}) maps, corrected for extinction using the extinction law for the local ISM from Chiar & Tielens (2006) and the silicate-based extinction $A_{\rm V}(9.85\ \mu{\rm m})$ (Figs.4.8 and 4.9). The molecular hydrogen lines H_2 S(1) 17.0 μm, H_2 S(2) 12.3 μm, and H_2 S(3) 9.7 μm (from the IRS/SL map) are shown in the *left panel*. The *right panel* shows (from top to bottom) the fine-structure line [Cl II]14.37 μm, and the the PAH features at 11.3 μm and 12.7 μm. After correcting for extinction, the [Cl II] line and the PAH features also peak at about the same position of the H_2O maser.

Table 4.1: LINE FLUXES[a] FROM THE 10×10 APERTURE IRS/SH MAP.

Line	λ_0[b] [μm]	Flux [10^{-21} W cm^{-2}]	Flux(A_V)[c] [10^{-21} W cm^{-2}]	FWHM[d] [km s^{-1}]
[S IV]	10.51	1.61	10.14	382.68
		0.08	0.52	30.54
H_2 0-0 S(2)	12.28	154.07	528.74	526.13
		1.99	6.86	6.28
[Ne II]	12.81	1201.08	3733.63	612.62
		118.85	355.09	30.93
[Ne V]	14.32	5.34	17.09	586.24
		0.12	0.39	15.71
[Cl II]	14.37	12.82	40.90	504.09
		0.10	0.32	4.59
[Ne III]	15.55	127.01	438.43	640.71
		2.79	9.98	13.16
H_2 0-0 S(1)	15.55	252.60	997.46	553.12
		7.64	34.15	20.55
[S III]	18.71	74.87	257.92	330.17
		1.36	4.91	5.84

[a] The flux densities of each line are given in the first row. The row below shows the corresponding uncertainties. These are the fluxes obtained from the co-added spectra of the whole 10×10 aperture of the SH map described in Sect. 4.3.

[b] Rest wavelength of the lines.

[c] Flux density corrected for extinction using the silicate-based $A_V(9.85\mu m)$ estimated in Sec. 4.3.4. Note that this extinction correction may not be valid for every component. For the AGN BLR the extinction is given by the X-ray-derived H_2 columns of $> 10^{24}$ cm^{-2}, while for the AGN NLR it should be far less (because it does not originate from behind the torus walls).

[d] Line width in km s^{-1} obtained from the Gaussian fit.

rived extinction towards the starburst ring may be accurate to correct the fluxes of the starburst tracers. However, this estimate is unlikely to probe all the obscuration towards the AGN. Hence, the flux density derived for the [Ne v] 14.32 μm corresponds only to the best lower limit we can derive from the current data. Figures 4.10 and 4.11 show the same set of maps as in Figs. 4.5 and 4.6, but corrected for extinction using the estimated $A_V(9.85\ \mu m)$ map. Note that after correcting for extinction, all the fine-structure emission lines, the average 14.5–15.0 μm continuum, and the PAH features peak at about the same position of the H_2O maser. The H_2 lines show an offset of about 43 pc ($\sim 2.3''$, one pixel) with respect to the water maser. However, there is a difference of only $< 1''$ between the centroids obtained from a two-dimensional gaussian profile fit of all the lines.

With the aim to determine whether the line emission maps are resolved, we retrieved a partial map of 3×3 SH slit pointings of the star P Cygni (AOR 13049088). The map consists of $5''$ steps parallel to the slit and $2''$ steps perpendicular to the

slit, similar to the map spacing we have for NGC 4945. These pointings lead to a 10×3 pixel map. In order to test the continuum drop off along the (10 pixels) slit, 2×2 aperture spectra were extracted in the same way we do for the SH maps of NGC 4945. Then the continuum flux at 15 μm was measured in each position, resulting in a mostly gaussian variation of the flux along the slit. The FWHM ranges from 6 to 7 arcsec between 10 and 19 microns, far less than the ratio 19/10 expected over this range for the PSF of a diffraction limited telescope. The same procedure was applied to the 12×6 map of the star KsiDra used by Pereira-Santaella et al. (2010) (AORs 16294912 and 16340224). In this case, a FWHM in the range $5.8'' - 6.4''$ was found in both the parallel and the perpendicular (to the slit) directions. For the particular case of the [Ne v] line, a gaussian fit of the uncorrected for extinction map indicates that this emission is only marginally resolved along the major axis, given its FWHM of $6.4''$. Along the minor axis the FWHM is $7.3''$. After extinction correction, the [Ne v] emission appears unresolved. The other emission lines (uncorrected for extinction) are well resolved (FWHM$> 7''$).

The integrated flux densities of the co-added spectra from the whole 10×10 aperture of the IRS/SH map (described in Sec. 4.3) are summarized in Table 4.1. In this work we include only the fluxes of the most prominent emission lines. These integrated fluxes are larger than those reported by Bernard-Salas et al. (2009), because our 10×10 aperture is larger than the SH staring aperture. In Table 4.1 we also include the fluxes corrected with the silicate-based extinction $A_{\rm V}(9.85\ \mu{\rm m})$, and the line widths (FWHM) as estimated from the Gaussian fit.

4.4 Discussion

4.4.1 Rotation in the nuclear region

Even though the spectral resolution (R∼600) of the IRS/SH module is relatively low in comparison to the resolution used in most kinematic studies, we used the SH spectra to determine shifts in the velocity of various lines. Pereira-Santaella et al. (2010) studied the validity of the SH velocity fields by using synthetic spectra. They found that the distortion of the wavelength scale introduced by the telescope pointing uncertainties limits the accuracy of the velocity estimates up to $\pm 10\ {\rm km\,s^{-1}}$, regardless of the S/N of the spectra, for sources which are neither point sources nor uniformly extended sources (e.g., the nuclear region of NGC 4945). Considering as well the uncertainty in the absolute wavelength calibration (~ 10% of a pixel), which does depend on the S/N of individual spectra, Pereira-Santaella et al. estimated uncertainties of $10 - 30\ {\rm km\,s^{-1}}$ in the SH velocity fields, and concluded that variations of $> 20\ {\rm km\,s^{-1}}$ in the velocity maps are likely to be real.

The derived velocity fields of the [Ne ii] 12.81 μm, [Ne iii] 15.56 μm, and H_2 S(2) 17.0 μm lines are shown in Fig. 4.12. These correspond to the lines with the highest S/N ($\gtrsim 100$) in the SH spectra throughout the whole region mapped, and therefore the velocity fields derived from them are considered to be reliable. We also include the velocity field of the [Ne v] 14.32 μm line, although with a much

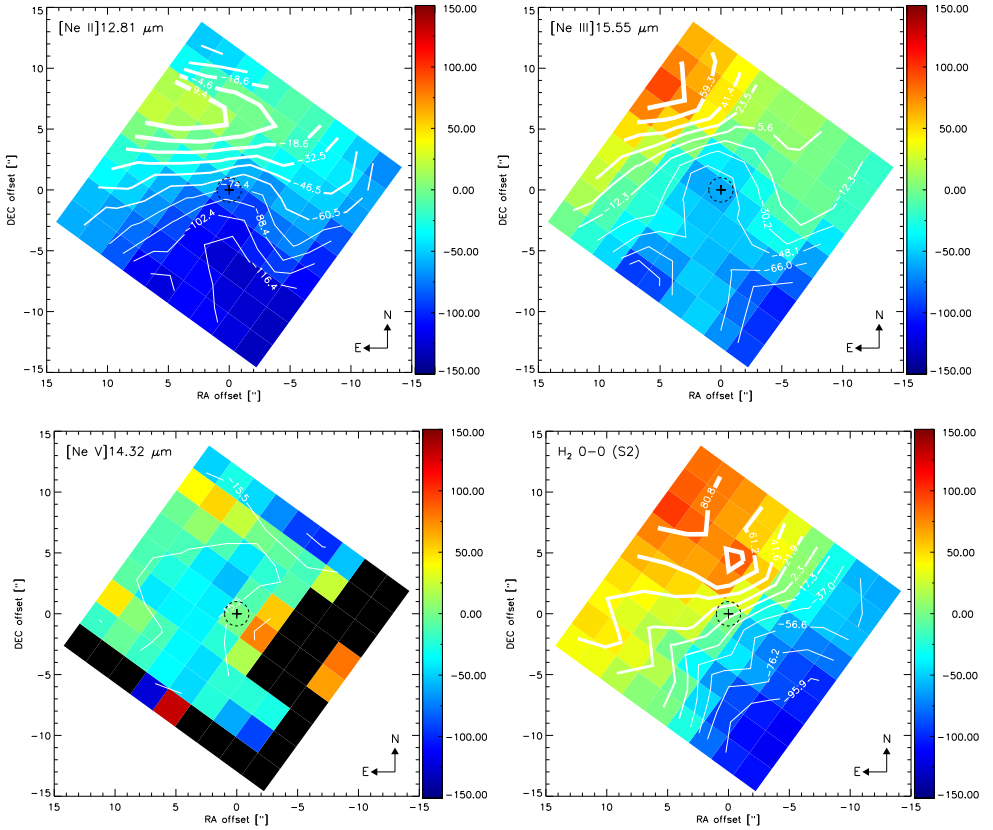

Figure 4.12: Velocity fields of the fine-structure lines [Ne II] 12.81 μm (*top left panel*), [Ne III] 15.56 μm (*top right panel*), [Ne V] 14.32 μm (*bottom left panel*), and the molecular hydrogen line H_2 0-0 S(2) 17.0 μm (*bottom right panel*). The maps, covering a region of $\sim 20.7'' \times 20.7''$ ($\sim 383 \times 383$ pc^2), are consistent with a rotating disk, with the exception of the [Ne V] line, which present a relatively uniform (most likely not spectrally resolved) velocity field.

lower S/N ranging from ~ 1 to ~ 100 throughout the map. The pixels with less than a 3σ detection level (mostly found at the edges of the map, where the S/N is the lowest) in the [Ne V] line have been blackened.

Given that the galaxy major axis runs at $\sim 45^o$, we find that the velocity fields of the [Ne II], [Ne III], and H_2 S(2) lines are consistent with a rotating disk in the region of $\sim 20.7'' \times 20.7''$ covered by the SH map, which corresponds to a physical scale of $\sim 383 \times 383$ pc^2. These velocity fields are in agreement with the velocity curves estimated for the H I Pfβ and H_2 0-0 S(9) lines by Spoon et al. (2003, their Fig.7), given the rotation of 45^o between the north-south axis of the respective figures, and the fact that the inclination of the nuclear disk has been estimated to be smaller ($\sim 62^o$) than the inclination ($\sim 80^o$) of the large-scale galactic disk (Chou et al., 2007).

On the other hand, the relatively uniform central region of the [Ne v] velocity field may be due to the lack of spectral resolution and the lower (factor 10 to 100) S/N level obtained in this line. This implies that we are unable to spectrally resolve, at a reliable level, the rather small ($\lesssim 50\ \mathrm{km\,s^{-1}}$) velocity shifts in the [Ne v] line. Nevertheless, with a higher spectral resolution we would expect a weaker rotation of [Ne v] in comparison to the rotation shown by the starburst tracers (from about $-120\ \mathrm{km\,s^{-1}}$ to $\sim 100\ \mathrm{km\,s^{-1}}$). If the [Ne v] is exclusively related to the AGN NLR, it would mean that the NLR gas does not feel the gravitational pull of the large gas mass interior to the starburst ring. But it would feel the pull from the SMBH, which cannot be resolved spatially with Spitzer-IRS. Besides, the group of three pixels, next (~ 43 pc) to the adopted location of the AGN (the H_2O maser), shows positive velocities (in the range $\sim 10 - 70\ \mathrm{km\,s^{-1}}$) which is opposite to the characteristics of the velocity fields of the starburst tracers. This might be a sign of the kinematically decoupled component discovered at the center of the disk with interferometric maps of the $J = 2 \rightarrow 1$ transitions of ^{12}CO, ^{13}CO, and C^{18}O (Chou et al., 2007). However, higher spectral and spatial resolution observations of the [Ne v] line are required to reliably conclude on this.

4.4.2 Excitation temperature of H_2

For LTE conditions, and an ortho-to-para ratio of 3 (Neufeld et al., 2006, their Fig.13), we can estimate the excitation temperature of the molecular hydrogen throughout the region mapped with the IRS/SH module, from the ratio between the flux density of the H_2 S(2) 12.3 μm and H_2 S(1) 17.0 μm lines as

$$T_{ex} = -\frac{T_{up}^{\mathrm{S(2)}} - T_{up}^{\mathrm{S(1)}}}{log(F_{\mathrm{S(2)}}\nu_{\mathrm{S(1)}}A_{\mathrm{S(1)}}g_{\mathrm{S(1)}}) - log(F_{\mathrm{S(1)}}\nu_{\mathrm{S(2)}}A_{\mathrm{S(2)}}g_{\mathrm{S(2)}})}\ \ \mathrm{K}, \qquad (4.4)$$

where $F_{\mathrm{S(1)}}$ and $F_{\mathrm{S(2)}}$ are the integrated flux densities of the H_2 S(1) and S(2) lines, ν is the corresponding rest frequency ($\sim 1.75 \times 10^{13}$ Hz for S(1) and $\sim 2.44 \times 10^{13}$ Hz for S(2)), and A and g are the respective Einstein A-coefficients and statistical weights of each transition. The upper level energy T_{up} of the transitions is in units of K.

Figure 4.13 shows the IRS/SH maps (not corrected for extinction) of the H_2 S(2) to H_2 S(1) total flux ratio (*top left panel*), and the corresponding map of the excitation temperature T_{ex} (K) (*bottom left panel*) of the molecular hydrogen, estimated from eq.(4.4). The peak excitation temperature of $\sim 528 \pm 31$ K is reached about 43 pc ($\gtrsim$2.3″) to the north of the H_2O maser. The *right panels* of Fig. 4.13 show the H_2 S(2)/S(1) ratio and the estimated excitation temperature from the respective H_2 fluxes corrected for extinction with the silicate-based $A_{\mathrm{V}}(9.85\ \mu\mathrm{m})$. The correction for extinction leads to a peak temperature of 421 K, which is about 100 K lower than the temperature derived from the non-corrected fluxes. However, the distribution of the temperature, and the position of its peak value, do not change.

Since LIRGs and ULIRGs are complex systems, the H_2 gas is not expected to be at a single temperature. Besides, a long line of sight can probe different excitation

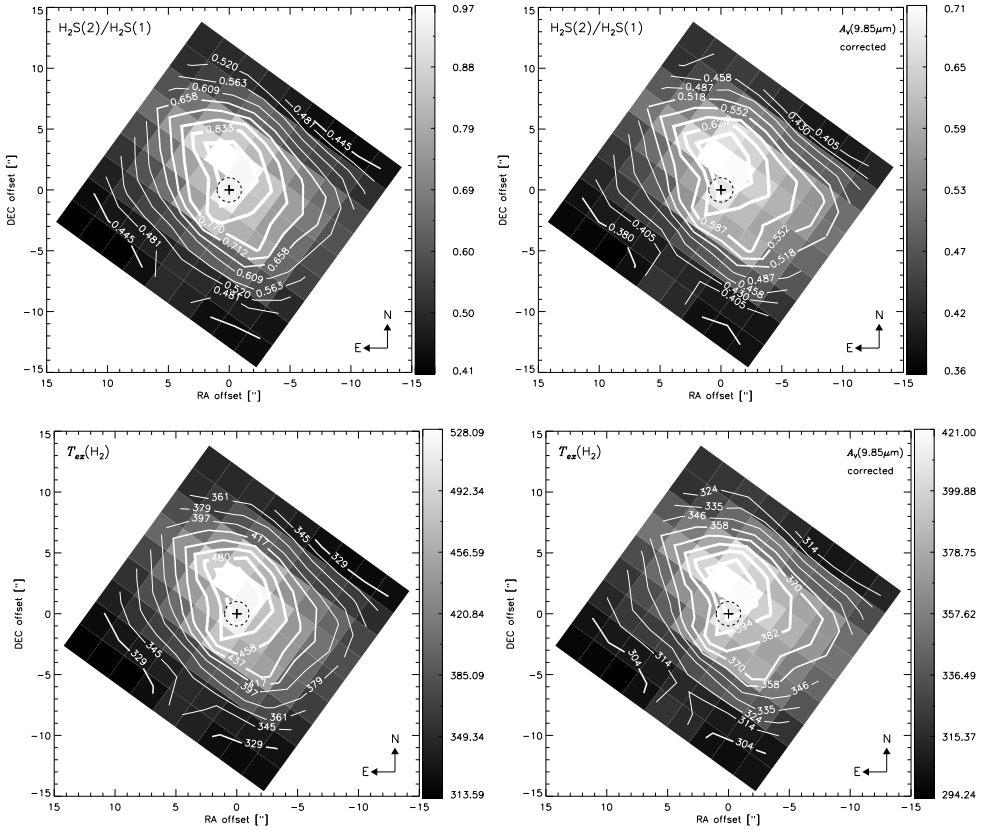

Figure 4.13: *Left panels* - IRS/SH maps of the H_2 S(2) to H_2 S(1) total flux ratio (*top left panel*), and the map of the estimated T_{ex} (K) of the molecular hydrogen. The peak excitation temperature of $\sim$528 K is reached about 43 pc ($\gtrsim$2.3″) to the north of the H_2O maser. *Right panels* - Same as above, but using the extinction corrected fluxes of the H_2 S(2) and S(1) lines. The extinction correction leads to an $\sim$100 K lower peak temperature.

environments (e.g., PDRs, shocks) like in the sample of galaxies studied by Roussel et al. (2007). Previous estimates of the excitation temperature, based on SWS observations of the (0-0) S(0) and S(1) fluxes detected in the nucleus of NGC 4945, led to a cooler H_2 component with $T_{ex} \sim 160$ K (corresponding to about 9% of the total H_2 mass), while a temperature $T_{ex} \sim 380$ K (about 0.4% of H_2 mass) was estimated from the S(1) and S(2) fluxes (Spoon et al., 2000, their Table 6), which is in close agreement with our result considering the size of the big SWS slit. This excitation temperature is similar to the temperature $T_{ex} = 365 \pm 50$ K derived for the low-energy transitions in NGC 1377 (Roussel et al., 2006), but higher than the temperature of $T_{ex} = 292 \pm 6$ K estimated from the S(0)-S(3) lines observed in NGC 6240 (Higdon et al., 2006). Since we cannot use the map of the H_2 S(3) 9.7 μm line due to the mismatch between the SH and SL modules mentioned in Sec. 4.3, we

are not able to infer accurately the mass of the warm H_2 mass using only the S(1) and S(2) lines. In fact, even if we had been able to use the S(3) line as an extinction probe, most of the warm mass is revealed by the S(0) line in combination with the S(1) line. The S(3) map from the LH module has far lower resolution, which makes it difficult to compare with the SH and SL maps.

4.4.3 Tracing the starburst ring

The [Ne II] and [S III] fine-structure lines are our cleanest tracers of star formation (H II regions). If an AGN is present the [Ne III] and [S IV] lines will have contributions from both the starburst and the AGN. That is, the [Ne III] map may not be suitable to trace the starburst if an AGN is present. However, in NGC4945 the AGN contamination to [Ne III] is likely low, given the faintness of [Ne V].

The [Ne III] 15.56/[Ne II] 12.81 line ratio (*middle left panel* in Fig. 4.14) ranges between ∼0.13 and ∼0.27 above and below the major axis of the region mapped. The difference with the lowest ratios (0.06–0.13), which are found along the northeast-southwest axis, is more pronounced than in the [Ne V] 14.32/[Ne II] 12.81 line ratios. The [Ne III]/[Ne II] line ratios obtained with the extinction correction (*middle right panel* in Fig. 4.14) are just ∼9% larger than without correction. This relatively small change after the extinction correction is because even in a high-extinction situation the differential extinction between [Ne III] and [Ne II] is small, given that both lines are closely spaced in wavelength and not in one of the silicate features. The [Ne III]/[Ne II] ratio at the position of the H_2O maser is about 10% lower than the ratio obtained from the fluxes of the 10×10 co-added spectrum (Table 4.1). The lowest ratio of ∼0.06 is observed at about 131 pc (∼7.3″) southwest of the H_2O maser.

Since in starburst environments the [Ne II] and [Ne III] emission lines are expected to be driven mainly by photo-ionization (e.g., Ho & Keto, 2007), the lower ratios found along the northeast-southwest axis are likely due to a [Ne II] emission enhanced by the starburst ring. Even though these low ratios are consistent with a ratio [Ne III]/[Ne II]≤0.1 found in shocks (Binette et al., 1985) where the low ionization line [Ne II] can also be enhanced (Voit, 1992). On the other hand, the highest [Ne III]/[Ne II] ratios found above and below the major axis are larger than those typically found in shocks. Note that only our 10×10 co-added [Ne V]/[Ne II] ratio (from Table 4.1) can be compared to other galactic nuclei, as the 10×10 aperture is comparable to the size probed in any of the more distant galaxy nuclei.

The [Ne III]/[Ne II]$\sim 0.08 - 0.1$ ratios observed along the starburst ring are in close agreement with the ratios observed in some galaxies of the ISO starburst sample and are consistent with burst timescale models predicting a relatively short-lived starburst of $5 - 8$ Myr (Thornley et al., 2000, their Fig.6). In the whole region mapped, we observe ratios [Ne III]/[Ne II]< 0.3, which are a factor ~ 3 lower than the ratios observed in the sample of quasars reported by Veilleux et al. (2009). However, the ratio [Ne III]/[Ne II]~ 0.07 observed at the nucleus of NGC 4945 is comparable to the ratios observed in the nucleus of 5 (out of 16) galaxies in the sample of LIRGs studied in Pereira-Santaella et al. (2010, their Fig.14).

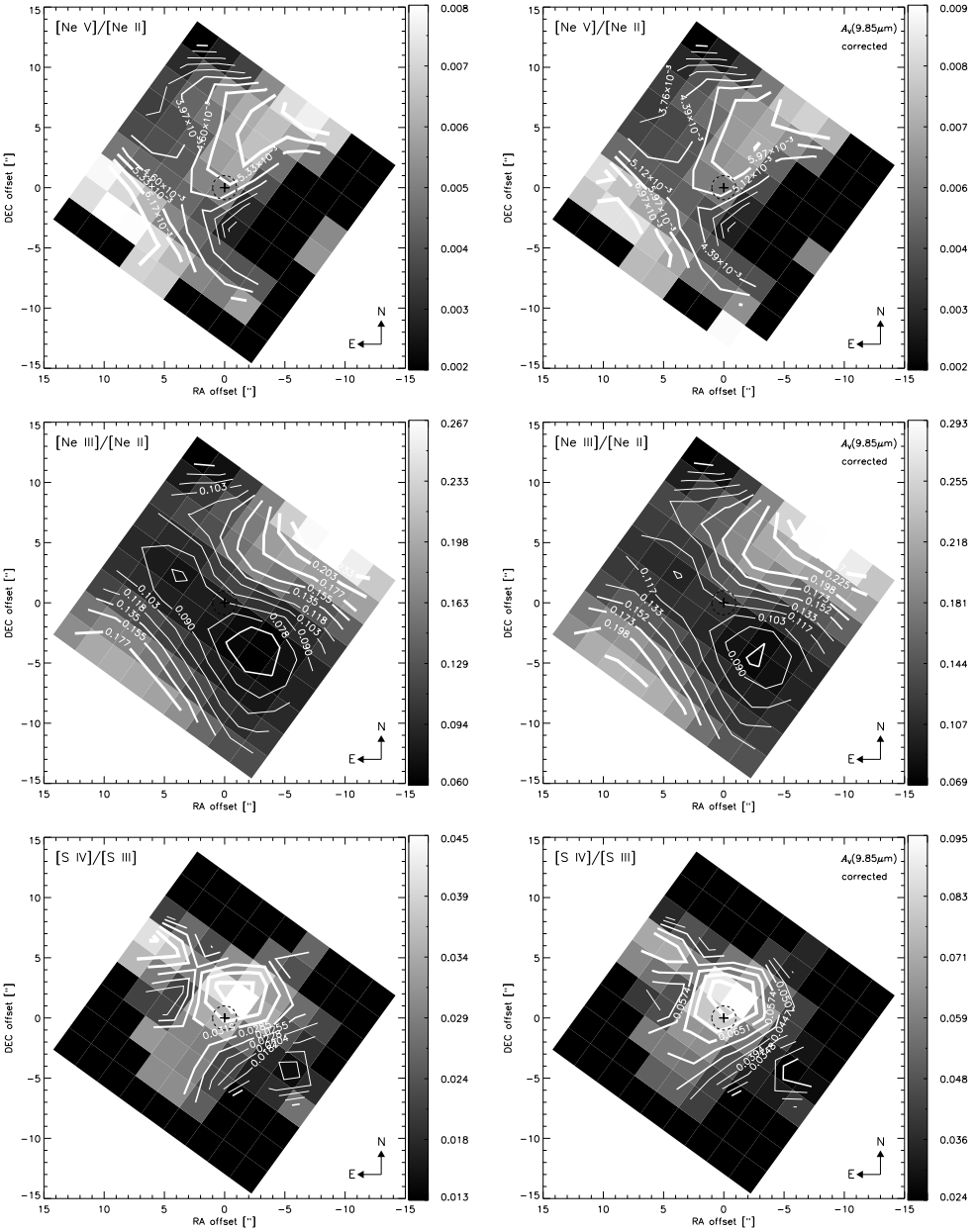

Figure 4.14: *Left panels* - Integrated flux density ratios between the fine-structure lines (from top to bottom) [Ne V] 14.32/[Ne II] 12.81, [Ne III] 15.56/[Ne II] 12.81, and [S IV] 10.51/[S III] 18.71. *Right panels* - Same as above, but considering the fluxes corrected for extinction. The blackened pixels correspond to pixels with a $<3\sigma$ detection level in the faintest emission lines [Ne V] 14.32 μm and [S IV] 10.51 μm.

The *bottom* panels of Fig. 4.14 show the [S IV] 10.51/[S III] 18.71 line ratio map corrected (*bottom right*) and not corrected (*bottom left*) for extinction. Like in the case of the [Ne V] line, the pixels with a $<3\sigma$ detection level are blackened. Because [S IV] is sitting close to the deepest point of the silicate absorption feature at 9.7 μm (Fig.4.2), the ratios corrected for extinction are a factor $\sim$2 larger than those obtained without correction. In both cases the highest ratio is found about 43 pc northwest of the H_2O maser. The uncorrected for extinction map-averaged ratios (from the fluxes in Table 4.1) of [Ne III]/[Ne II]~ 0.11 and [S IV]/[S III]~ 0.02 are similar (within 10%) to the ratios obtained from the SH staring observations by Bernard-Salas et al. (2009). They position NGC 4945 among the sources with the lowest hardness of the radiation field in their sample of starburst galaxies, which, according to Bernard-Salas et al., may be an indication of an old (or small) population of massive stars in NGC 4945. However, this can be conclude only for the outermost surface that we can probe with [S IV] and [S III] lines, and we cannot rely much on the extinction corrected data for this analysis, since the [S IV]/[S III] ratio depends more on the extinction law used than the [Ne III]/[Ne II] ratio.

4.4.4 Starburst or AGN dominated [Ne V] emission?

If shocks can be excluded, the [Ne V] fine-structure line would be our cleanest tracer of AGN activity. Galaxies with a predominant AGN component have typical [Ne V]/[Ne II] line flux ratios of $0.8-2$ (e.g., Sturm et al., 2002; Armus et al., 2007). On the other hand, starburst galaxies have a strict upper limit $<$0.01 for the [Ne V]/[Ne II] flux ratios (e.g., Sturm et al., 2002; Verma et al., 2003; Farrah et al., 2007; Bernard-Salas et al., 2009). The *top left panel* of Fig. 4.14 shows the IRS/SH map of the [Ne V] 14.32/[Ne II] 12.81 line ratio in the nucleus of NGC 4945. The pixels with a $<3\sigma$ detection level in the faintest emission line [Ne V] 14.32 μm have been blackened and they are not considered in the analysis. The extinction corrected [Ne V] 14.32/[Ne II] 12.81 line ratios are shown in the *top right panel* of Fig. 4.14. In either case, corrected or not corrected for extinction, our measured [Ne V]/[Ne II] line ratios are consistent with those observed in starburst galaxies rather than with AGN dominated galaxies. If we assume that the [Ne V] emission is driven by the AGN, the low ratios observed can be due either to an *excess* [Ne II] emission from the starburst, or to a heavily obscured AGN, which is consistent with the assumption that the silicate-based extinction $A_V(9.85\ \mu\mathrm{m})$ estimated in Sec. 4.3.4 is just a lower limit for the extinction to the AGN narrow line region (NLR).

There are several scenarios that may cause the true extinction to be higher than our silicate-based estimate: (1) PAH emission originating from dusty PDRs along the line of sight (a so-called *mixed extinction* scenario); (2) foreground, low-extinction PAH emission fills up a deep silicate feature associated with the buried AGN. If we were to observe a ratio of at least 0.8 at the position of the H_2O maser, where the not corrected for extinction [Ne V]/[Ne II] ratio is $\sim$0.005, we would require an extinction $A_V \sim 5500$ mag. Note that a [Ne V]/[Ne II] ratio about 10% smaller is obtained using the fluxes of the 10$\times$10 co-added spectrum (Table 4.1).

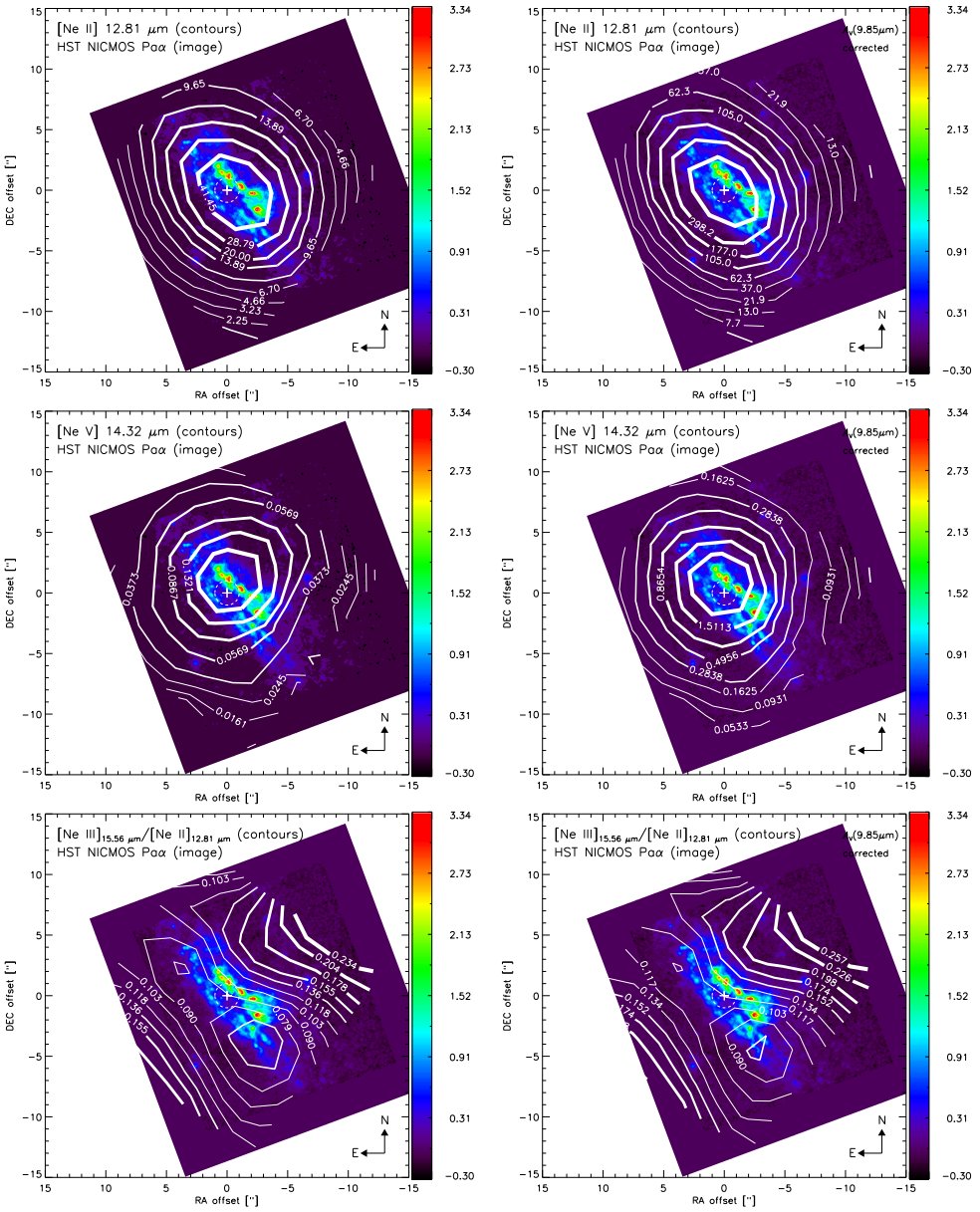

Figure 4.15: HST NICMOS image of Paα (in units of 10^{-21} W cm^{-2}) of the nucleus of NGC 4945 (Marconi et al., 2000). The contours (labelled) are the fine-structure lines [Ne II] 12.81 μm (*top panels*) and [Ne V] 14.32 μm (*middle panels*). The *left panels* show the fluxes (10^{-21} W cm^{-2}) without correction for extinction, while the *right panels* show the extinction corrected fluxes, using the silicate-based extinction $A_{\rm V}(9.85\ \mu{\rm m})$ (Fig. 4.8). The not corrected [Ne V] flux peaks at about 43 pc to the northwest of the H_2O maser (Fig. 4.5), while the extinction corrected [Ne V] line peaks at about the same position as [Ne II] and the H_2O maser (Fig. 4.10). The *bottom panels* show the [Ne III] 15.55 μm/[Ne II] 12.81 μm line ratio, corrected and not corrected for extinction. In both cases the ratio is lower along the starburst ring traced by the Paα line, while it increases along the conical cavity (Marconi et al., 2000).

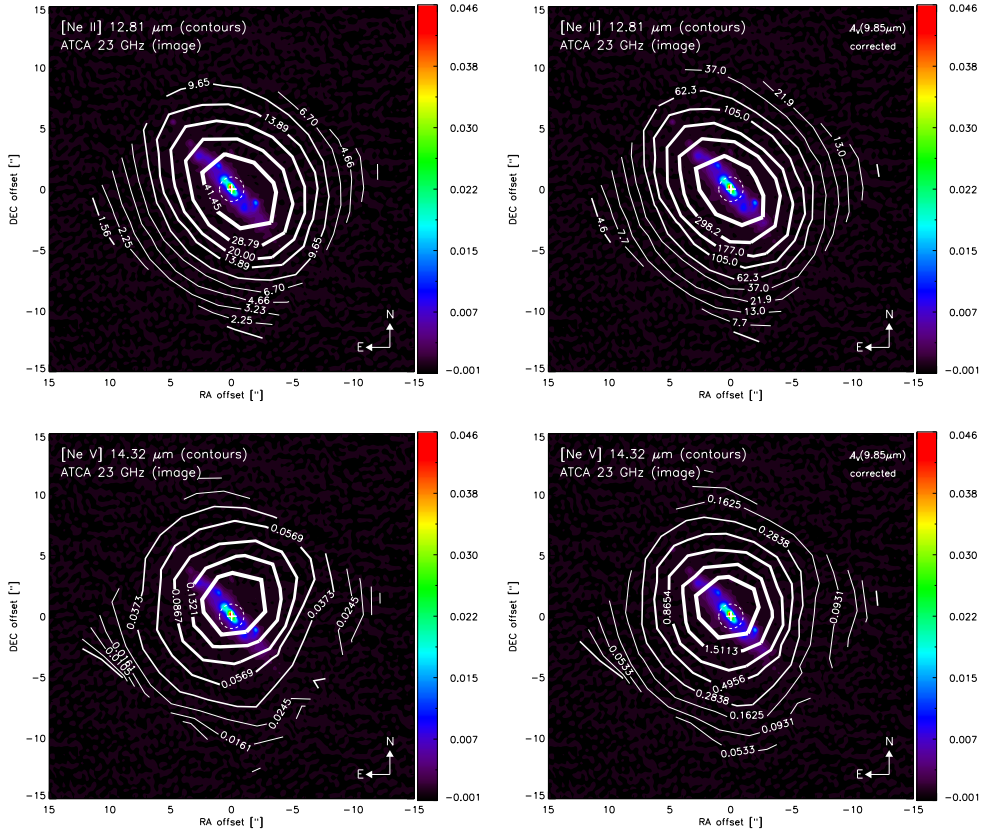

Figure 4.16: ATCA 23 GHz image (in units of Jy $\mathrm{beam}^{-}1$) of the nucleus of NGC 4945 (Lenc & Tingay, 2009). The contours (labelled) are the fine-structure lines [Ne II] 12.81 μm (*top panels*) and [Ne V] 14.32 μm (*bottom panels*). The *left panels* show the fluxes (10^{-21} W cm^{-2}) without correction for extinction, while the *right panels* show the extinction corrected fluxes, using the silicate-based extinction $A_{\mathrm{V}}(9.85\ \mu\mathrm{m})$ (Fig. 4.8). The dashed-line circle represents the $\pm 1''$ pointing accuracy of Spitzer. The reference ($\Delta\alpha = 0, \Delta\delta = 0$) is marked with a cross and corresponds to the position R.A.(J2000)=13:05:27.477, Dec.(J2000)=-49:28:05.57 of the H_2O maser (Greenhill et al., 1997). The main radio emission coincides with the position of the H_2O maser, and with the peak emission of the extinction corrected [Ne V] and [Ne II] lines (Fig. 4.10).

Such high values of extinction are consistent with the extreme absorbing column $N_{\mathrm{H}} \sim 4 \times 10^{24}\ \mathrm{cm}^{-2}$ estimated from X-ray observations towards the AGN Broad Line Region (BLR) of NGC 4945 (Done et al., 2003). The NLR should be less extinguished, though.

Figure 4.15 shows the HST NICMOS image of Paα of the nucleus of NGC 4945 (Marconi et al., 2000). The contours are the fine-structure lines [Ne II] 12.81 μm (*top panels*) and [Ne V] 14.32 μm (*bottom panels*). The *left panels* show the fluxes without correction for extinction, while the *right panels* show the extinction corrected fluxes, using the silicate-based extinction $A_{\mathrm{V}}(9.85\ \mu\mathrm{m})$ estimated in Sec.4.3.4. The not corrected [Ne V] flux peaks at about 43 pc to the northwest of

the H_2O maser (Fig. 4.5), just above the $\sim 5''$ radius starburst ring traced by the Paα flux. Instead, the extinction corrected [Ne v] line peaks at about the same position as [Ne ii] and the H_2O maser (Fig. 4.10), inside the starburst ring. We also notice a difference in shape of the extinction-corrected [Ne ii] and [Ne v] emission. The [Ne ii] emission is elongated along the direction of the Paα starburst ring. The [Ne v] emission, however, is not, which is consistent with the AGN driven interpretation of [Ne v]. The [Ne iii] 15.55 μm/[Ne ii] 12.81 μm line ratios are lower along the starburst ring traced by the Paα line, while there is an increasing gradient that seems to mimic the conical-shaped cavity traced by the H_2 1-0 S(1) line (Marconi et al., 2000).

Figure 4.16 shows the ATCA 23 GHz image of the nucleus of NGC 4945 (Lenc & Tingay, 2009). The contours (labelled) are the fine-structure lines [Ne ii] 12.81 μm (*top panels*) and [Ne v] 14.32 μm (*bottom panels*). The *left panels* show the fluxes (10^{-21} W cm^{-2}) without correction for extinction, while the *right panels* show the extinction corrected fluxes. The main radio emission coincides with the position of the H_2O maser, and with the peak emission of the extinction corrected [Ne v] and [Ne ii] lines (Fig. 4.10).

4.5 Final remarks

We have mapped the central region of NGC 4945 with the SH and SL modules of the Spitzer InfraRed Spectrograph. From the SH spectral cubes we produced maps of fine-structure emission lines [S iv] at 10.51 μm, [Ne ii] at 12.81 μm, [Ne iii] at 15.56 μm, [S iii] at 18.71 μm, the AGN narrow-line region tracer [Ne v] at 14.32 μm, and the molecular hydrogen lines, H_2 S(2) and H_2 S(1) at 12.3 μm and 17.0 μm, respectively. From the SL spectral cubes we obtained maps of the H_2 S(3), and the silicate absorption feature at 9.7 μm.

We present the first map of [Ne v] 14.32 μm towards the nucleus of NGC 4945 with flux detection levels down to 0.017×10^{-21} W cm^{-2}. We produced and estimated an extinction map $A_V(9.85\ \mu\mathrm{m})$ based on the apparent strength of the 9.7 μm silicate absorption feature. All the emission lines corrected for extinction peak at about the same position of the H_2O maser. On the other hand, the hydrogen lines peak at about 43 pc away from the H_2O maser. However, their centroid (from a gaussian profile fit) is less than 1 arcsec different than the centroid obtained for the other extinction corrected lines.

The [Ne v]/[Ne ii] ratios observed in the region mapped are consistent with those observed in starbursts rather than in AGNs. The [Ne iii]/[Ne ii] ratios observed along the starburst ring are likely due to an excess [Ne ii] emission driven by the starburst ring.

In order to observe a ratio of at least 0.8 (as expected in most AGNs) at the position of the H_2O maser, we would require an $A_V \sim 5500$ mag, which is consistent with the extreme (X-ray derived) column $N_H \sim 4 \times 10^{24}$ cm^{-2} (Done et al., 2003), obscuring all the way down to the AGN BLR.

4.6 Future work

We need to investigate whether the difference observed in the rotation gradient between the [Ne II] and the H_2 0-0 S(2) lines is significant (Fig. 4.12), and what this indicates if so. We also need to check whether the extinction corrected [Ne V] emission (Fig.4.10) is consistent with a point-source origin, or if it is spatially extended.

Given the inferred supernova rate $> 0.1(v/10^4)\ \mathrm{yr}^{-1}$ by Lenc & Tingay (2009), it will be interesting to investigate whether the [Ne V] 14.32 μm (uncorrected for extinction) emission may have an origin in supernova remnants rather than from an AGN NLR. For this we could use the observed [Ne V] luminosity from supernova remnant RCW103 (Oliva et al., 1999) to make a prediction for the number of supernovae needed to power the observed [Ne V] luminosity in NGC 4945.

We also need to analyze the ratios between the other starburst tracers (e.g., [S III], [Ne III], [Ne II]) and compare them with ratios given in the literature. Also the hardness of the radiation field, and the electron density, can be estimated from these diagnostics.

Although it has been claimed that the variation of the PSF size with wavelength within each IRS module is negligible (Pereira-Santaella et al., 2010, their appendix A), we would like to check at which level (e.g., <20%, <10%) this is valid for our IRS/SH maps at fairly different wavelengths, like the pivots at 5.3 μm and 13.55 μm used to estimate the local mid-IR continuum for the silicate absorption feature at 9.7 μm (Sec.4.3.4), as well as for the ratios between lines at separated wavelengths, like [S III] 18.71 μm and [S IV] 10.51 μm.

Acknowledgements

We thank Alessandro Marconi for providing the HST NICMOS images, and Emil Lenc for the ATCA 23 GHz image. We are grateful to the SPITZER/SINGS team for their support during and after the observations. We thank Varoujian Gorjian for providing the Spitzer-MIPS 24 μm map of the central region of NGC 4945.

5

Structure, Chemistry and Dynamics of an AGN torus

– J.P. Pérez-Beaupuits, K. Wada, M. Spaans –

Many efforts have been made to model the mass and dynamical evolution of the circumnuclear gas in active galactic nuclei (AGN). However, chemical evolution has not been included in detail in current three-dimensional (3-D) hydrodynamic simulations. The UV and X-ray radiation from the AGN can drive the chemistry of the gas and affect the thermodynamics, as well as the excitation of the ISM. Therefore, we estimate the effects (in terms of chemical abundances and excitation) of X-ray irradiation from the AGN itself for the atomic and molecular gas of a 3-D hydrodynamic model of an AGN torus. The hydrodynamical model follows the formation of H_2 out of the H I phase according to the evolving ambient ISM conditions. We estimate the abundance of different atomic and molecular species from an XDR/PDR chemical model that depends on the local hydrogen density and impinging X-ray flux at each grid element in the computational box. A 3-D radiative transfer code that uses multi-zone escape probability techniques with fixed directions was adapted to use the hydrodynamical model (temperature, density and velocity field) as input, and to estimate the level populations of different transitions of the atoms and molecules in the XDR/PDR model. A line tracing approach is then used to obtain line intensities and profiles for arbitrary viewing angles. We found an average XDR-derived temperature of $\gtrsim 1$ to ~ 100 times higher than the average temperature estimated in the X-ray free hydrodynamical model within the inner ± 20 pc region, where the X-ray flux is $F_X \gtrsim 1.1$ erg s^{-1} cm^{-2}. The average H_2 XDR-derived density, instead, follows an inverse relation with the X-ray flux, being lower (by factors up to $\sim 10^4$) than the average density of the hydrodynamical model in the inner ± 10 pc region. We emphasize the importance of coupling between hydrodynamical simulations, XDR/PDR chemical models, and radiative transfer, to estimate the abundances of different species and their line intensities. Exploratory predictions for the CO $J = 1 \rightarrow 0$ and $J = 6 \rightarrow 5$ lines indicate that CO $J = 1 \rightarrow 0$ is not always a good tracer of $n_{\rm H}$ in the central ($\lesssim 60$ pc) region of the AGN.

Paper in preparation

5.1 Introduction

The formation and growth of a central black hole and its interaction with intense star-forming regions is one of the topics most debated in the context of galaxy evolution. There is observational evidence for a common physical process from which most active galactic nuclei (AGNs) and starbursts originate (e.g., Soltan, 1982; Magorrian et al., 1998; Ferrarese & Merritt, 2000; Graham et al., 2001; Häring & Rix, 2004). A plausible scenario considers that starbursts, super-massive black hole growth, and the formation of red elliptical and submillimeter galaxies, are connected through an evolutionary sequence caused by mergers between gas-rich galaxies (Hopkins et al., 2006, 2008; Tacconi et al., 2008; Narayanan et al., 2009, 2010). In this scenario, the starbursts and (X-ray producing) AGNs seem to be coeval, and the interaction processes between them (phase d and e in Figure 1 by Hopkins et al. 2008), that dominate the formation and emission of molecular gas, is one of the long-standing issues concerning active galaxies.

Numerous molecules tracing different (AGN and starburst driven) gas chemistry have been detected in Galactic and (active) extragalactic environments. Studies have shown that chemical differentiation observed within Galactic molecular clouds is also seen at larger ($\sim$100 pc) scales in nearby galaxies (e.g., Henkel et al., 1987; Nguyen-Q-Rieu et al., 1991; Martín et al., 2003; Usero et al., 2004; Tacconi et al., 2008; Pérez-Beaupuits et al., 2007, 2009, 2010; Baan et al., 2010).

The evolution of the ISM in the inner 100 pc region around a 10^8 $M_\odot$ supermassive black hole (SMBH) was investigated by Wada & Norman (2002) (hereafter WN02) using three-dimensional (3-D) Euler-grid hydrodynamic simulations. They took into account self-gravity of the gas, radiative cooling and heating due to supernovae (SNe). A clumpy and filamentary torus-like structure was found to be reproduced on a scale of tens of pc around the SMBH, with highly inhomogeneous ambient density and temperature, and turbulent velocity field. Their results indicated that AGNs could be obscured by the circumnuclear material. This represents theoretical support for observational evidence showing that some AGNs are obscured by nuclear starbursts (e.g., Levenson et al., 2001, 2007; Ballantyne, 2008, and references therein).

Several efforts have been made to estimate the molecular line emission from the nuclear region in these 3-D hydrodynamic simulations, and to compare the results with observational data. For instance, Wada & Tomisaka (2005) (hereafter WT05) derived molecular line intensities emitted from the nuclear starburst region around a SMBH in an AGN. They used the 3-D hydrodynamic simulations (density, temperature, and velocity field data) of the multi-phase gas modeled by WN02 as input for 3-D non-LTE radiative transfer calculations of ^{12}CO and ^{13}CO lines. They found that the CO-to-H_2 conversion factor (X-factor) is not uniformly distributed in the central 100 pc and the X-factor for ^{12}CO $J = 1 \rightarrow 0$ is not constant with density, in contrast with the ^{12}CO $J = 3 \rightarrow 2$ line.

Similarly, the role of the HCN and HCO^+ high-density tracers in the inhomogeneous molecular torus of WN02 was studied by Yamada et al. (2007) (hereafter YWT07). These non-LTE radiative transfer calculations suggested a complicated

excitation state of the rotational lines of HCN (with maser action) and HCO^+, regardless of the spatially uniform chemical abundance assumed.

However, all these previous efforts to estimate the molecular line emissions from the central 100 pc of an AGN leave room for improvements. First of all, the radiative cooling in the simulations by WN02 are not consistent with the chemical abundances in the cold and dense gas because (collisional) formation and (radiative) destruction of H_2 by far ultraviolet radiation (FUV) was not included. Therefore, the cold and dense gas in the simulations by WN02 does not necessarily represent the dusty molecular gas phase around an AGN.

Hence, in order to study the distribution and structures of the various density regimes of the H_2 gas, the 3-D hydrodynamic simulations of WN02 were extended by Wada, Papadopoulos & Spaans (2009) (hereafter WPS09) to solve the nonequilibrium chemistry of hydrogen molecules along with the hydrodynamics. The formation of H_2 on dust and its radiative destruction by far ultraviolet radiation (FUV) from massive stars are also included in the model by WPS09. This allows to track the evolution of molecular hydrogen and its interplay with the H I phase in the central $64 \times 64 \times 32$ pc region. Thus, the radiative cooling in the model by WPS09 is more consistent with the chemical abundances expected in the cold ISM, in comparison with the models by WN02. Different SN rates and strengths of the uniform FUV field were also explored in order to study their effects on the structures of molecular gas.

On the other hand, the inhomogeneous density and temperature structures observed in the 3-D hydrodynamic models are not the only factors that drive molecular abundances and excitation conditions of molecular lines. There is observational and theoretical evidence in the literature that supports different chemical evolution scenarios due to X-ray and UV radiation from the central AGN and circumnuclear starburst, as well as mechanical heating produced by turbulence and supernovae (e.g., Kohno et al., 2001, 2007; Kohno, 2005; Imanishi & Wada, 2004; Imanishi et al., 2006a,b; Imanishi & Nakanishi, 2006; Aalto et al., 2007b; Meijerink et al., 2007; García-Burillo et al., 2007; Loenen et al., 2008; García-Burillo et al., 2008; Pérez-Beaupuits et al., 2009). The strong UV and X-ray radiation from the AGN and accretion disk could affect both the dynamics and excitation of the molecular gas (e.g., Ohsuga & Umemura, 2001a,b; Meijerink et al., 2007). However, the radiation field from the AGN itself was not taken into account in the earlier estimates of molecular line emissions from hydrodynamical simulations.

A preliminary estimate of the potential effects of hard X-rays ($E > 1$ keV) on the molecular gas was done by WPS09 using the X-ray Dissociated Region (XDR) models of Meijerink & Spaans (2005). It was found that XDR chemistry may change the distribution of H_2 around an AGN, if X-ray effects are explicitly included in the hydrodynamic model. The X-ray chemistry depends mainly on H_X/n, where H_X is the X-ray energy deposition rate and n is the number density of the gas (Maloney et al., 1996). Although the H_2 abundance is robust in a clumpy medium like the one found in the hydrodynamical models, the temperature of the gas affected by an X-ray flux is expected to be a factor of ~ 5 higher than that found in standard

models of a Photon Dominated Region (PDR; e.g., Hollenbach & Tielens 1999), for $log(H_X)/n > 26$ (Meijerink et al., 2007). This is because the ionization heating by X-rays is more efficient than photoelectric emission by dust grains. The higher temperatures of the molecular gas will therefore produce stronger emission in the pure rotational H_2 lines (e.g., S(0) and S(1) at 28 μm and 17 μm, respectively).

Other molecular and atomic lines have also been suggested as tracers of the AGN and starburst activity in nearby galaxies ($z < 1$) as well as in high ($z \geq 1$) redshift galaxies. Spaans & Meijerink (2008) studied the possibility of using ^{12}CO and H_2 emission lines to trace a young population of accreting massive ($\geq 10^6\ M_\odot$) black holes at redshifts $z = 5 - 20$ and radiating close to the Eddington limit. An enhancement in the intensities of various ^{12}CO transitions up the rotational ladder, as well as other molecular and atomic lines like ^{13}CO, HCN, HCO^+, [C I], [C II], [O I] and [N II], is also expected to be observed when X-ray irradiation dominates the local gas chemistry (Meijerink et al., 2007; Spaans & Meijerink, 2008). Simulations of quasars at $z \sim 6$ with massive ($10^{12} - 10^{13}\ M_\odot$) halos and different merging histories showed that mid-J ^{12}CO lines are highly excited by a starburst, while high velocity peaks are expected to be produced by AGN-driven winds (Narayanan et al., 2008b,a). It was further found by Narayanan et al. (2009) that the compact ^{12}CO spatial extents, broad linewidths and high excitation conditions observed in Submillimetre Galaxies (SMGs) at $z \sim 2$ can be explained if SMGs are a transition phase of major merging events.

In this work we use the XDR/PDR chemical model by Meijerink & Spaans (2005) to estimate the abundances of more than 100 species (atoms and molecules) at each grid point in the computational box of the extended 3-D hydrodynamical models of an AGN torus by WPS09. We also estimate the actual X-ray flux emerging from the AGN, derived from the central black hole mass. Flux attenuation by photo absorption of X-rays along the ray path and the distance from the central black hole is included. Thus, we estimate non-homogeneous abundances at each grid point that depend on the local density and impinging X-ray flux. An extended version of the non-LTE 3-D radiative transfer code β3D by Poelman & Spaans (2005) is used to compute the level populations of any molecule or atom for which collision data exist in the LAMDA* database (Schöier et al., 2005). Molecular and atomic line intensities and profiles are calculated with a line tracing approach for an arbitrary viewing angle. The organization of this article is as follows. In Sec. 5.2 we describe the numerical method. The results and analysis are presented in Sec. 5.3. The final remarks and future work are presented in Sec. 5.4.

5.2 Numerical Method

The three-dimensional hydrodynamic model of the AGN torus used in this work includes inhomogeneous density fields and mechanical heating effects due to turbulence and supernova explosions, with a resolution (pixel size) of 0.25 pc in diameter.

* http://www.strw.leidenuniv.nl/∼moldata/

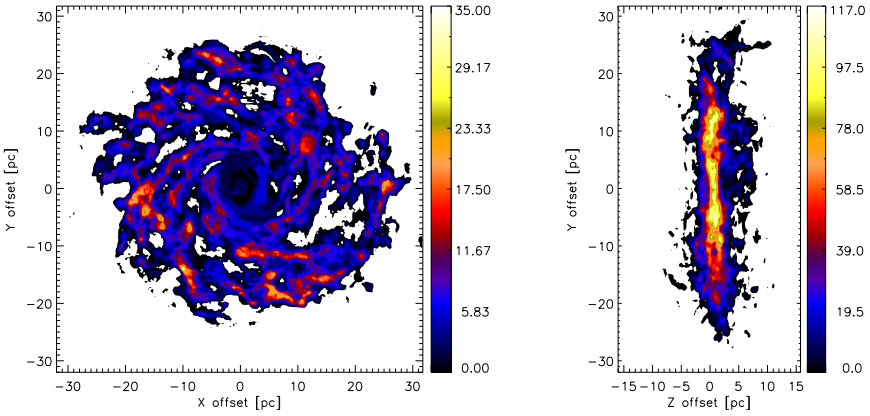

Figure 5.1: Number of grid elements in the 3-D hydrodynamical model that has both density $n(\mathrm{H_2})$ higher than 10^2 cm^{-3} and temperature T_k lower than 10^4 K, along the line-of-sight of the X-Y plane (*left*) and the Z-Y plane (*right*). These are the grid elements that would contribute the most to the emission of molecular gas irradiated by the X-ray flux emitted from the central SMBH.

Detailed descriptions of the hydrodynamic equations and simulations can be found in WPS09. The 3-D hydrodynamic model considers the formation and destruction of H_2 in a self-consistent way, including formation of H_2 on grains, and the destruction of it by FUV radiation. This allows the code to compute the total density, local temperature (and velocity field) as well as the fraction of H_2 at each grid element. The hydrodynamical code runs for an equivalent time of $\gtrsim 3.5$ Myr until it reaches a quasi-steady state (WN02), and the gas forms a highly inhomogeneous and clumpy torus with some spiral structures, and it comprises a flared disk of H_2 gas with ~ 50 pc in diameter, and about 10 pc in height (WPS09, their Fig.2c).

One of the main criticism that hydrodynamical models receive in general, is that the density (and temperature) distribution that they show does not mimic closely actual observations of the gas structure and distribution in galaxies and galaxy nuclei (like in WPS09, their Fig.2a&b). However, observational data do not show the actual density or temperature of the gas either. The information we get from observations is the intensity and distribution of particular atomic and molecular emission (or absorption) lines, from which the ambient conditions (density, temperature and radiation field) can be estimated. Therefore, hydrodynamical models need to be complemented with atomic and gas chemistry that allow us to infer how the emission of different species would look like given the density and temperature structure obtained from the hydrodynamic simulations.

One aspect that needs to be kept in mind is that not all the grid elements shown in density and temperature distribution maps of the 3-D code by WPS09 will contribute to the emission of, particularly, molecular lines. Figure 5.1 shows the number of grid elements with relatively cold temperature ($T_K \leq 10^4$ K) and moderate density ($n(\mathrm{H_2}) \geq 10^2$ cm^{-3}) that can contribute to the molecular emission emerging

along the line-of-sight of the face-on (X-Y plane) and edge-on (Z-Y plane) viewing angles. At higher temperatures and lower densities, the fractional abundances of molecular species would be very low ($< 10^{-10}$) and their contribution to the molecular emission lines would be negligible due to the low collisional excitation. The structure observed then is quite different than when considering the full density and temperature distribution at any cross section of the computational box. Although the maps of the main contributing grid elements represent a close estimate of the structure that we would expect to observe in molecular emission, they do not take into account the optical depth effects nor the (sub-)thermal excitation of the molecular energy levels that are treated in the radiative transfer calculations described in Sec. 5.2.3. The actual structure of emission lines then depends on the local density, temperature, and the radiation flux impinging at each grid element.

The heating of the gas and dust by X-rays emanating from the AGN, as well as the chemical abundances in the cold (< 500 K) gas, are not computed in hydrodynamical models. Including the (time dependent) chemical evolution at each step in the hydrodynamical simulations would take too long with the current computational resources. Therefore, after a realization of the state-of-art 3-D hydrodynamical simulation, the XDR/PDR code by Meijerink & Spaans (2005) is used to estimate the chemical abundances, based on the local density and impinging X-ray flux at each grid cell of the computational box. This code is the first combined XDR-PDR chemical model, depth dependent up to large columns ($N_{\rm H} \sim 10^{25}$ cm^{-2}), and considers a large (over 100 species) chemical network. In the following sections we describe the calculation of the X-ray flux, and the impact that it has on the chemistry and heating of the atomic and molecular gas around the AGN.

5.2.1 The X-ray flux

For our 3-D hydrodynamical model we have a $M_{BH} = 1.3 \times 10^7 M_\odot$ super massive black hole (SMBH) (WPS09), so we can estimate the monochromatic luminosity of the AGN model at the rest frame wavelength $\lambda = 510$ nm as follows

$$\lambda L_\lambda(510\ \mathrm{nm}) = 10^{44} \times \left[\frac{10^{-7}}{a}\left(\frac{M_{BH}}{M_\odot}\right)\right]^{1/b} \qquad \mathrm{erg\ s^{-1}}. \tag{5.1}$$

With $a = 5.71^{+0.46}_{-0.37}$ and $b = 0.545 \pm 0.036$ (e.g., Kaspi et al., 2000) we have $\lambda L_\lambda(510\ \mathrm{nm}) = 6.62 \times 10^{42}$ erg s^{-1}. Using the same bolometric to monochromatic luminosity factor as in Kaspi et al. (2000) we can determine the bolometric (total radiant energy) luminosity as $L_{bol} \approx 9\lambda L_\lambda(510\ \mathrm{nm})$ erg s^{-1}.

The incident specific flux is assumed to have a spectral shape of the form

$$F_i(E) = F_0 \left(\frac{E}{1\ \mathrm{keV}}\right)^\alpha exp\left(-E/E_c\right) \qquad \mathrm{erg\ s^{-1}\ cm^{-2}\ eV^{-1}}, \tag{5.2}$$

where $E = h\nu$ eV, $\alpha \approx 0.9$ is the characteristic spectral index of the power-law components of Seyfert 1 galaxies (e.g., Pounds et al., 1990; Madejski et al., 1995; Zdziarski et al., 1995), E_c is the cut-off energy which can be $\gtrsim 100$ keV, 200 keV or

550 keV depending on the sample of AGNs (e.g., Madejski et al., 1995), and F_0 is set to match the flux estimated from eq.(5.2) at the central grid point in the data cube. Only the hard X-rays between 1 keV and 100 keV are relevant for the X-ray chemical model. So we integrate eq.(5.2) over this energy range in order to obtain the total bolometric flux

$$F_{bol} = \int_{1\ \mathrm{keV}}^{100\ \mathrm{keV}} F_0 \left(\frac{E}{1\ \mathrm{keV}}\right)^{\alpha} e^{-E/E_c} dE \qquad \mathrm{erg\ s^{-1}\ cm^{-2}}. \tag{5.3}$$

Considering that only ∼10% (Schleicher et al., 2010) of the total luminosity is emitted in X-rays, we have that $F_{bol} = 0.1 \times L_{bol}/4\pi r_0^2$, where r_0 is the distance from the central black hole which, for our purpose, is assumed to be the size of a grid cell ($r_0 = \parallel \vec{r}_0(x_0, y_0, z_0) \parallel = 0.25$ pc) for the central unresolved grid point. From this we find that $F_0 \approx 9.6 \times 10^2$ erg s^{-1} cm^{-2} eV^{-1}.

For the rest of the cells, at position $\vec{r}(x, y, z)$ in the cube (a vector) the flux decreases not only with the square of the distance $r = \parallel \vec{r}(x, y, z) - \vec{r}_0(x_0, y_0, z_0) \parallel$ from the central black hole, but also because of the opacity $\tau(E, \vec{r})$ of each grid cell at position $\vec{r}(x, y, z)$ along the radial path. The opacity is defined as

$$\tau(E, \vec{r}) = \sigma_{pa}(E) N_{\mathrm{H}}(\vec{r}), \tag{5.4}$$

where $\sigma_{pa}(E)$ is the photoelectric absorption cross section per hydrogen nucleus, and $N_{\mathrm{H}}(\vec{r})$ is the total column density of hydrogen along the radial path from the central black hole to the position $\vec{r}$ in the computational box. The photoelectric absorption is calculated from all the species as

$$\sigma_{pa}(E) = \sum_i \mathcal{A}_i^{total} \sigma_i(E), \tag{5.5}$$

with the total (gas and dust) elemental abundances, $\mathcal{A}_i^{total}$, taken from Meijerink & Spaans (2005), and the X-ray absorption cross sections, $\sigma_i(E)$, from Verner & Yakovlev (1995). The total bolometric flux $F_{bol}(\vec{r})$ (erg s^{-1} cm^{-2}) impinging on an arbitrary grid cell at position $\vec{r}$ is then calculated as

$$F_{bol}(\vec{r}) = \left(\frac{0.25\ \mathrm{pc}}{r}\right)^2 \int_{1\ \mathrm{keV}}^{100\ \mathrm{keV}} F_0 \left(\frac{E}{1\ \mathrm{keV}}\right)^{\alpha} e^{-E/E_c} e^{-\tau(E,\vec{r})} dE. \tag{5.6}$$

Figure 5.2 shows the X-ray flux estimated for the 3-D hydrodynamical model by WPS09 at the X-Y plane, 7 pc below the mid-plane of the AGN torus (*left panel*), as well as the flux in the actual X-Y mid-plane (*middle panel*). The *right panel* shows the flux in the Y-Z plane. The grid cells with different densities cause more or less absorption of the X-ray flux along the radial path from the central SMBH, producing shadow-like shapes and an inhomogeneous flux field.

This total bolometric X-ray flux (from now on F_X) is used along with the total density of a grid cell as input parameters of the XDR/PDR chemistry code to estimate the abundances of several species. The formalism is described in the next section.

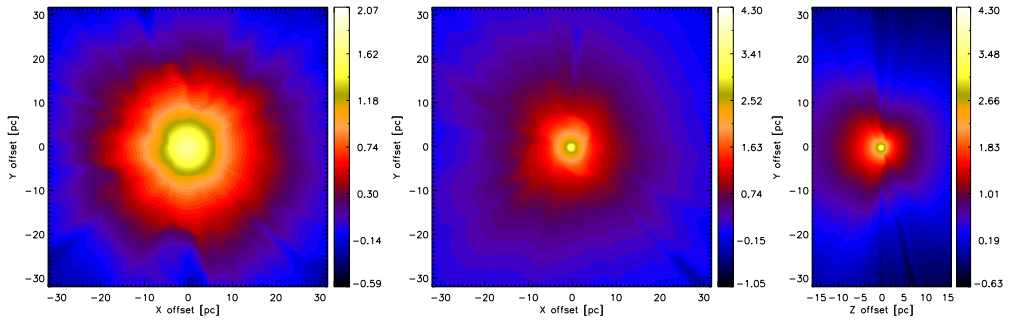

Figure 5.2: Impinging bolometric X-ray flux (in logarithmic scale and units of $\mathrm{erg\ s^{-1}\ cm^{-2}}$) as seen in (*left*) the X-Y plane 7 pc below the mid-plane of the AGN torus; (*middle*) the flux in the actual X-Y mid-plane (the accretion disk); and (*right*) the flux seen in the Y-Z plane. Note that the X-ray flux distribution is not homogeneous. The shadow-like shapes are due to the X-ray absorption by the grid cells with different densities found along the radial path from the AGN.

5.2.2 Chemical abundances and temperature

For each grid point in the computational box we have the total density and temperature from the 3-D hydrodynamic model. Since each grid point represents a physical (unresolved) scale of 0.25 pc, we also know the total column density that the impinging radiation flux will go through. Thus, the total density, the radiation flux, and the column density of each grid point are used as input parameters for the XDR/PDR chemical model by Meijerink & Spaans (2005) to compute the densities and fractional abundances of different species at different column densities throughout the 0.25 pc slab. In addition, we also get the temperature of the gas (as a function of the column density) derived self-consistently from the chemical and thermal balance computed in the XDR/PDR code. Hence, we can compare the temperatures and H_2 densities estimated from the 3-D hydrodynamical model with those computed considering the X-ray effects (see Sec. 5.3.2).

Figure 5.3 shows the fractional abundances of some species as a function of the column density for impinging radiation fluxes of $160\ \mathrm{erg\ cm^{-2}\ s^{-1}}$ (left panel) and $1.6\ \mathrm{erg\ cm^{-2}\ s^{-1}}$ (right panel). The slab represents a single unresolved grid point in the computational box, with fixed scale (resolution) of $d = 0.25$ pc and total hydrogen density $n_{\mathrm{H}} = 10^5\ \mathrm{cm^{-3}}$. This gives a total column density of $N_{\mathrm{H}} = n_{\mathrm{H}} \times d \approx 10^{23}\ \mathrm{cm^{-2}}$, which is marked with a vertical slashed-dotted line. The XDR/PDR model, though, was executed to compute the abundances of the species up to a column of $10^{25}\ \mathrm{cm^{-2}}$ in order to show how deep the X-rays can penetrate depending on the strength of the radiation field. For the strong X-ray flux (left panel) and the actual column density ($\sim 8 \times 10^{22}\ \mathrm{cm^{-2}}$) of the slab, the abundances of molecules like HCO^+ will be negligible. Since the scale of the grid points is fixed, a slab denser than $10^5\ \mathrm{cm^{-3}}$ would be required in order to observe a significant abundance of HCO^+ at larger ($N_{\mathrm{H}} > 10^{23}\ \mathrm{cm^{-2}}$) columns. Conversely, a weaker

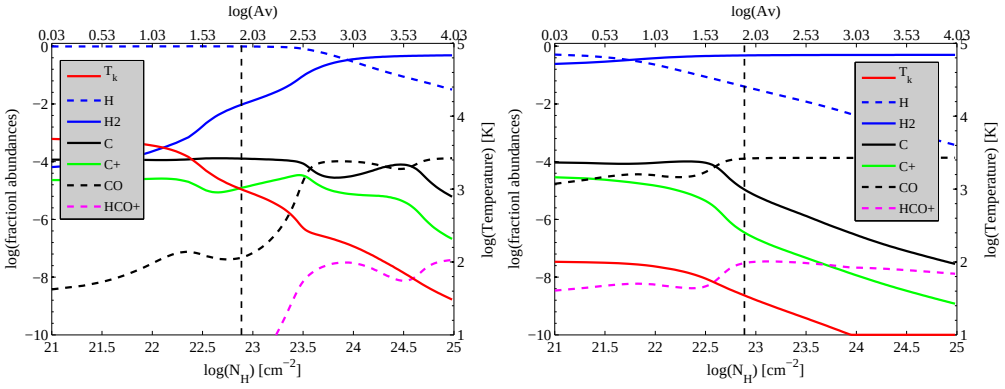

Figure 5.3: *Left panel* – Fractional abundances of various atomic and molecular species in a slab that represents one unresolved grid cell of $d = 0.25$ pc scale and density of $n_{\rm H} = 10^5$ cm^{-3}, in the 3-D hydrodynamic model. The X-ray flux of 160 erg cm^{-2} s^{-1} penetrates from the left side of the slab and affects the chemistry as it is absorbed throughout the column of gas and dust. The vertical dashed-dotted line indicates the total column density $N_{\rm H} = n_{\rm H} \times d \approx 8 \times 10^{22}$ cm^{-2} of the slab. For this particular X-ray flux, a denser slab would be required to observe a significant abundance of molecules like HCO$^+$. *Right panel* – Fractional abundance for the same slab as above, but with an impinging radiation flux of 1.6 erg cm^{-2} s^{-1}. Note the higher abundances of H_2, CO, and HCO$^+$at lower column densities, while the abundance of H, C and C$^+$ decrease earlier and faster throughout the slab. The overall temperature is also lower in this case.

radiation flux of 1.6 erg cm^{-2} s^{-1} (right panel) impinging on the slab will produce a higher abundance of e.g., H_2, CO, HCO$^+$ at lower column densities, while H, C and C$^+$ would be less abundant, in a column averaged sense, than in the previous case. An overall lower temperature is also observed when the radiation flux is weaker, since X-ray photons are completely absorbed at a column of $\gtrsim 10^{24}$ cm^{-2}.

Since a grid point of the 3-D hydrodynamic model is unresolved, and the chemical abundances given by the XDR/PDR code depend on the column density, we estimate an abundance that is *representative* for the particular slab and for each species in the chemical network from the abundances observed throughout the slab of 0.25 pc scale. We compute the total fractional abundance $< \mathcal{A}_X >$ of the species X=^{12}CO, HCN, etc., as

$$< \mathcal{A}_X >= \frac{\int n_X(l)\, dl}{\int n_{\rm H}\, dl}, \tag{5.7}$$

where $n_X(l)$ (cm^{-3}) is the density of the species X at the layer l (cm) in the cloud, and $n_{\rm H}$ is the total density of the slab, so the denominator is actually the total column density $N_{\rm H}$ (cm^{-2}) of a particular grid point.

Because the variation of the abundance of a species through the slab is different for every species (e.g., [C I] is more abundant at the edge of the slab where T is high, while ^{12}CO is more abundant deep into the slab, where T is low), we require a gas temperature that is representative of the layers in the slab where the abun-

dance of the species is higher (since those layers contribute the most to the line emission). Therefore, we compute an abundance-weighted average temperature, throughout an unresolved grid point, as

$$< T_X >= \frac{\int \mathcal{A}_X(l) T(l)\, dl}{\int \mathcal{A}_X(l)\, dl}, \tag{5.8}$$

which gives different temperatures for different species in the same grid point. For instance, with the lower ($1.6\ \mathrm{erg\ cm^{-2}\ s^{-1}}$) X-ray flux (*right panel* in Fig. 5.3) the total fractional abundance of CO is $\sim 10^{-4}$ with an abundance-weighted average temperature of ~ 37 K. While for C we have an abundance of $\sim 3 \times 10^{-5}$ and a representative temperature of ~ 66 K.

Due to the large number of grid elements in the hydrodynamical model ($256 \times 256 \times 128 \sim 8.4 \times 10^6$ data points) we require an optimized process in order to run the XDR/PDR code for the essential grid elements. Our criteria was to process only the grid points with total density larger than $100\ \mathrm{cm^{-3}}$ and temperature lower than 10^4 K. This is because lower gas densities will have little weight in the excitation of the molecular species, while higher temperatures would lead to mostly ionized gas. Once the abundances and abundance-weighted average temperatures have been determined for the selected grid elements of the 3-D hydrodynamical model, we can proceed to perform the radiative transfer calculations for the entire cube.

5.2.3 3-D radiative transfer and line tracing

The advanced 3-D radiative transfer code β3D (Poelman & Spaans, 2005) has been optimized for heavy memory usage, to be able to use the $256 \times 256 \times 128$ (elements) data cube of the low resolution (0.25 pc scale) 3-D hydrodynamical models by WPS09. In principle, the temperature, density and velocity field derived from the hydrodynamical simulations can be used as the ambient conditions for the radiative transfer formalism. However, the temperature and molecular hydrogen density derived from the XDR model are found to be significantly different, as discussed in Sec. 5.3.2. A multi-zone approach is used, in which the calculation of the level populations in a grid cell depends on the level populations of all the other cells through the different escape probabilities connecting adjacent grid points (Poelman & Spaans, 2005, 2006).

The collisional rates available in the LAMDA database (Schöier et al., 2005) are used in a similar way as in the 1-D and 2-D radiative transfer codes RADEX (van der Tak et al., 2007) and RATRAN (Hogerheijde & van der Tak, 2000), to calculate the level populations of different atomic and molecular species (e.g. [C I], [C II], [O I], ^{12}CO, ^{13}CO, HCN, HCO$^+$, HNC, CN, etc.). For this we use the commonly adopted main collision partner H_2 for the radiative transfer calculations in all the molecules. Although the contribution of helium atoms to the total collision density for CO is just about 10^{-2} larger, we also include (for completeness) He as an additional collision partner by extrapolating (see Appendix 5.4) the rate coefficients reported in Cecchi-Pestellini et al. (2002).

The line intensities, including kinematic structures in the gas, and optical depth effects, are computed with a ray-tracing approach for arbitrary rotation (viewing) angles about any of the three axes of the computational box. The emerging specific intensity is computed using the escape probability formalism described in Poelman & Spaans (2005)

$$dI_{\nu}^{z} = \frac{1}{4\pi} n_i A_{ij} h\nu_{ij} \beta\left(\tau_{ij}\right) \left(\frac{S_{ij} - I_b^{loc}(\nu_{ij})}{S_{ij}} \right) \phi(\nu_{ij}) dz \ , \tag{5.9}$$

where dI_{ν}^{z} has units of $[\mathrm{erg\ cm^{-2}\ s^{-1}\ sr^{-1}\ Hz^{-1}}]$ and τ_{ij} is the *cumulative optical depth* from the edge of the ray path to the z^{th} layer, and increases away from the observer.

5.3 Analysis and results

Once the level populations of particular transitions have been estimated with the radiative transfer code, and the line tracing at a particular inclination angle has been completed, the resulting two-dimensional emission map can be exported into a regular FITS data cube. This data cube can in turn be processed by practically any single-dish or interferometric data reduction package and visualization tool.

5.3.1 CO maps

The map of the $J = 1 \rightarrow 0$ emission line of ^{12}CO, from the inner $\sim 5 \times 5 \times 5$ pc^3 of the AGN torus, is shown in Fig. 5.4 using the *view* task of the GILDAS/CLASS data reduction package. The line intensity has been rescaled assuming a distance of 1 Mpc for the source, in order to obtain the spatial scale in arcseconds. The effects of the velocity field are observed in the different velocity shifts across the region mapped. The spectral lines, produced by the different grid elements found along the line-of-sight through each pixel of the map, are distributed around the arbitrary systemic velocity chosen for this system. This distribution is consistent with gas rotating around the AGN. The spectral lines reveal the non-homogeneous distribution of the ambient conditions, and kinematics of the gas, at the particular inclination angle of 45^o about the X-axis.

The total hydrogen column density N_{H}, through a face-on viewing angle of the 3-D hydrodynamical model, is shown in the *top left panel* of Fig. 5.5. As it is expected, the total column density of the CO molecule $N(\mathrm{CO})$ (*top right panel*) follows a similar distribution, although with about three orders of magnitude lower columns. The *left* and *right bottom panels* of Fig. 5.5 show the surface brightness of the CO $J = 1 \rightarrow 0$ and $J = 6 \rightarrow 5$ lines, respectively. These correspond to the brightness observed at the surface of the face-on data cube (i.e., not scaled for an arbitrary distance to the source). It is remarkable that the CO $J = 6 \rightarrow 5$ line traces more gas and structure than the CO $J = 1 \rightarrow 0$ line, which is about twice as weak

http://iram.fr/IRAMFR/GILDAS/

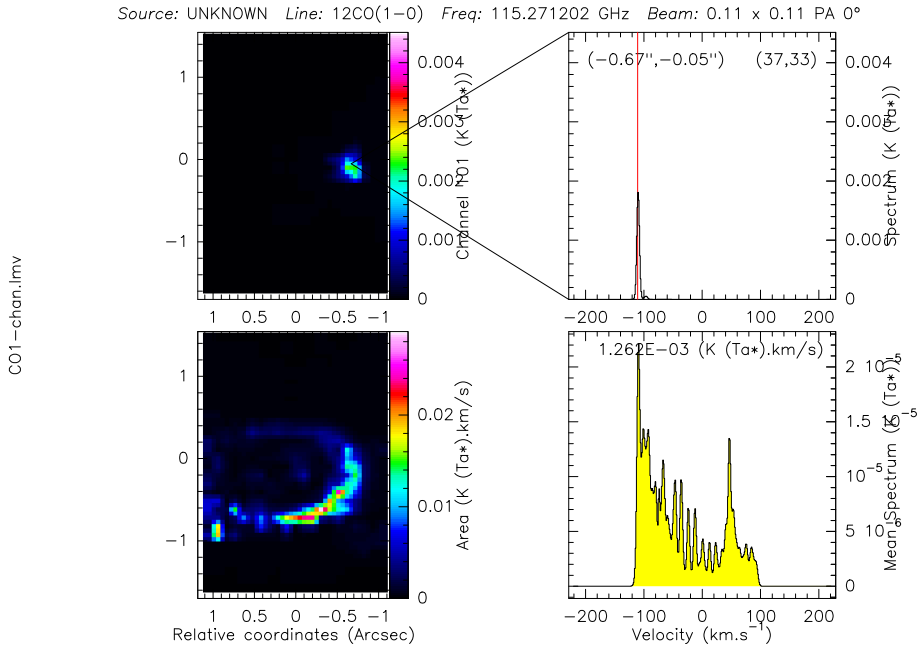

Figure 5.4: ^{12}CO $J = 1 \rightarrow 0$ emission line for the inner $21 \times 21 \times 21$ grid cells ($\sim 5 \times 5 \times 5$ pc^3) of the original cube, at an adopted distance of 1 Mpc, and with an inclination angle of 45^o about the X-axis. The maps and spectra are produced using the *view* task of the GILDAS/CLASS data reduction package.

at its peak intensity. The very clumpy structure shown by the CO $J = 1 \rightarrow 0$ line does not resemble the total CO column density (*top right* in Fig. 5.5), while the CO $J = 6 \rightarrow 5$ line does. This can be explained by an optically thick $J = 1 \rightarrow 0$ line ($N(\mathrm{CO}) > 10^{18}$ cm^{-2}) and by the abscence of cold (< 100 K) gas, specially at the inner ± 5 pc of the AGN torus. This indicates that, by just considering the excitation of CO, the $J = 1 \rightarrow 0$ line will not always be a good tracer of hydrogen column density n_{H} in the central region ($\lesssim 60$ pc) of an AGN.

As an exercise for comparison with future observations, we simulate a raster map of the AGN torus by adopting a distance $D = 3.82$ Mpc (the distance to NGC 4945, see Chap. 4) to the source, and by convolving the surface brightness maps with a single dish beam of FWHM=$0.15''$ (about 11 pixels in the original map). This corresponds to a spatial scale of ~ 0.92 pc at the distance chosen. A step size of one third the FWHM (about 4 pixels) degrades the original image from 256×256 to a 61×61 pixels image. Figure 5.6 shows the resulting flux density maps of the CO $J = 1 \rightarrow 0$ (*left*) and CO $J = 6 \rightarrow 5$ (*right*) lines. The smearing effect of the relatively large beam produces the loss of the intricate structure observed in the original maps with 0.25 pc resolution shown in Fig. 5.5.

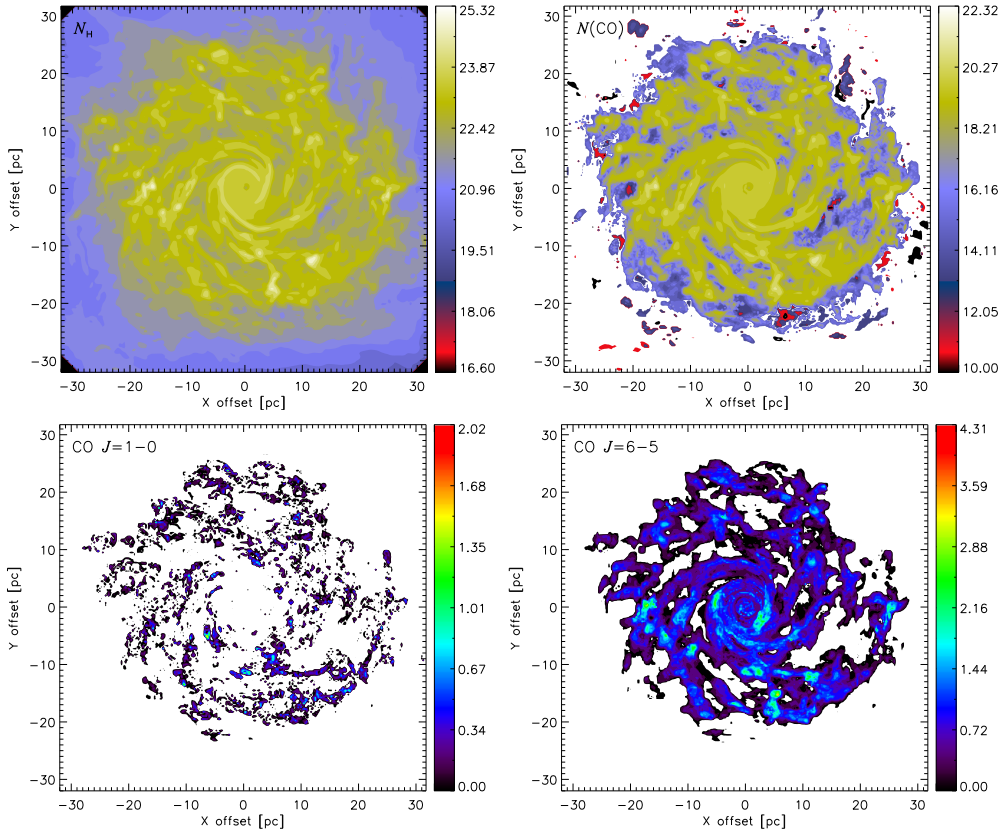

Figure 5.5: *Top panels* - Face-on view of the column density (units of cm^{-2}) of hydrogen N_{H} (*left*) and CO column $N(\mathrm{CO})$ (*right*) in logarithmic scale. *Bottom panels* - Surface brightness maps of the CO $J = 1 \rightarrow 0$ (*left*) and $J = 6 \rightarrow 5$ (*right*) lines (in units of 10^{-4} erg s^{-1} cm^{-2} sr^{-1}), as observed at the surface of the face-on data cube. Note that the CO $J = 1 \rightarrow 0$ emission does not trace the same regions as the CO $J = 6 \rightarrow 5$, nor resembles the total CO column density (*top right*).

5.3.2 Temperature and density driven by X-rays

In order to investigate the impact of the X-ray flux on the temperature and molecular hydrogen density of the gas, we compare the temperature T_{HYD} obtained from the hydrodynamical model with the temperature T_{XDR} derived from the XDR chemical model. We took a strip volume of $64 \times 1.25 \times 1.5$ pc^3 along the X-axis, and around the center of the Y-axis ($\Delta \mathrm{Y} = 0$) and Z-axis ($\Delta \mathrm{Z} = 0$) of the 3-D cube. We use this *thin* volume so we can have similar X-ray fluxes (decreasing mostly with the radial distance) impinging at each grid element of the 1.25×1.5 pc^2 slices of the volume. We computed the average temperature and H_2 density of the 1.25×1.5 pc^2 slices at each ΔX grid element. At the resolution of 0.25 $\mathrm{pc/element}$ we have 30 grid elements per slice, which is a good compromise between a representative number of

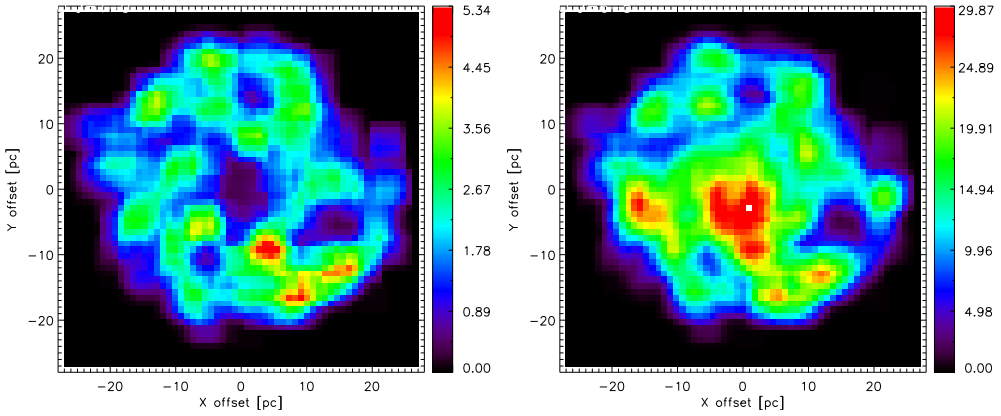

Figure 5.6: Face-on view of the flux density (in units of 10^{-15} erg s^{-1} cm^{-2}) of the CO $J = 1 \rightarrow 0$ (*left*) and CO $J = 6 \rightarrow 5$ (*right*) lines, as mapped with a single dish beam of FWHM=0.15″ (~ 0.92 pc) and adopting a distance $D = 3.82$ Mpc to the source. Note how the relatively large beam smears out the intricate structure observed in the maps with the original resolution (0.25 pc) shown in Fig. 5.5.

grid elements, and a fairly constant impinging X-ray flux at each slice.

The *top panel* of Fig. 5.7 shows the average temperature $T_{\rm HYD}$ (K) estimated in the 3-D hydrodynamical model (*solid line*) at each ΔX grid element. The corresponding average temperature $T_{\rm XDR}$ (K) obtained from the XDR chemical model is shown with a *gray line*. Only the grid elements with $T_{\rm HYD} < 10^4$ K were used in the XDR model, and they are shown with filled circles. The average $T_{\rm XDR}/T_{\rm HYD}$ ratio (*gray line + filled circles*) and the average X-ray flux (*solid black line*) F_X (erg s^{-1} cm^{-2}) are shown in the *bottom panel* of Fig. 5.7. The average relative temperature is directly related to the impinging flux at each ΔX grid element, and decreases as the X-ray flux decreases. The temperature derived from the XDR model is higher ($T_{\rm XDR}/T_{\rm HYD} > 1$) than the one estimated in the hydrodynamical model. Both temperatures tend to be equal ($T_{\rm XDR}/T_{\rm HYD} \approx 1$, *dashed line*) at radial positions where the X-ray flux decreases to $F_X \sim 1.1$ erg s^{-1} cm^{-2}. This corresponds to the inner ± 20 pc (X-axis offset) of the torus, which is consistent with an effective number (attenuation) density n_{eff} larger than 10^5 cm^{-3}, for an equivalent radiation field of $G_0 \sim 0.7 \times 10^3$ in Habing units (Schleicher et al., 2010, their Fig.2).

In the *top panel* of Fig. 5.8 the average density of molecular hydrogen $n({\rm H_2})_{\rm HYD}$ along a $64 \times 1.25 \times 1.5$ pc^3 strip volume is shown. The density estimated in the 3-D hydrodynamical model is shown by the *solid line*, and the corresponding average $n({\rm H_2})_{\rm XDR}$ density obtained from the XDR chemical model is shown with the *gray line + filled circle*. Only the data points for grid cells with $T_{\rm HYD} < 10^4$ K are shown in the figure. In this case, the relative H_2 density seems to be inversely related to the impinging flux. That is, the average $n({\rm H_2})_{\rm XDR}$ density derived from the XDR model is lower (by factors up to $\sim 10^4$) than the average H_2 density of the hydrodynamical model. This is observed in the inner ± 10 pc region around the

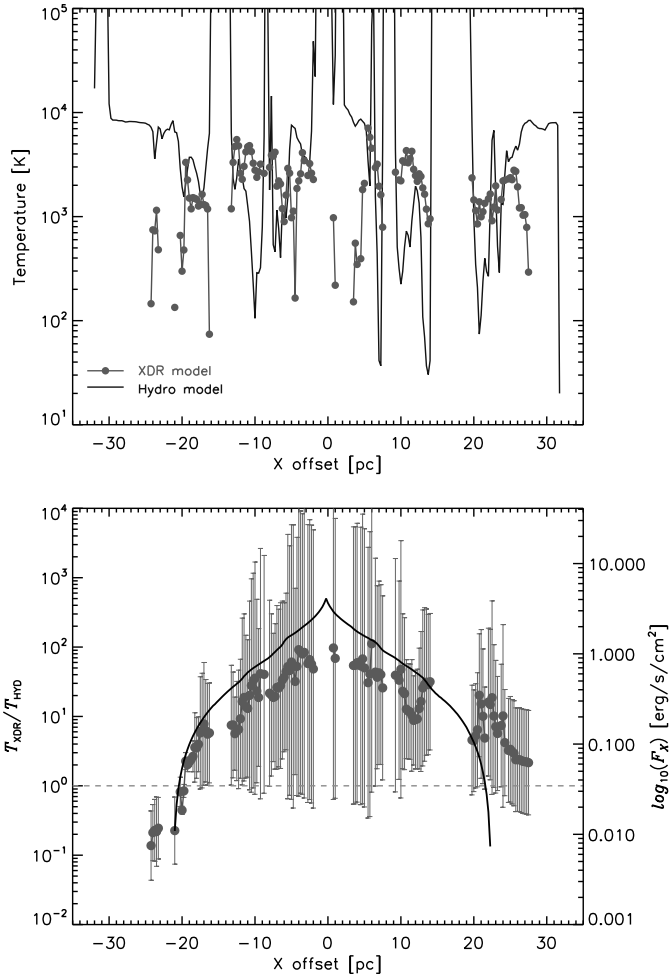

Figure 5.7: *Top panel* - Average temperature $T_{\rm HYD}$ (in units of K) of the gas along a $64 \times 1.25 \times 1.5$ pc^3 strip volume, as estimated in the 3-D hydrodynamical model (*black line*) and the corresponding average temperature $T_{\rm XDR}$ obtained from the XDR chemical model (*gray line*). The filled circles show the actual data points obtained with the XDR model in grid cells with $T_{\rm HYD} < 10^4$ K. *Bottom panel* - Average $T_{\rm XDR}/T_{\rm HYD}$ ratio (*gray line + filled circles*) and the average X-ray flux (*solid black line*) F_X (erg s^{-1} cm^{-2}) in log_{10} scale. The standard deviation at each ΔX offset is shown by the error bars. The relative average temperature is directly related to the impinging flux at each grid point. The average temperature $T_{\rm XDR}$ is predominantly higher than $T_{\rm HYD}$ in the inner ± 20 pc around the center of the AGN torus. The *dashed line* indicates where $T_{\rm XDR}/T_{\rm HYD} = 1$, which coincides with an X-ray flux of $F_X \sim 1.1$ erg s^{-1} cm^{-2}.

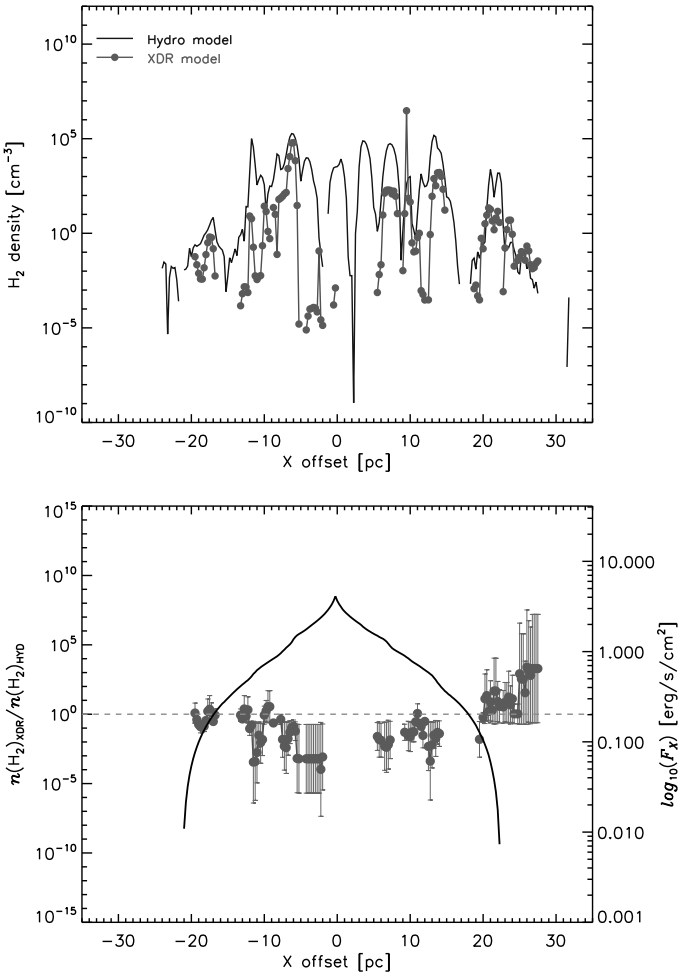

Figure 5.8: *Top panel* - Average density of molecular hydrogen $n(\mathrm{H_2})_{\mathrm{HYD}}$ (in units of cm^{-3}) of the gas along a $64 \times 1.25 \times 1.5$ pc^3 strip volume, as estimated in the 3-D hydrodynamical model (*solid line*) and the corresponding average $n(\mathrm{H_2})_{\mathrm{XDR}}$ density obtained from the XDR chemical model (*gray line + filled circle*). The filled circles show the actual data points obtained with the XDR model in grid cells with $T_{\mathrm{HYD}} < 10^4$ K. *Bottom panel* - Average $n(\mathrm{H_2})_{\mathrm{XDR}}/n(\mathrm{H_2})_{\mathrm{HYD}}$ ratio (*gray line + filled circle*) and the average X-ray flux (*solid black line*) F_X ($\mathrm{erg\ s^{-1}\ cm^{-2}}$) in log_{10} scale. The standard deviation of the relative density at each ΔX offset is shown by the error bars. The *dashed line* shows where $n(\mathrm{H_2})_{\mathrm{XDR}}/n(\mathrm{H_2})_{\mathrm{HYD}} = 1$. The relative $n(\mathrm{H_2})$ density is roughly inversely related to the impinging flux, being smaller closer (higher F_X) to the center of the AGN torus. The $n(\mathrm{H_2})_{\mathrm{XDR}}$ density is lower than $n(\mathrm{H_2})_{\mathrm{HYD}}$ across the radial distance from the center, until about $\Delta\mathrm{X} = 21$ pc, where the magnitude of the flux drops below $\sim 1\ \mathrm{erg\ s^{-1}\ cm^{-2}}$. This shift in the relation is due to the SNe that are considered in the hydrodynamical model, but not in the XDR model, which have a stronger contribution to the dissociation of the $\mathrm{H_2}$ molecular gas.

center of the AGN torus. This is mostly the consequence of relatively *thin* slabs ($N_{\rm H} < 10^{23}$ cm^{-2}) being irradiated by a rather strong ($F_X > 1.6$ erg s^{-1} cm^{-2}) X-ray flux in the proximities of the torus center, as described in Sec. 5.2.2 and shown in Fig.5.3. However, at ΔX $\sim$ 21 pc the X-ray flux dependance between H_2 and abundance is inverted. This change is explained by the SNe that are considered in the hydrodynamical model at those distances, but they are not included in the XDR model. The SNe produce a stronger dissociation of the H_2 molecular gas in the hydrodynamical model than the weakened X-ray flux in the XDR model, which allows its survival.

5.4 Final remarks and future work

Comparisons between total hydrogen column density, $N({\rm CO})$ and CO lines, suggest that the CO $J = 1 \rightarrow 0$ line is not always a good tracer of $n_{\rm H}$ in the central ($\lesssim 60$ pc) region of an AGN torus.

The average temperature derived from the XDR model can be a factor ~ 1 to ~ 100 higher than the average temperature estimated in the hydrodynamical model within a ± 20 pc radius away from the torus, where the X-ray flux decreases down to $F_X \sim 1.1$ erg s^{-1} cm^{-2}. On the other hand, the average H_2 density follows an inverse relation with the X-ray flux.

The average XDR-derived density $n(H_2)$ is lower (by factors up to $\sim 10^4$) than the average density of the hydrodynamical model in the inner ± 10 pc around the AGN. The relation between the X-ray flux and the molecular hydrogen density also depends on the non-uniform density distribution of the gas. This is consistent with the fluctuations of the column density distribution of H_2 explored by WPS09 for different viewing angles and, as expected, the largest $N(H_2)$ columns are found at a viewing angle ~ 0 (i.e., edge-on). These facts imply that molecules will tend to disappear at the central ($\lesssim 20$ pc) region. But, depending on the viewing angle, and for total hydrogen columns $\gtrsim 10^{24}$ cm^{-2} like in the case of, for instance, the ULIRG NGC 4945 (Chap. 4), molecules can survive and emission lines like, e.g., high-J CO, [C II], [Ne II] and [Ne V], can be bright.

Using the flux density maps of CO will allow us to compute the actual H_2 mass to CO $J = 1 \rightarrow 0$ luminosity ratio of our models, and to compare with the ratio given by the higher-J CO lines. We also would like to explore the morphology and distribution of the warm ionized medium traced by the [C II] 158 μm fine-structure line, estimated assuming a two-level atom system (e.g., Hollenbach et al., 1991). Its correlation with the CO $J = 1 \rightarrow 0$ can also be addressed (e.g., Crawford et al., 1985; Stacey et al., 1991).

Acknowledgements

We are grateful to Aycin Aykutalp and Seyit Hocuk for their help and advise in using the Gemini supercomputers at the Kapteyn Institute. We are also thankful

to Dieter Poelman for initial discussions and help with the original $\beta 3D$ radiative transfer code. Molecular Databases that have been helpful include the NASA/JPL, LAMDA and NIST.

APPENDIX: Rotational excitation of CO by He

We used the rate coefficients for pure rotational de-excitation of CO by collisions with He atoms reported in Cecchi-Pestellini et al. (2002). The original rate coefficients are given for the first 15 rotational levels and for ten different temperatures from 5 to 500 K. In order to extend the available rates to higher rotational levels and temperatures, we followed the methodology for linear molecules described by Schöier et al. (2005), which was used to produce the LAMDA* database.

We first extrapolated the downward collisional rate coefficients ($\Delta J = J_u \rightarrow J_l, J_u > J_l$) in temperature (up to 2000 K) using the modified version of the analytic approximation given by de Jong et al. (1975) and presented by Bieging et al. (1998):

$$\gamma_{ul} = A(\Delta J)\ y\ exp\left[-B(\Delta J)\ y^{1/4}\right] \times exp\left[-C(\Delta J)\ y^{1/2}\right], \tag{5.10}$$

where $y = \Delta E_{ul}/kT$ and the three parameters A, B, and C are determined by least-squares fits to the original set of Cecchi-Pestellini et al. (2002) rate coefficients for each ΔJ. Then we extrapolated the collisional rate coefficients to include higher rotational levels (up to $J = 40$) by fitting the rate coefficients (in natural logarithmic scale) connecting the ground rotational state to a second order polynomial

$$ln(\gamma_{J0}) = a + bJ + cJ^2, \tag{5.11}$$

with a, b, and c parameters determined from the fit, for each temperature. The Infinite Order Sudden (IOS) approximation (e.g., Goldflam et al., 1977) was used to calculate the whole matrix of state-to-state rate coefficients from the coefficients connecting the ground state γ_{L0}

$$\gamma_{JJ'} = (2J'+1) \sum_{L=|J-J'|}^{L=J+J'} (2L+1) \begin{pmatrix} J & J' & L \\ 0 & 0 & 0 \end{pmatrix}^2 \gamma_{L0}, \tag{5.12}$$

$$\text{where the term} \quad \begin{pmatrix} J & J' & L \\ 0 & 0 & 0 \end{pmatrix}, \tag{5.13}$$

is the Wigner 3-j symbol that designates the Clebsch-Gordan coefficients (e.g., Tuzun et al., 1998), and references therein). The IOS approximation provides an accurate description of the collisional rates if the rotational energy differences are small compared to the kinetic energy of the colliding molecules. In cases where this condition is not satisfied, it is possible to approximately correct for the deviations by multiplying the summation in eq.(5.12) with the adiabaticity correction factor given by Depristo et al. (1979) and McKee et al. (1982)

$$A(L,J) = \frac{6 + (\alpha L)^2}{6 + (\alpha J)^2}, \quad \text{with } \alpha = 0.13\ B_0\ l\ \left(\frac{\mu}{T}\right)^{1/2}, \tag{5.14}$$

where B_0 is the rotational constant of the colliding molecule in cm^{-3} ($B_0 = 1.9225$ cm^{-3} for CO), $l = 3$ Å is a typical scattering length, μ is the reduced mass of the colliding system in amu ($\mu \approx 3.5$ amu for CO-He), and T is the kinetic temperature.

* http://www.strw.leidenuniv.nl/~moldata/

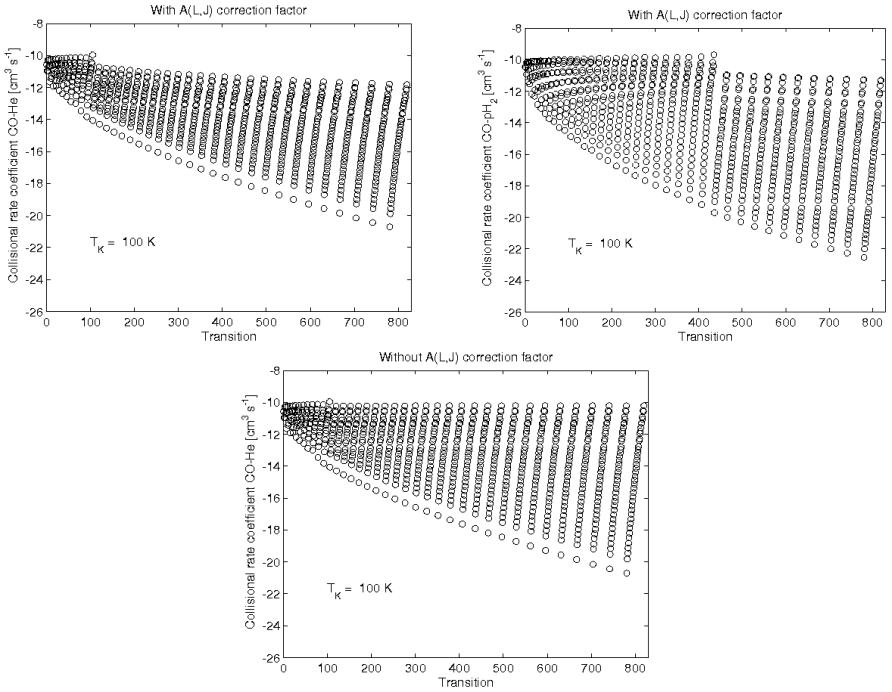

Figure 5.9: *Top left panel* - Collisional rate coefficients (cm^3 s^{-1}) for CO with para-H_2 as collision partner. *Top right panel* - Collisional rate coefficients for CO colliding with He with the wrong Wigner 3-j function. *Bottom panel* - Collisional rate coefficients for CO-He collision partners with the correct Wigner 3-j function.

However, the $A(L,J)$ correction factor should be used only if $E_L > E_J$ and $(E_L - E_J) \gg E_K$, where $E_{J,L}$ is the energy of the CO rotational levels L, J and E_K is the kinetic energy of the collision partners. The top left panel of Fig.5.9 shows the deviations introduced by the $A(L,J)$ factor when used arbitrarily to extrapolate the rate coefficients of CO colliding with He. The top right panel of Fig.5.9 shows similar discontinuities in the extrapolated rate coefficients between CO and para-H_2 presented in the current LAMDA molecular data. Similar deviations are observed for ortho-H_2. This means that the extrapolated LAMDA molecular data for CO need to be corrected. Although, the original CO-H_2 rate coefficients obtained from Flower (2001) and Wernli et al. (2006) go up to $J = 29$, and since we do not explore CO transitions above $J = 20$ we can still use the LAMDA molecular data without corrections.

In the case of the CO-He colliding system the conditions for using the $A(L,J)$ adiabaticity factor are not satisfied for the temperatures and energy levels considered here, and the IOS approximation given by eq.(5.12) yields results with 10%–15% accuracy (Goldflam et al., 1977). The final extrapolated rate coefficients used in this work for the system CO-He are shown in the bottom panel of Fig.5.9.

6

CHAMP$^+$ observations of warm gas in M17 SW

– J.P. Pérez-Beaupuits, M. Spaans, M.R. Hogerheijde, R. Güsten, A. Baryshev and W. Boland –

Sub-millimeter and Far-IR observations have shown the presence of a significant amount of warm (few hundred K) and dense ($n(\mathrm{H_2}) \geq 10^4$ cm^{-3}) gas in sources ranging from active star-forming regions to the vicinity of the Galactic center. Since the main cooling lines of the gas phase are important tracers of the interstellar medium in Galactic and extragalactic sources, proper and detailed understanding of their emission and the ambient conditions of the emitting gas, is necessary for a robust interpretation of the observations. With high resolution ($7'' - 9''$) maps ($\sim 3 \times 3$ pc^2) of mid-J molecular lines we aim to probe the physical conditions and spatial distribution of the warm (50 to several hundred K) and dense gas ($n(\mathrm{H_2}) > 10^5$ cm^{-3}) across the interface region of the nearly edge-on M17 SW nebula. We have used the dual color multiple pixel receiver CHAMP$^+$ on the APEX telescope to obtain a $5'.3 \times 4'.7$ map of the $J = 6 \rightarrow 5$ and $J = 7 \rightarrow 6$ transitions of ^{12}CO, the ^{13}CO $J = 6 \rightarrow 5$ line, and the $^3P_2 \rightarrow {}^3P_1$ 370 μm fine-structure transition of [C I] in M17 SW. LTE and non-LTE radiative transfer models are used to constrain the ambient conditions. The warm gas extends up to a distance of ~ 2.2 pc from the M17 SW ridge. The ^{13}CO $J = 6 \rightarrow 5$ and [C I] 370 μm lines have a narrower spatial extent of about 1.3 pc along a strip line at P.A=63°. The structure and distribution of the [C I] $^3P_2 \rightarrow {}^3P_1$ 370 μm map indicate that its emission arises from the interclump medium with densities on the order of 10^3 cm^{-3}. The warmest gas is located along the ridge of the cloud, close to the ionization front. An LTE approximation indicates that the excitation temperature of the embedded clumps reaches ~ 120 K. The non-LTE model suggests that the kinetic temperature at four selected positions cannot exceed 230 K in clumps of a density of $n(\mathrm{H_2}) \sim 5 \times 10^5$ cm^{-3} and that the warm ($T_k > 100$ K) and dense ($n(\mathrm{H_2}) \geq 10^4$ cm^{-3}) gas traced by the mid-J ^{12}CO lines represents just about 2% of the bulk of the molecular gas. The clump volume-filling factor ranges between 0.04 and 0.11 at these positions.

Originally published in *Astronomy & Astrophysics*, Vol. 510, A87 (2010)

6.1 Introduction

The heating and cooling balance in photon-dominated regions (PDRs) remains an active study of research. The comprehensive understanding of PDRs requires observations of large areas close to radiation sources and of a wide wavelength range covering various emissions of atoms, molecules, and grains. In particular, mid-J CO lines have been detected in almost all known massive Galactic star forming regions (e.g., Orion Nebula, W51, Cepheus A, NGC 2024). This indicates that warm ($T_K \geq 50$ K) and dense ($n(H_2) \geq 10^4$ cm^{-3}) gas is common and probably of importance in most OB star forming regions. The mid-J CO lines detected in regions like, e.g., M17, Cepheus A and W51 have relatively narrow line widths of 5–10 km s^{-1}, although not as narrow as the line widths observed in cold quiescent cloud cores.

Observations of the $J = 6 \rightarrow 5$ and $J = 7 \rightarrow 6$ transitions of ^{12}CO in several massive star forming regions indicate that the warm emitting gas is confined to narrow (< 1 pc) zones close to the ionization front. These observations favor photoelectric heating of the warm gas by UV radiation fields outside the HII regions (e.g., Harris et al., 1987; Graf et al., 1993; Yamamoto et al., 2001; Kramer et al., 2004, 2008). Nevertheless, shocks may also be an important source of heating in high velocity wing sources like Orion, W51 and W49 (Jaffe et al., 1987).

Because of its nearly edge-on geometry and the large amount of observational data available in the literature, M17 SW is one of the best Galactic regions to study the entire structure of PDRs from the exciting sources to the ionization front, and the succession (or not) of H_2, [C I] and CO emissions, as predicted by PDR models (Icke et al., 1980; Felli et al., 1984; Meixner et al., 1992; Meijerink & Spaans, 2005). M17 SW is also one of the few star-forming regions for which the magnetic field strength can be measured in the PDR interface and where the structure of the neutral and molecular gas seems to be dominated by magnetic pressure rather than by gas pressure (Pellegrini et al., 2007).

M17 SW is a giant molecular cloud at a distance of 2.2 kpc, illuminated by a highly obscured ($A_v > 10$ mag) cluster of several OB stars (among $\gtrsim 100$ stars) at about 1 pc to the east (Beetz et al., 1976; Hanson et al., 1997). It also harbours a number of candidate young stellar objects that have recently been found (Povich et al., 2009). Several studies of molecular emission, excitation and line profiles (e.g., Snell et al., 1984; Martin et al., 1984; Stutzki & Guesten, 1990) from the M17 SW core indicate that the structure of the gas is highly clumped rather than homogeneous. Emission of [C I] and [C II] was detected more than a parsec into the molecular cloud along cuts through the interface region (Keene et al., 1985; Genzel et al., 1988; Stutzki et al., 1988). These results, as well as those found in other star-forming regions like S106, the Orion Molecular Cloud, and the NGC 7023 Nebula (e.g., Gerin & Phillips, 1998; Yamamoto et al., 2001; Schneider et al., 2002, 2003; Mookerjea et al., 2003) do not agree with the atomic and molecular stratification predicted by standard steady-state PDR models. However, the extended [C I] $^3P_1 \rightarrow {}^3P_0$ and ^{13}CO $J = 2 \rightarrow 1$ emissions in S140 have been successfully explained by a stationary but clumpy PDR model (Spaans, 1996; Spaans & van Dishoeck, 1997). Hence, the lack of stratification in [C I], [C II] and CO is a result that can be

expected for inhomogeneous clouds, where each clump acts as an individual PDR. On the other hand, a partial face-on illumination of the molecular clouds would also suppress stratification.

Based on analysis of low-J lines of ^{12}CO, ^{13}CO and CH_3CCH data, the temperature towards the M17 SW cloud core has been estimated as 50–60 K, whereas the mean cloud temperature has been found to be about 30–35 K (e.g., Guesten & Fiebig, 1988; Bergin et al., 1994; Wilson et al., 1999; Howe et al., 2000; Snell et al., 2000). Temperatures of ~ 275 K have been estimated from NH_3 observations (Guesten & Fiebig, 1988) towards the VLA continuum arc, which agrees with estimates from highly excited ^{12}CO transitions (Harris et al., 1987). Multitransition CS and HC_3N observations indicate that the density at the core region of M17 SW is about 6×10^5 cm^{-3} (e.g., Snell et al., 1984; Wang et al., 1993; Bergin et al., 1996). On the other hand, densities up to 3×10^6 cm^{-3} have been estimated towards the north rim with multitransition observations of NH_3, which indicates that ammonia is coexistent with high density material traced in CS and HCN (Guesten & Fiebig, 1988). The UV radiation field G_0 has been estimated to be on the order of 10^4 in units of the ambient interstellar radiation field (1.2×10^{-4} ergs s^{-1} cm^{-1} sr^{-1}, Habing 1968; Meixner et al. 1992).

However, most of the millimeter-wave molecular observations in M17 SW are sensitive only to low temperatures (< 100 K), and the few available data of mid-J CO and [C I] lines (consisting mostly of cuts across the ionization front and observations at a few selected positions) are limited in spatial resolution and extent (e.g., Harris et al., 1987; Stutzki et al., 1988; Genzel et al., 1988; Stutzki & Guesten, 1990; Meixner et al., 1992; Graf et al., 1993; Howe et al., 2000). Therefore, in this work we present maps ($\sim 3 \times 3$ pc^2) of mid-J molecular (^{12}CO and ^{13}CO) and atomic ([C I]) gas with an excellent high resolution ($9.4'' - 7.7''$), which advances existing work in M17 SW.

The observations were done with CHAMP$^+$ (Carbon Heterodyne Array of the MPIfR) on the Atacama Pathfinder EXperiment (APEX*) (Güsten et al., 2006). The multiple pixels at two submm frequencies of CHAMP$^+$ allow the efficient mapping of ∼arcmin regions, and provide the ability to observe simultaneously the emission from the $J = 6 \rightarrow 5$ and $J = 7 \rightarrow 6$ rotational transitions of ^{12}CO at 691.473 GHz and 806.652 GHz, respectively. We also observed the $J = 6 \rightarrow 5$ transition of ^{13}CO at 661.067 GHz and the $^3P_2 \rightarrow {}^3P_1$ 370 μm (hereafter: $2 \rightarrow 1$) fine-structure transition of [C I] at 809.342 GHz.

Since the gas phase cools mainly via the atomic fine structure lines of [O I], [C II], [C I] and the rotational CO lines (e.g., Kaufman et al., 1999; Meijerink & Spaans, 2005), these carbon bearing species presented here are very important coolants in the interstellar medium (ISM) of a variety of sources in the Universe, from Galactic star forming regions, the Milky Way as a galaxy, and external galaxies up to high redshifts (e.g., Fixsen et al., 1999; Weiß et al., 2003; Kramer et al., 2005; Bayet et al., 2006; Jakob et al., 2007).

* This publication is based on data acquired with the Atacama Pathfinder Experiment (APEX). APEX is a collaboration between the Max-Planck-Institut fur Radioastronomie, the European Southern Observatory, and the Onsala Space Observatory

The case of M17 SW can be considered as a proxy for extra galactic star forming regions. M17 SW is not special, nor does it need to be, compared to other massive star-forming regions like Orion, W49, Cepheus A, or W51. Still, it does allow feedback effects, expected to be important for starburst and active galaxies, to be studied in great spatial detail. A comparison of the local line ratios to the extra-galactic regions can then shed light on the properties of massive star-forming regions that drive the energetics of active galaxies. Our results will be of great use for future high resolution observations, since molecular clouds of the size of the maps we present will be resolved by ALMA at the distance (~ 14 Mpc) of galaxies like NGC 1068.

The main purpose of this work is to explore the actual spatial distribution of the mid-J ^{12}CO and [C I] lines in M17 SW and to test the ambient conditions of the warm gas. A simple LTE model based on the ratio between the ^{12}CO and ^{13}CO$J = 6 \rightarrow 5$ lines is used to probe the temperature of the warm ($T_K \sim 100$ K) and dense ($n_{\rm H} > 10^5$ cm^{-3}) molecular gas. Then a non-LTE model is used to test the ambient conditions at four selected positions. In a follow-up work we will present an elaborate model of these high resolution data.

The most frequent references to Stutzki et al. (1988), Stutzki & Guesten (1990) and Meixner et al. (1992) will be cited as S88, SG90 and M92, respectively. The organization of this article is as follows. In Sect. 6.2 we describe the observations. The maps of the four lines observed are presented in Sect. 6.3. The modeling and analysis of the ambient conditions are presented in Sect. 6.4, and the conclusions and final remarks are presented in Sect. 6.5.

6.2 Observations

We have used the dual color heterodyne array receiver CHAMP$^+$ (Kasemann et al., 2006; Güsten et al., 2008), providing 2×7 pixels, on the APEX telescope during July 2008 to map the $J = 6 \rightarrow 5$ and $J = 7 \rightarrow 6$ lines of ^{12}CO simultaneously, and - in a second coverage - the ^{13}CO $J = 6 \rightarrow 5$ and [C I] $J = 2 \rightarrow 1$. We observed a region of about $5'.3 \times 4'.7$ (3.4 pc $\times$ 3.0 pc) in on-the-fly (OTF) slews in R.A. (~ 320 arcsec long), subsequent scans spaced by $4''$ in declination. The observations were done in total power mode, nodding the antenna prior to each OTF slew to a reference position $180''$ east of the SAO star 161357. The latter is used as a reference throughout the paper, with R.A(J2000)=18:20:27.64 and Dec(J2000)=-16:12:00.90. We used Sgr B2(N) as a reference for continuum poiting. Calibration measurements were performed regularly every ∼10 min with a cold liquid nitrogen (LN2) load and an ambient temperature load. The data were processed with the APEX real-time calibration software (Muders et al., 2006), assuming an image sideband suppression of 10 dB.

We used the Fast Fourier Transform Spectrometer (FFTS) as backend with a fixed bandwidth of 1.5 GHz and 1024 channels. We used the two IF groups of the FFTS with an offset of ± 460 MHz between them. The spectral resolution was smoothed to about 1 km s^{-1}, while the line widths are between 4 km s^{-1} and 9

$\mathrm{km\,s^{-1}}$, so they are well resolved. The on-source integration time per dump and pixel was 1 second only. However, oversampling with $4''$ spacing, all the seven pixels of CHAMP$^+$ covered a given grid position at least once. So, after adding all the subscans from both IF channels, and after convolving the maps with the corresponding beam size, the total integration time in the central $5' \times 4'$ region of the maps varied between about 50 and 80 seconds per grid cell.

The SSB system temperatures are typically about 2000 K and 6000 K respectively for the low and high frequency bands. The spatial resolution varies between $9.4''$ for the ^{13}CO $J = 6 \rightarrow 5$ transition in the low frequency band (at 661 GHz - the nominal beam at 691 GHz is $8.4''$) and $7.7''$ for the high frequency band (809 GHz). All data in the paper were converted to the line brightness temperature $T_B = \eta_f \times T_A^*/\eta_c$, using a forward efficiency (η_f) of 0.95 and beam coupling efficiencies (η_c) of 0.45 and 0.43 (at 661 GHz and 809 GHz, respectively) as determined towards Jupiter* (Güsten et al., 2008). We assumed brightness temperatures of 150 K (at 660 GHz) and 145 (at 815 GHz) for Jupiter (Griffin et al., 1986). This coupling efficiency was chosen because in velocity-space (velocity channels) the size of the M17 clumps is Jupiter-like, which had a size $\sim 38.7''$ at the time of the observations. The calibrated data were reduced with the GILDAS† package CLASS90.

6.3 Results

6.3.1 Integrated line temperature maps

Figure 6.1 shows the maps of the temperatures, integrated between 5 $\mathrm{km\,s^{-1}}$ and 35 $\mathrm{km\,s^{-1}}$, of ^{12}CO $J = 6 \rightarrow 5$ (*top*) with the contour lines of ^{12}CO $J = 7 \rightarrow 6$, and the velocity integrated temperature of ^{13}CO $J = 6 \rightarrow 5$ (*bottom*) with the contour lines corresponding to [C I] $J = 2 \rightarrow 1$. All the maps were convolved to the largest beam size ($9.4''$) of the ^{13}CO $J = 6 \rightarrow 5$ line, obtaining a grid size of about $4.7'' \times 4.7''$. The peak integrated temperatures of the ^{12}CO $J = 6 \rightarrow 5$ and $J = 7 \rightarrow 6$ lines are 852 K $\mathrm{km\,s^{-1}}$ and 925 K $\mathrm{km\,s^{-1}}$ respectively. These lines follow a similar spatial distribution. The peak integrated temperatures of ^{13}CO $J = 6 \rightarrow 5$ and [C I] $J = 2 \rightarrow 1$ are 420 K and 282 K. respectively, and the peak of [C I] is shifted towards the inner side of the interface region at about 0.55 pc ($\sim 50''$). The ionization front traced by the high resolution ($10'' \times 7''$) map of the 21 cm continuum emission (Brogan & Troland, 2001) as well as the ionizing stars identified by Beetz et al. (1976) and Hanson et al. (1997) are shown in Fig. 6.2, with ^{12}CO $J = 6 \rightarrow 5$ (white contour lines) and [C I] $J = 2 \rightarrow 1$ (green contour lines) overlaid. The transition between the hot ($T_k > 300$ K) atomic gas and the warm ($T_k > 100$ K) molecular gas can be seen due to the almost edge-on geometry of M17 SW.

The *left panel* of Fig. 6.3 shows the variation of the integrated temperature of all the lines across the ionization front (strip line at P.A=90° in Fig. 6.1). Due to the limited S/N the ^{12}CO $J = 7 \rightarrow 6$ and [C I] $J = 2 \rightarrow 1$ strip lines have been

* http://www.mpifr.de/div/submmtech/heterodyne/champplus/ champmain.html
† http://www.iram.fr/IRAMFR/GILDAS

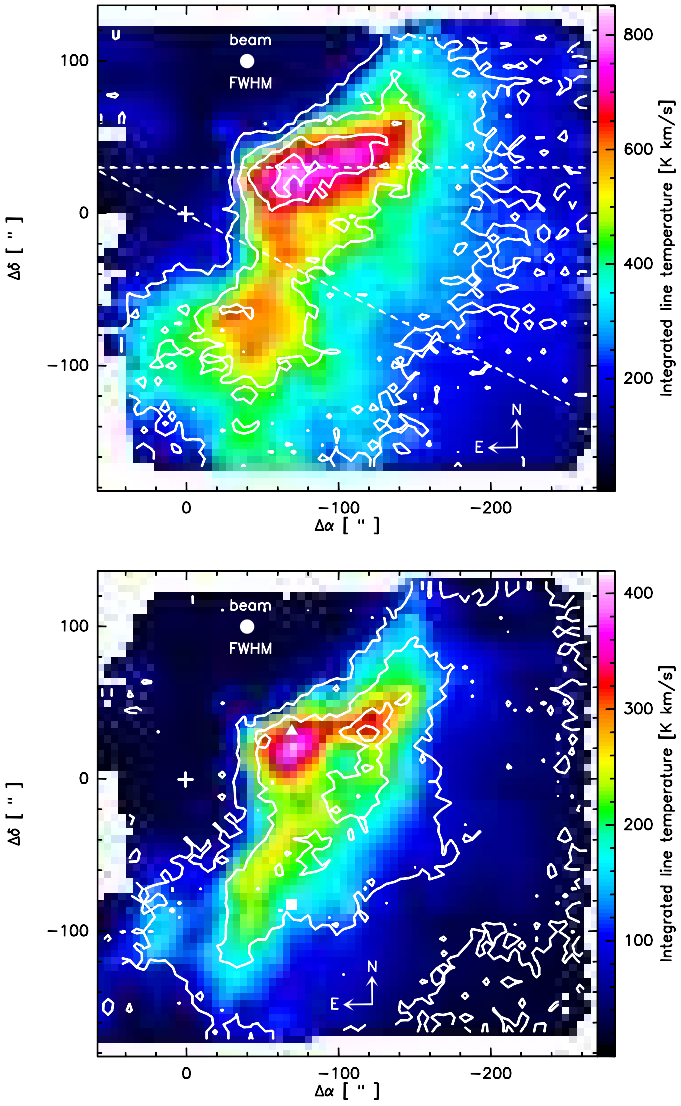

Figure 6.1: *Top* - Color map of the integrated temperature of ^{12}CO $J = 6 \rightarrow 5$ in M17 SW. The contour lines correspond to the ^{12}CO $J = 7 \rightarrow 6$, which has a peak emission of 925 K km s^{-1}. The countour levels are the 25%, 50%, 75% and 90% of the peak emission. Dashed lines correspond to the E-W and NE-SW strip lines at PA=90° and PA=63°, respectively. *Bottom* - Color map of the integrated temperature of ^{13}CO $J = 6 \rightarrow 5$ and the contour levels (as described before) of [C I] $J = 2 \rightarrow 1$ with a peak emission of 282 K km s^{-1}. The filled *triangle* and *square* mark selected positions where ambient conditions are estimated from. The reference position ($\Delta\alpha = 0$, $\Delta\delta = 0$), marked with a cross, corresponds to the SAO star 161357 at R.A(J2000)=18:20:27.6483 and Dec(J2000)=-16:12:00.9077.

smoothed spatially with respect to the strip direction. The [C I] $J = 2 \rightarrow 1$ line starts peaking up at about 0.1 pc ($\sim 10''$) after the molecular lines and presents a smooth transition towards the inner part of the cloud, forming a plateau at about

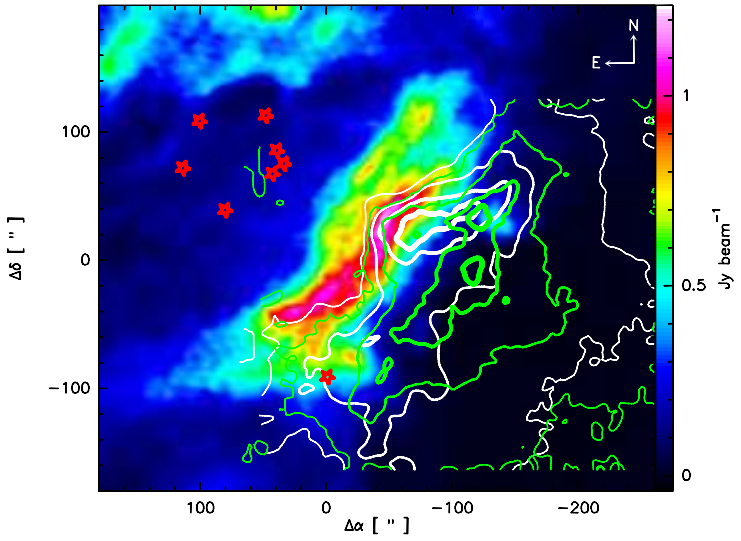

Figure 6.2: Color map of the 21 cm continuum emission (Jy beam^{-1}) in M17 SW with a $10'' \times 7''$ resolution by Brogan & Troland (2001). The *white* contour lines correspond to the ^{12}CO $J = 6 \rightarrow 5$ with a peak emission of 830 K km s^{-1}, while the *green* contour lines correspond to the [C I] $J = 2 \rightarrow 1$ with a peak emission of 260 K km s^{-1}. The countour levels (from thin to thick) are the 25%, 50%, 75% and 90% of the peak emission. The *red stars* indicate the O and B ionizing stars (Beetz et al., 1976; Hanson et al., 1997). The reference position ($\Delta\alpha = 0$, $\Delta\delta = 0$) is the same as in Fig 6.1. These ^{12}CO and [C I] maps have a slightly lower integrated temperature than in Fig. 6.1 because they were convolved with a $20''$ beam to smooth the contour lines.

$\Delta\alpha = -100''$, from where it increases its emission until the peak is reached at about $\Delta\alpha = -120''$. The peak of [C I] correlates with a secondary peak seen in ^{13}CO. However, the main peak emission of the latter correlates with the peak of the ^{12}CO lines along this strip line.

The strip line at P.A.=63° (*right panel* of Fig. 6.3) can be compared with Fig.5 in M92, and Fig.2 in S88. At this position angle, there is no marked plateau in the [C I] emission, and the peak of the [C I] line is closer to the peaks of the ^{12}CO and ^{13}CO lines. The dip in ^{12}CO $J = 2 \rightarrow 1$ at about $\Delta\alpha = -120''$ is an artifact. The integrated temperature of the ^{12}CO $J = 2 \rightarrow 1$, $J = 6 \rightarrow 5$ and $J = 7 \rightarrow 6$ lines have a comparable strength deep ($\Delta\alpha > -160''$) into the M17 SW complex.

6.3.2 The complex internal structure of M17 SW

Figure 6.4 shows the spectra at selected positions along the NE-SW strip line at P.A. 63°. The main-beam temperature of the spectra is shifted by 70 K at each offset position. This set of spectra can be compared with the ^{12}CO and C^{18}O $J = 2 \rightarrow 1$ spectra along the same strip line of Fig.8 in S88. The warm gas ($T_K > 50$ K), traced by the mid-J ^{12}CO lines, is as extended as the cold gas ($T_K < 50$ K) traced by the ^{12}CO$J = 2 \rightarrow 1$ line deeper into the cloud. On the other hand, the ^{13}CO $J = 6 \rightarrow 5$ and [C I] $J = 2 \rightarrow 1$ lines are strongly detected in a narrower spatial extent of about

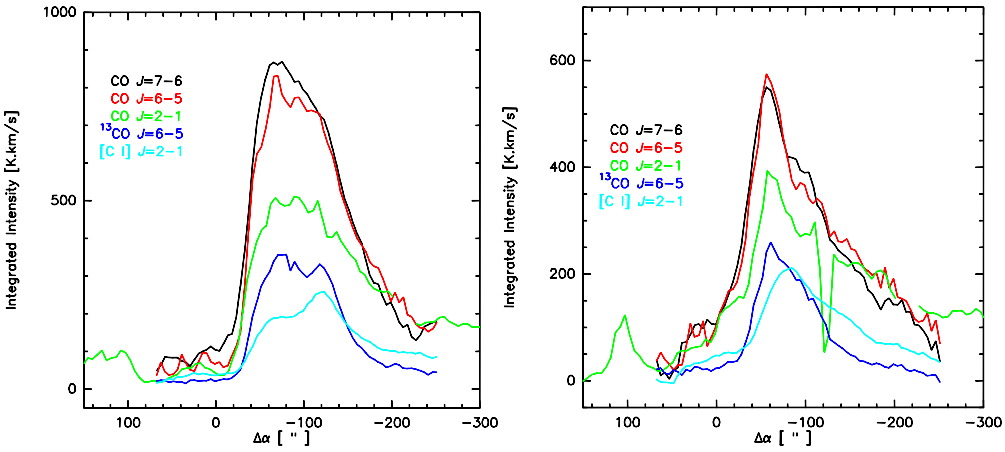

Figure 6.3: *Left panel* - Strip lines of the velocity integrated intensities of ^{12}CO J=7–6 (black), ^{12}CO J=6–5 (red), ^{12}CO J=2–1 (green) (adapted from S88), ^{13}CO J=6–5 (blue) and [C I] J=2–1 (cyan) at $\Delta\delta = 30''$ (P.A. 90°) across the ionization front of M17 SW. *Right panel* - Strip lines at P.A. 63° ($\Delta\delta = \Delta\alpha/2$). The X-axis corresponds to the actual offset in R.A. of the maps shown in Fig. 6.1. Hence, $\Delta\alpha = 0''$ is the R.A. of the reference illuminating star SAO 161357.

1.3 pc, similar to the extent of the C^{18}O $J = 2 \rightarrow 1$ emission.

Multilevel molecular line observations in CS, ^{12}CO, ^{13}CO and C^{18}O and in several fine structure lines ([C I], [C II], [Si II],[O I]) indicate that M17 SW consists of numerous high density clumps ($n(\mathrm{H_2}) > 10^4$ cm^{-3}) from which the [O I], [Si II] and mid-J CO lines emanate. This dense gas is found within a relatively warm (~ 50 K) and less dense ($n(\mathrm{H_2}) \sim 3 \times 10^3$ cm^{-3}) molecular gas (interclump medium), which in turn is surrounded by a diffuse halo ($n(\mathrm{H_2}) \sim 300$ cm^{-3}) which is the source of the very extended [C I] and [C II] emission (Snell et al., 1984, 1986; Evans et al., 1987, S88, SG90, M92).

From the C^{18}O observations in M17 SW a beam-averaged ($13''$) column density of $\sim 8 \times 10^{23}$ cm^{-2} has been estimated for the cloud core and masses in the range $\sim 10 - 2000\ M_\odot$ for the CO clumps (SG90). A comparable mass range ($\sim 10 - 120\ M_\odot$) was lately estimated from submillimeter continuum observations in the northern part of M17 (Reid & Wilson, 2006), although the region mapped by Reid & Wilson (2006) adjoins, but does not overlap with M17 SW.

Figure 6.5 shows representative velocity channel maps of the ^{12}CO $J = 6 \rightarrow 5$ (*top left*) and $J = 7 \rightarrow 6$ (*top right*) lines in M17 SW. These are the main-beam brightness temperatures averaged over two and three velocity channels between 18.2 km s^{-1} and 19.9 km s^{-1}. These are similar to the velocity channels shown in Fig.3 by SG90. The fact that the C^{18}O $J = 2 \rightarrow 1$ line traces colder ($T_K < 50$ K) and less dense ($n_H \sim 3 \times 10^3$ cm^{-3}) gas than the ^{12}CO lines is reflected in the different velocity integrated maps (Fig. 6.1) and in the channel maps of these lines. In theory the critical densities (at $T_K = 100$ K) of the ^{12}CO $J = 6 \rightarrow 5$ and $J = 7 \rightarrow 6$ lines are $n_{crit} \sim 2.7 \times 10^5$ cm^{-3} and $n_{crit} \sim 4.4 \times 10^5$ cm^{-3}, respectively, which corresponds to a difference of a factor ~ 1.6. However, this difference is not directly translated

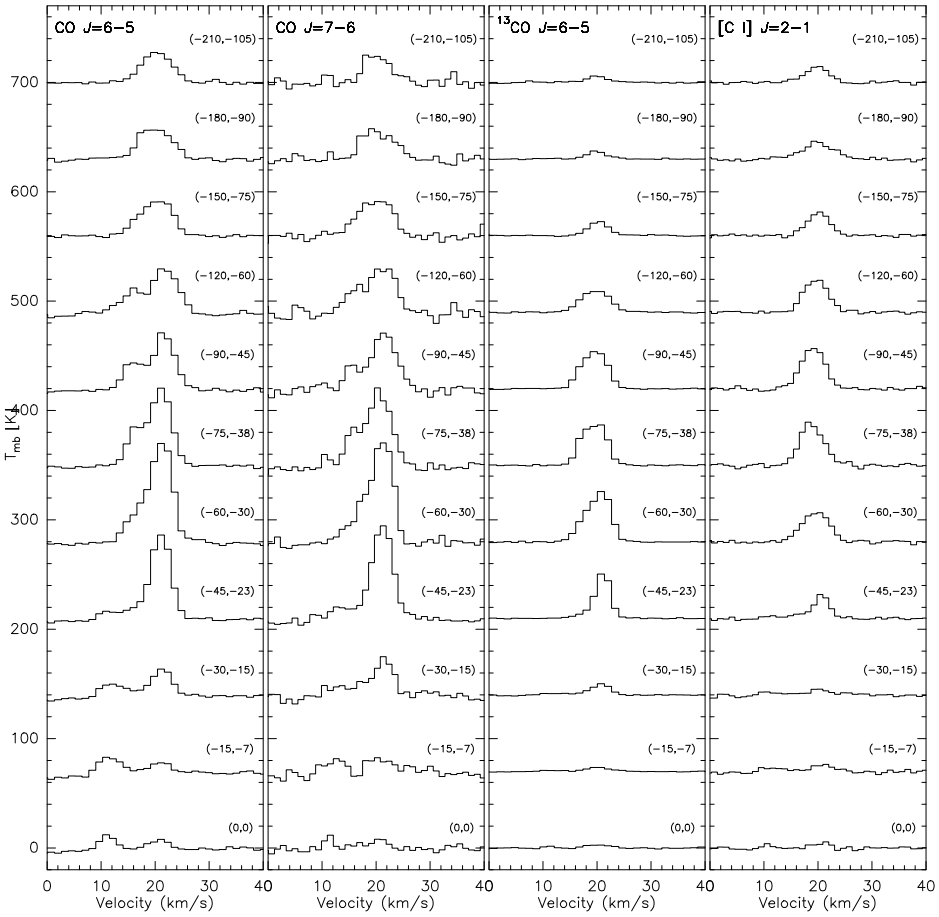

Figure 6.4: Selected spectra of ^{12}CO $J = 6 \rightarrow 5$, ^{12}CO $J = 7 \rightarrow 6$, ^{13}CO $J = 6 \rightarrow 5$ and [C I] $J = 2 \rightarrow 1$ along the NE-SW strip line (see Fig. 6.1). The positions in arcsecs are the offsets with respect to the reference position at R.A(J2000)=18:20:27.6483 and Dec(J2000)=-16:12:00.9077. The spectra are the average spectra within $\pm 2''$ of the indicated offset positions and smoothed to 1 $\mathrm{km\,s^{-1}}$ velocity resolution.

into a different clumpyness. This is reflected in the similar clumpy structure seen in the channel maps of these mid-J ^{12}CO lines.

Even though the critical density of the ^{13}CO $J = 6 \rightarrow 5$ line is similar to that of the ^{12}CO ($n_{crit} \sim 2.4 \times 10^5$ $\mathrm{cm^{-3}}$) the south-east region of its channel map (*bottom left*) differs from that seen with the ^{12}CO lines. This could be due to a change in the temperature of the gas, or to a variation in the ^{13}CO column density in that region. Since ^{13}CO is much more optically thin than ^{12}CO (abundance ratio of about $50 - 70$), this difference in the map can be expected. In Sections 6.4.2 and 6.4.3 we discuss the optical depths.

On the other hand, the [C I] $J = 2 \rightarrow 1$ channel map (*bottom right*) shows a

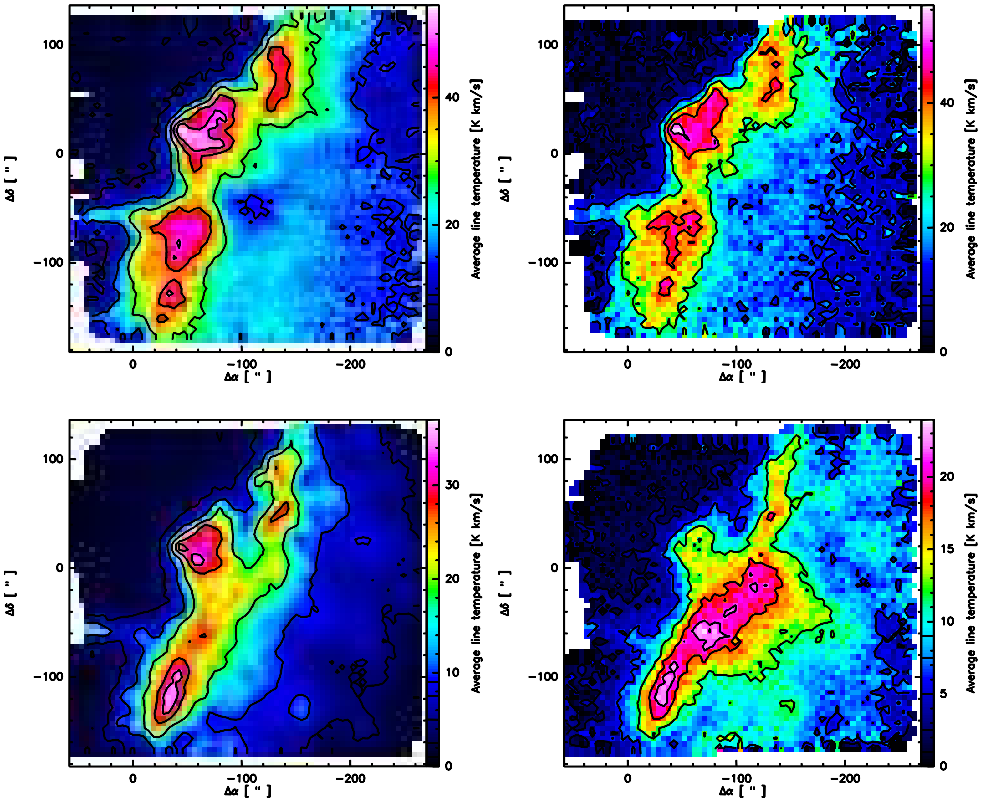

Figure 6.5: *Top panel* - Channel maps of the main-beam brightness temperature of ^{12}CO $J = 6 \rightarrow 5$ (*left*) and $J = 7 \rightarrow 6$ (*right*) averaged over two and three velocity channels, between 18.2–19.9 $\mathrm{km\,s^{-1}}$, respectively. The contour lines are as described in Fig.1, with peak-integrated line temperatures of 54.5 $\mathrm{K\,km\,s^{-1}}$ and 55.7 $\mathrm{K\,km\,s^{-1}}$ for the $J = 6 \rightarrow 5$ and $J = 7 \rightarrow 6$ lines, respectively. *Bottom panel* - Channel maps of ^{13}CO $J = 6 \rightarrow 5$ (*left*) and [C I] $J = 2 \rightarrow 1$ (*right*), averaged over two velocity channels between 18.4–19.7 $\mathrm{km\,s^{-1}}$. Contours are as in the top panel, and the peak-integrated line temperatures are 37.0 $\mathrm{K\,km\,s^{-1}}$ and 23.9 $\mathrm{K\,km\,s^{-1}}$.

completely different structure and distribution than the ^{12}CO and the isotope lines. Since the critical density of this line is about 2.8×10^3 $\mathrm{cm^{-3}}$, its emission is likely emerging partly from the interclump medium mentioned above.

6.4 Discussion

6.4.1 Self-absorption in the mid-J ^{12}CO lines?

The complex structure of the ^{12}CO $J = 1 \rightarrow 0$, $J = 2 \rightarrow 1$, and $J = 3 \rightarrow 2$ line profiles has been attributed to strong self-absorption effects (e.g., Rainey et al., 1987; Stutzki et al., 1988). Martin et al. (1984) also reported a flat topped spectrum of ^{12}CO $J = 3 \rightarrow 2$, attributed to self-absorption or saturation at velocities near the

line center and gave details about the effects of macroturbulent clumpy medium in the line profiles.

A double peaked structure in the ^{13}CO $J = 1 \rightarrow 0$ line was also reported by Lada (1976). Rainey et al. considered that this double peaked structure in ^{13}CO suggests that either this line is optically thick or that the double peaked structure is due to more than one cloud component. The latter is the interpretation favored by Rainey et al. in view of the available data at that time.

Phillips et al. (1981) presented a self-absorption LTE model that considers a ^{12}CO cloud of uniform temperature T_k in front of a hot background source of a temperature T_{bg}, at the same central velocity. The velocity dispersion of the background cloud is considered to be larger than that of the foreground cloud, so the self-absorption effect is seen mostly at the line center. This model indicates that, depending on the total column density of ^{12}CO, the self-absorption effect will be stronger in the $J = 2 \rightarrow 1$ and $J = 3 \rightarrow 2$ lines than in the $J = 1 \rightarrow 0$ line, with decreasing intensity as the transition number J increases. This is indeed observed in Fig.12 of S88 for the ^{12}CO $J = 4 \rightarrow 3$, $J = 3 \rightarrow 2$, $J = 2 \rightarrow 1$, and $J = 1 \rightarrow 0$ lines.

We reproduced the model by Phillips et al., including the higher-J lines of ^{12}CO. The *top panel* of Fig. 6.6 shows the model with the same background and foreground temperatures used by Phillips et al.. This model implies that, for a background temperature $T_{bg} = 64$ K and a foreground kinetic temperature $T_k = 15$ K, the lower-J lines (J=1,2,3,4) of the background cloud start showing self-absorption at the line center for lower column densities ($N/\Delta V$ = 10^{14} - 10^{15} cm^{-2} km s^{-1}). Instead, the higher-J lines (J=5,6,7) need larger columns ($N/\Delta V$ = 10^{15} - 10^{17} cm^{-2} km s^{-1}) in order to be affected by self-absorption. For a velocity dispersion of $\Delta V = 5$ km s^{-1}, the upper limits of these ^{12}CO columns would correspond to extinctions A_v of ~ 0.1 mag and ~ 10 mag, respectively.

The *bottom panel* of of Fig. 6.6 shows the model for a background temperature $T_{bg} = 150$ K and a foreground temperature $T_k = 30$ K (from S88). In this case the lower-J lines show self-absorption at the same range of columns as before, while the higher-J lines start showing self-absorption at a narrower range of columns ($N/\Delta V$=10^{15} - 10^{16} cm^{-2} km s^{-1}). A remarkable characteristic of these models (top and bottom panels of Fig. 6.6) is that all the J lines are expected to be strongly self-absorbed at columns larger than 10^{18} cm^{-2} km s^{-1}, which is similar to the column density estimated by S88. Another characteristic is that the ^{12}CO emission of the higher-J lines are also expected to decrease with the transition number J, and be weaker than the low-J lines. However, the ^{12}CO $J = 7 \rightarrow 6$ line seems to break this rule, as can be seen in fig.12 of S88. The high peak temperature observed in the ^{12}CO $J = 7 \rightarrow 6$ line is missing in the lower-J lines. Even considering a calibration uncertainty of 20%, the ^{12}CO $J = 7 \rightarrow 6$ line (observed at offset position $(-100'', 0'')$, bottom panel of Fig.12 in S88) will be as strong as the $J = 4 \rightarrow 3$ line (at least at the peak intensity) but still stronger than the $J = 2 \rightarrow 1$ line.

On the other hand, the ^{12}CO $J = 7 \rightarrow 6$ line seems to be asymmetric, with a *left shoulder* weaker than the *right shoulder*, which may be due to self-absorption produced by a colder foreground cloud with slightly lower center velocity than the

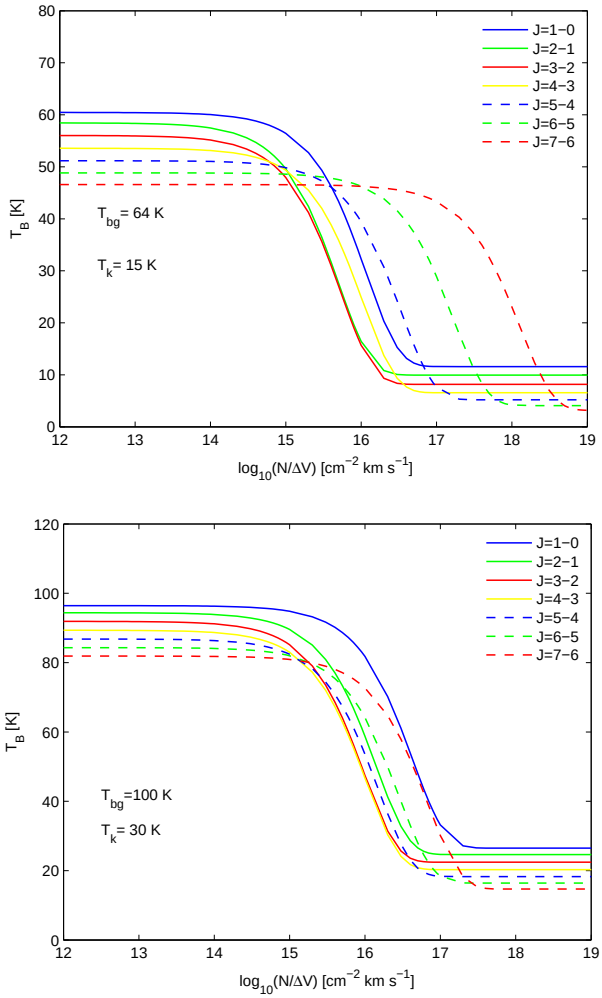

Figure 6.6: *Top panel* - Expected brightness temperature at the center of the ^{12}CO lines for a warm background cloud with a temperature $T_{bg} = 64$ K and a colder foreground-absorbing cloud with a temperature $T_k = 15$ K. *Bottom panel* - Same as in the top panel, but for a background temperature $T_{bg} = 100$ K and a foreground temperature of $T_k = 30$ K.

warmer clump traced by the $J = 7 \rightarrow 6$ line. However, that weaker left shoulder of the mid-J line is still brighter than the corresponding shoulder of the lower-J lines, in most of the velocity range and in both positions $(-100'', 0'')$ and $(-60'', -30'')$ - assuming a low ($< 10\%$) uncertainty in the calibration of the data. This is not what would be expected in the self-absorption scenario proposed by Phillips et al. (1981).

Figure 6.4 shows that the ^{13}CO $J = 6 \rightarrow 5$ line has a similar asymmetry as the ^{12}CO lines, at positions $(-45'', -23'')$ and $(-60'', -30'')$. But it shows only one component at the other positions. This difference may be related to a gradient in the temperature (or total column density) of the foreground cloud that produces self-absorption in the first two positions, but not in the others. Instead, [C I] $J = 2 \rightarrow 1$ shows similar asymmetry as ^{12}CO at positions $(-45'', -23'')$, $(-150'', -75'')$ and $(-180'', -90'')$, and an opposite asymmetry at position $(-75'', -38'')$. Given that there is no strong evidence for self-absorption in neither the ^{13}CO lines nor in the [C I] lines and that the ^{13}CO lines are mostly optically thin, it is unlikely that the observed asymmetries of the ^{13}CO and [C I] lines are produced by self-absorption. Hence, we agree with Rainey et al. (1987) in that this complex structure is more likely due to more than one kinematical component along the line of sight. And this could also be the case for the mid-J ^{12}CO lines.

Therefore, the observational facts and the models suggest that the self absorption effect, if present, should have little impact on the mid-J lines, and a few cloud components at different central velocities could also explain the complex structure of the line profiles. The asymmetry of the profiles suggests that self-absorption affects mostly one wing of the line profile, while the peak temperatures seems to be the least affected velocity channel in the mid-J lines. Hence, in the following sections we test the ambient conditions of the warm gas based on the ratios between the peak main-beam temperatures of the ^{12}CO and ^{13}CO $J = 6 \rightarrow 5$ and $J = 7 \rightarrow 6$ lines.

6.4.2 Optical depth and excitation temperature (LTE)

Since we have the maps of the ^{12}CO and the ^{13}CO $J = 6 \rightarrow 5$ lines, we can estimate the optical depth and the excitation temperature of these lines, assuming local thermal equilibrium (LTE), from the ratio between their peak main-beam temperature T_{mb} observed between the 5 $\mathrm{km\,s^{-1}}$ and 35 $\mathrm{km\,s^{-1}}$ velocity channels. This will provide at least a lower limit for the kinetic temperature in M17 SW. Then we will estimate the ambient conditions at four selected positions based on a non-LTE model of the ratio between the peak T_{mb} temperatures of the ^{12}CO $J = 6 \rightarrow 5$ and $J = 7 \rightarrow 6$ lines (hereafter referred as ^{12}CO $\frac{7-6}{6-5}$ line ratio). The temperature and densities obtained in this way will be compared to those values estimated in previous work.

In LTE the radiation temperature can be approximated (e.g., Kutner, 1984; Bergin et al., 1994) by the expression:

$$T_R = [J_\nu(T_{ex}) - J_{\mathrm{bg}}][1 - e^{-\tau_\nu}], \tag{6.1}$$

where the term $J_\nu(T)$ is the Planck's function evaluated at a frequency ν and temperature T, and multiplied by the factor $\frac{\lambda^2}{2k}$ to obtain the intensity in K. So it is defined as:

$$J_\nu(T) = \frac{h\nu/k}{e^{h\nu/kT} - 1}. \tag{6.2}$$

We use the full $J_\nu(T)$ function since the Rayleigh-Jeans (R-J) approximation (commonly applied when $h\nu \ll kT$) does not hold for the high frequency lines studied in this work. For the R-J approximation to be true, we require $T \gg 300$ K, which is a much higher temperature than what we expect to trace with our observations.

The background radiation $J_{\rm bg}$ is a composite between the cosmic microwave background radiation (CMB), as a blackbody function at 2.73 K, and the diluted infrared radiation remitted by dust. That is:

$$J_{\rm bg} = J_\nu(2.73) + \tau_d J_\nu(T_d), \tag{6.3}$$

where τ_d is the effective optical depth of the warm surface layer, adopted from Hollenbach et al. (1991), and it is defined as $\tau_d = \tau_{100\mu{\rm m}}(100\mu{\rm m}/\lambda)$. For M17 SW we adopted an emission optical depth at 100 μm of $\tau_{100\mu{\rm m}} = 0.106$ and the average dust temperature $T_d = 50$ K from M92. We tried both, with and without the dust contribution to the background radiation, and we found that the contribution of the radiation by dust continuum emission is negligible at frequencies on the order of 690 GHz and 810 GHz. Nevertheless, all the following analysis includes the dust contribution for completeness.

For extended (resolved) sources like the clumps in M17 SW, the radiation temperature is well estimated by the observed main-beam brightness temperature T_{mb}. Hence, we use that quantity in the following analysis. From the LTE approximation we can assume that the excitation temperatures T_{ex} of ^{12}CO and ^{13}CO $J = 6 \rightarrow 5$ are the same, although the terms $J_\nu(T_{ex})$ are not exactly the same because of the slightly (~ 4%) different frequencies of the ^{12}CO and ^{13}CO lines. So, from equation (6.1) the ratio between ^{12}CO and ^{13}CO can be approximated as:

$$\frac{T_{mb}(^{12}{\rm CO}\ J=6-5)}{T_{mb}(^{13}{\rm CO}\ J=6-5)} \approx \frac{1 - e^{-\tau(^{12}{\rm CO}\ J=6-5)}}{1 - e^{-\tau(^{13}{\rm CO}\ J=6-5)}}, \tag{6.4}$$

Following the work by Wilson et al. (1999), we adopt a constant [^{12}CO/^{13}CO] abundance ratio of 50 for M17 SW, which is approximately the value measured at a similar Galactic radius towards the W51 region (Langer & Penzias, 1990). Assuming that the optical depth is proportional to the total column density of the molecules and, hence, to the abundance ratio between them, we can estimate that $\tau(^{12}{\rm CO}) \approx 50\tau(^{13}{\rm CO})$. The ^{13}CO line is usually optically thin, so $\tau(^{13}{\rm CO})$ could be taken out of the exponential in Eq. 6.4 and estimated directly. However, we do not really know if this holds true for the entire M17 SW region, so we do not apply further approximations and we solve Eq. 6.4 for $\tau(^{13}{\rm CO})$ with a numerical method (Newton-Raphson).

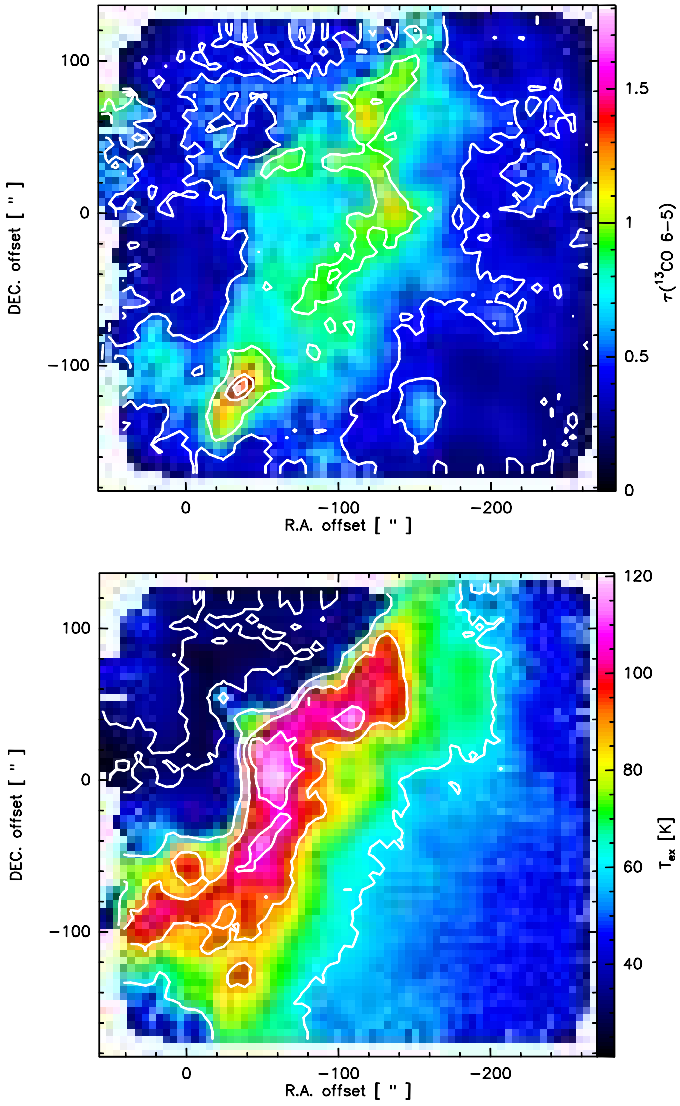

Figure 6.7: LTE approximation of the optical depth (*top*) of the ^{13}CO $J = 6 \rightarrow 5$ and the excitation temperature (*bottom*) of the ^{13}CO and ^{12}CO $J = 6 \rightarrow 5$ lines in M17 SW. Contours are the 10%, 25%, 50%, 75% and 90% of the peak value, which is 1.9 for $\tau(^{13}\mathrm{CO}\ 6-5)$ and 120 K for T_{ex}.

The *top panel* in Fig. 6.7 shows the $\tau(^{13}\mathrm{CO})$ map. The ^{13}COline is optically thin in most of the region, with some optically thick spots (e.g., $\Delta\alpha = -30, \Delta\delta = -110$). Knowing $\tau(^{13}\mathrm{CO})$ we can estimate T_{ex} from equation (6.2) using either tracer, considering that the T_{ex} estimated using ^{12}CO is just $\sim 0.6\%$ higher than that estimated using ^{13}CO. The T_{ex} map is shown in the *bottom panel* of Fig. 6.7. This map indicates that the warmest gas is located along the ridge of the cloud,

close to the ionization front. The temperature in this region ranges between 40 and 120 K, and the peak temperature is located at around ($\Delta\alpha = -60, \Delta\delta = 10$). If we consider only the gas with temperatures ≥ 80 K, the warm gas would be confined to a zone of about $40''$ (~ 0.44 pc) next to, and along, the HII region, which agrees with previous results found by Graf et al. (1993). If the gas were thermalized, this could be the actual map of the kinetic temperature of the gas. Otherwise, the T_{ex} map can be considered as a lower limit of T_K. Since in velocity space the clumps cover the whole beam, this would imply that the ^{12}CO and ^{13}CO molecules are subthermal in the $J = 6 \rightarrow 5$ transition. That is, the density of the gas and the column density of ^{12}CO and ^{13}CO may be insufficient to thermalize these transitions. A more detailed analysis is presented in the next section.

6.4.3 Ambient condition at selected positions (non-LTE)

Figure 6.8 shows the spectra of all the observed lines extracted at four different positions in the map. The *top panel* shows the spectra observed at position A ($\Delta\alpha = -70'', \Delta\delta = +32''$), close to the peak emission of the ^{12}CO lines. All the lines show a double component structure with the secondary component peaking at ~ 25 $\mathrm{km\,s^{-1}}$. The *middle top panel* shows the spectra at position B ($\Delta\alpha = -70'', \Delta\delta = -82''$), where the velocity-integrated temperature corresponds to about 50% of the peak emission. Here only the ^{12}CO $J = 7 \rightarrow 6$ line seems to have a dip at the line center. However, because of the low S/N in the high frequency band, this dip may be likely due to noise. The *middle bottom panel* shows the spectra at position C ($\Delta\alpha = -60'', \Delta\delta = -30''$), which corresponds to the peak of the NE–SW strip scan reported in S88 and Graf et al. (1993), with beams of $40''$ and $8''$, respectively. The *bottom panel* shows the spectra at position D ($\Delta\alpha = -100'', \Delta\delta = 0''$), which is close to the continuum far-IR peak, also reported in S88. Since we do not have dedicated observations at these positions, we extracted the spectra from the nearest pixels in our maps, convolved to the largest beam ($9.4''$) of the ^{13}CO $J = 6 \rightarrow 5$ line. So the spectra shown in Fig. 6.8 are the convolved spectra centered within $\pm 1''$ of the indicated coordinates. This is justified because we have oversampled data.

Table 6.1 shows the Gaussian fits of the spectra obtained at the four selected positions. Two Gaussian components were needed to fit the lines, except at position B, where only one component was used. The main components of the ^{12}CO lines have a line width that is about 8–9 $\mathrm{km\,s^{-1}}$ at position A, while the ^{13}CO has a line width of about 3 $\mathrm{km\,s^{-1}}$ narrower. The [C I] line is the narrowest line, with a line width of ~ 4 $\mathrm{km\,s^{-1}}$. At position B, the ^{12}CO lines are the widest of the four lines with about 8 $\mathrm{km\,s^{-1}}$ and the ^{13}CO and [C I] lines have about half the line width of the ^{12}CO lines. At position C and D the Gaussian parameters of the ^{12}CO $J = 7 \rightarrow 6$ presented uncertainties of $\sim 50\%$ when let free in the fitting. However, because the line shape of the ^{12}CO $J = 7 \rightarrow 6$ and $J = 6 \rightarrow 5$ transitions are very similar, we set the line width of the $J = 7 \rightarrow 6$ transition to the value found for the $J = 6 \rightarrow 5$ line. The line width of the main components of the ^{12}CO lines at position C and D are ~ 6 $\mathrm{km\,s^{-1}}$, that is about 2 $\mathrm{km\,s^{-1}}$ narrower than the lines observed at positions A and B. This difference can be due to a higher optical depth towards the latter

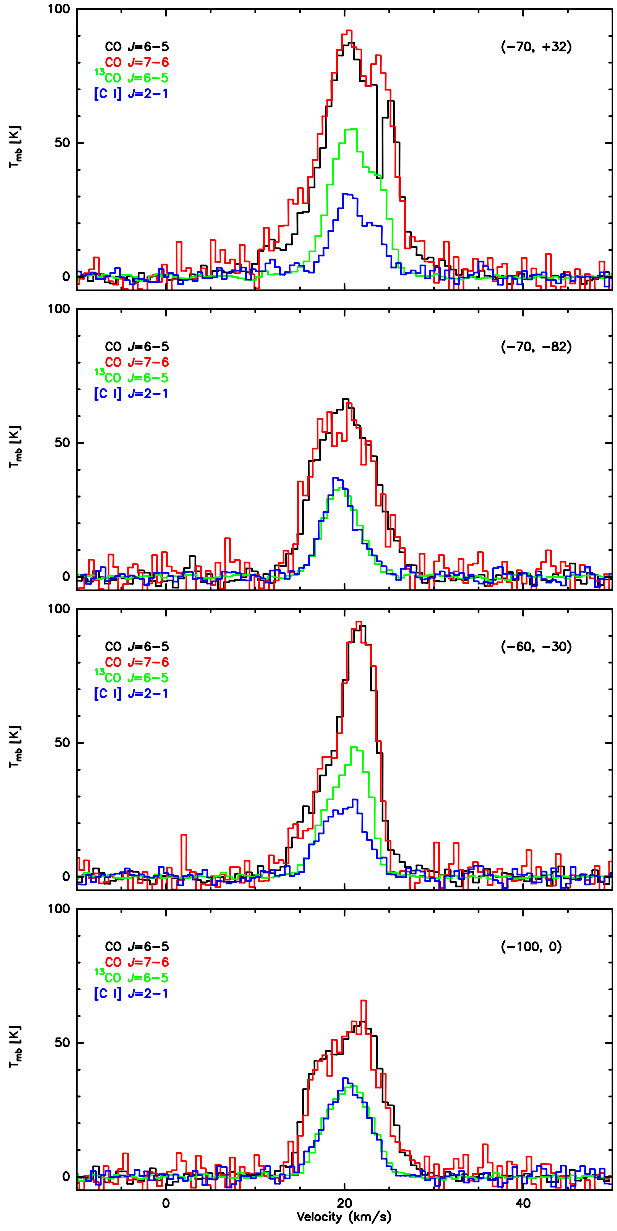

Figure 6.8: *Top* - Spectra of the four lines observed in M17 SW at position A ($\Delta\alpha = -70'', \Delta\delta = +32''$), close to the peak emission in the ^{12}CO and ^{13}CO maps. *Middle top* - Spectra observed at position B ($\Delta\alpha = -70'', \Delta\delta = -82''$), where the integrated line temperatures are about 50% of the peak emission. *Middle bottom* - Spectra observed at position C ($\Delta\alpha = -60'', \Delta\delta = -30''$), the peak of the NE–SW strip scan. *Bottom* - Spectra observed at position D ($\Delta\alpha = -100'', \Delta\delta = 0''$), close to the continuum far-IR peak.

Table 6.1: M17 SW line parameters derived from Gaussian fits, at four selected positions.

Molecule–J	I_{mb} [K km s^{-1}]	V [km s^{-1}]	T_{mb} [K]	ΔV [km s^{-1}]
Position A $(-70'', +32'')$				
^{12}CO J=6–5	723.1±7.5	20.4±0.04	82.9±1.5	8.2±0.11
	44.6±3.3	25.1±0.03	31.5±2.9	1.3±0.07
^{12}CO J=7–6	825.4±24.1	20.3±0.13	84.6±3.6	9.2±0.28
	56.9±12.8	24.2±0.15	26.5±7.3	2.0±0.32
^{13}CO J=6–5	301.2±4.2	20.2±0.04	54.7±1.1	5.2±0.08
	51.3±3.6	23.9±0.04	21.2±1.7	2.3±0.09
[C I] J=2–1	138.5±11.5	20.2±0.16	30.0±3.8	4.3±0.42
	29.9±10.1	23.6±0.18	12.7±5.2	2.2±0.51
Position B $(-70'', -82'')$				
^{12}CO J=6–5	537.4±6.9	19.7±0.05	65.7±1.3	7.7±0.11
^{12}CO J=7–6	528.5±16.1	19.5±0.12	62.2±2.8	7.9±0.26
^{13}CO J=6–5	166.7±1.6	19.3±0.02	33.5±0.5	4.7±0.05
[C I] J=2–1	169.7±4.2	19.2±0.06	34.4±1.4	4.6±0.14
Position C $(-60'', -30'')$				
^{12}CO J=6–5	220.4±3.1	17.9±0.04	33.7±0.6	6.1±0.06
	365.8±4.9	21.9±0.03	86.2±1.6	3.9±0.05
^{12}CO J=7–6	220.2±16.8	17.9±0.31	33.6±2.6	6.1[a]
	367.1±16.4	21.9±0.08	86.5±4.0	3.9[a]
^{13}CO J=6–5	145.7±11.5	18.9±0.17	29.8±2.7	4.6±0.21
	120.3±11.3	21.8±0.05	36.9±3.6	3.1±0.09
[C I] J=2–1	41.6±27.6	17.5±0.55	12.1±8.6	3.2±0.77
	124.5±28.6	20.7±0.48	24.9±7.3	4.5±0.72
Position D $(-100'', 0'')$				
^{12}CO J=6–5	136.1±10.9	16.8±0.09	34.6±3.2	3.7±0.17
	374.4±11.6	21.8±0.09	57.9±2.5	6.1±0.18
^{12}CO J=7–6	114.1±11.5	16.9±0.19	29.1±3.2	3.7[a]
	369.7±18.9	21.6±0.15	57.2±3.4	6.1[a]
^{13}CO J=6–5	82.7±4.2	18.4±0.09	20.0±1.3	3.9±0.15
	131.3±4.1	21.6±0.05	28.7±0.9	4.2±0.04
[C I] J=2–1	95.9±5.2	18.7±0.17	17.9±1.5	5.0±0.30
	120.9±1.5	21.4±0.06	24.5±1.3	4.6±0.24

[a] The uncertainty of this parameter was larger than 50% when let free in the Gaussian fitting. We set its value accordingly to the one found for the corresponding Gaussian component of the ^{12}CO J=6–5 line.

positions or to the contribution of a few fast-moving cloudlets (Martin et al., 1984; Graf et al., 1993).

The ^{12}CO $\frac{7-6}{6-5}$ line ratio between the peak main-beam temperatures T_{mb} obtained from the Gaussian fit of the main components is 1.02 ± 0.05 at position A, 0.95 ± 0.05 at position B, 1.00 ± 0.05 at position C, and 0.99 ± 0.07 at position D. From these line ratios we can estimate the ambient conditions for these particular positions. We have used the non-LTE radiative transfer code RADEX* (van der Tak et al., 2007) to estimate the average ambient conditions (kinetic temperature, density and column density) of the molecular gas. We assumed collisional excitation by molecular hydrogen. We also assumed an homogeneous spherical symmetry in the clumps for the escape-probability formalism. The collision rates between ^{12}CO and ortho- and para-H_2 are taken from Wernli et al. (2006), and can be found in the LAMDA database (Schöier et al., 2005). As in the LTE case, we used the cosmic microwave background radiation at 2.73 K, and we also tested the non-LTE model with and without the infrared radiation remitted by dust (eq.6.3) as the background source. It was found also for this case that the dust continuum emission produces a negligible effect in the non-LTE model at the frequencies of the ^{12}CO $J = 6 \rightarrow 5$ and $J = 7 \rightarrow 6$ lines. We explored molecular hydrogen densities between 10^4 cm^{-3} and 10^7 cm^{-3}, temperatures between 5 K and 500 K, and ^{12}CO column densities between 10^{10} cm^{-2} and 10^{18} cm^{-2}.

Figure 6.9 shows the possible ambient conditions required to reproduce the ^{12}CO $\frac{7-6}{6-5}$ line ratios, and the peak T_{mb} of the ^{12}CO $J = 6 \rightarrow 5$ line observed at position A (*left panel*) and B (*right panel*). A wide range of temperatures (100 – 450 K) and densities ($> 3 \times 10^4$ cm^{-3}) are possible solutions for a ^{12}CO column density per line width $N(^{12}\mathrm{CO})/\Delta V \sim 5 \times 10^{16}$ cm^{-2} km^{-1} s.

Figure 6.10 shows the possible ambient conditions estimated for position C (*left panel*) and D (*right panel*). The combinations of temperatures and densities required to reproduce the line ratios and peak temperatures are similar to those found for position A and B, although the range of possible temperatures (for a given density) at position D is larger than at the other positions. The column densities differ due to the different line strengths observed at the four positions (Table 6.1).

In order to constrain the range of solutions we can adopt the average 5×10^5 cm^{-3} density estimated by M92, which is also similar to the mean density of the clumps estimated by SG90. This is a sensitive assumption for a collision dominated scenario since this density is larger than the critical density of both ^{12}CO lines for $T_K \geq 20$ K. However, at this density (5×10^5 cm^{-3}) the temperature cannot be higher than 230 K in order to reproduce the line ratio and the peak T_{mb} of the ^{12}CO $J = 6 \rightarrow 5$ line observed at position A. And it cannot be higher than 150 K at position B. At position C the limit is about 220 K, and at position D it is about 200 K. These are lower kinetic temperatures than the 1000 K estimated for the dense clumps in the three-component model proposed by M92. Our upper limits for the kinetic temperature agree with the results reported in previous work (e.g., Harris et al., 1987, S88, SG90). From the map of the excitation temperature T_{ex} estimated

* http://www.sron.rug.nl/∼vdtak/radex/radex_manual.pdf

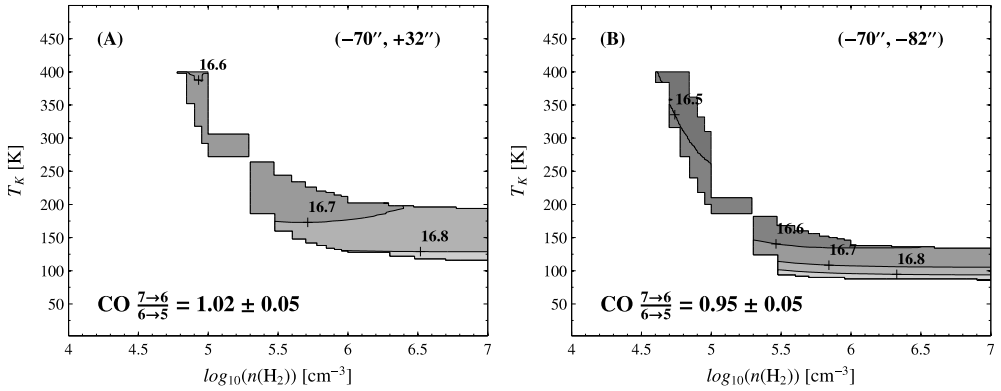

Figure 6.9: *Left* - The gray scale and contours represent the average (log_{10} scale) column density per line width ($\mathrm{cm}^{-2}\,\mathrm{km}^{-1}\,\mathrm{s}$) required to reproduce the observed ^{12}CO $\frac{7-6}{6-5}$ line ratio between the peak main-beam temperatures T_{mb} and the the peak T_{mb} of the ^{12}CO $J = 6 \rightarrow 5$ line observed at position A ($\Delta\alpha = -70'', \Delta\delta = +32''$), for different kinetic temperatures T_K and densities $n(\mathrm{H}_2)$. *Right* - Same as top, but at position B ($\Delta\alpha = -70'', \Delta\delta = -82''$).

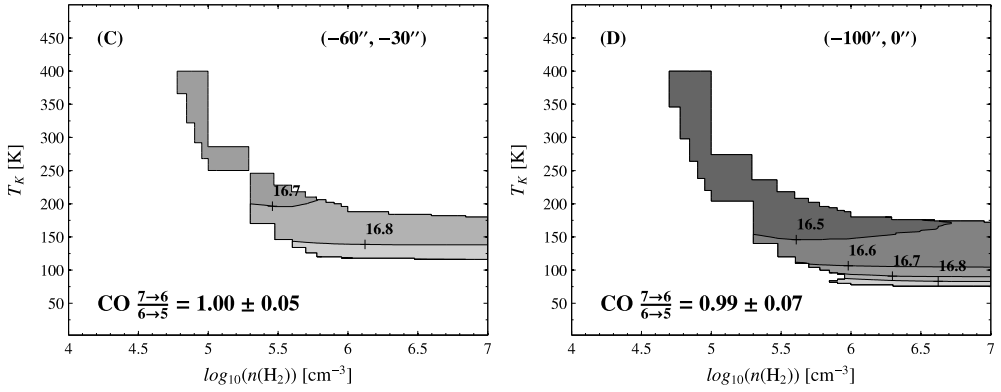

Figure 6.10: *Left* - The gray scale and contours represent the average (log_{10} scale) column density per line width ($\mathrm{cm}^{-2}\,\mathrm{km}^{-1}\,\mathrm{s}$) required to reproduce the observed ^{12}CO $\frac{7-6}{6-5}$ line ratio between the peak main-beam temperatures T_{mb} and the the peak T_{mb} of the ^{12}CO $J = 6 \rightarrow 5$ line observed at position C ($\Delta\alpha = -60'', \Delta\delta = -30''$), for different kinetic temperatures T_K and densities $n(\mathrm{H}_2)$. *Right* - Same as top, but at position D ($\Delta\alpha = -100'', \Delta\delta = 0''$).

from the LTE model (Fig. 6.7), the lower limits for T_K would be ~ 110 K and ~ 80 K at position A & C and B & D, respectively. These are similar (within 30%) to the lowest temperatures obtained with the non-LTE models (Figs. 6.9 and 6.10).

According to the radiative transfer model, temperatures up to 400 K and higher are also possible, but they require densities of $< 10^5$ cm^{-3} in order to reproduce the observed line ratios and peak temperatures. These densities and temperatures are consistent with the estimates made based on previous observations of the ^{12}CO $J = 7 \rightarrow 6$ and $J = 14 \rightarrow 13$ lines (Harris et al., 1987, SG90). On the other hand, clumps with densities of $> 10^6$ cm^{-3} could also reproduce the observed ratios and peak T_{mb} in all the positions at temperatures ≤ 200 K. However, these would be at the lower limit of the temperature range estimated in Harris et al. (1987) and SG90. The densities and temperatures found for M17 SW are similar to those found in W3 Main (Kramer et al., 2004), but higher (although compatible) than the kinetic temperatures found in Carina, where lower limits between 30 K and 50 K were estimated (Kramer et al., 2008).

6.4.4 Column densities at selected positions

The column density per line width $N(^{12}\mathrm{CO})/\Delta V$ at position A varies over a small range of $4 - 6 \times 10^{16}$ cm^{-2} km^{-1} s. If we consider an average line width of 8.7 km s^{-1} estimated for the ^{12}CO $J = 6 \rightarrow 5$ and $J = 7 \rightarrow 6$ lines (Table 6.1) and the average $N(\mathrm{CO})/\Delta V = 5 \times 10^{16}$ cm^{-2} km^{-1} s, we have a total column density of $N(^{12}\mathrm{CO}) \approx 4 \times 10^{17}$ cm^{-2}.

The model indicates that at position B the ^{12}CO column density per line width would be $\sim 4 \times 10^{16}$ cm^{-2} km^{-1} s. The average line width of the lines at position B is ~ 7.7 km s^{-1} (Table 6.1), which gives a total column density of $N(^{12}\mathrm{CO}) \approx 3 \times 10^{17}$ cm^{-2}, similar to the column found at position A. At positions C and D the average column densities per line width are $\sim 8 \times 10^{16}$ cm^{-2} km^{-1} s and $\sim 5 \times 10^{16}$ cm^{-2} km^{-1} s, respectively. Considering a line width of ~ 6 km s^{-1} we obtain similar column densities as in the previous two positions. That is $N(^{12}\mathrm{CO}) \approx 5 \times 10^{17}$ cm^{-2} and $N(^{12}\mathrm{CO}) \approx 3 \times 10^{17}$ cm^{-2} for positions C and D, respectively. At positions A and C the lines are optically thin, with τ ranging from about 0.6 to 1 for $T_K \geq 150$ K. At temperatures of ≤ 150 K, the lines become optically thick ($1 \leq \tau \leq 3$). The optically thin limit at positions B and D is reached at $T_K \sim 120$ K, with about the same ranges of optical depths as before, for temperatures higher or lower than 120 K.

Assuming a density of 5×10^5 cm^{-3} and average temperatures of 200 K at position A and 150 K at position B, the non-LTE model indicates that ^{13}COcolumn densities of $\sim 1.5 \times 10^{17}$ cm^{-2} and $\sim 7.4 \times 10^{16}$ cm^{-2} would be required to reproduce the observed strength (Table 6.1) of the ^{13}CO$J = 6 \rightarrow 5$ line at these positions, respectively. For a temperature of 200 K, the ^{13}COcolumn density at position C and D would be $\sim 5.6 \times 10^{16}$ cm^{-2}. And the excitation temperatures would be ~ 180 K at position A, C and D, and ~ 140 K at position B, which are higher temperatures than estimated with the LTE approximation. However, these excitation temperatures are just between 10 and 20 K lower than the assumed kinetic temperatures,

which indicates that these lines are close (within 10%) to the thermal equilibrium.

From their $C^{18}O$ $J = 2 \rightarrow 1$ observations, S88 estimated a ^{12}CO beam-averaged column density of $\sim 2 \times 10^{19}$ cm^{-2}, considering a [^{12}CO]/[$C^{18}O$] abundance ratio of 500. Hence, the column densities found for the four selected positions in M17 SW suggest that the warm ($T_k > 100$ K) and dense ($n(H_2) \geq 10^4$ cm^{-3}) gas traced by the mid-J ^{12}CO lines represent $\lesssim 2\%$ of the bulk of the cold ($T_k < 50$ K) and less dense ($n(H_2) \sim 10^3$ cm^{-3}) gas traced by the low-J ^{12}CO lines.

6.4.5 Volume-filling factors

The clump volume-filling factor Φ_V can be estimated from the ratio between the average volume density n_{av} per beam and the average clump density $n_{clump} \sim 5 \times 10^5$ cm^{-3} derived from the non-LTE model (e.g., Kramer et al., 2004). The average volume density per beam can be estimated from the total column density of the gas and the line of sight extent of the cloud (D_{cloud}). That is $n_{av} \sim N(H_2)/D_{cloud}$. Following the work by Howe et al. (2000) we can assume a ^{13}CO abundance ratio of 1.5×10^{-6} relative to H_2, and estimate the hydrogen column densities of $N_A(H_2) \sim 2.3 \times 10^{23}$ cm^{-2}, $N_B(H_2) \sim 1.1 \times 10^{23}$ cm^{-2}, and $N_{C,D}(H_2) \sim 8.4 \times 10^{22}$ cm^{-2}, for the four selected positions.

The line of sight extent of the cloud is a difficult parameter to estimate. From a $13''$ (~ 0.14 pc) beam-averaged column density of $N(H_2) \sim 8 \times 10^{23}$ cm^{-2}, a volume-filling factor of 0.13 was estimated by SG90. While Howe et al. (2000) reported a Φ_V of ~ 0.002 from the total column density of $N(H_2) \sim 4 \times 10^{22}$ cm^{-2} estimated at the peak column density of their ^{13}CO $J = 1 \rightarrow 0$ map, and assuming a cloud extent of 3 pc, which was deconvolved from the $4'$ beam of the SWAS space telescope. The line of sight extent should be larger than the smallest possible clump size (~ 0.1 pc) that we can deconvolve from our $9.4''$ beam. But we do not think it can be as large as 3 pc, which is about the size of the maps we present here. This holds true at least for the region of bright ^{12}CO and ^{13}CO emission close to the ionization front, where our four selected positions are taken from. If we take the average between the upper (3 pc) and lower (0.1 pc) limits of the cloud extent, we would obtain a cloud size of ~ 1.6 pc. This line of size extent of the cloud is uncertain, but perhaps more realistic given the geometry of M17 SW and the high resolution of our maps. Besides, it is similar to the diameter of the [C I]emitting region (≈ 1 pc) estimated by Genzel et al. (1988), and the narrow spatial extension (~ 1.3 pc) of the ^{13}CO $J = 6 \rightarrow 5$ and [C I] 370 μm lines along the strip line at P.A=63° (Figs. 6.3 and 6.4).

Using the total column densities estimated for the four selected positions and $D_{cloud} = 1.6$ pc, the average volume densities at position A and B would be $\sim 5.3 \times 10^4$ cm^{-3} and $\sim 2.5 \times 10^4$ cm^{-3}, respectively, and $\sim 1.9 \times 10^4$ cm^{-3} at position C and D. This in turn yields volume-filling factors $\Phi_V = n_{av}/n_{clump}$ of ~ 0.106, ~ 0.050 and 0.038 at positions A, B and C/D respectively. These volume-filling factors, as well as the total hydrogen densities estimated here, are larger than those estimated by Howe et al. (2000), but smaller than the ones reported in SG90. This is an expected and reasonable result since the ^{13}CO $J = 6 \rightarrow 5$ line traces only the warm and dense clumps and not the interclump medium. Besides, the volume-filling factors

estimated at the four selected positions agree closely with those estimated in other star-forming regions using clumpy PDR models (e.g. S140, W3 Main; Spaans & van Dishoeck 1997; Kramer et al. 2004).

6.4.6 Jeans stability of the clumps

With an average density of 5×10^5 cm^{-3} and an average clump size of 0.2 pc in diameter, which gives a typical total clump mass of $\sim 100\ M_\odot$ in molecular hydrogen, M92 estimated that these clumps are not in pressure equilibrium with the interclump gas (with average density 3×10^3 cm^{-3} and temperature of 200 K), but rather that they are self-gravitating. With these parameters and a temperature of about 1000 K, the Jeans mass and radius should be about $1500\ M_\odot$ and 0.3 pc, respectively. Hence these clumps are not near the collapsing regime. Even with our upper limits for the temperatures of the clumps of 230 K and 150 K at position A and B, and 220 K and 200 K at position C and D, respectively, the Jeans mass and radius of these clumps would still be larger than those estimated with the average density of 5×10^5 cm^{-3}. Temperatures of < 170 K would be required to break the Jeans stability at that density. This means that the clumps at position B should have a slightly lower density of $\sim 3 \times 10^5$ cm^{-3} (or lower) to be Jeans-stable at a temperature of about 150 K (or higher).

6.5 Conclusions

We have used the dual-color heterodyne receiver array of 7 pixels CHAMP$^+$ on the APEX telescope to map a region of about 3.4 pc $\times$ 3.0 pc in the $J = 6 \rightarrow 5$ and $J = 7 \rightarrow 6$ lines of ^{12}CO, the ^{13}CO $J = 6 \rightarrow 5$ and the $^3P_2 \rightarrow {}^3P_1$ 370 μm ($J = 2 \rightarrow 1$) fine-structure transition of [C I] in M17 SW nebula.

The completely different structure and distribution of the $^3P_2 \rightarrow {}^3P_1$ 370 μm emission and its critical density indicate that this emission arises from the interclump medium ($\sim 3 \times 10^3$ cm^{-3}). On the other hand, the mid-J lines of ^{12}CO and the isotope emissions arise from the high density ($\sim 5 \times 10^5$ cm^{-3}) and clumpy region.

The spatial extent of the warm gas (40-230 K) traced by the ^{12}CO $J = 7 \rightarrow 6$ line is about 2.2 pc from the ridge of the M17 SW complex, which is smaller than the extent observed in the low-J ^{12}CO and C^{18}O lines reported in previous work. The ^{13}CO $J = 6 \rightarrow 5$ and [C I] 370 μm lines, have a narrower spatial extent of about 1.3 pc along a strip line at P.A=63°.

An LTE approximation of the excitation temperature provides lower limits for the kinetic temperature. The warmest gas is located along the ridge of the cloud, close to the ionization front. In this region the excitation temperatures range between 40 and 120 K. A non-LTE estimate of the ambient conditions at four selected positions of M17 SW indicates that the high density clumps ($\sim 5 \times 10^5$ cm^{-3}) cannot have temperatures higher than 230 K. The warm ($T_k > 100$ K) and dense ($n(\mathrm{H_2}) \geq 10^4$ cm^{-3}) gas traced at the four selected positions by the mid-J ^{12}CO

lines represents $\sim$ 2% of the bulk of the molecular gas traced by the low-J ^{12}CO lines. Volume-filling factors of the warm gas ranging from 0.04 to 0.11 were found at these positions.

Acknowledgements

We are grateful to the MPfIR team and the APEX staff for their help and support during and after the observations. We are grateful to J. Stutzki for providing the low-J ^{12}CO data and to C. Brogan for providing the 21 cm map. We thank the referee for the careful reading of the manuscript and constructive comments. Molecular Databases that have been helpful include the NASA/JPL, LAMDA and NIST. The construction of CHAMP$^+$ is a collaboration between the Max-Planck-Institut für Radioastronomie Bonn, SRON Groningen, the Netherlands Research School for Astronomy (NOVA), and the Kavli Institute of Nanoscience at Delft University of Technology, with support from the Netherlands Organization for Scientific Research (NWO) grant 600.063.310.10.

7

Diffuse and dense irradiated gas in M17 SW: [C I], HCN and HCO^+

– J.P. Pérez-Beaupuits, M. Spaans and R. Güsten –

Stars are formed in dense molecular clouds. These star-forming regions are impacted by radiative feedback from UV and X-ray sources. The influence of these radiation fields is reflected in the chemistry and thermodynamics of the gas. To probe with high resolution ($13'' - 18''$) the ambient conditions and spatial distribution, as well as the influence of UV and (hard) X-rays, of the diffuse ($n(\mathrm{H_2}) \sim 10^3$ cm^{-3}) and dense gas ($n(\mathrm{H_2}) > 10^5$ cm^{-3}) toward the core of M17 SW. The dual colour single pixel receiver FLASH on the APEX telescope was used to map a 4.1 pc $\times$ 4.7 pc region in emission from the $^3P_1 \rightarrow {}^3P_0$ 609 μm fine-structure transition of [C I], and the APEX-2 SIS receiver was used to map the emission from the $J = 4 \rightarrow 3$ transition of HCN and HCO^+ in a smaller region of 2.6 pc $\times$ 1.3 pc. The small scale ($\sim 13''$) spatial distribution of the [C I] $^3P_1 \rightarrow {}^3P_0$ 609 μm fine-structure transition is similar to that shown in earlier observations of the $^3P_2 \rightarrow {}^3P_1$ 370 μm transition. The [C I]$_{370\ \mu\mathrm{m}}$/[C I]$_{609\ \mu\mathrm{m}}$ integrated temperature ratio is > 1 in most of the region mapped, which indicates optically thin emission. Conversely, the HCN and HCO^+ $J = 4 \rightarrow 3$ transitions also show similar distributions at the brightest emission regions. However, the HCO^+ $J = 4 \rightarrow 3$ line is a factor $\sim 1 - 6$ brighter than that of HCN across the region mapped, and presents more extended emission. In the optically thin limit, the excitation temperature of [C I] ranges between 40 K and 100 K in the inner region of M17 SW. While excitation temperatures > 100 K are found along the eastern edge of the cloud. The column density of [C I] ranges between $\sim 4 \times 10^{17}$–10^{19} cm^{-2} in the region where the [C I] integrated temperature is larger than 50% of its peak emission. The unusually high (up to ~ 6) HCO^+/HCN $J = 4 \rightarrow 3$ integrated temperature ratio is argued to be an indication of irradiation by heavily obscured X-ray sources or to be the result of a lower excitation temperature of HCN.

Submitted to *Astronomy & Astrophysics* (2010)

7.1 Introduction

In order to advance our understanding of the ambient conditions of star formation, observations of large areas of known massive Galactic star forming regions (e.g., Orion Nebula, W51, Cepheus A, NGC 2024) have been done over a wide wavelength range. These observations include emissions of atoms, molecules, and grains, and they usually cover areas close to the radiation sources.

The warm emitting gas seems to be confined to narrow (< 1 pc) zones close to the ionization front, according to observations of mid-J (e.g. $J = 6 \rightarrow 5$ and $J = 7 \rightarrow 6$) transitions of ^{12}CO in several massive star forming regions (e.g., Harris et al., 1987; Graf et al., 1993; Yamamoto et al., 2001; Kramer et al., 2004, 2008; Pérez-Beaupuits et al., 2010). Although shocks can be an important source of heating in high velocity wing objects like Orion, W51 and W49 (Jaffe et al., 1987), the mid-J ^{12}CO observations favor a photoelectric heating of the warm gas located beyond the H II region driven by the UV radiation field emerging from an ionizing source, the so-called photon-dominated region (PDR).

A vast amount of data also shows that molecular clouds are clumpy over a wide range of scales, from giant molecular clouds containing smaller subclouds to small dense cores within the subclouds. The clumpiness of molecular clouds is relevant for the understanding of fragmentation processes that can lead to density condensations of a size that may collapse to form stars (e.g., Carr, 1987; Hocuk & Spaans, 2010). Several efforts have been made over the past years to identify clumps, their size, line width and mass, among other parameters. The complex line profiles observed in optically thin lines like [C I], CS, C^{18}O, ^{13}CO and their velocity-channel maps, are indicative of the clumpy structure of molecular clouds and allow for a robust estimation of their clump mass spectra (e.g., Carr, 1987; Loren, 1989; Stutzki & Guesten, 1990; Hobson, 1992; Kramer et al., 1998, 2004; Pérez-Beaupuits et al., 2010).

In contrast to [C II] 158 μm and [O I] 63 μm, PDR models predict that the intensity of the [C I] fine structure lines do not have a strong dependence on UV energy density (e.g., Hollenbach & Tielens, 1999). Therefore, in a clumpy cloud irradiated by UV photons, the intensity of the [C I] emission is expected to be proportional to the number of photodissociation surfaces of clumps along the line of sight (e.g., Spaans, 1996; Howe et al., 2000; Kramer et al., 2004).

Inhomogeneous and clumpy clouds, as well as a partial face-on illumination, in star-forming regions like M17 SW, S106, S140, the Orion Molecular Cloud, and the NGC 7023 Nebula, seem to produce extended emission of atomic lines like [C I] and [C II], and suppress the stratification in [C II], [C I] and CO expected from standard steady-state PDR models (e.g., Keene et al., 1985; Genzel et al., 1988; Stutzki et al., 1988; Gerin & Phillips, 1998; Yamamoto et al., 2001; Schneider et al., 2002, 2003; Mookerjea et al., 2003; Pérez-Beaupuits et al., 2010). A clumpy PDR model was required to explain the extended [C I] $^3P_1 \rightarrow {}^3P_0$ and ^{13}CO $J = 2 \rightarrow 1$ emission in S140 (Spaans & van Dishoeck, 1997).

Massive star forming regions like the Omega Nebula M17, with a rather edge-on view, are ideal sources to study the clumpy structure of molecular clouds, as well

as the chemical and thermodynamic effects of the nearby ionizing sources. The south-west region of M17 (M17 SW) concentrates molecular material in a clumpy structure. Models based on far-IR and sub-millimeter observations (Stutzki et al., 1988; Meixner et al., 1992) suggest that the distribution and intensity of the emissions observed in the M17 SW complex can be explained with high density ($n(\mathrm{H_2}) \sim 5 \times 10^5$ cm^{-3}) clumps embedded in an interclump medium ($n(\mathrm{H_2}) \sim 3 \times 10^3$ cm^{-3}) and surrounded by a diffuse halo ($n(\mathrm{H_2}) \sim 300$ cm^{-3}).

The central cluster of more than 100 stars that illuminates M17 SW is NGC 6618 (e.g., Lada et al., 1991; Hanson et al., 1997). The two components of the massive binary CEN1 (Kleinmann, 1973; Chini et al., 1980) are part of the central cluster NGC 6618 and are separated by $\sim 1''.8$. This source, originally classified as a double O or early B system by Kleinmann (1973), is actually composed of two O4 visual binary stars, named CEN 1a (NE component) and CEN 1b (SW component), and it appears to be the dominant source of photo-ionization in the whole M17 region (Hoffmeister et al., 2008).

The components of the CEN1 O4+O4 binary are also the brightest X-ray sources detected in a short (40 ks) *Chandra* ACIS exposure of the stellar population in the M17 region (Broos et al., 2007). This exposure detected 886 X-ray sources, with 771 of them having a stellar counterpart in IR images. A new long (~ 300 ks) exposure of the same field yielded a combined dataset of ~ 2000 X-ray sources (Getman et al., 2010, Townsley et al., in preparation). Spectral analysis of 598 sources with the highest photometric significance in the initial set, yielded estimated absorbing column densities of up to $N_{\mathrm{H}} \approx 5 \times 10^{23}$ cm^{-2} ($A_V \sim 250 - 300$ mag.) with a temperature (energy) range $0.5\ \mathrm{keV} \leq kT \leq 8\ \mathrm{keV}$ in the observed total band. The total luminosities (t) estimated in this band, corrected for absorption (c), range from $L_{t,c} \sim 6 \times 10^{29}$ erg s^{-1} to $L_{t,c} \sim 2 \times 10^{33}$ erg s^{-1}.

Although the brightest X-ray sources are CEN 1a and CEN 1b from the central NGC 6618 cluster, other stellar concentrations of ~ 40 heavily obscured ($E_{median} \geq 2.5$ keV, $A_V > 10$ mag) X-ray sources are distributed along the eastern edge of the M17 SW molecular core. The densest concentration of X-ray sources coincides with the well known star-forming region M17-UC1 and the concentration ends at around the Kleinmann-Wright Object (see Fig. 7.4 for an overview).

Since hard X-ray photons (> 1 keV) can penetrate much deeper into a cloud than far-UV photons ($6 - 13.6$ eV), high temperatures are maintained to much greater depths into the clouds. Also in contrast with PDR models, in X-ray dominated regions (XDRs, e.g., Maloney et al. 1996; Meijerink & Spaans 2005) a transition layer $\mathrm{C^+} \rightarrow \mathrm{C} \rightarrow \mathrm{CO}$ is not well-defined, and these species can actually co-exist, while large columns of neutral carbon can be produced, with fractional abundance of $\sim 10^{-5} - 10^{-4}$ (e.g., Meijerink & Spaans, 2005). A similar effect can be expected in a PDR with enhanced cosmic-ray rates (e.g., Meijerink et al., 2006).

Thus, the extended emission of [C I] and [C II] observed in M17 SW could be the result of its clumpy structure, but also be a consequence of its embedded X-ray sources. In fact, the abundances of molecular species like HNC, $\mathrm{HCO^+}$, CN, and SiO are also expected to be enhanced by hard X-ray irradiation (e.g., Usero et al.,

2004; Meijerink & Spaans, 2005; Aalto et al., 2007b).

In an earlier paper we presented high resolution maps of mid-J CO lines and the $^3P_2 \rightarrow {}^3P_1$ fine-structure transition of [C I] (Pérez-Beaupuits et al., 2010). In this study we present a new high resolution map of the $^3P_1 \rightarrow {}^3P_0$ fine-structure transition of [C I], and maps of the $J = 4 \rightarrow 3$ transition of HCN and HCO^+.

We are particularly interested in these molecules (HCN and HCO^+) because they have been extensively used in previous efforts to disentangle the driving source of power, star formation vs. black hole accretion, in the nuclear region of active galaxies (e.g., Sternberg et al., 1994; Kohno et al., 1999, 2001; Kohno, 2003, 2005; Usero et al., 2004; Pérez-Beaupuits et al., 2007; García-Burillo et al., 2008; Loenen et al., 2008; Krips et al., 2008; Pérez-Beaupuits et al., 2009).

Given the relative youth ($\lesssim 1$ Myr, e.g., Lada et al. 1991; Hanson et al. 1997 of the main ionizing cluster (NGC 6618) of M17 SW, and the absence of evolved stars, it is likely that supernovae have not yet occurred. This makes M17 SW an ideal place to study the interactions of massive stars with their surrounding gas/dust and stellar disks, without the influence of nearby supernovae. This allows us to study the effects of X-rays on [C I], HCN, and HCO^+ in a rather isolated environment.

This study of M17 SW can be considered as one more Galactic template for extra-galactic star forming regions. The properties and feedback effects of massive star forming regions, studied at small scale and with high resolution in the Milky Way, are expected to drive the energetics of active galaxies. Therefore, we expect that our results will be important for future high resolution observations where similar regions in extra-galactic sources will be studied in great spatial detail with, e.g., ALMA (Schleicher et al., 2010).

The organization of this article is as follows. In Sect. 7.2 we describe the observations. The maps of the four lines observed are presented in Sect. 7.3. The modelling and analysis of the ambient conditions are presented in Sect. 7.4. The conclusions and final remarks are presented in Sect. 7.5.

7.2 Observations

We have used the lower frequency band of the dual channel DSB receiver FLASH (Heyminck et al., 2006) on the Atacama Pathfinder EXperiment (APEX*; Güsten et al. 2006) during October 2009, to map the $^3P_1 \rightarrow {}^3P_0$ 609 μm (hereafter: $1 \rightarrow 0$) fine-structure transition of [C I] at 492.161 GHz. The observed region covers about $6'.2 \times 7'.2$ (4.1 pc $\times$ 4.7 pc) compared to the $5'.3 \times 4'.7$ (3.4 pc $\times$ 3.0 pc) area previously mapped for [C I] $J = 2 \rightarrow 1$ with CHAMP$^+$ (Pérez-Beaupuits et al., 2010). The [C I] $J = 1 \rightarrow 0$ was done in on-the-fly (OTF) slews in R.A. (~ 360 arcsec long). Because the beam size of APEX at 492 GHz is about $12''.7$ the subsequent scans in Declination and R.A. were spaced $6''$ apart.

* This publication is based on data acquired with the Atacama Pathfinder Experiment (APEX). APEX is a collaboration between the Max-Planck-Institut für Radioastronomie, the European Southern Observatory, and the Onsala Space Observatory

We also observed HCN $J = 4 \rightarrow 3$ at 354.506 GHz during July 2008, during the same period as the [C I] $J = 2 \rightarrow 1$ map was done, and HCO^+ $J = 4 \rightarrow 3$ 356.734 GHz during June 2009, using the APEX-2 heterodyne SIS receiver (Risacher et al., 2006). With the single pixel receiver, the regions mapped in HCN and HCO^+ are smaller than that of [C I], covering just about $4' \times 2'$ (2.6 pc $\times$ 1.3 pc) due to the visibility of M17 SW and other priority projects during the observing campaigns. The HCN and HCO^+ $J = 4 \rightarrow 3$ maps were done in raster slews in R.A. of $\sim 240''$ long and subsequent scans in Declination with spacing of $8''$, since the APEX beam size at 357 GHz is about $17.6''$.

The total power mode was used for the observations, nodding the antenna prior to each OTF (and raster) slew to an off-source position $180''$ east of the SAO star 161357. The latter is used as reference position ($\Delta\alpha = 0$, $\Delta\delta = 0$) in the maps and throughout the paper, with R.A(J2000)=18:20:27.64 and Dec(J2000)=-16:12:00.90. The reference for continuum pointing was Sgr B2(N) and the pointing accuracy was kept below $3''$ for all the maps. In the facility cabin of APEX there is a closed cycle cooler offering cold temperature with a liquid nitrogen (LN2) load and an ambient temperature load. Calibration measurements with these loads were performed every $\sim$10 minutes. The data were processed during the observations with the APEX real-time calibration software (Muders et al., 2006), assuming an image sideband suppression of 10 dB (APEX-2) and equal gains for FLASH-460.

The Fast Fourier Transform Spectrometer (FFTS) was used as backend with a fixed bandwidth of 1.5 GHz and 2048 channels for the [C I] $J = 1 \rightarrow 0$ map and 1.0 GHz bandwidth and 8192 channels for the HCN and HCO^+ $J = 4 \rightarrow 3$ maps. We used the two IF groups of the FFTS without offsets between them. The on-source integration time per dump was 1 second for the OTF map of [C I] $J = 1 \rightarrow 0$, and 10 seconds for the HCN and HCO^+ $J = 4 \rightarrow 3$ maps. The median DSB system noise temperature of FLASH was about 810 K for [C I], and the median SSB system temperatures of the APEX-2 receiver were about 470 K and 380 K, for HCN and HCO^+, respectively.

Observations toward Jupiter were performed to estimate the beam coupling efficiency ($\eta_c \approx 0.59$) of FLASH (Heyminck et al., 2006), assuming a brightness temperature of 158 K for the Jovian planet at 492 GHz, as interpolated from data reported in Griffin et al. (1986). A beam coupling efficiency of 0.73 was assumed for the APEX-2 receiver at the frequencies of HCN and HCO^+ $J = 4 \rightarrow 3$ (Güsten et al., 2006; Risacher et al., 2006). With these beam coupling efficiencies, and a forward efficiency (η_f) of 0.95, we converted all data to line brightness temperature scale, $T_B = \eta_f \times T_A^*/\eta_c$. The reduction of these calibrated data, as well as the maps shown throughout the paper, were done using the GILDAS* package CLASS90.

* http://www.iram.fr/IRAMFR/GILDAS

7.3 Results

7.3.1 The [C I] integrated temperature maps

Figure 7.1 shows the maps of the temperature, integrated between 10 $\mathrm{km\,s^{-1}}$ and 28 $\mathrm{km\,s^{-1}}$, of [C I] $J = 1 \rightarrow 0$ (*top*) and $J = 2 \rightarrow 1$ (*bottom*) which was convolved to the largest beam size ($12''.7$) of the $J = 1 \rightarrow 0$ line. Therefore, the peak integrated temperature of the [C I] $J = 2 \rightarrow 1$ line is ~ 20 $\mathrm{K\,km\,s^{-1}}$ lower than the peak previously reported in Pérez-Beaupuits et al. (2010). The peak integrated temperatures of the maps shown here are 205 $\mathrm{K\,km\,s^{-1}}$ and 262 $\mathrm{K\,km\,s^{-1}}$ for the [C I] $J = 1 \rightarrow 0$ and $J = 2 \rightarrow 1$ lines, respectively. These lines follow a similar spatial distribution and their respective peaks are located at about the offset position $\Delta\alpha = -120'', \Delta\delta = 30''$, approximately 0.88 pc ($\sim 80''$ at P.A. $90°$) from the ridge. They both present extended emission, not like a stratified PDR.

The critical density ($n_{cr} \sim 10^3$ $\mathrm{cm^{-3}}$ for collisions with o-/p-H_2 at 100 K; from the LAMDA* database, Schöier et al. 2005) and upper-level energy ($E_u \approx 24$ K for $J = 1 \rightarrow 0$, and $E_u \approx 62$ K for $J = 2 \rightarrow 1$) of [C I] enable us to trace the diffuse ISM and asses its temperature. In section 7.4.2 we estimate the excitation temperature of [C I] from the ratio between the two transitions and assuming optically thin emission. From this excitation temperature, the optical depths of both lines and the column density of [C I] can be estimated as well. This is done in section 7.4.2.

7.3.2 The HCN and HCO^+ integrated temperature maps

The HCN and HCO^+ $J = 4 \rightarrow 3$ lines ($n_{cr} \sim 10^8$ $\mathrm{cm^{-3}}$ and $n_{cr} \sim 9 \times 10^6$ $\mathrm{cm^{-3}}$ at 100 K, respectively, and both with $E_u \approx 43$ K) probe much denser regions than [C I]. The maps of the velocity ($10 - 28$ $\mathrm{km\,s^{-1}}$) integrated temperature of the HCN and HCO^+ $J = 4 \rightarrow 3$ lines are shown in the *top* and *middle* panel of Fig.7.2, respectively. The HCO^+ map was convolved with the slightly larger beam size ($17.7''$) of the HCN $J = 4 \rightarrow 3$ line, in order to have the same number of pixels per map. The pixel size is $-8.9'' \times 8.9''$ which ensures Nyquist sampling of the spectra in both (R.A. and Dec.) directions.

The peak integrated temperatures are 96 $\mathrm{K\,km\,s^{-1}}$ and 136 $\mathrm{K\,km\,s^{-1}}$, for HCN and HCO^+, respectively. The brightest regions of both lines have a similar spatial distribution. However, the velocity-integrated temperature of the HCO^+ $J = 4 \rightarrow 3$ line is a factor $\sim 1 - 6$ brighter than that of the HCN line, as shown in the *bottom* panel of Fig.7.2. The HCO^+ $J = 4 \rightarrow 3$ emission is also more extended than the HCN one, particularly towards the northern edge of the cloud core where the ratio is larger.

In order to reduce uncertainties, we compute the HCO^+/HCN ratio only in the region where the integrated temperature in both lines is brighter than 5% of their peak values. Because these maps were not done simultaneously we also consider the role of the relative pointing errors in our results. Since the pointing accuracy in both maps is $< 3''$ we know that the relative pointing errors would be at most $\sim 6''$,

* http://www.strw.leidenuniv.nl/∼moldata/

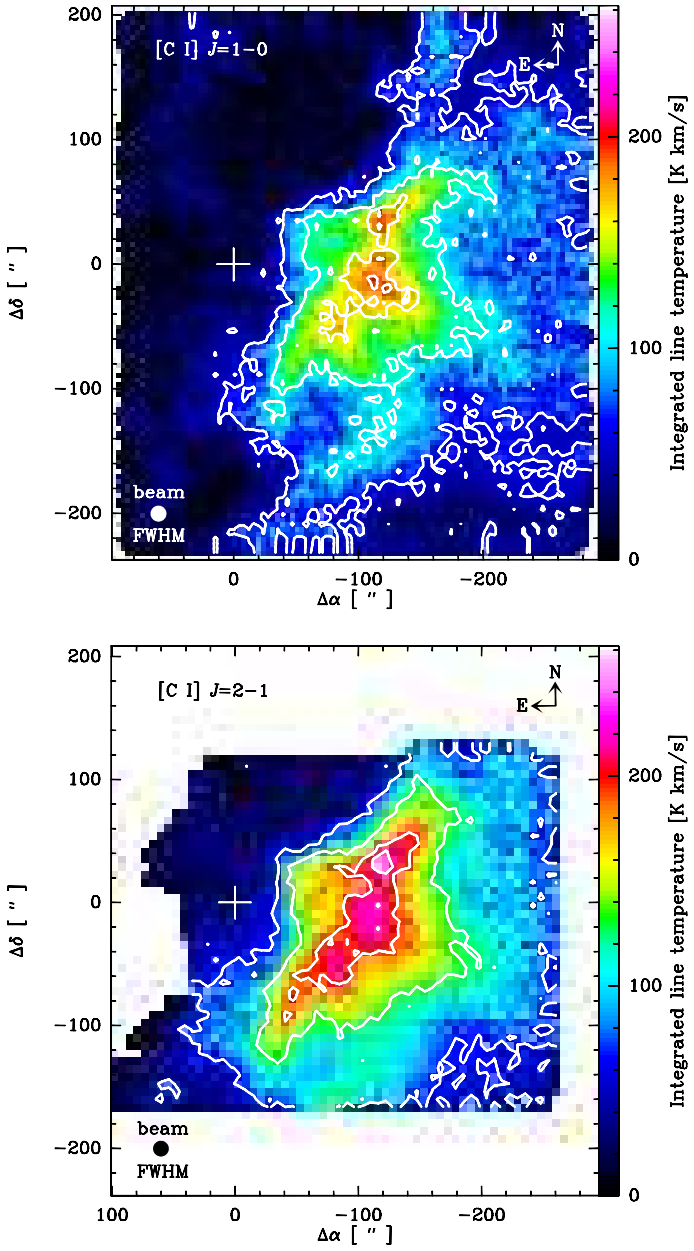

Figure 7.1: *Top* - Colour map of the integrated temperature of [C I] $J = 1 \rightarrow 0$ in M17 SW. The peak emission is 205 K km s^{-1}. The contour levels are 25%, 50%, 75% and 90% of the peak emission. *Bottom* - Colour map of the integrated temperature of [C I] $J = 2 \rightarrow 1$ (from Pérez-Beaupuits et al. 2010) convolved to the beam size ($\sim 12.7''$) of the [C I] $J = 1 \rightarrow 0$ line, with a peak emission of 262 K km s^{-1}. The contour levels are as described above. The reference position ($\Delta\alpha = 0$, $\Delta\delta = 0$), marked with a cross, corresponds to the SAO star 161357 at R.A(J2000)=18:20:27.65 and Dec(J2000)=-16:12:00.91.

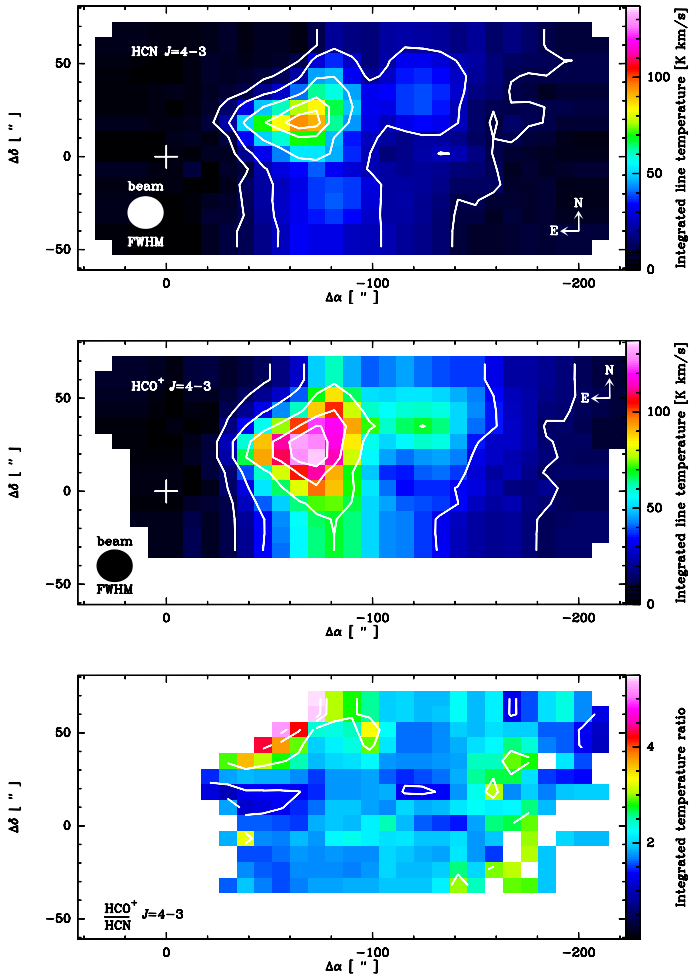

Figure 7.2: *Top* - Colour map of the integrated temperature of HCN $J = 4 \rightarrow 3$ in M17 SW. The peak emission is 96 $\mathrm{K\,km\,s^{-1}}$. The countour levels are the 10%, 25%, 50%, 75% and 90% of the peak emission. *middle* - Colour map of the integrated temperature of HCO^+ $J = 4 \rightarrow 3$, with a peak emission of 136 $\mathrm{K\,km\,s^{-1}}$ and contour levels as described before. *Bottom* - Map of the HCO^+/HCN $J = 4 \rightarrow 3$ line ratio. The ratio ranges from ~ 1 to ~ 5.5 in the region where both lines are brighther than 5% of their peak intensities. The contour lines correspond to the HCN $J = 4 \rightarrow 3$ map and are defined as before, from thin to thick. The reference position ($\Delta\alpha = 0$, $\Delta\delta = 0$), marked with a cross, corresponds to the SAO star 161357 at R.A(J2000)=18:20:27.65 and Dec(J2000)=-16:12:00.91.

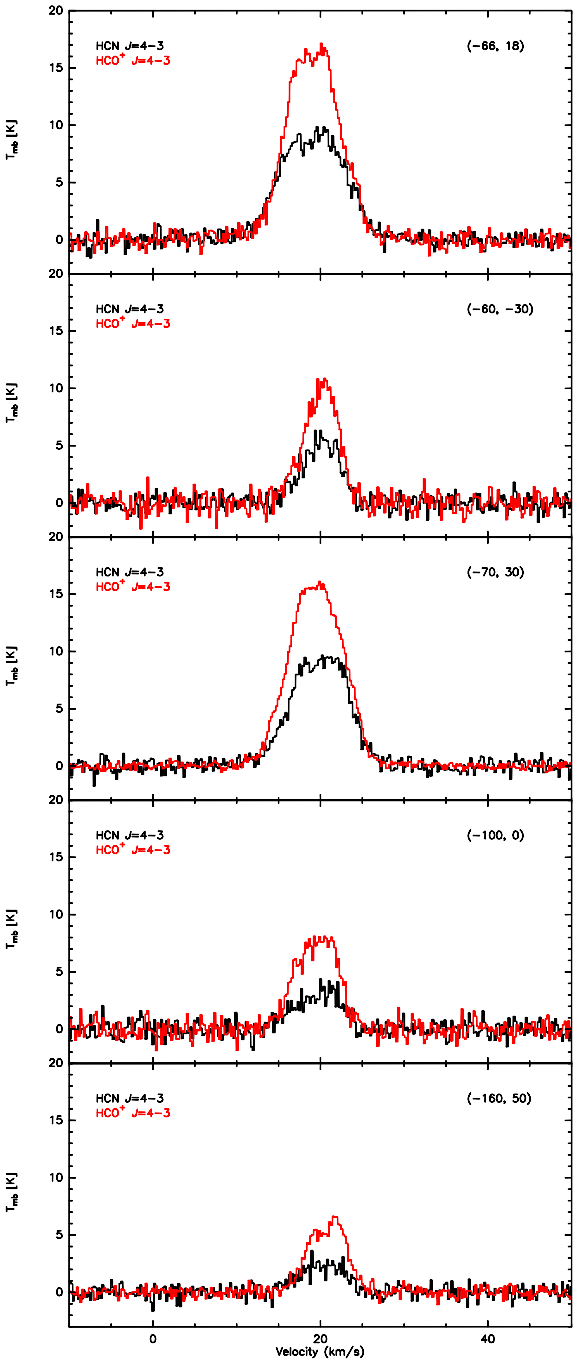

Figure 7.3: Spectra of the HCN and HCO^+ $J = 4 \rightarrow 3$ lines at selected positions towards M17 SW. The top panel shows the spectra at the position ($\Delta\alpha = -66'', \Delta\delta = +18''$) of the peak integrated temperature of the HCO^+ map. The middle panel corresponds to the spectra at position ($\Delta\alpha = -60'', \Delta\delta = +50''$) where the HCO^+/HCN $J = 4 \rightarrow 3$ line ratio (~ 5.5) is the largest in the region mapped.

which is smaller than the pixel size of the maps. Therefore, we can exclude the pointing errors as the cause of the high ratios observed, specially at the northern edge of the cloud core. On the other hand, the broader emission of the HCO^+ $J = 4 \rightarrow 3$ line was also observed in the $J = 3 \rightarrow 2$ transition by Hobson (1992), who reported a more extended emission of HCO^+ further into the H^+ region.

Fig. 7.3 shows the spectra of HCN and HCO^+ $J = 4 \rightarrow 3$ at selected positions. The spectra at position ($\Delta\alpha = -66'', \Delta\delta = +18''$) correspond to the peak integrated temperature of HCO^+. The spectra at position ($\Delta\alpha = -60'', \Delta\delta = +50''$) correspond to the largest ratio (~ 5.5) between the velocity-integrated temperatures at the northern edge of the cloud core. The other spectra correspond to positions where both lines are weaker. The line profiles of both lines match very well in all the positions, which indicates that the difference in intensities is not a consequence of different line widths.

Similar high HCO^+/HCN $J = 4 \rightarrow 3$ line ratios have been observed in other Galactic star forming regions (e.g., W49A, Peng et al. 2007) and in active galaxies (e.g., NGC 1068, Pérez-Beaupuits et al. 2009). Although these ratios are characteristic of X-ray dominated regions (XDRs) (e.g., Meijerink & Spaans, 2005; Meijerink et al., 2007) we discuss in Sec. 7.4.3 other possible mechanisms that can lead to similar results. Indeed, if the intensity of HCO^+ is as strong as HCN (or stronger) it may be due to relatively high kinetic temperatures, strong UV radiation fields, and low densities (e.g., Fuente et al., 1993; Chin et al., 1997; Brouillet et al., 2005; Christopher et al., 2005; Zhang et al., 2007; Meijerink et al., 2007).

7.4 Discussion

7.4.1 The ionization front

The ionization front traced by the high resolution ($10'' \times 7''$) map of the 21 cm continuum emission (Brogan & Troland, 2001), as well as the ionizing stars identified by Beetz et al. (1976) and Hanson et al. (1997), are shown in Figure 7.4. The HCN $J = 4 \rightarrow 3$ (white contour lines) and [C I] $J = 1 \rightarrow 0$ (green contour lines) are overlaid. The densest concentration of heavily obscured X-ray sources coincides with the M17-UC1 star forming region, and their location is indicated with *black circles*. The median energy of these sources is $E_{median} > 2.5$ keV ($A_V \geq 10$ mag) which can penetrate columns larger than 10^{23} cm^{-2} (Meijerink & Spaans, 2005, e.g.,[). These X-ray sources correspond to the $\sim 40'' \times 40''$ field shown in Fig.10 by Broos et al. (2007). The coordinates were obtained from the VizieR online catalogue*. Note that the HCN and HCO^+ lines peak in a similar region, close to the X-ray sources in the UC1 complex. While the [C I] peaks at ~ 0.4 pc away from the HCO^+ peak.

Figure 7.5 shows the variation of the integrated temperature of several lines across the ionization front. This corresponds to the strip line at P.A=90° shown in Pérez-Beaupuits et al. (2010), where the ^{12}CO, ^{13}CO, and [C I] $J = 2 \rightarrow 1$ are reproduced from. Every strip lines was smoothed spatially (in two pixels with respect to

* http://vizier.cfa.harvard.edu/viz-bin/VizieR?-source=J/ApJS/ 169/353

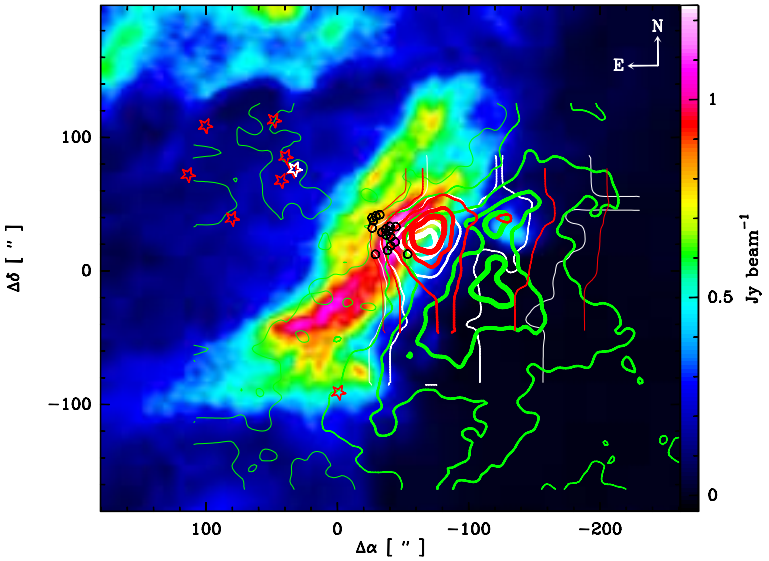

Figure 7.4: Colour map of the 21 cm continuum emission (Jy beam^{-1}) in M17 SW with $10'' \times 7''$ resolution by Brogan & Troland (2001). The *white* contour lines correspond to the HCN $J = 4 \rightarrow 3$ transition with a peak emission of $\sim$ 90 K km s^{-1}. The *blue* contour lines correspond to the HCO$^+$ $J = 4 \rightarrow 3$ transition with a peak emission $\sim$ 130 K km s^{-1}. While the *green* contour lines correspond to the [C I] $J = 1 \rightarrow 0$ with a peak emission of $\sim$ 200 K km s^{-1}. The contour levels (from thin to thick) are the 10%, 25%, 50%, 75% and 90% of the peak emission. The *red stars* show the location of O and B ionizing stars, while the *white* star corresponds to the X-ray counter part of the CEN1 (NE component) binary system (Beetz et al., 1976; Hanson et al., 1997; Broos et al., 2007). The *black circles* correspond to the heavily obscured ($E_{median} > 2.5$ keV, $A_V \geq 10$ mag) population of X-ray sources around the M17-UC1 region (Fig.10 in Broos et al. 2007; coordinates from the VizieR catalogue). The reference position ($\Delta\alpha = 0$, $\Delta\delta = 0$) is the same as in Fig 7.1. The [C I], HCN and HCO$^+$ maps have a slightly lower integrated temperature than in Fig. 7.1 and Fig. 7.2 because they were convolved to a $30''$ beam resolution to smooth the contour lines.

their respective original resolutions) along the strip direction. We do not show here the strip lines at P.A.=63° because we do not have HCN and HCO$^+$ data at lower declinations.

The HCO$^+$ and HCN $J = 4 \rightarrow 3$ lines have their peaks between offset $-60''$ and $-80''$ in R.A., which corresponds to the peaks of the ^{13}CO and ^{13}CO lines. On the other hand, both [C I] lines peak at about $-120''$ offset, i.e., ~ 0.8 pc from the ridge. These peaks coincide with a secondary peak of ^{13}CO, and a second peak observed at a slight offset ($\sim 10''$) in the HCO$^+$ and HCN lines.

The [C I] (369μm) $J = 2 \rightarrow 1$ is brighter than the (609μm) $J = 1 \rightarrow 0$ along the strip line, and throughout the whole region mapped (Fig. 7.1). The same is observed for the HCN and HCO$^+$ lines, where the HCO$^+$ $J = 4 \rightarrow 3$ line is unusually brighter (for Galactic standards) than the HCN line. From the ratio between the [C I] lines, the excitation conditions of the diffuse gas can be estimated. Similarly, the ratio between the HCO$^+$ and HCN $J = 4 \rightarrow 3$ lines can give hints to the origin of the bright HCO$^+$. These will be discussed in the following sections.

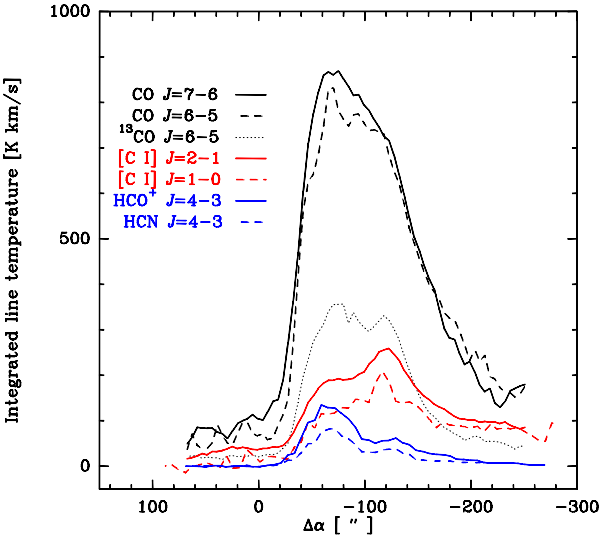

Figure 7.5: The strip lines of the velocity integrated temperature of ^{12}CO $J = 7 \rightarrow 6$ (black), ^{12}CO $J = 6 \rightarrow 5$ (black dashed), ^{13}CO $J = 6 \rightarrow 5$ (black dotted) and [C I] $J = 2 \rightarrow 1$ (red) are the same as in Fig. 3 by Pérez-Beaupuits et al. (2010). The new strips lines in [C I] $J = 1 \rightarrow 0$ (red dashed), HCO$^+$ $J = 4 \rightarrow 3$ (blue), and HCN $J = 4 \rightarrow 3$ (blue dashed) are taken at the same declination $\Delta\delta = 30''$ (P.A. $90°$) across the ionization front of M17 SW. All the strip lines are smoothed spatially with respect to the strip direction. The X-axis corresponds to the actual offset in R.A. of the maps shown in Figs. 7.1 and 7.2. The offset, $\Delta\alpha = 0''$ in R.A. correspond to the reference illuminating star SAO 161357.

7.4.2 The diffuse gas in M17 SW

The [C I] 369μm / [C I] 609μm ratio

The *top panel* of Fig. 7.6 shows the colour map of the ratio $R = I([\text{C I}]\ J = 2 \rightarrow 1)/I([\text{C I}]\ J = 1 \rightarrow 0)$ between the velocity-integrated temperatures of the [C I] lines, and the contour lines corresponding (from thin to thick) to 10%, 25%, 50%, 75% and 90% of the peak emission of [C I] $J = 2 \rightarrow 1$ (Fig. 7.1). The ratio is larger than unity (indicating optically thin emission, where the line intensities are proportional to the upper state column density; e.g., Zmuidzinas et al. 1988) in most of the region mapped. Ratios lower than unity, which are expected for optically thick emission, are also observed mostly in the inner region of M17 SW, about 1.5 pc ($\sim 140''$) from the ionization front.

In order to ensure a high enough S/N ratio in the R map, we set to zero the pixels where any of the two [C I] lines is lower than 5% of their corresponding peak integrated temperature. In most of the region mapped the ratios are < 3. Only a few pixels in the map show higher ratios (up to about 5) at sparse locations between the ionization front and the ionizing OB stars. For better clarity of the colour map we set the maximum scale value to 2.11 in the *top panel* of Fig. 7.6. The value of 2.11 in the line ratio R derives from the optically thin and LTE approximation (e.g., Schneider et al., 2003; Kramer et al., 2004) used to estimate the excitation

temperature of [C I] in the next section. The ratio R ranges between 1.0 and 1.5 in most of the region where the integrated temperature of the [C I] $J = 2 \rightarrow 1$ line is brighter than 50% of its peak.

These ratios match the values expected in a PDR environment with low density ($\lesssim 10^3$ cm^{-3}) and relatively low radiation fields ($G_0 \lesssim 10^3$) as shown by Meijerink et al. (2007, their Fig.3). These densities agree well with previous estimates (e.g., Meixner et al., 1992).

The excitation temperature of [C I]

In the optically thin limit (which holds for the region mapped where $R > 1$ in the *top panel* of Fig. 7.6) we can estimate the excitation temperature T_{ex} of [C I] from the ratio R as: $T_{ex} = 38.8/ln(2.11/R)$ K (e.g., Schneider et al., 2003). The *bottom panel* of Fig. 7.6 shows the map of the estimated T_{ex} in logarithmic scale. The excitation temperature ranges between $\sim$ 40 K and $\sim$ 100 K in the inner region, whereas temperatures $>$ 100 K are found along the eastern edge of the M17 SW complex, close to the ionization front. This result is in agreement with a previous LTE estimate of the excitation temperature of ^{12}CO (Pérez-Beaupuits et al., 2010), earlier estimates from [C I] $J = 2 \rightarrow 1$ observations (e.g., Genzel et al., 1988) and from a multi-line NH_3 study (Guesten & Fiebig, 1988). The ratios larger than 2.11 found between the ionization front and the ionizing stars (as mentioned in the previous section) would lead to negative excitation temperatures in the optically thin and LTE approximation. Note, however, that ratios larger than 2 can be found in PDR and XDR environments, depending on the local density and incident radiation fields (e.g., Meijerink et al., 2007, their Fig.3).

Optical depths and column density of [C I]

From the excitation temperature and the peak intensity of the [C I] $J = 1 \rightarrow 0$ and $J = 2 \rightarrow 1$ lines, the optically thin approximation also allows us to estimate the optical depths of both lines. Knowing the excitation temperature and the optical depth of the $J = 1 \rightarrow 0$ line, the column density N([C I]) can be computed as well. For detailed formulae see Schneider et al. (2003).

Fig. 7.7 shows the optical depth τ of the $J = 1 \rightarrow 0$ line (*top left panel*), which appears to be more optically thin ($\tau \leq 1$) than the $J = 2 \rightarrow 1$ line (*top right panel*). Optically thick ($\tau \geq 1$) emission is found mostly in the $J = 2 \rightarrow 1$ line at the inner region mapped, where this line is brighter than 75% of its peak intensity. In order to compare the optical depths, the colour scale in the *middle panel* was fixed at the same maximum value as in the $J = 1 \rightarrow 0$ line. Although τ up to about 4.7 were found in the $J = 2 \rightarrow 1$ line. This is not self-consistent with the initial assumption of optically thin regime. Therefore, the excitation temperature and column densities estimated for those particular pixels must be considered carefully.

The column density N (cm^{-2}) of [C I] (*bottom panel* of Fig. 7.7) ranges between $\sim 10^{17.6}$ cm^{-2} and $\sim 10^{19}$ cm^{-2} in most of the region where the maps show a strong ($\geq$ 50% of the peak integrated temperature) [C I] emission.

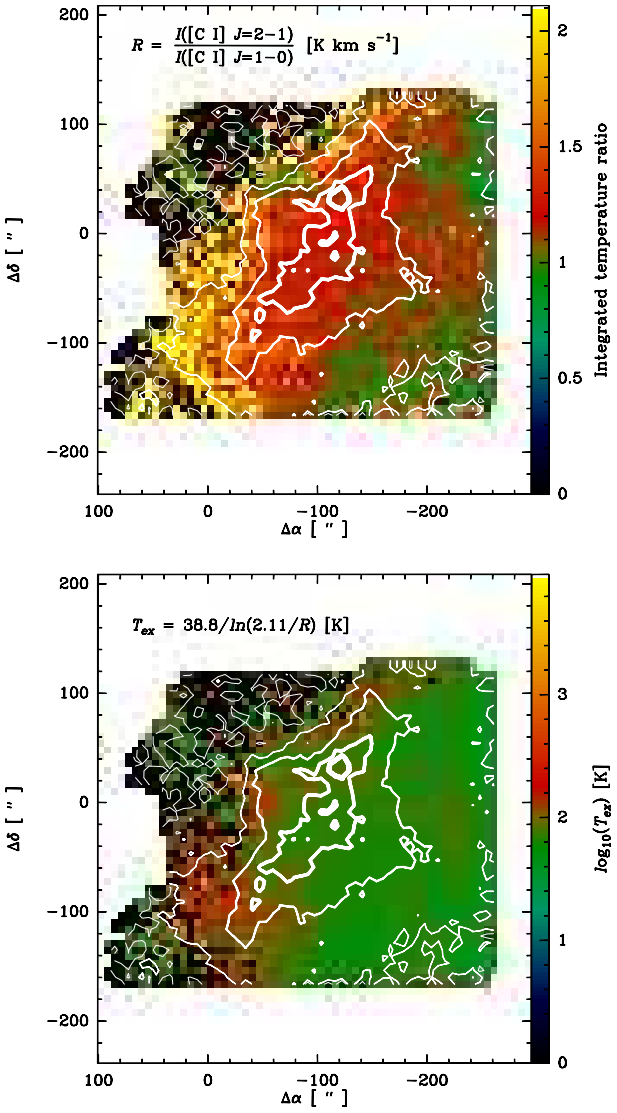

Figure 7.6: *Top panel* - Map of the ratio $R = I([\mathrm{CI}]\ J = 2 \rightarrow 1)/I([\mathrm{CI}]\ J = 2 \rightarrow 1)$ between the velocity-integrated temperatures of the $J = 2 \rightarrow 1$ and $J = 1 \rightarrow 0$ transitions of [C I]. *Bottom panel* - Map of the excitation temperature of [C I] estimated from the ratio R, assuming the lines are in the optically thin regime ($R > 1$), which holds for most of the region mapped. As in Fig. 7.1, the contour lines correspond (from thin to thick) to 10%, 25%, 50%, 75% and 90% of the peak emission of [C I] $J = 2 \rightarrow 1$.

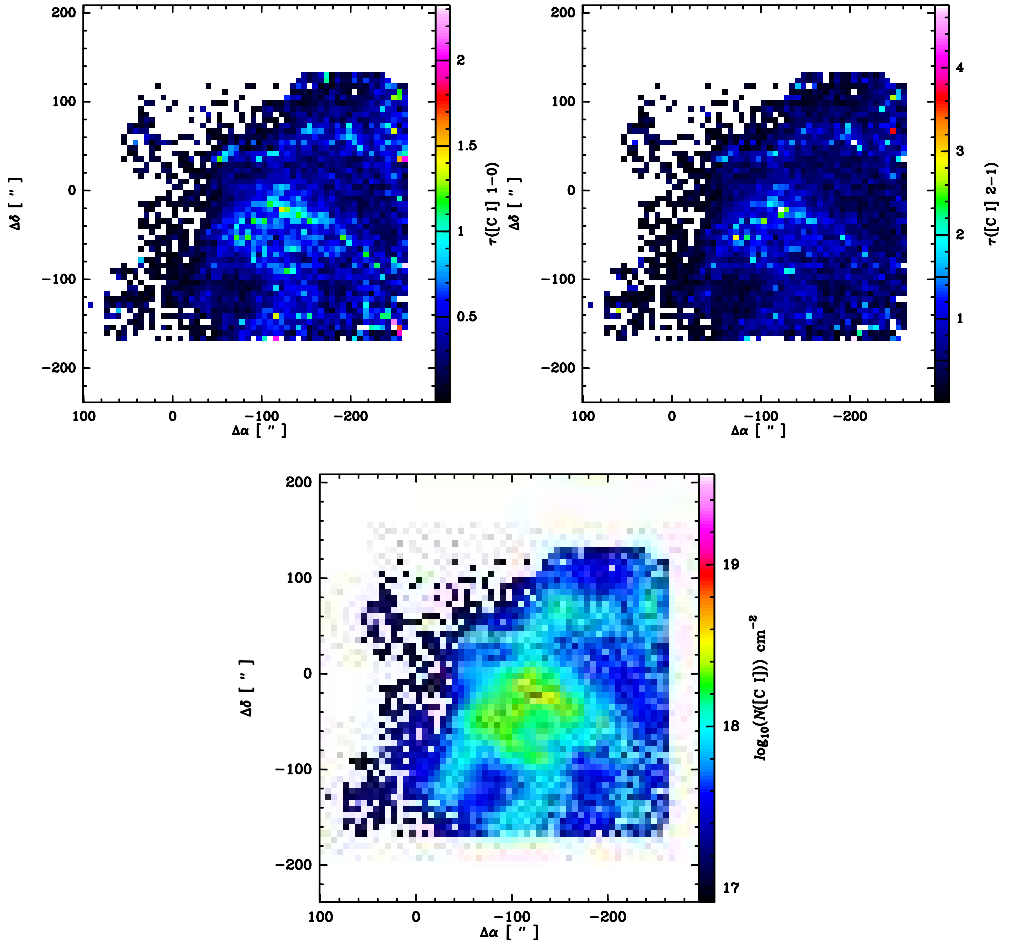

Figure 7.7: Maps of the optical depths τ of [C I] $J = 1 \rightarrow 0$ (*top left panel*), $J = 2 \rightarrow 1$ (*top right panel*), and the column density N (*Bottom panel*) of [C I], calculated in the optically thin approximation.

7.4.3 The dense gas in M17 SW

Origin of the bright HCO^+ in M17 SW

An HCO^+/HCN $J = 4 \rightarrow 3$ line ratio larger than unity can be reproduced by standard PDR models with Galactic UV radiation fields ($G_0 \gtrsim 10^2$), in gas with densities *lower* than $\sim 2 \times 10^4$ cm^{-3} (e.g., Meijerink et al., 2007). However, earlier observations of HCO^+ and HCN $J = 3 \rightarrow 2$ data in M17 SW allowed to estimate densities of about 5×10^5 cm^{-3} and 10^6 cm^{-3} for the HCO^+ and HCN clumps, respectively (Hobson, 1992). Therefore, a standard PDR scenario *cannot* explain the high (> 1) HCO^+/HCN $J = 4 \rightarrow 3$ line ratios.

On the other hand, PDRs with elevated cosmic-ray rates (about 200×Galactic $\sim 5 \times 10^{-15}$ s^{-1}) can enhance the abundance of HCO^+ with respect to HCN, and line

intensity ratios similar to those observed in M17 SW can be expected (Meijerink et al., 2006). However, there is no evidence for recent supernovae in M17 SW, so the cosmic-ray rates in this region are not expected to be high enough to reproduce the observed results. These leave three possible mechanisms that can lead to the high HCO^+/HCN ratios: (1) a high optical depths or subthermal excitation of HCN, (2) mid-IR pumping of HCO^+, and (3) high ionization flux from embedded X-ray sources. We discuss these alternatives in the following sections.

Optical depth effects and subthermal excitation

The typical optical depths of the HCO^+ and HCN clumps were found to be $\sim$20 and $\sim$100, respectively, for the $J = 3 \rightarrow 2$ lines (Hobson, 1992). So both lines are optically thick, with a factor ~ 5 between their optical depths. From the molecular and collision data reported in the LAMDA database, we know that in both molecules the Einstein-A coefficient of the $J = 4 \rightarrow 3$ line is about 2.5 times larger than that of the $J = 3 \rightarrow 2$ line of the respective molecules. Similarly, the upper energy level and the critical density of the higher transition are a factor $\sim$1.7 and $\sim$2.5, respectively, larger than those of the $J = 3 \rightarrow 2$ line. Since these factors between the transitions are practically the same for both molecules, we can assume that the optical depth of the HCN $J = 4 \rightarrow 3$ line is also about 5 times larger than that of the HCO^+ $J = 4 \rightarrow 3$ line, and most likely they are both optically thick as well.

The critical densities of the HCO^+ and HCN $J = 4 \rightarrow 3$ lines are $\sim 9 \times 10^6$ cm^{-3} and $\sim 10^8$ cm^{-3}, respectively, for temperatures between 20 K and 100 K. However, the gas densities estimated from the $J = 3 \rightarrow 2$ lines are on the order of 10^6 cm^{-3} (Hobson, 1992). Therefore, both HCO^+ and HCN $J = 4 \rightarrow 3$ lines are subthermally excited, and the lines are clearly detected because of their large optical depths.

The higher optical depth of HCN may lead to a saturated and flat-topped line profile (e.g., Martin et al., 1984; Solomon et al., 1987). This characteristic is observed in both HCN and HCO^+ lines (Fig. 7.3). However, according to Hobson (1992) the high optical depths found for the $J = 3 \rightarrow 2$ lines are consistent with the presence of about 3–4 (rather than 1) individually optically thick clumps (at different systemic velocities) along the line of sight, which yield the shape of the observed line profiles. Therefore, optical depth effects can be ruled out as the cause of the high HCO^+/HCN $J = 4 \rightarrow 3$ line ratio.

On the other hand, a larger filling factor of HCO^+ may also lead to a stronger line brightness. However, the HCN and HCO^+ molecules reach their peak abundances at similar depths (column densities) in a molecular cloud (e.g., Hollenbach & Tielens, 1999; Meijerink & Spaans, 2005). Therefore, they are expected to co-exist at the typically observed $\tau = 1$ surfaces, which leads to similar filling factors. This is supported by the size of the HCN clumps, which were found to be just marginally smaller than the HCO^+ clumps, down to the scale of the $19''$ telescope beam used by (Hobson, 1992). Therefore, different filling factors can also be excluded as the cause of the brighter HCO^+ emission.

Since HCN and HCO^+ are expected to co-exist at similar depths in a cloud, the kinetic temperature of their surrounding gas must also be similar. But the critical

density of the HCO^+ $J = 4 \rightarrow 3$ line is about one order of magnitude lower than that of HCN, which makes HCO^+ more easily excited (collisionally) in single-phase molecular gas. These leaves open the possibility of a lower excitation temperature of the HCN $J = 4 \rightarrow 3$ line as the explanation for the unusually high HCO^+/HCN $J = 4 \rightarrow 3$ line ratio.

Still, we cannot really conclude on this because the optical depths of the $J = 3 \rightarrow 2$ lines, as well as the ambient densities, were estimated assuming standard relative abundances in molecular clouds (from Irvine et al. 1987) of 2×10^{-8} and 3×10^{-9} for HCN and HCO^+, respectively (Hobson, 1992). Thus, the effects of UV and X-ray irradiation, that can enhance (or suppress) the abundance of one molecule with respect to the other (e.g., Maloney et al., 1996; Hollenbach & Tielens, 1999; Meijerink & Spaans, 2005) were not taken into account in the earlier analysis of the lower transition lines. Therefore, our current data do not allow us to determine whether the stronger HCO^+ $J = 4 \rightarrow 3$ line brightness is due to a lower excitation temperature of the HCN $J = 4 \rightarrow 3$ line or because of an unusual enhancement of the HCO^+ abundance. A future excitation analysis based on the $4 \rightarrow 3/3 \rightarrow 2$ line ratio of both molecules will shed light on this issue.

Infrared pumping of the molecular gas

In environments where the UV/X-ray surface brightness is high enough to heat the dust up to several hundred K, like in AGNs or bright starbursts, strong HCN emission may be explained by the infrared radiative pumping scenario (e.g., Aalto et al., 1995; García-Burillo et al., 2006; Guélin et al., 2007; Aalto et al., 2007b), since hot dust produces strong mid-infrared continuum emission in the 10–30 μm wavelength range.

Because the HCN molecule has its first bending mode at 14.0 μm wavelength, the surrounding molecular gas can be vibrationally excited by absorbing these infrared 14.0 μm photons, and the subsequent cascade process can enhance HCN rotational lines in the sub-millimeter and millimeter range. According to Guélin et al. (2007), the infrared pumping scenario may also work for molecules like HCO^+ and HNC, because they have similar transitions at 12.1 μm and 21.7 μm, respectively, and fairly large Einstein-A coefficients ($A \approx 1 - 7$ s^{-1}, Nezu et al. 1999).

Earlier ISO/SWS infrared observations (in the $\sim 10 - 40$ μm wave range) toward M17 SW allowed to estimate temperatures between 105 K and 130 K for the amorphous carbon grains, while the silicate grain temperature was estimated to be in the range 55–63 K (Jones et al. 1999). From the Wien's displacement law $\lambda_{max} T = b$ (with $b = 2.898 \times 10^{-6}$ Knm), we have that the continuum (black body) radiation peaks at $\lambda_{max} \gtrsim 20$ μm. Therefore, if we assume that these dust temperatures are high enough to pump the HCO^+ molecule, then HNC and HCN must be affected even more by this process.

If the infrared pumping scenario is at work for these particular molecules, absorption features must be detected in infrared spectra at 12.1 μm (HCO^+), 14.0 μm (HCN), and 21.7 μm (HNC). We do not have high resolution IR spectra to check if this is the case in the core of M17 SW. However, these wavelengths, and the Wien's

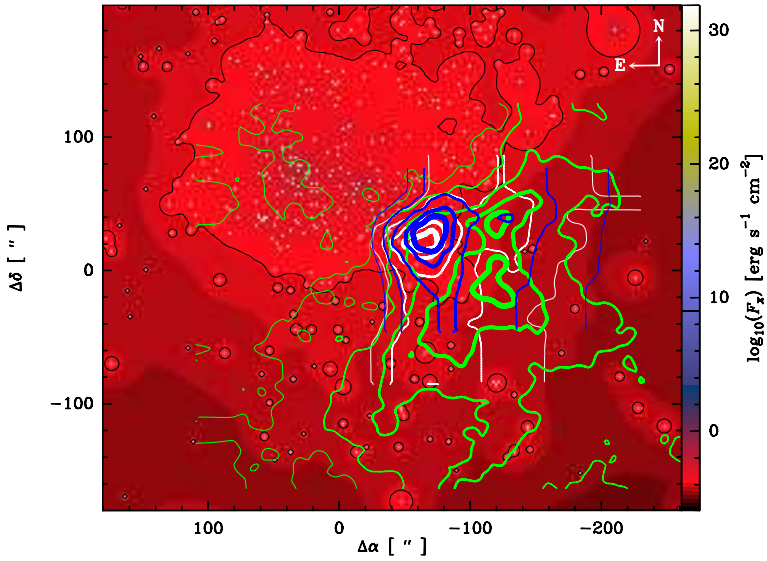

Figure 7.8: Colour map of the hard ($2 - 8$ keV band) X-ray flux F_x (erg cm^{-2} s^{-1}) estimated from the thermal plasma fits of the photometrically selected *Chandra*/ACIS sources by Broos et al. (2007) (coordinates and luminosities from the VizieR catalogue). The *black* contour lines demarcate the $log_{10}(F_x) = -4.1$ flux level. The *white* contour lines correspond to the HCN $J = 4 \rightarrow 3$ transition with a peak emission of ~ 90 K km s^{-1}. The HCO$^+$ $J = 4 \rightarrow 3$ transition, with peak emission ~ 130 K km s^{-1}, is shown with *blue* contour lines. While the *green* contour lines correspond to [C I] $J = 1 \rightarrow 0$ with a peak emission of ~ 200 K km s^{-1}. The contour levels (from thin to thick) are 10%, 25%, 50%, 75% and 90% of the peak emission. The reference position ($\Delta\alpha = 0$, $\Delta\delta = 0$) is the same as in the previous figures.

law, imply that the HNC molecule would be easier to pump by the IR photons than HCN, while HCO$^+$ would be the most difficult one to be affected by this process.

The X-ray sources in M17 SW

Typically, the HCO$^+$ lines are stronger in XDRs than in PDRs by a factor of at least three. This is consequence of the higher ionization degree in XDRs (Meijerink & Spaans, 2005), leading to an enhanced HCO$^+$ formation rate. The HCO$^+$ abundance is high over a much wider range of ionization rates than HCN (Lepp & Dalgarno, 1996, their Figs. 2 and 3). Therefore, we also study the possibility of an over-abundance of HCO$^+$ produced by X-ray sources embedded in the molecular gas of M17 SW.

Using the luminosities estimated from thermal plasma (546 sources) and power law (52 sources) fits of the photometrically selected *Chandra*/ACIS sources by (Broos et al., 2007), we estimate the total X-ray luminosities of all these 598 sources in M17 SW. Knowing the coordinates and luminosities of the combined 598 X-ray sources (from the VizieR catalogue) we estimate the cumulative flux at any position in our maps, considering that the flux decreases with the square of the distance d

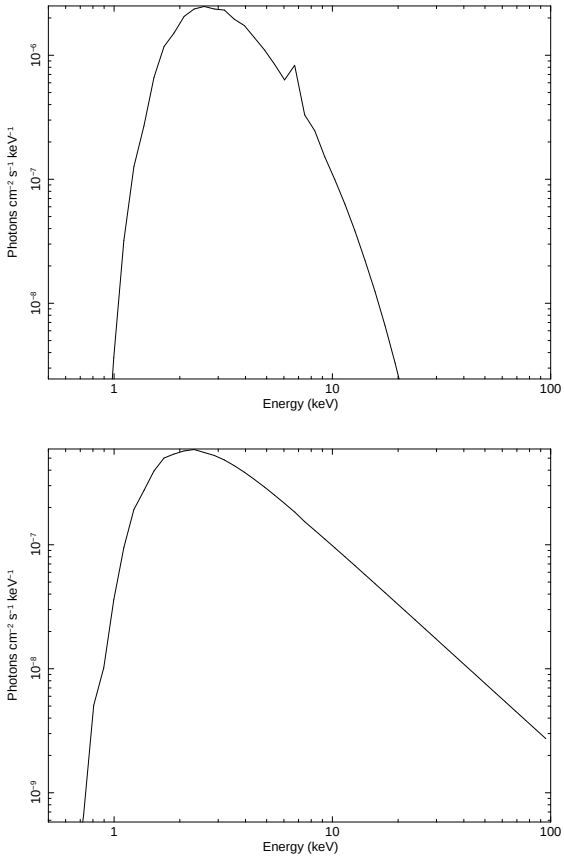

Figure 7.9: *Top panel* - Thermal plasma fit of the *Chandra*/ACIS source 387 with $kT = 3.5$ keV. *Bottom panel* - Power law fit of the *Chandra*/ACIS source 547 with photon index $\gamma = 1.6$ (the model parameters are from Broos et al. 2007, and the VizieR online catalogue). The models are reproduced with the Xspec package (http://heasarc.gsfc.nasa.gov/docs/xanadu/xspec).

from a particular X-ray source.

In the literature we find several estimates of the distance to M17. The distance ranges from 1.3 kpc (Hanson et al., 1997) to 2.2 kpc (Chini et al., 1980). The latter was used as reference in our previous work. In this paper we adopt a distance of ~ 1.6 kpc estimated from a more recent study by Nielbock et al. (2001), which is consistent with the results from Townsley et al. (2003) and with the NIR study of Jiang et al. (2002). At the distance of 1.6 kpc, one arcsecond ($1''$) corresponds to ~ 0.0078 pc in the projected R.A.–Dec. plane of M17. This allows us to estimate the projected distance between a pixel in our maps and a given X-ray source, and therefore, the flux $F_x = L_t/4\pi d^2$ (erg cm^{-2} s^{-1}) at each pixel of the map, from all the 598 available luminosities L_t of the total observed X-ray band (between 0.5 keV and 8 keV).

However, the X-ray sources emit significantly in the higher (>10 keV) energy

band that is not observed by Chandra. Hence, we used model fits to estimate the integrated X-ray luminosities up to 50 keV. Since the thermal plasma models (top panel in Fig. 7.9) of 546 sources present a sharp decay at energies >10 keV, their contribution to the integrated luminosity is not significant. However, the power-law fit models (bottom panel in Fig. 7.9) of 52 sources did contribute about one order of magnitude in ambient X-ray flux since their energy decay is not as steep as that of the thermal plasma models. These extended integrated luminosities of the thermal plasma models correspond to lower limits only since we do not actually know the X-ray spectrum for energies higher than 8 keV. Therefore, higher energy photons could make a larger contribution to the X-ray flux emerging from those sources, if they have power-law tails.

Note that we are assuming that all the X-ray sources are in the same plane (i.e. at the same distance from us), and we do not have the full 3-D distribution of density clumps that would allow us to estimate the photoelectric absorption of the low energy (< 10 keV) photons along a path between an X-ray source and a particular clump in M17 SW (e.g., Maloney et al., 1996; Meijerink & Spaans, 2005).

Integrating the flux contribution from all the 598 X-ray sources with estimated luminosities between 0.5 keV and 50 keV, we obtain the map of the hard X-ray flux F_x shown in Fig. 7.8. The [C I] $J = 1 \rightarrow 0$, as well as the HCN and HCO^+ $J = 4 \rightarrow 3$ transitions are overlaid. The peak intensities of HCN and HCO^+ coincide with a region where the estimated X-ray flux is $F_x \gtrsim 8 \times 10^{-5}$ erg cm^{-2} s^{-1} (demarcated with the *black* contour lines). Whereas the [C I] peak intensity tends to avoid this region. The impinging flux is about three orders of magnitude lower than what is usually adopted in XDR models, where higher radiation fluxes are expected to emerge from the accretion process of an AGN or stellar super-winds (e.g., Meijerink & Spaans, 2005; Meijerink et al., 2007; Spaans & Meijerink, 2007).

In order to drive an XDR, an X-ray source with a luminosity of about 10^{32} erg s^{-1} would be required to be within a few arcsecs of the region of the HCO^+ $4 \rightarrow 3$ peak emission (or large HCO^+/HCN $4 \rightarrow 3$ line ratio). The high density ($n(H_2) > 10^5$ cm^{-3}) of the gas in the core of M17 SW, and the fact that many more X-ray sources were found outside the molecular region of M17 SW, while no X-ray sources were detected by *Chandra*/ACIS within a radius of $\sim 10''$ (~ 0.08 pc) around the peak HCO^+ emission ($\Delta\alpha \approx -68$,$\Delta\delta \approx 18$), suggests that all X-ray photons with energy <10 keV are heavily absorbed by the large column density of the gas. If we assume a standard abundance for [C I] of 1.4×10^{-4} (e.g., Meijerink & Spaans, 2005) and a [C I] column density of $\sim 10^{18}$ cm^{-2} (Fig. 7.7) estimated at the peak of HCO^+, we get a total column density of at least $N_{\rm H} \sim 10^{22}$ cm^{-2}, which corresponds to the column contributed *only* by the diffuse gas surrounding the dense molecular gas in that region. While such diffuse gas column suffices to absorb all $\sim$1 keV photons already, the molecular hydrogen column density has been estimated to be as large as $\sim 8 \times 10^{23}$ cm^{-2} (Stutzki & Guesten, 1990), which can easily absorb the higher (>1 keV) energy photons. Therefore, future observations at higher energies ($kT > 10$ keV) are required in order to detect any heavily obscured X-ray source in the dense core of M17 SW.

7.5 Conclusions

We used the dual channel DSB receiver FLASH (Heyminck et al., 2006) on the APEX telescope, to map (with $12''.7$ resolution) a region of about $4.1\ \mathrm{pc} \times 4.7\ \mathrm{pc}$ in the $^3P_1 \rightarrow {}^3P_0$ 609 μm ($J = 1 \rightarrow 0$) fine-structure transition of [C I], and a smaller region of about $2.6\ \mathrm{pc} \times 1.3\ \mathrm{pc}$ in the $J = 4 \rightarrow 3$ lines of HCN and HCO^+ (with $17.5''$ resolution) in the M17 SW nebula.

Using our earlier observation of the $^3P_2 \rightarrow {}^3P_1$ 370 μm ($J = 2 \rightarrow 1$) fine-structure line of [C I], we found that the [C I] $I(J = 2 \rightarrow 1)/I(J = 1 \rightarrow 0)$ ratio is larger than unity in most of the region. This indicates optically thin emission, which allows us to estimate the excitation temperature T_{ex} of [C I]. We found that T_{ex} ranges between ~ 40 K and ~ 100 K in the inner region, and > 100 K along the easthern edge of M17 SW. In the optically thin limit the [C I] column density ranges between $\sim 10^{17.6}\ \mathrm{cm}^{-2}$ and $\sim 10^{19}\ \mathrm{cm}^{-2}$ in most of the region where the [C I] emission is ≥ 50% of its peak integrated temperature.

We found that the HCO^+/HCN $J = 4 \rightarrow 3$ line ratio is larger than unity in all of the region mapped, which cannot be explained with a standard PDR model. We discuss different mechanisms (elevated cosmic-ray rates, filling factors, optical depth and excitation effects, infrared pumping, and X-ray irradiation) that could reproduce this result. We conclude that the most likely mechanisms that can produce the bright HCO^+ emission is the radiation emitted by embedded X-ray sources or a lower excitation temperature of HCN.

The analysis of the X-ray energy (between 0.5 keV and 50 keV) budget estimated from *Chandra*/ACIS observations leads to an X-ray flux irradiating the dense core of M17 SW that is not sufficient to drive an XDR. However, the energy budget analysis and the X-ray spectral model fits, are limited to the observed 0.5 keV – 8 keV band. Since about 91% of the ACIS X-ray sources are modeled with thermal plasma fits (which have a sharp cut-off at $\sim 10\ \mathrm{keV}$), we miss information on all the high energy ($>$10 keV) photons that can contribute significantly to the total X-ray flux. The low energy photons ($<$10 keV) are completely absorbed by the large ($N_{\mathrm{H}} > 10^{22}\ \mathrm{cm}^{-2}$) column densities observed in the dense core of M17 SW. Observations at high energy are needed to reveal the heavily obscured X-ray sources, and to allow for a complete energy budget analysis.

Likewise, a further excitation analysis based on the ratio between the $J = 4 \rightarrow 3$ and lower transitions of HCN and HCO^+ is required to distinguish between a lower excitation temperature of HCN and an unusually higher abundance of HCO^+.

Acknowledgements

We are grateful to the MPIfR team and the APEX staff for their help and support during and after the observations. We are grateful to C. Brogan for providing the 21 cm map, and to B. Hiemstra and B. Beygu for helpful discussions on *Chandra* and X-ray data analysis. Molecular Databases that have been helpful include the NASA/JPL and LAMDA.

8

Highlights and Outlook

The most relevant results and conclusions obtained from the studies described throughout the thesis are presented in this final chapter. The not fully understood problems and further proposed investigation are described afterwards.

8.1 Remarks

Single dish observations of the $J = 3 \rightarrow 2$ transition of HNC and HCN, and the $J = 2 \rightarrow 1$ and $J = 1 \rightarrow 0$ lines of CN, are presented (Chap. 2) for the HNC-luminous Seyfert galaxies NGC 1068, NGC 1365, NGC 3079, NGC 2623, and NGC 7469. From the $J = 3 \rightarrow 2/J = 1 \rightarrow 0$ line ratios we estimate the excitation conditions of HCN and HNC in these galaxies. We conclude that in two of these galaxies (NGC 1068, NGC 3079) the HNC emission emerges from gas with densities $n(\mathrm{H_2}) \lesssim 10^5\ \mathrm{cm^{-3}}$, where the chemistry is dominated by ion-neutral reactions. The observed HCN/HNC and CN/HCN line ratios favor a PDR scenario, rather than an XDR one, which is consistent with previous indications of a starburst component in the central region of these galaxies. However, the $N(\mathrm{HNC})/N(\mathrm{HCN})$ column density ratios observed in NGC 3079 are consistent only with those found in XDR environments. However, since the starburst region is of a larger angular scale than the AGN, its effects can be contaminating the observations (through the larger beam size of the $J = 1 \rightarrow 0$ lines), leading to the favored PDR scenario found with our models.

The excitation conditions of HCN, HNC, and CN are estimated (Chap. 3) toward the nuclear region of NGC 1068, based on line intensity ratios and radiative transfer models. A first-order estimate, based on single dish observations of the $J = 1 \rightarrow 0$ lines from different telescopes (beam sizes), leads to starburst contribution factors of 0.58 and 0.56 for the CN and HCN, respectively. We find that the bulk emission of HCN, HNC, CN, and the high-J HCO^+ emerges from dense gas ($n(\mathrm{H_2}) \geq 10^5\ \mathrm{cm^{-3}}$). However, the low-$J$ HCO^+ lines (dominating the HCO^+ column density) trace less dense ($n(\mathrm{H_2}) < 10^5\ \mathrm{cm^{-3}}$) and colder ($T_K \leq 20$ K) gas, whereas the high-J HCO^+ emerges from warmer (> 30 K) gas than the other molecules. The HCO^+ $J = 4 \rightarrow 3$ line intensity, compared to the lower transition lines and to the

HCN $J = 4 \rightarrow 3$ line, support the influence of a local XDR environment. The estimated $N(\mathrm{CN})/N(\mathrm{HCN}) \sim 1-4$ column density ratios are indicative of an XDR/AGN environment with a possible contribution of grain-surface chemistry induced by X-rays or shocks.

The first Spitzer IRS maps of the nuclear region of NGC 4945 in the fine-structure line [Ne V] at 14.32 μm, the deep silicate absorption feature at 9.7 μm, and other emission lines, are presented (Chap. 4). We estimate an extinction (A_{V}) map based on the apparent strength of the 9.7 μm absorption feature. The peak emission of most of the extinction corrected lines coincides (within $\sim 1''$, or ~ 18 pc at the distance of 3.7 Mpc) with the position of the H_2O maser, adopted as the location of the AGN. The [Ne V]/[Ne II] ratios obtained in all the mapped regions are lower than the ratios typically observed in AGNs. Whereas the [Ne III]/[Ne II] ratios observed along the starburst ring are consistent with the ratios expected in shocks. This is interpreted as an excess [Ne II] emission driven by the starburst ring, or by SN remnants. An extinction $A_{\mathrm{V}} \sim 5500$ mag is needed in order to obtain a typical AGN [Ne V]/[Ne II] line ratio of ~ 0.8 towards the H_2O maser. This high extinction is consistent with the extreme column density $N_{\mathrm{H}} > 10^{24}$ cm^{-2} obscuring the AGN BLR of NGC 4945, as estimated from X-ray observations.

The chemical abundances and excitation aspects of X-ray irradiation (XDR) by an AGN are studied (Chap. 5) for the molecular gas in a 3-D hydrodynamic model of an AGN torus. Line intensities are estimated using a 3-D radiative transfer code based on multi-zone escape probability techniques with fixed directions. We found an average XDR-derived temperature about $\gtrsim 1$ to ~ 100 times higher than the average temperature estimated in the hydrodynamical model within the inner ± 20 pc radius from the torus, where the X-ray flux is $F_X \gtrsim 1.1$ erg s^{-1} cm^{-2}. The average H_2 XDR-derived density, instead, follows an inverse relation with the X-ray flux, being lower (by factors up to $\sim 10^4$) than the average density of the hydrodynamical model in the inner ± 20 pc around the AGN.

The CHAMP$^+$ receiver on the APEX telescope was used (Chap. 6) to map (with $7'' - 9''$ resolution, or $0.07 - 0.1$ pc at the distance of 2.2 kpc) the M17 SW star-forming region in mid-J transitions of ^{12}CO, ^{13}CO, and in the 370 μm fine-structure line of [C I]. The warm gas was found to extend up to a distance of ~ 2.2 pc from the M17 SW ridge. The structure and distribution of the [C I] $^3P_2 \rightarrow {}^3P_1$ 370 μm map indicate that its emission arises from the interclump medium with densities of $\sim 10^3$ cm^{-3}. A non-LTE model suggests that the kinetic temperature at four selected positions cannot exceed 230 K in clumps with density of $n(\mathrm{H_2}) \sim 5 \times 10^5$ cm^{-3}, and that the warm ($T_k > 100$ K) and dense ($n(\mathrm{H_2}) \geq 10^4$ cm^{-3}) gas traced by the mid-J ^{12}CO lines represents just about 2% of the bulk of the molecular gas. The clump densities lead to clump volume-filling factors of $0.04 - 0.11$ at these positions.

The APEX/FLASH receiver was used (Chap. 7) to map the 609 μm fine-structure line of [C I] toward M17 SW. Maps of the HCN and HCO$^+$ $J = 4 \rightarrow 3$ lines are also presented. We compare the 609 μm fine-structure line of [C I] with the transition at 370 μm presented in Chap. 6. The [C I]$_{370\ \mu\mathrm{m}}$/[C I]$_{609\ \mu\mathrm{m}}$ integrated temperature ratio is > 1 in most of the region mapped. Assuming optically thin emission, the

excitation temperature of [C I] ranges between 40 K and 100 K in the inner region of M17 SW. While excitation temperatures > 100 K are found along the eastern edge of the cloud. The column density of [C I] ranges between $\sim 4 \times 10^{17}$–10^{19} cm^{-2} in the region where the [C I] integrated temperature is larger than 50% of its peak emission. The HCO^+ $J = 4 \rightarrow 3$ line was found to be a factor $\sim 1 - 6$ brighter than HCN across the region mapped, and presents more extended emission. This unusually high HCO^+/HCN $J = 4 \rightarrow 3$ line ratio is argued to be an indication of irradiation by heavily obscured X-ray sources, or to be the result of a lower excitation temperature of HCN.

8.2 Prospects

Intense star formation, black hole accretion and the coalescence of active galactic nuclei are crucial phases in galaxy evolution. How these processes interact and drive feedback in galaxy centers, and the impact that they have on the (mostly dense, molecular) interstellar medium and star forming gas, is far from understood.

The physical properties of AGNs and the surrounding gas are often obscured at IR and optical wavelengths due to dust and large ($N_{\mathrm{H}} \sim 10^{24}$ cm^{-2}) absorbing columns of gas. However, (sub)-millimeter and X-ray observations do reveal these hidden processes. And high resolution observations at (sub-)millimeter wavelengths can shed light on the interaction and feedback processes between the accreting black hole and the starburst activity. Specifically, one needs a better understanding of the radiative (UV and X-ray photons), mechanical (supernova shocks and outflows) and chemical (heavy element pollution) feedback processes in nuclei of galaxies. Studies of atomic and molecular emission triggered by these processes can advance our understanding of the interaction (and feedback) between these processes in galaxy centers, and the impact that they have on the (mostly dense, molecular) interstellar medium and star-forming gas.

High spatial resolution observations of Galactic star-forming regions (e.g., M17 SW) and the Galactic center are particularly important since molecular clouds of the size of maps ($\sim 3 \times 3$ pc^2) recently reported (Chap. 7 and 6) will be resolved spatially by ALMA*, at the distance of nearby galaxies like the prototypical Seyfert NGC 1068 ($D \sim 14$ Mpc, Chap. 2 and 3) or the LIRG NGC 4945 ($D \sim 3.7$ Mpc, Chap. 4). As such, star-forming regions in our own Milky Way can serve as templates for a direct comparison with such regions in active galaxies that will become observable with ALMA in the coming years.

The (sub-)millimeter and mid-IR data I have collected for galaxies like NGC 1068, and the deeply buried AGN of NGC 4945 (Chaps. 2, 3 and 4), will provide diagnostics for unification models of Seyfert galaxies and the observable effects of viewing angle. Interferometric studies I am performing with collaborators, of the ambient conditions and kinematics of the molecular gas in the merging system Arp 299 will give insights to young starbursts, prior to the turning on period of an AGN, and pave the road for future higher resolution observations with ALMA.

* http://www.almaobservatory.org/

The higher excitation lines of CO, the bright fine-structure lines of neutral and ionized atomic carbon, nitrogen and oxygen that are (and will be) accessible with current and future instruments like APEX*/CHAMP+, Herschel†/SPIRE & PACS and SOFIA‡/GREAT will allow to explore the dense, warm and hot (feedback affected) gas in the Galactic center, nearby galaxies, AGNs and starbursts. These lines will be used to probe the physical conditions within regions of active star formation in low and high metallicity environments, allowing the investigation of the role that metallicity plays in the physical structure of star-forming gas and its effect on the resulting line emission.

All these observational data will be used to constrain theoretical models based on the high resolution (pixel size of $\sim 0.25 - 20$ pc in diameter) 3-D hydrodynamical and chemical simulations of galactic nuclei and galaxies (Chap. 5). The line intensity maps of several molecular and atomic species, obtained from the 3-D radiative transfer code, will then be used to guide and interpret future extra-galactic observations that will be performed with the facilities mentioned above.

* http://www.mpifr.de/div/mm/technology_projects/apex.html
† http://sci.esa.int/science-e/www/area/index.cfm?fareaid=16
‡ http://www.sofia.usra.edu/

Bibliography

Aalto S., 2004, in Astronomical Society of the Pacific Conference Series, Vol. 320, The Neutral ISM in Starburst Galaxies, S. Aalto, S. Huttemeister, & A. Pedlar, ed., pp. 3–+

—, 2008, Ap&SS, 313, 273

Aalto S., Booth R. S., Black J. H., Johansson L. E. B., 1995, A&A, 300, 369

Aalto S., Monje R., Martín S., 2007a, A&A, 475, 479

Aalto S., Polatidis A. G., Hüttemeister S., Curran S. J., 2002, A&A, 381, 783

Aalto S., Spaans M., Wiedner M. C., Hüttemeister S., 2007b, A&A, 464, 193

Aharonian F., Akhperjanian A. G., Barres de Almeida U., Bazer-Bachi A. R., Becherini Y., Behera B., et al., 2008, A&A, 492, L25

Albrecht M., Krügel E., Chini R., 2007, A&A, 462, 575

Alonso-Herrero A., Rieke G. H., Colina L., Pereira-Santaella M., García-Marín M., Smith J., Brandl B., Charmandaris V., Armus L., 2009, ApJ, 697, 660

Armus L., Bernard-Salas J., Spoon H. W. W., Marshall J. A., Charmandaris V., et al., 2006, ApJ, 640, 204

Armus L., Charmandaris V., Bernard-Salas J., Spoon H. W. W., Marshall J. A., et al., 2007, ApJ, 656, 148

Armus L., Charmandaris V., Spoon H. W. W., Houck J. R., Soifer B. T., Brandl B. R., Appleton P. N., Teplitz H. I., Higdon S. J. U., Weedman D. W., Devost D., Morris P. W., Uchida K. I., van Cleve J., Barry D. J., Sloan G. C., Grillmair C. J., Burgdorf M. J., Fajardo-Acosta S. B., Ingalls J. G., Higdon J., Hao L., Bernard-Salas J., Herter T., Troeltzsch J., Unruh B., Winghart M., 2004, ApJS, 154, 178

Baan W. A., Henkel C., Loenen A. F., Baudry A., Wiklind T., 2008, A&A, 477, 747

Baan W. A., Loenen A. F., Spaans M., 2010, A&A, 516, A40+

Ballantyne D. R., 2008, ApJ, 685, 787

Barnard R., Stiele H., Hatzidimitriou D., Kong A. K. H., Williams B. F., Pietsch W., Kolb U. C., Haberl F., Sala G., 2008, ApJ, 689, 1215

Baum S. A., Gallimore J. F., O'Dea C. P., Buchanan C. L., Noel-Storr J., Axon D. J., Robinson A., Elitzur M., Dorn M., Staudaher S., 2010, ApJ, 710, 289

Bayet E., Gerin M., Phillips T. G., Contursi A., 2006, A&A, 460, 467

Beetz M., Elsaesser H., Weinberger R., Poulakos C., 1976, A&A, 50, 41

Bergin E. A., Goldsmith P. F., Snell R. L., Ungerechts H., 1994, ApJ, 431, 674

Bergin E. A., Snell R. L., Goldsmith P. F., 1996, ApJ, 460, 343

Bergvall N., Laurikainen E., Aalto S., 2003, A&A, 405, 31

Bernard-Salas J., Spoon H. W. W., Charmandaris V., Lebouteiller V., Farrah D., Devost D., Brandl B. R., Wu Y., Armus L., Hao L., Sloan G. C., Weedman D., Houck J. R., 2009, ApJS, 184, 230

Binette L., Dopita M. A., Tuohy I. R., 1985, ApJ, 297, 476

Black J. H., van Dishoeck E. F., 1991, ApJ, 369, L9

Blandford R. D., 1999, in Astronomical Society of the Pacific Conference Series, Vol. 182, Galaxy Dynamics - A Rutgers Symposium, D. R. Merritt, M. Valluri, & J. A. Sellwood, ed., pp. 87–+

Brandl B. R., Bernard-Salas J., Spoon H. W. W., Devost D., Sloan G. C., Guilles S., Wu Y., Houck J. R., Weedman D. W., Armus L., Appleton P. N., Soifer B. T., Charmandaris V., Hao L., Higdon J. A., Marshall S. J., Herter T. L., 2006, ApJ, 653, 1129

Brock D., Joy M., Lester D. F., Harvey P. M., Ellis Jr. H. B., 1988, ApJ, 329, 208

Brogan C. L., Troland T. H., 2001, ApJ, 550, 799
Broos P. S., Feigelson E. D., Townsley L. K., Getman K. V., Wang J., Garmire G. P., Jiang Z., Tsuboi Y., 2007, ApJS, 169, 353
Brouillet N., Muller S., Herpin F., Braine J., Jacq T., 2005, A&A, 429, 153
Brusa M., Civano F., Comastri A., Miyaji T., Salvato M., Zamorani G., et al., 2010, ApJ, 716, 348
Bryant P. M., Scoville N. Z., 1999, AJ, 117, 2632
Carr J. S., 1987, ApJ, 323, 170
Carroll B. W., Ostlie D. A., 2006, An introduction to modern astrophysics and cosmology, Carroll, B. W. & Ostlie, D. A., ed.
Casoli F., Combes F., Dupraz C., Gerin M., Encrenaz P., Salez M., 1988, A&A, 192, L17
Cecchi-Pestellini C., Bodo E., Balakrishnan N., Dalgarno A., 2002, ApJ, 571, 1015
Chandrasekhar S., 1950, Radiative transfer., Chandrasekhar, S., ed.
Chiar J. E., Tielens A. G. G. M., 2006, ApJ, 637, 774
Chin Y., Henkel C., Whiteoak J. B., Millar T. J., Hunt M. R., Lemme C., 1997, A&A, 317, 548
Chini R., Elsaesser H., Neckel T., 1980, A&A, 91, 186
Chou R. C. Y., Peck A. B., Lim J., Matsushita S., Muller S., Sawada-Satoh S., Dinh-V-Trung, Boone F., Henkel C., 2007, ApJ, 670, 116
Christopher M. H., Scoville N. Z., Stolovy S. R., Yun M. S., 2005, ApJ, 622, 346
Churchwell E., Babler B. L., Meade M. R., Whitney B. A., Benjamin R., Indebetouw R., Cyganowski C., Robitaille T. P., Povich M., Watson C., Bracker S., 2009, PASP, 121, 213
Cid Fernandes R., Heckman T., Schmitt H., González Delgado R. M., Storchi-Bergmann T., 2001, ApJ, 558, 81
Crawford M. K., Genzel R., Townes C. H., Watson D. M., 1985, ApJ, 291, 755
Curran S. J., Aalto S., Booth R. S., 2000, A&AS, 141, 193
Davies R., Genzel R., Tacconi L., Mueller Sanchez F., Sternberg A., 2006, ArXiv Astrophysics e-prints
Davies R. I., Sánchez F. M., Genzel R., Tacconi L. J., Hicks E. K. S., Friedrich S., Sternberg A., 2007, ApJ, 671, 1388
Davies R. I., Sternberg A., Lehnert M. D., Tacconi-Garman L. E., 2005, ApJ, 633, 105
Davies R. I., Tacconi L. J., Genzel R., 2004, ApJ, 602, 148
Depristo A. E., Augustin S. D., Ramaswamy R., Rabitz H., 1979, J. Chem. Phys., 71, 850
Done C., Madejski G. M., Smith D. A., 1996, ApJ, 463, L63+
Done C., Madejski G. M., Życki P. T., Greenhill L. J., 2003, ApJ, 588, 763
Dultzin-Hacyan D., Benitez E., 1994, A&A, 291, 720
Elitzur M., Asensio Ramos A., 2006, MNRAS, 365, 779
Evans II N. J., Davis J. H., Mundy L. G., Vanden Bout P., 1987, ApJ, 312, 344
Farrah D., Afonso J., Efstathiou A., Rowan-Robinson M., Fox M., Clements D., 2003, MNRAS, 343, 585
Farrah D., Bernard-Salas J., Spoon H. W. W., Soifer B. T., Armus L., Brandl B., Charmandaris V., Desai V., Higdon S., Devost D., Houck J., 2007, ApJ, 667, 149
Felli M., Churchwell E., Massi M., 1984, A&A, 136, 53
Ferrarese L., Merritt D., 2000, ApJ, 539, L9
Fixsen D. J., Bennett C. L., Mather J. C., 1999, ApJ, 526, 207
Flower D. R., 2001, MNRAS, 328, 147

Fuente A., García-Burillo S., Gerin M., Teyssier D., Usero A., Rizzo J. R., de Vicente P., 2005, ApJ, 619, L155
Fuente A., Martin-Pintado J., Cernicharo J., Bachiller R., 1993, A&A, 276, 473
Fuente A., Martin-Pintado J., Gaume R., 1995, ApJ, 442, L33
Galliano E., Pantin E., Alloin D., Lagage P. O., 2005, MNRAS, 363, L1
Gao Y., Solomon P. M., 1997, in IAU Symposium, Vol. 170, IAU Symposium, W. B. Latter, S. J. E. Radford, P. R. Jewell, J. G. Mangum, & J. Bally, ed., pp. 419–+
—, 1999, ApJ, 512, L99
García-Burillo S., Combes F., Usero A., Graciá-Carpio J., 2007, New Astronomy Review, 51, 160
—, 2008, Journal of Physics Conference Series, 131, 012031
García-Burillo S., Fuente A., Usero A., Martín-Pintado J., 2004, in Astronomical Society of the Pacific Conference Series, Vol. 320, The Neutral ISM in Starburst Galaxies, S. Aalto, S. Huttemeister, & A. Pedlar, ed., pp. 15–+
García-Burillo S., Graciá-Carpio J., Guélin M., Neri R., Cox P., Planesas P., Solomon P. M., Tacconi L. J., Vanden Bout P. A., 2006, ApJ, 645, L17
Genzel R., Harris A. I., Stutzki J., Jaffe D. T., 1988, ApJ, 332, 1049
Genzel R., Lutz D., Sturm E., Egami E., Kunze D., Moorwood A. F. M., Rigopoulou D., Spoon H. W. W., Sternberg A., Tacconi-Garman L. E., Tacconi L., Thatte N., 1998, ApJ, 498, 579
Gerin M., Phillips T. G., 1998, ApJ, 509, L17
Getman K. V., Feigelson E. D., Broos P. S., Townsley L. K., Garmire G. P., 2010, ApJ, 708, 1760
Goldflam R., Kouri D. J., Green S., 1977, J. Chem. Phys., 67, 4149
Goldreich P., Scoville N., 1976, ApJ, 205, 144
Goulding A. D., Alexander D. M., 2009, MNRAS, 398, 1165
Graciá-Carpio J., García-Burillo S., Planesas P., Colina L., 2006, ApJ, 640, L135
Graf U. U., Eckart A., Genzel R., Harris A. I., Poglitsch A., Russell A. P. G., Stutzki J., 1993, ApJ, 405, 249
Graham A. W., Erwin P., Caon N., Trujillo I., 2001, ApJ, 563, L11
Greenhill L. J., Moran J. M., Herrnstein J. R., 1997, ApJ, 481, L23+
Griffin M. J., Ade P. A. R., Orton G. S., Robson E. I., Gear W. K., Nolt I. G., Radostitz J. V., 1986, Icarus, 65, 244
Guainazzi M., Matt G., Brandt W. N., Antonelli L. A., Barr P., Bassani L., 2000, A&A, 356, 463
Guélin M., Salomé P., Neri R., García-Burillo S., Graciá-Carpio J., Cernicharo J., Cox P., Planesas P., Solomon P. M., Tacconi L. J., vanden Bout P., 2007, A&A, 462, L45
Guesten R., Fiebig D., 1988, A&A, 204, 253
Güsten R., Baryshev A., Bell A., Belloche A., Graf U., et al., 2008, in Society of Photo-Optical Instrumentation Engineers (SPIE) Conference Series, Vol. 7020, Society of Photo-Optical Instrumentation Engineers (SPIE) Conference Series
Güsten R., Nyman L. Å., Schilke P., Menten K., Cesarsky C., Booth R., 2006, A&A, 454, L13
Habing H. J., 1968, Bull. Astron. Inst. Netherlands, 19, 421
Hanson M. M., Howarth I. D., Conti P. S., 1997, ApJ, 489, 698
Häring N., Rix H., 2004, ApJ, 604, L89
Harris A. I., Stutzki J., Genzel R., Lugten J. B., Stacey G. J., Jaffe D. T., 1987, ApJ, 322, L49
Hegmann M., Kegel W. H., Sedlmayr E., 2007, A&A, 469, 223

Helfer T. T., Blitz L., 1995, ApJ, 450, 90
Henkel C., Jacq T., Mauersberger R., Menten K. M., Steppe H., 1987, A&A, 188, L1
Herbst E., 1999, in Astrophysics and Space Science Library, Vol. 241, Millimeter-Wave Astronomy: Molecular Chemistry & Physics in Space., W. F. Wall, A. Carramiñana, & L. Carrasco, ed., pp. 341–+
—, 2005, in ESA Special Publication, Vol. 577, ESA Special Publication, A. Wilson, ed., pp. 205–210
Heyminck S., Kasemann C., Güsten R., de Lange G., Graf U. U., 2006, A&A, 454, L21
Hicks E. K. S., Davies R. I., Malkan M. A., Genzel R., Tacconi L. J., Sánchez F. M., Sternberg A., 2009, ApJ, 696, 448
Higdon S. J. U., Armus L., Higdon J. L., Soifer B. T., Spoon H. W. W., 2006, ApJ, 648, 323
Hirota T., Yamamoto S., Kawaguchi K., Sakamoto A., Ukita N., 1999, ApJ, 520, 895
Ho L. C., Keto E., 2007, ApJ, 658, 314
Hobson M. P., 1992, MNRAS, 256, 457
Hockney R. W., Eastwood J. W., 1981, Computer Simulation Using Particles, Hockney, R. W. & Eastwood, J. W., ed.
Hocuk S., Spaans M., 2010, A&A, 510, A110+
Hoffmeister V. H., Chini R., Scheyda C. M., Schulze D., Watermann R., Nürnberger D., Vogt N., 2008, ApJ, 686, 310
Hogerheijde M. R., van der Tak F. F. S., 2000, A&A, 362, 697
Hollenbach D. J., Takahashi T., Tielens A. G. G. M., 1991, ApJ, 377, 192
Hollenbach D. J., Tielens A. G. G. M., 1999, Reviews of Modern Physics, 71, 173
Hopkins P. F., Cox T. J., Kereš D., Hernquist L., 2008, ApJS, 175, 390
Hopkins P. F., Hernquist L., Cox T. J., Robertson B., Springel V., 2006, ApJS, 163, 50
Houck J. R., Roellig T. L., van Cleve J., Forrest W. J., Herter T., et al., 2004, ApJS, 154, 18
Howe J. E., Ashby M. L. N., Bergin E. A., Chin G., Erickson N. R., Goldsmith P. F., et al., 2000, ApJ, 539, L137
Hunt L. K., Malkan M. A., 2004, ApJ, 616, 707
Hüttemeister S., Henkel C., Mauersberger R., Brouillet N., Wiklind T., Millar T. J., 1995, A&A, 295, 571
Icke V., Gatley I., Israel F. P., 1980, ApJ, 236, 808
Imanishi M., 2002, ApJ, 569, 44
—, 2003, ApJ, 599, 918
Imanishi M., Dudley C. C., Maloney P. R., 2006a, ApJ, 637, 114
Imanishi M., Nakanishi K., 2006, PASJ, 58, 813
Imanishi M., Nakanishi K., Kohno K., 2006b, AJ, 131, 2888
Imanishi M., Wada K., 2004, ApJ, 617, 214
Irvine W. M., Goldsmith P. F., Hjalmarson A., 1987, in Astrophysics and Space Science Library, Vol. 134, Interstellar Processes, D. J. Hollenbach & H. A. Thronson Jr., ed., pp. 561–609
Itoh T., Done C., Makishima K., Madejski G., Awaki H., Gandhi P., Isobe N., Dewangan G. C., Griffthis R. E., Anabuki N., Okajima T., Reeves J. N., Takahashi T., Ueda Y., Eguchi S., Yaqoob T., 2008, PASJ, 60, 251
Ivison R. J., Morrison G. E., Biggs A. D., Smail I., Willner S. P., Gurwell M. A., Greve T. R., Stevens J. A., Ashby M. L. N., 2008, MNRAS, 390, 1117
Iwasawa K., Koyama K., Awaki H., Kunieda H., Makishima K., Tsuru T., Ohashi T., Nakai N., 1993, ApJ, 409, 155

Jaffe D. T., Harris A. I., Genzel R., 1987, ApJ, 316, 231
Jakob H., Kramer C., Simon R., Schneider N., Ossenkopf V., Bontemps S., Graf U. U., Stutzki J., 2007, A&A, 461, 999
Jiang Z., Yao Y., Yang J., Ando M., Kato D., Kawai T., Kurita M., Nagata T., Nagayama T., Nakajima Y., Nagashima C., Sato S., Tamura M., Nakaya H., Sugitani K., 2002, ApJ, 577, 245
Jones M. H., Lambourne R. J. A., 2004, An Introduction to Galaxies and Cosmology, Jones, M. H. & Lambourne, R. J. A., ed.
Jura M., 1974, ApJ, 190, L33+
Jura M., York D. G., 1978, ApJ, 219, 861
Juvela M., Padoan P., Nordlund Å., 2001, ApJ, 563, 853
Kalkofen W., 1984, Methods in radiative transfer, Kalkofen, W., ed.
Karachentsev I. D., Tully R. B., Dolphin A., Sharina M., Makarova L., et al., 2007, AJ, 133, 504
Kasemann C., Güsten R., Heyminck S., Klein B., Klein T., Philipp S. D., Korn A., Schneider G., Henseler A., Baryshev A., Klapwijk T. M., 2006, in Society of Photo-Optical Instrumentation Engineers (SPIE) Conference Series, Vol. 6275, Society of Photo-Optical Instrumentation Engineers (SPIE) Conference Series
Kaspi S., Smith P. S., Netzer H., Maoz D., Jannuzi B. T., Giveon U., 2000, ApJ, 533, 631
Kaufman M. J., Wolfire M. G., Hollenbach D. J., Luhman M. L., 1999, ApJ, 527, 795
Keene J., Blake G. A., Phillips T. G., Huggins P. J., Beichman C. A., 1985, ApJ, 299, 967
Khachikian E. Y., Weedman D. W., 1974, ApJ, 192, 581
Kleinmann D. E., 1973, Astrophys. Lett., 13, 49
Koda J., Sofue Y., Kohno K., Nakanishi H., Onodera S., Okumura S. K., Irwin J. A., 2002, ApJ, 573, 105
Kohno K., 2003, in Astronomical Society of the Pacific Conference Series, Vol. 289, The Proceedings of the IAU 8th Asian-Pacific Regional Meeting, Volume I, S. Ikeuchi, J. Hearnshaw, & T. Hanawa, ed., pp. 349–352
—, 2005, in American Institute of Physics Conference Series, Vol. 783, The Evolution of Starbursts, S. Hüttmeister, E. Manthey, D. Bomans, & K. Weis, ed., pp. 203–208
Kohno K., Kawabe R., Ishizuki S., Vila-Vilaró B., 1999, Advances in Space Research, 23, 1011
Kohno K., Kawabe R., Shibatsuka T., Matsushita S., 2000, in Astronomical Society of the Pacific Conference Series, Vol. 217, Imaging at Radio through Submillimeter Wavelengths, J. G. Mangum & S. J. E. Radford, ed., pp. 364–+
Kohno K., Matsushita S., Vila-Vilaró B., Okumura S. K., Shibatsuka T., Okiura M., Ishizuki S., Kawabe R., 2001, in Astronomical Society of the Pacific Conference Series, Vol. 249, The Central Kiloparsec of Starbursts and AGN: The La Palma Connection, J. H. Knapen, J. E. Beckman, I. Shlosman, & T. J. Mahoney, ed., pp. 672–+
Kohno K., Nakanishi K., Imanishi M., 2007, in Astronomical Society of the Pacific Conference Series, Vol. 373, The Central Engine of Active Galactic Nuclei, L. C. Ho & J.-W. Wang, ed., pp. 647–+
Koss M., Mushotzky R., Veilleux S., Winter L., 2010, ApJ, 716, L125
Kourganoff V., 1952, Basic methods in transfer problems; radiative equilibrium and

neutron diffusion, Kourganoff, V., ed.
Kraemer S. B., Ruiz J. R., Crenshaw D. M., 1998, ApJ, 508, 232
Kramer C., Cubick M., Röllig M., Sun K., Yonekura Y., et al., 2008, A&A, 477, 547
Kramer C., Jakob H., Mookerjea B., Schneider N., Brüll M., Stutzki J., 2004, A&A, 424, 887
Kramer C., Mookerjea B., Bayet E., Garcia-Burillo S., Gerin M., Israel F. P., Stutzki J., Wouterloot J. G. A., 2005, A&A, 441, 961
Kramer C., Stutzki J., Rohrig R., Corneliussen U., 1998, A&A, 329, 249
Krips M., Neri R., García-Burillo S., Martín S., Combes F., Graciá-Carpio J., Eckart A., 2008, ApJ, 677, 262
Kutner M. L., 1984, Fundamentals of Cosmic Physics, 9, 233
Lacy J. H., Baas F., Allamandola L. J., van de Bult C. E. P., Persson S. E., McGregor P. J., Lonsdale C. J., Geballe T. R., 1984, ApJ, 276, 533
Lada C. J., 1976, ApJS, 32, 603
Lada C. J., Depoy D. L., Merrill K. M., Gatley I., 1991, ApJ, 374, 533
Lada C. J., Oppenheimer M., Hartquist T. W., 1978, ApJ, 226, L153
Langer W. D., Penzias A. A., 1990, ApJ, 357, 477
Larson R. B., Tinsley B. M., 1978, ApJ, 219, 46
Lenc E., Tingay S. J., 2006, AJ, 132, 1333
—, 2009, AJ, 137, 537
Lepp S., Dalgarno A., 1996, A&A, 306, L21
Levenson N. A., Sirocky M. M., Hao L., Spoon H. W. W., Marshall J. A., Elitzur M., Houck J. R., 2007, ApJ, 654, L45
Levenson N. A., Weaver K. A., Heckman T. M., 2001, ApJ, 550, 230
Li C., Kauffmann G., Heckman T. M., White S. D. M., Jing Y. P., 2008, MNRAS, 385, 1915
Liou M., Steffen C. J., 1993, Journal of Computational Physics, 107, 23
Loenen A. F., Spaans M., Baan W. A., Meijerink R., 2008, A&A, 488, L5
Loren R. B., 1989, ApJ, 338, 902
Lutz D., Maiolino R., Moorwood A. F. M., Netzer H., Wagner S. J., Sturm E., Genzel R., 2002, A&A, 396, 439
Madejski G. M., Zdziarski A. A., Turner T. J., Done C., Mushotzky R. F., Hartman R. C., Gehrels N., Connors A., Fabian A. C., Nandra K., Celotti A., Rees M. J., Johnson W. N., Grove J. E., Starr C. H., 1995, ApJ, 438, 672
Magorrian J., Tremaine S., Richstone D., Bender R., Bower G., Dressler A., Faber S. M., Gebhardt K., Green R., Grillmair C., Kormendy J., Lauer T., 1998, AJ, 115, 2285
Maloney P. R., Hollenbach D. J., Tielens A. G. G. M., 1996, ApJ, 466, 561
Marconi A., Oliva E., van der Werf P. P., Maiolino R., Schreier E. J., Macchetto F., Moorwood A. F. M., 2000, A&A, 357, 24
Martig M., Bournaud F., 2008, MNRAS, 385, L38
Martin H. M., Hills R. E., Sanders D. B., 1984, MNRAS, 208, 35
Martín S., Mauersberger R., Martín-Pintado J., García-Burillo S., Henkel C., 2003, A&A, 411, L465
Martin-Pintado J., de Vicente P., Fuente A., Planesas P., 1997, ApJ, 482, L45+
McKee C. F., Storey J. W. V., Watson D. M., Green S., 1982, ApJ, 259, 647
Meijerink R., Spaans M., 2005, A&A, 436, 397
Meijerink R., Spaans M., Israel F. P., 2006, ApJ, 650, L103
—, 2007, A&A, 461, 793
Meixner M., Haas M. R., Tielens A. G. G. M., Erickson E. F., Werner M., 1992, ApJ,

390, 499
Mihalas D., 1978, Stellar atmospheres /2nd edition/, Hevelius, J., ed.
Mookerjea B., Ghosh S. K., Kaneda H., Nakagawa T., Ojha D. K., Rengarajan T. N., Shibai H., Verma R. P., 2003, A&A, 404, 569
Moorwood A. F. M., Lutz D., Oliva E., Marconi A., Netzer H., Genzel R., Sturm E., de Graauw T., 1996a, A&A, 315, L109
—, 1996b, A&A, 315, L109
Moorwood A. F. M., Oliva E., 1988, A&A, 203, 278
—, 1994, ApJ, 429, 602
Moorwood A. F. M., van der Werf P. P., Kotilainen J. K., Marconi A., Oliva E., 1996c, A&A, 308, L1+
Muders D., Hafok H., Wyrowski F., Polehampton E., Belloche A., König C., Schaaf R., Schuller F., Hatchell J., van der Tak F., 2006, A&A, 454, L25
Narayanan D., Cox T. J., Hayward C. C., Younger J. D., Hernquist L., 2009, MNRAS, 400, 1919
Narayanan D., Cox T. J., Kelly B., Davé R., Hernquist L., Di Matteo T., Hopkins P. F., Kulesa C., Robertson B., Walker C. K., 2008a, ApJS, 176, 331
Narayanan D., Hayward C. C., Cox T. J., Hernquist L., Jonsson P., Younger J. D., Groves B., 2010, MNRAS, 401, 1613
Narayanan D., Li Y., Cox T. J., Hernquist L., Hopkins P., Chakrabarti S., Davé R., Di Matteo T., Gao L., Kulesa C., Robertson B., Walker C. K., 2008b, ApJS, 174, 13
Neufeld D. A., Melnick G. J., Sonnentrucker P., Bergin E. A., Green J. D., Kim K. H., Watson D. M., Forrest W. J., Pipher J. L., 2006, ApJ, 649, 816
Nezu M., Amano T., Kawaguchi K., 1999, Journal of Molecular Spectroscopy, 198, 186
Ngeow C., Kanbur S. M., 2006, ApJ, 642, L29
Nguyen Q., Jackson J. M., Henkel C., Truong B., Mauersberger R., 1992, ApJ, 399, 521
Nguyen-Q-Rieu, Henkel C., Jackson J. M., Mauersberger R., 1991, A&A, 241, L33
Nielbock M., Chini R., Jütte M., Manthey E., 2001, A&A, 377, 273
Nord M., Lazio T. J. W., Kassim N. E., Goss W. M., Duric N., 2003, in Bulletin of the American Astronomical Society, Vol. 35, Bulletin of the American Astronomical Society, pp. 1368–+
Norman C., Scoville N., 1988, ApJ, 332, 124
Ohsuga K., Umemura M., 2001a, A&A, 371, 890
—, 2001b, ApJ, 559, 157
Oliva E., Moorwood A. F. M., Drapatz S., Lutz D., Sturm E., 1999, A&A, 343, 943
Oliva E., Salvati M., Moorwood A. F. M., Marconi A., 1994, A&A, 288, 457
Osterbrock D. E., Ferland G. J., 2006, Astrophysics of gaseous nebulae and active galactic nuclei, Osterbrock, D. E. & Ferland, G. J., ed.
Papadopoulos P. P., Allen M. L., 2000, ApJ, 537, 631
Pedlar A., Muxlow T., Wills K. A., 2003, in Revista Mexicana de Astronomia y Astrofisica, vol. 27, Vol. 15, Revista Mexicana de Astronomia y Astrofisica Conference Series, J. Arthur & W. J. Henney, ed., pp. 303–307
Pellegrini E. W., Baldwin J. A., Brogan C. L., Hanson M. M., Abel N. P., Ferland G. J., Nemala H. B., Shaw G., Troland T. H., 2007, ApJ, 658, 1119
Peng T., Wyrowski F., van der Tak F., Walmsley M., Weiss A., Menten K. M., 2007, in Molecules in Space and Laboratory
Pereira-Santaella M., Alonso-Herrero A., Rieke G. H., Colina L., Díaz-Santos T.,

Smith J., Pérez-González P. G., Engelbracht C. W., 2010, ApJS, 188, 447
Pérez-Beaupuits J. P., Aalto S., Gerebro H., 2007, A&A, 476, 177
Pérez-Beaupuits J. P., Spaans M., Hogerheijde M. R., Güsten R., Baryshev A., Boland W., 2010, A&A, 510, A87+
Pérez-Beaupuits J. P., Spaans M., van der Tak F. F. S., Aalto S., García-Burillo S., Fuente A., Usero A., 2009, A&A, 503, 459
Phillips J. A., Lazio T. J. W., 1995, ApJ, 442, L37
Phillips T. G., Knapp G. R., Wannier P. G., Huggins P. J., Werner M. W., Neugebauer G., Ennis D., 1981, ApJ, 245, 512
Planesas P., Gomez-Gonzalez J., Martin-Pintado J., 1989, A&A, 216, 1
Planesas P., Scoville N., Myers S. T., 1991, ApJ, 369, 364
Poelman D. R., Spaans M., 2005, A&A, 440, 559
—, 2006, A&A, 453, 615
Poncelet A., Doucet C., Perrin G., Sol H., Lagage P. O., 2007, A&A, 472, 823
Pounds K. A., Nandra K., Stewart G. C., George I. M., Fabian A. C., 1990, Nature, 344, 132
Povich M. S., Churchwell E., Bieging J. H., Kang M., Whitney B. A., Brogan C. L., Kulesa C. A., Cohen M., Babler B. L., Indebetouw R., Meade M. R., Robitaille T. P., 2009, ApJ, 696, 1278
Rainey R., White G. J., Gatley I., Hayashi S. S., Kaifu N., Griffin M. J., Monteiro T. S., Cronin T. S., Scivetti A., 1987, A&A, 171, 252
Reid M. A., Wilson C. D., 2006, ApJ, 644, 990
Rice W., Lonsdale C. J., Soifer B. T., Neugebauer G., Kopan E. L., Lloyd L. A., de Jong T., Habing H. J., 1988, ApJS, 68, 91
Rieke G. H., Lebofsky M. J., 1985, ApJ, 288, 618
Risacher C., Monje R., Vassilev V., Pavolotsky A., Belitsky V., 2006, in Society of Photo-Optical Instrumentation Engineers (SPIE) Conference Series, Vol. 6275, Society of Photo-Optical Instrumentation Engineers (SPIE) Conference Series
Robson I., 2004, Active Galactic Nuclei and Supermassive Black Holes, Mason, J., ed., pp. 231–+
Roche P. F., Aitken D. K., 1984, MNRAS, 208, 481
Rodríguez-Ardila A., Viegas S. M., 2003, MNRAS, 340, L33
Rodriguez-Espinosa J. M., Rudy R. J., Jones B., 1987, ApJ, 312, 555
Rodriguez-Franco A., Martin-Pintado J., Fuente A., 1998, A&A, 329, 1097
Rohlfs K., Wilson T. L., 2004, Tools of radio astronomy, Rohlfs, K. & Wilson, T. L., ed.
Roussel H., Helou G., Hollenbach D. J., Draine B. T., Smith J. D., et al., 2007, ApJ, 669, 959
Roussel H., Helou G., Smith J. D., Draine B. T., Hollenbach D. J., et al., 2006, ApJ, 646, 841
Rybicki G. B., 1972, in Line Formation in the Presence of Magnetic Fields, pp. 145–+
—, 1984, Escape probability methods, Kalkofen, W., ed., pp. 21–64
Rybicki G. B., Lightman A. P., 1986, Radiative Processes in Astrophysics, Rybicki, G. B. & Lightman, A. P., ed.
Sánchez F. M., Davies R. I., Genzel R., Tacconi L. J., Eisenhauer F., Hicks E. K. S., Friedrich S., Sternberg A., 2009, ApJ, 691, 749
Sanders D., Ishida C., 2004, in Astronomical Society of the Pacific Conference Series, Vol. 320, The Neutral ISM in Starburst Galaxies, S. Aalto, S. Huttemeister,

& A. Pedlar, ed., pp. 230–+
Sanders D. B., Ishida C. M., Mazzarella J. M., Veilleux S., Surace J. A., Guyon O., Jensen J. B., Kim D., 2004, in IAU Symposium, Vol. 222, The Interplay Among Black Holes, Stars and ISM in Galactic Nuclei, T. Storchi-Bergmann, L. C. Ho, & H. R. Schmitt, ed., pp. 477–484
Sanders D. B., Mirabel I. F., 1996, ARA&A, 34, 749
Sandqvist A., 1999, A&A, 343, 367
Sandqvist A., Joersaeter S., Lindblad P. O., 1995, A&A, 295, 585
Sani E., Lutz D., Risaliti G., Netzer H., Gallo L. C., Trakhtenbrot B., Sturm E., Boller T., 2010, MNRAS, 403, 1246
Schilke P., Walmsley C. M., Pineau Des Forets G., Roueff E., Flower D. R., Guilloteau S., 1992, A&A, 256, 595
Schinnerer E., Eckart A., Tacconi L. J., Genzel R., Downes D., 2000, ApJ, 533, 850
Schleicher D. R. G., Spaans M., Klessen R. S., 2010, A&A, 513, A7+
Schneider N., Simon R., Kramer C., Kraemer K., Stutzki J., Mookerjea B., 2003, A&A, 406, 915
Schneider N., Simon R., Kramer C., Stutzki J., Bontemps S., 2002, A&A, 384, 225
Schöier F. L., van der Tak F. F. S., van Dishoeck E. F., Black J. H., 2005, A&A, 432, 369
Scoville N. Z., Matthews K., Carico D. P., Sanders D. B., 1988, ApJ, 327, L61
Scoville N. Z., Sanders D. B., 1987, in Astrophysics and Space Science Library, Vol. 134, Interstellar Processes, D. J. Hollenbach & H. A. Thronson Jr., ed., pp. 21–50
Seyfert C. K., 1943, ApJ, 97, 28
Smith J. D. T., Armus L., Dale D. A., Roussel H., Sheth K., Buckalew B. A., Jarrett T. H., Helou G., Kennicutt Jr. R. C., 2007, PASP, 119, 1133
Smith K. L., Shields G. A., Bonning E. W., McMullen C. C., Rosario D. J., Salviander S., 2010, ApJ, 716, 866
Snell R. L., Erickson N. R., Goldsmith P. F., Ulich B. L., Lada C. J., Martin R. N., Schulz A., 1986, ApJ, 304, 780
Snell R. L., Goldsmith P. F., Erickson N. R., Mundy L. G., Evans II N. J., 1984, ApJ, 276, 625
Snell R. L., Howe J. E., Ashby M. L. N., Bergin E. A., Chin G., Erickson N. R., Goldsmith P. F., Harwit M., Kleiner S. C., Koch D. G., Neufeld D. A., Patten B. M., Plume R., Schieder R., Stauffer J. R., Tolls V., Wang Z., Winnewisser G., Zhang Y. F., Melnick G. J., 2000, ApJ, 539, L97
Sobolev V. V., 1963, A treatise on radiative transfer.
Soifer B. T., Neugebauer G., Matthews K., Becklin E. E., Ressler M., Werner M. W., Weinberger A. J., Egami E., 1999, ApJ, 513, 207
Solomon P. M., Barrett J. W., 1991, in IAU Symposium, Vol. 146, Dynamics of Galaxies and Their Molecular Cloud Distributions, F. Combes & F. Casoli, ed., pp. 235–+
Solomon P. M., Downes D., Radford S. J. E., 1992, ApJ, 387, L55
Solomon P. M., Rivolo A. R., Barrett J., Yahil A., 1987, ApJ, 319, 730
Soltan A., 1982, MNRAS, 200, 115
Sonnentrucker P., Friedman S. D., Welty D. E., York D. G., Snow T. P., 2002, ApJ, 576, 241
—, 2003, ApJ, 596, 350
Spaans M., 1996, A&A, 307, 271
Spaans M., Meijerink R., 2007, ApJ, 664, L23
—, 2008, ApJ, 678, L5
Spaans M., van Dishoeck E. F., 1997, A&A, 323, 953

Spinoglio L., Malkan M. A., Smith H. A., González-Alfonso E., Fischer J., 2005, ApJ, 623, 123
Spoon H. W. W., Koornneef J., Moorwood A. F. M., Lutz D., Tielens A. G. G. M., 2000, A&A, 357, 898
Spoon H. W. W., Marshall J. A., Houck J. R., Elitzur M., Hao L., Armus L., Brandl B. R., Charmandaris V., 2007, ApJ, 654, L49
Spoon H. W. W., Moorwood A. F. M., Pontoppidan K. M., Cami J., Kregel M., Lutz D., Tielens A. G. G. M., 2003, A&A, 402, 499
Stacey G. J., Geis N., Genzel R., Lugten J. B., Poglitsch A., Sternberg A., Townes C. H., 1991, ApJ, 373, 423
Sternberg A., Genzel R., Tacconi L., 1994, ApJ, 436, L131
Sturm E., Lutz D., Verma A., Netzer H., Sternberg A., Moorwood A. F. M., Oliva E., Genzel R., 2002, A&A, 393, 821
Stutzki J., Guesten R., 1990, ApJ, 356, 513
Stutzki J., Stacey G. J., Genzel R., Harris A. I., Jaffe D. T., Lugten J. B., 1988, ApJ, 332, 379
Stutzki J., Winnewisser G., 1985, A&A, 144, 13
Tacconi L. J., Genzel R., Blietz M., Cameron M., Harris A. I., Madden S., 1994, ApJ, 426, L77+
Tacconi L. J., Genzel R., Smail I., Neri R., Chapman S. C., Ivison R. J., Blain A., Cox P., Omont A., Bertoldi F., Greve T., Förster Schreiber N. M., Genel S., Lutz D., Swinbank A. M., Shapley A. E., Erb D. K., Cimatti A., Daddi E., Baker A. J., 2008, ApJ, 680, 246
Tachikawa H., Iyama T., Fukuzumi T., 2003, A&A, 397, 1
Talbi D., Ellinger Y., Herbst E., 1996, A&A, 314, 688
Taniguchi Y., Kameya O., Nakai N., Kawara K., 1990, ApJ, 358, 132
Tennyson J., 2005, Astronomical spectroscopy : an introduction to the atomic and molecular physics of astronomical spectra, Tennyson, J., ed.
Thornley M. D., Schreiber N. M. F., Lutz D., Genzel R., Spoon H. W. W., Kunze D., Sternberg A., 2000, ApJ, 539, 641
Tielens A. G. G. M., Hollenbach D., 1985, ApJ, 291, 722
Tomono D., Terada H., Kobayashi N., 2006, ApJ, 646, 774
Townsley L. K., Feigelson E. D., Montmerle T., Broos P. S., Chu Y., Garmire G. P., 2003, ApJ, 593, 874
Turner B. E., Ziurys L. M., 1988, Interstellar molecules and astrochemistry, Kellermann, K. I. & Verschuur, G. L., ed., pp. 200–254
Tuzun R. E., Burkhardt P., Secrest D., 1998, Computer Physics Communications, 112, 112
Umemura M., Fukue J., Mineshige S., 1999, Advances in Space Research, 23, 1095
Usero A., García-Burillo S., Fuente A., Martín-Pintado J., Rodríguez-Fernández N. J., 2004, A&A, 419, 897
Usero A., García-Burillo S., Martín-Pintado J., Fuente A., Neri R., 2006, A&A, 448, 457
van Breugel W., Filippenko A. V., Heckman T., Miley G., 1985, ApJ, 293, 83
van der Tak F. F. S., Black J. H., Schöier F. L., Jansen D. J., van Dishoeck E. F., 2007, A&A, 468, 627
Veilleux S., Osterbrock D. E., 1987, ApJS, 63, 295
Veilleux S., Rupke D. S. N., Kim D., Genzel R., Sturm E., et al., 2009, ApJS, 182, 628
Verma A., Lutz D., Sturm E., Sternberg A., Genzel R., Vacca W., 2003, A&A, 403,

829
Verner D. A., Yakovlev D. G., 1995, A&AS, 109, 125
Viti S., Caselli P., Hartquist T. W., Williams D. A., 2001, A&A, 370, 1017
Voit G. M., 1992, ApJ, 399, 495
Wada K., 2001, ApJ, 559, L41
Wada K., Norman C. A., 2001, ApJ, 547, 172
—, 2002, ApJ, 566, L21
Wada K., Papadopoulos P. P., Spaans M., 2009, ApJ, 702, 63
Wada K., Tomisaka K., 2005, ApJ, 619, 93
Wall W. F., Jaffe D. T., Bash F. N., Israel F. P., Maloney P. R., Baas F., 1993, ApJ, 414, 98
Wang Y., Jaffe D. T., Evans II N. J., Hayashi M., Tatematsu K., Zhou S., 1993, ApJ, 419, 707
Watabe Y., Umemura M., 2005, ApJ, 618, 649
Weiß A., Henkel C., Downes D., Walter F., 2003, A&A, 409, L41
Werner M. W., Roellig T. L., Low F. J., Rieke G. H., Rieke M., Hoffmann W. F., Young E., Houck J. R., et al., 2004, ApJS, 154, 1
Wernli M., Valiron P., Faure A., Wiesenfeld L., Jankowski P., Szalewicz K., 2006, A&A, 446, 367
Whittet D. C. B., ed., 2003, Dust in the galactic environment
Wild W., Harris A. I., Eckart A., Genzel R., Graf U. U., Jackson J. M., Russell A. P. G., Stutzki J., 1992, A&A, 265, 447
Willett K. W., Stocke J. T., Darling J., Perlman E. S., 2010, ApJ, 713, 1393
Wilson A. S., 1988, A&A, 206, 41
Wilson C. D., Howe J. E., Balogh M. L., 1999, ApJ, 517, 174
Yamada M., Wada K., Tomisaka K., 2007, ApJ, 671, 73
Yamamoto S., Maezawa H., Ikeda M., Ito T., Oka T., et al., 2001, ApJ, 547, L165
Zdziarski A. A., Johnson W. N., Done C., Smith D., McNaron-Brown K., 1995, ApJ, 438, L63
Zhang J. S., Henkel C., Mauersberger R., Chin Y., Menten K. M., Tieftrunk A. R., Belloche A., 2007, A&A, 465, 887
Zmuidzinas J., Betz A. L., Boreiko R. T., Goldhaber D. M., 1988, ApJ, 335, 774

Nederlandse samenvatting

Op een typische heldere nacht onder de noordelijke hemel van Chili is het mogelijk om, met het blote oog, een uitgerekte donkere wolk te ontwaren die een heldere verdikking bedekt, omringd door ontelbaar veel sterren. Op de foto (*rechts*) genomen door Alexandru Tudorica aan de voet van het Cerro Tololo Inter-American Observatorium (CTIO), ongeveer $500\ \mathrm{km}$ ten noorden van Santiago, Chili, zijn de sterrenbeelden Schorpioen (linksboven) en Boogschutter (rechtsonder) te zien. De vage witte verdikking is het centrum van ons sterrenstelsel, de Melkweg (MW) – een vertaling van *Via Lactea* uit het Latijn.

Omdat het vlak van de Melkweg een hoek van $\sim 60^\circ$ maakt met de ecliptica (het vlak van de omloopbaan van de Aarde), zien we vanaf de Aarde het centrum van de Melkweg vrijwel volledig van opzij. Daardoor wordt de heldere kern van de Melkweg verduisterd door al het materiaal dat zich tussen de sterren bevindt. Dit materiaal vormt de donkere band op de foto, en is samengesteld uit vele wolken van interstellair gas en stof dat aanwezig is in de spiraalarmen van de Melkweg.

De Melkweg aan het zuidelijke hemelhalfrond, gezien vanuit het noorden van Chili. De heldere kern van de Melkweg is zichtbaar in het midden van de foto. Deze opname is gemaakt met een digitale fotocamera door Alexandru Tudorica.

Door de sterke verduistering als gevolg van gas en stof – dat vooral invloed heeft in het visuele spectraalgebied – zijn indirecte methodes en waarnemingen bij andere golflengtes (bijv. millimeter-, sub-millimeter-, infrarood-, en röntgengolven) nodig om de kernen van de meeste sterrenstelsels, incl. de MW, te bestuderen. Aangenomen wordt dat de meerderheid van de sterrenstelsels een superzwaar zwart gat in hun kern bevatten. Deze kernen vertonen verschillende niveau's van helderheid, stervormingsactiviteit, en snelheid waarmee materie hun zwarte gaten instroomt. Men heeft ontdekt dat zelfs ons eigen sterrenstel (de Melkweg) in het centrum een zwart gat herbergt. De MW is echter minder helder en minder actief dan veel andere sterrenstelsels die intense stervormingsactiviteit ondergaan. Dit suggereert dat de MW tegenwoordig in een betrekkelijk rustige staat verkeert.

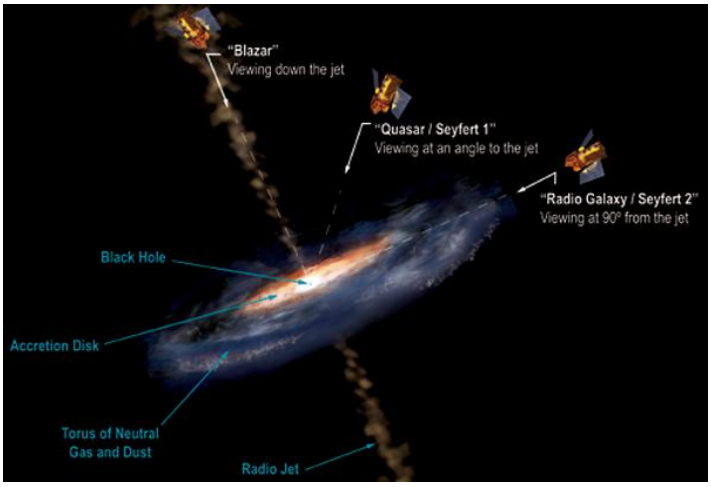

Artistieke weergave van een Actieve Galactische Kern (Engels: 'Active Galactic Nucleus', AGN) en de interpretatie van de unificatietheorie die afhangt van de gezichtslijn naar het centrale gedeelte van het sterrenstelsel. De extreme lichtkracht van een AGN wordt aangedreven door een superzwaar zwart gat in het centrum. Sommige AGN's hebben zogenaamde 'stralen', andere niet. *Annotaties in het figuur, vanaf boven, met de klok mee:* 'Blazar': gezichtslijn parallel aan de straal – 'Quasar / Seyfert 1': gezichtslijn onder een hoek t.o.v. de straal – 'Radiosterrenstelsel / Seyfert 2': gezichtslijn onder een hoek van 90° t.o.v. de straal – Radio-straal – Torus van neutraal gas en stof – Accretieschijf – Zwart gat. *Rechten afbeelding: Aurore Simonnet, Sonoma State University.*

Het spectrum van een normaal sterrenstelsel zoals de MW wordt gedomineerd door warmtestraling en heeft een vorm die overeenkomt met een composiet van zwarte-lichaamsstraling uitgezonden door miljarden sterren en interstellair gas en stof. Normaalgesproken ligt het maximum van zo'n spectrum in het visuele of nabij-infrarode spectraalgebied. Bij een actief sterrenstelsel daarentegen, wordt een belangrijk deel van de algehele lichtkracht (of energieproductie) geleverd door een niet-thermisch proces. Ten opzichte van normale sterrenstelsels vertonen ze een hogere lichtkracht ($\gtrsim 10 \times L_{\rm MW}$*), die voornamelijk voortkomt uit de centrale gebieden. Afhankelijk van het soort actief sterrenstelsel kan de uitgestraalde energie worden waargenomen via infrarood- (IR), radio-, ultraviolet- (UV), röntgen- en gammastraling.

Wat de meeste actieve sterrenstelsels met elkaar gemeen hebben is een Actieve Galactische Kern (Engels: 'Active Galactic Nucleus', AGN). In de figuur *hierboven* is het algemeen geaccepteerde model voor een AGN afgebeeld, dat uitgaat van de aanwezigheid van een superzwaar zwart gat – tussen de 10^6 en 10^9 maal de massa van de Zon ($M_\odot$) – in het centrum van het sterrenstelsel. Een torus van gas en stof, die het centrale gedeelte van het sterrenstelsel overschaduwt, voedt het zwarte gat via een afgeplatte accretieschijf van dicht materiaal. Regelmatig komen grote hoeveelheden zwaartekrachtsenergie vrij vanuit de accretieschijf, in de vorm

* waarin $L_{\rm MW}$ de lichtkracht van de Melkweg representeert, $\sim 2 \times 10^{10}$ maal de lichtkracht van de Zon ($L_\odot$).

van krachtig uitstromende stralen van heet plasma. Volgens deze beschrijving van sterrenstelselkernen zijn de waargenomen verschillen tussen verscheidene soorten actieve sterrenstelsels simpelweg een gevolg van variërende kijkhoeken en accretiesnelheden – dit geldt als de *unificatietheorie* voor actieve sterrenstelsels.

Sommige van de verschillende soorten actieve sterrenstelsels staan bekend als Seyfert-sterrenstelsels; dit zijn vooral stelsels met een spiraalvorm en een kleine kern die ongeveer tien maal meer licht uitzendt dan de gehele MW. Hun helderheid kan fluctueren op tijdschalen van ongeveer een maand, en hun spectra vertonen brede verboden emissielijnen (bijv. [O II], [O III], [N II], [Ne III], [Ne V], [S III], [S IV]), die overeenkomen met sterk geïoniseerd gas. Seyfert-sterrenstelsels manifesteren zich bovendien sterk in IR-, UV- en röntgenstraling.

Terwijl in een normaal sterrenstelsel per jaar in de orde van 1 $M_\odot$ aan sterren wordt gevormd, vertonen andere soorten actieve sterrenstels, zogenaamde 'sterexplosiestelsels', een uitzonderlijk hoge stervormingssnelheid (tussen 10 en 300 $M_\odot$ aan sterren per jaar) in hun binnenste kiloparsec*. Dit soort sterrenstelsels kan de voortdurende stervormingsexplosie zo'n $10^8 - 10^9$ jaar volhouden, hetgeen veel korter is dan de evolutietijdschaal van een sterrenstelsel. Omdat alleen díe wolken met de hoogste dichtheden voldoende materiaal kunnen leveren om sterren te vormen, zijn stervormingsgebieden diep verborgen in gas en stof. Dit materiaal absorbeert de UV-straling van de pasgevormde sterren. Doordat deze verduisterende stofwolken opgewarmd worden en vervolgens hun energie opnieuw uitstralen, is een sterexplosiestelsel vooral duidelijk zichtbaar in het infrarood.

Waarnemingen hebben bewijs geleverd voor een fysiek verband tussen AGN's en explosieve stervormingsactiviteit rondom de kern. De ver-IR-eigenschappen van Seyfert-sterrenstelsels blijken vergelijkbaar te zijn met die van sterexplosiestelsels. Enerzijds doen zich in veel Seyfert-stelsels stervormingsexplosies voor, zowel rondom de kern als verborgen in de kern. Anderzijds zijn ook diep ingegraven AGN's ontdekt in veel sterrenstelsels die oorspronkelijk waren geclassificeerd als sterexplosiestelsels.

Intensieve stervorming, accretie op een zwart gat en het samensmelten van actieve sterrenstelsels zijn cruciale fases in de evolutie van sterrenstelsels. Het is verre van duidelijk hoe deze processen op elkaar inwerken, hoe ze terugkoppeling in kernen van sterrenstelsels voortdrijven, en welke invloed ze hebben op het (voornamelijk dichte, moleculaire) interstellair medium en het stervormende gas. De bestraling door UV- en röntgenfotonen, en ook andere thermodynamische processen die verantwoordelijk zijn voor de terugkoppeling (bijv. turbulentie en schokken) in de stervormingsgebieden en nabij het centrum van actieve sterrenstelsels, zijn de oorzaak voor de excitatie van atomen en de vorming van vele moleculen. Door atomaire en moleculaire emissie te bestuderen die wordt veroorzaakt door bovengenoemde processen, kunnen we de interactie en terugkoppelingsprocessen tussen het groeiende zwarte gat en de stervormingsactiviteit leren begrijpen, en zo ook hun effect op het (vooral dichte, moleculaire) interstellair medium en het stervormende gas.

* Een kiloparsec komt overeen met ongeveer 3000 lichtjaar, of ongeveer 3×10^{19} meter.

Moleculaire en atomaire emissie in nabije actieve sterrenstels

Dit proefschrift is gewijd aan het onderzoeken van fysieke omstandigheden van het interstellair medium in AGN's en stervormingsgebieden in onze Melkweg, waarbij vooral millimeter-waarnemingen van enkelvoudige telescopen worden gebruikt. Ik begin met een onderzoek naar excitatie-omstandigheden van dicht gas ($n(\mathrm{H_2}) > 10^4\ \mathrm{cm^{-3}}$) in een groep Seyfert-sterrenstelsels, gebruik makend van stralingsoverdrachtmodellen (Hfdst. 2). Eén van de doelen is het achterhalen van de bron van heldere emissie van het HNC-molecuul dat is waargenomen in die sterrenstelsels. Ik pak vragen aan als: 'Is er een grote hoeveelheid koud, verborgen gas?', en: 'Wordt de chemie overheersd door ion-neutraal-reacties of door röntgenbestraling?'. Vervolgens bestudeer ik het specifieke geval van het prototypische Seyfert-sterrenstelsel NGC 1068 en probeer onderscheid te maken tussen bijdrages van de AGN en de stervormingsring door middel van waarnemingen van hoge-J-overgangen van moleculen in gas van hoge dichtheid (Hfdst. 3). Hier maak ik een inschatting van – en corrigeer de waarnemingen voor – de bijdrage van de stervormingsexplosie, die mogelijk de emissie in de lage-J-overgangen 'vervuilen'. Waarnemingen van meer overgangen maken een betere bepaling van de omgevingsomstandigheden mogelijk, die afgeleid worden uit de stralingsoverdrachtmodellen. Later neem ik de stap naar het mid-infrarode spectraalgebied om verschillende aspecten van de AGN en de stervormingsexplosie te bestuderen in het nabije sterrenstelsel NGC 4945 (Hfdst. 4). De hoofddoelen zijn het bepalen van de verdeling van het interstellair medium en het koppelen van de emissie van fijnstructuurlijnen aan verschillende bronnen van excitatie (bijv. stervormingsring, supernovaresten, uitstromende materie). In Hfdst. 5 ga ik dieper in op theoretische aspecten van de dynamische evolutie van gas in een AGN torus. Ik gebruik een drie-dimensionale (3D) hoge-resolutie (0.25 parsec per pixel) hydrodynamische simulatie en verwerk daarbij de abondanties van verscheidene moleculen die zijn afgeleid uit een chemisch evolutiemodel dat wordt gedreven door röntgenstraling. Het streven is het doorgronden van effecten van röntgen-straling vanuit de AGN op de temperatuur, vorming, en vernietiging van het moleculaire gas. Uiteindelijk bekijk ik een stervormingsgebied in onze Melkweg, de Omega-nevel (of M17), met hoge-resolutie waarnemingen van een enkelvoudige telescoop, om de eigenschappen van het warme gas te onderzoeken en om restricties te stellen aan de chemische modellen (Hfdst. 6 en 7).

Het is bijzonder belangrijk om hoge-resolutie-waarnemingen te doen van stervormingsgebieden in de Melkweg en het centrum daarvan, omdat moleculaire wolken met afmetingen van de kaarten ($\sim 3 \times 3\ \mathrm{parsec}^2$) uit Hfdst. 7 en 6 ruimtelijk zullen worden opgelost door ALMA* op de afstand van nabije sterrenstelsels, zoals het prototypische Seyfert-stelsel NGC 1068 ($D \sim 14$ megaparsec, Chap. 2 en 3) of het infrarood-heldere sterrenstelsel NGC 4945 ($D \sim 3.7$ megaparsec, Hfdst. 4). Op deze manier kunnen stervormingsgebieden in onze Melkweg als 'voorbeeld' dienen bij een directe vergelijking met zulke gebieden in actieve sterrenstelsels die in de komende jaren met ALMA waarneembaar zullen worden.

De millimeter- en mid-infrarood-gegevens die ik heb verzameld uit waarne-

* http://www.almaobservatory.org/

mingen van de sterrenstelsels NGC 1068 en NGC 4945 (Hfdst. 2, 3 en 4) zullen diagnostieken opleveren voor unificatiemodellen van sterrenstelsels en het effect van de kijkhoek. Interferometrische studies van de thermodynamica van moleculair gas in het samensmeltende systeem Arp 299 zullen inzicht verschaffen in hoe jonge stervormingsexplosies op gang worden gebracht, en zal de weg vrijmaken voor toekomstige waarnemingen met ALMA.

De hoger geëxciteerde lijnen van CO en de fijnstructuurlijnen van neutraal en geïoniseerd koolstof, stikstof en zuurstof zijn nu (of in de toekomst) bereikbaar met nieuwe instrumenten zoals APEX*/CHAMP$^+$, Herschel†/SPIRE & PACS en SOFIA‡/GREAT. Hiermee zal het mogelijk worden om het dichte en hete (door terugkoppeling beïnvloede) gas te bestuderen in het centrum van de Melkweg, in nabije sterrenstelsels, AGN's en sterexplosiestelsels. Deze lijnen zullen worden gebruikt om fysieke omstandigheden te meten in actieve stervormingsgebieden met laag en hoog 'metaalgehalte' (d.w.z.: alle elementen zwaarder dan He); dit opent de deur naar onderzoek hoe metaalgehalte een rol speelt in de fysieke structuur van stervormend gas en welk effect het heeft op emissielijnen. De waarnemingsgegevens zullen gebruikt worden om randvoorwaarden te stellen aan theoretische modellen die gebaseerd zijn op de 3-D hydrodynamische en chemische simulaties van kernen van sterrenstelsels (Hfdst. 5). De kaarten van moleculaire en atomaire lijnintensiteit, verkregen d.m.v. de 3-D stralingstransportcode, zullen gebruikt worden als leidraad bij de interpretatie van waarnemingen van objecten buiten onze Melkweg, die uitgevoerd zullen worden met de eerdergenoemde instrumenten.

* http://www.mpifr.de/div/mm/technology_projects/apex.html
† http://herschel.esac.esa.int/
‡ http://www.sofia.usra.edu/

Summary

ON a typical clear night in the northern sky of Chile it is possible to appreciate, with the naked eye, an elongated dark cloud covering a bright bulge surrounded by countless stars. In the picture (*right*) taken by Alexandru Tudorica at the foot of the Cerro Tololo Inter-American Observatory (CTIO), located about $500\ \mathrm{km}$ north of Santiago, Chile, the constellations of Scorpius (top left) and Sagittarius (bottom right) can be seen above and below, respectively, the dark lane crossing the sky. The white and fuzzy bulge is the center of our Galaxy, the Milky Way (MW) - translated from the Latin *Via Lactea*.
Because the Galactic plane is inclined by $\sim 60^\circ$ to the ecliptic (the plane of the Earth's orbit), the Galactic center is seen nearly edge-on from the Earth. Hence, all the material that lies between the stars, which corresponds to the dark lane in the picture and that is constituted by numerous clouds of interstellar gas and dust found in the spiral arms of the Galaxy, obscures the bright Galactic center.

The Milky Way in the Southern Hemisphere, with the bright Galactic center in the middle of the picture, as seen in the sky above the north of Chile. This is an image taken with a digital camera by Alexandru Tudorica.

Due to the strong gas and dust obscuration that affects mostly the visible region of the spectrum, indirect methods and observations at other wavelengths (e.g., millimeter, sub-millimeter, infra-red, and X-ray wavelengths) are required to study the galactic center of the majority of galaxies in the Universe, including the MW. The centers of most galaxies are believed to host a supermassive black hole, and they show different levels of brightness, star formation activity and accretion rates of matter into their black holes. Even our own Galaxy has been found to host a black hole in its center. However, the MW is less bright and active than many other galaxies undergoing strong star formation activity. This suggests that the MW is currently in a rather quiet state.

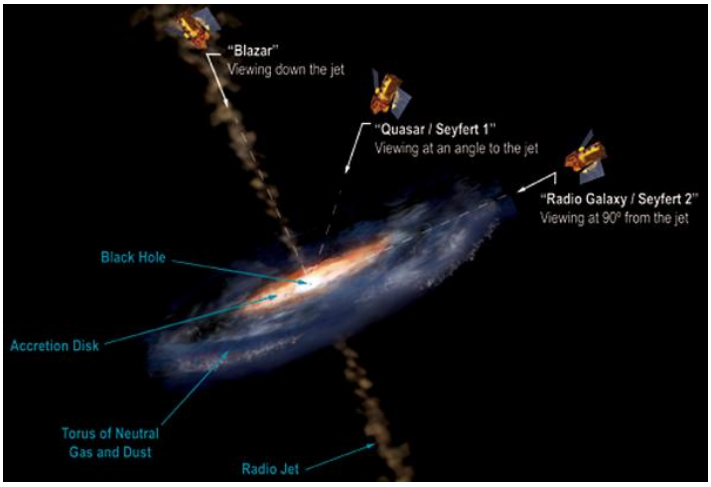

Artistic representation of an active galactic nucleus (AGN) and the interpretation of the unification theory depending on the line of sight to the central region. The extreme luminosity of an AGN is powered by a supermassive black hole at the center. Some AGN have jets, while others do not.
Image credit: Aurore Simonnet, Sonoma State University.

An ordinary galaxy like the MW shows a spectrum dominated by thermal emission and a spectral shape corresponding to a composite of black-body radiation (with a maximum usually in the visible or near-infrared region of the spectrum) emitted by billions of stars, interstellar gas and dust. Active galaxies instead show significant contribution to their overall luminosity (or energy output) by some process other than thermal emission. Usually they exhibit higher luminosities ($\gtrsim 10 \times L_{\rm MW}{}^{*}$) than a normal galaxy, emitted mainly from their central regions. Depending on the type of active galaxy, its emitted energy can be observed in the infrared (IR), radio, ultraviolet (UV), X-ray and gamma-ray regions of the electromagnetic spectrum.

What most active galaxies have in common is an Active Galactic Nucleus (AGN). The figure *above* shows the generally accepted model of an AGN, which assumes the presence of a supermassive black hole of between 10^6 and 10^9 times the mass of the Sun ($M_\odot$) located at the center of the galaxy. A torus of gas and dust, obscuring the central part of the galaxy, feeds the black hole through a flat accretion disk of dense material. Large amounts of gravitational energy are frequently released from the accretion disk in the form of powerful outflowing jets of hot plasma. This model of galaxy nuclei suggests that the differences observed between different types of active galaxies are simply a consequence of different viewing angles and different accretion rates – this is the *unification theory* of active galaxies.

Some of the several types of active galaxies are known as Seyfert galaxies, which are mostly spiral galaxies with a tiny core that is about ten times more luminous than the whole MW. Their brightness can fluctuate on time scales of about one month, and their spectra show broad forbidden emission lines (e.g., [O II], [O

* where $L_{\rm MW}$ is the luminosity of the Milky Way $\sim 2 \times 10^{10}$ times the luminosity of the Sun ($L_\odot$)

III], [N II], [Ne III], [Ne V], [S III], [S IV]) corresponding to highly ionized gas. Seyfert galaxies also show strong emission in the IR, UV, and X-ray spectral regions.

While ordinary galaxies only produce stars on the order of 1 $M_{\odot}$ per year, other types of active galaxies, known as starbursts, exhibit an exceptionally high star formation rate (between 10 and 300 $M_{\odot}$ of stars per year) in their central kilo parsec ($1\ \mathrm{parsec} \approx 3.086 \times 10^{16}\ \mathrm{meters}$). This type of galaxies can maintain the ongoing starburst for $10^8 - 10^9$ years, which is much shorter than the evolutionary timescale of a galaxy. Since only dense clouds can provide enough material to form stars, the star-forming regions are deeply obscured by gas and dust absorbing the UV radiation emitted by the newly formed stars. Hence, starburst galaxies show strong emission mainly in the infra-red region due to the re-radiation from the heated obscuring dust.

Observational evidence suggests a physical relationship between AGN and circumnuclear starburst activity. The far-IR properties of Seyfert galaxies have been found to be similar to those of starburst galaxies. Many Seyfert galaxies have circumnuclear starbursts and hidden nuclear starburst activity. On the other hand, deeply buried AGNs have been found in many galaxies originally classified as starbursts. Intense star formation, black hole accretion and the coalescence of active galactic nuclei are crucial phases in galaxy evolution. How these processes interact and drive feedback in galaxy centers, and the impact that they have on the (mostly dense, molecular) interstellar medium and star-forming gas, is far from understood. The irradiation by UV and X-ray photons, as well as other thermodynamical processes responsible for the feedback (e.g. turbulence and shocks) occurring in the star-forming regions and near the center of active galaxies, drive the excitation of atomic species, as well as the formation of many molecules. Studies of atomic and molecular emission triggered by the processes mentioned above can advance our understanding of the interaction and feedback processes between the accreting black hole and the starburst activity, and their effects on the (mostly dense, molecular) interstellar medium and star-forming gas.

Driving molecular and atomic emission in nearby active galaxies

This thesis is devoted to the study of the physical conditions of the interstellar medium (ISM) in AGNs and Galactic star-forming regions, using mostly single-dish millimeter observations. I first study the ambient (excitation) conditions of dense gas ($n(\mathrm{H_2}) > 10^4\ \mathrm{cm^{-3}}$) in a group of Seyfert galaxies using radiative transfer models (Chap. 2). One of the goals is to determine the source of the bright emission of the HNC molecule observed in those galaxies. Some of the questions I address here are: is there a large mass of cold hidden gas?, and is the chemistry dominated by ion-neutral reactions or by X-ray irradiation?. I then study the particular case of the prototypical Seyfert galaxy NGC 1068, and try to distinguish signatures of the contributions from the AGN and the starburst ring, by incorporating observational data of high-J transitions of dense gas tracers (Chap. 3). Here I estimate, and correct the observations for, the starburst contribution that may contaminate the emission of the low-J transitions. Observations of more transitions allow to better constrain

the ambient conditions derived from the radiative transfer models. Later, I venture into the mid-infrared spectral region to study different aspects of the AGN and starburst components in the nearby galaxy NGC 4945 (Chap. 4). The main goals are to determine the distribution of the ISM and to associate the emission of fine-structure lines to different sources of excitation (e.g., starburst ring, supernova remnants, outflows). In Chap. 5, I delve into theoretical aspects of the mass and dynamical evolution of the circumnuclear gas in an AGN torus. I use a three-dimensional (3-D) high-resolution (0.25 pc per pixel) hydrodynamic simulation and incorporate the abundances of several species derived from a model of chemical evolution driven by X-rays. The aim is to understand the effects of X-ray irradiation by the AGN on the temperature, formation and destruction of the molecular gas. I finally explore a Galactic star-forming region known as the Omega Nebula (or M17) with high resolution single dish observations, to study the properties of the warm gas and to constrain the chemical models (Chaps. 6 and 7).

High spatial resolution observations of Galactic star-forming regions and the Galactic center are particularly important since molecular clouds of the size of maps ($\sim 3 \times 3$ pc^2) reported in Chaps. 7 and 6 will be resolved spatially by ALMA*, at the distance of nearby galaxies like the prototypical Seyfert NGC 1068 ($D \sim 14$ Mpc, Chap. 2 and 3) or the luminous infrared galaxy NGC 4945 ($D \sim 3.7$ Mpc, Chap. 4). As such, star-forming regions in our own Milky Way can serve as templates for a direct comparison with such regions in active galaxies that will become observable with ALMA in the coming years.

The millimeter and mid-IR data that I have collected from observations toward the galaxies NGC 1068, and NGC 4945 (Chaps. 2, 3 and 4), will provide diagnostics for unification models of galaxies and the effects of viewing angle. Interferometric studies of the thermodynamics of molecular gas in the merging system Arp 299 will give insights to the triggering of young starbursts, and pave the road for future observations with ALMA.

The higher excitation lines of CO, the fine-structure lines of neutral and ionized atomic carbon, nitrogen and oxygen that are (and will be) accessible with current and future instruments like APEX†/CHAMP$^+$, Herschel‡/SPIRE & PACS and SOFIA§/GREAT will allow to explore the dense and hot (feedback affected) gas in the Galactic center, nearby galaxies, AGNs and starbursts. These lines will be used to probe the physical conditions in regions of active star formation with low and high metallicity (i.e., any element beyond He), allowing the investigation of the role that metallicity plays in the physical structure of star-forming gas and its effect on emission lines. The observational data will be used to constrain theoretical models based on the 3-D hydrodynamical and chemical simulations of galactic nuclei (Chap. 5). The line intensity maps obtained from the 3-D radiative transfer code, will be used to guide and interpret extra-galactic observations that will be done with the facilities mentioned above.

* http://www.almaobservatory.org/

† http://www.mpifr.de/div/mm/technology_projects/apex.html

‡ http://herschel.esac.esa.int/

§ http://www.sofia.usra.edu/

Acknowledgements

In a time when the economic crisis hit hard most countries, money have become an even more important concern for ordinary people. However, we are indeed privileged as PhD fellows, at least in the sense that we do not have to worry about "loosing" our jobs in the middle of the project. It is not till the end of the PhD thesis that we have to start looking for new opportunities and to face the ferocious competition and lack of suitable post-doc positions. Therefore, with all the due respect for the people around the world who does not share the same luck (thanks to the outrageous greed of few), my first words of gratitude are for the following organizations that provided me with financial support to enjoy a fairly comfortable life and enough fun during the last four years, and the additional support to participate in conferences, schools, working visits and observing trips: Kapteyn, RuG, LKBF, NWO, NAOJ, RadioNet and Cornell University.

Marco, since the very beginning you have shown a determined trust and confidence on me and my capabilities to pursue and finish my PhD. You never spared encouraging words and deeds. You not only guided me when I needed, but also gave me all the freedom to follow my own ideas and to work on my personal scientific interests. You encouraged me to grow not only as an observer, but also as a theoretician. Because of your knowledge, wisdom and flexibility to recognize and to deal with the different personalities and characterstics of each student, I consider you as an inspiring example of a Professor and supervisor. You realize that imposing your way and methodology to the students is not the right way. You understand that the right path for a person is its own path, and that the only thing they need is encouragement. The high quality and productive results of the ISM group you have built speaks by itself, and it is shown by the many PhD thesis finished on time and by the successful careers all those PhD's are pursuing as post-docs. And this work of yours cannot be outshined by what could be considered as one of the darkest periods in the Kapteyn institute. Because I trust you and I just cannot let low and disgraceful deeds and sayings pass by as if they were correct and normal, I went forward and stood for you during that period, despite of the subsequent looks of disapproval from few, the fearful and worrisome thoughts of some, and the indifference of others. But many shown their sympathy and support towards you, and their appeased minds and cheerful faces were worth all the struggle we went through. And no matter what the consequences are or how the story will end, you will always have my friendship, support, and respect.

To the management team and secretaries at Kapteyn: Thijs, Peter, Hennie, Lucia, Jackie, Geneke and Karina. Special thanks to Hennie and Jackie for being always very friendly, helpful and supportive; the Kapteyn computer team, Wim, Eite and Martin. I am specially grateful to Wim, who was always there to help me with the (fortunately) few software and hardware issues I had, and for being one of the few staff members that was willing to analyze and to talk about the internal affairs of the institute. Many thanks also for your nice sense of humor.

To the members of the ISM group and colleagues PhD students: Inga, Volker, Andrey, Floris, Seyit, Edo, Wilfred, Dieter, Christian, Chris, Matthieu, German, Zsofia, for the educative and enriching discussions during our biweekly group meetings with cakes and cookies.

Because of their help, support and friendly attitudes and initiatives during the two months I spent at the Cornell University in Ithaca, I am very grateful to Henrik, Jamie, Barbara, Vianney, Jero and Don.

To the Mani Thomas family: I am grateful for the educative discussions about Indian culture, religion and other affairs. I also enjoyed your very good homemade Indian food. Rajat, my deepest gratitude will remain towards you for the unconditional help that you offered to a RAMAS fellow from the very beginning. I am also grateful to you for the entertaining discussions about other sciences than astronomy, for the fun trips by bicycle and in your fancy Alfa Romeo, and for sharing the hilarious (and some times troublesome) adventures you got involved in thanks to your self-proclaimed “Indian magic”...

To my amazingly long lasting house mate, Matias, I enjoyed very much all those days *working at home*, and being fed by your delicious “tartas de verduras”, “pollo ambrossia”, and “rice with tuna fish, eggs and grained pecorino”. Although it was not on purpose, I feel proud of myself for being the responsible for the first time (and most likely the only time!) you have lost a flight during our never ending way back from Kracow xD ... I will be longing for those fun nights and weekends doing quests and instances together in WoW... Thanks a lot for all the mutual tolerance and understanding during those years shared at the house in Niuewe Kijk In’t Jatstraat.

To the bar tenders of the bar “de Minaar”, thanks for your kindness and patience during all those long and crazy nights I spent there with my foreign fellows, and for allowing me to convert your bar into a dancing floor till sunrise...

Thomas, you always were a very cool fellow and a pleasant company for all those long nights at bars, clubs and billiard games during the time we were both single. Your dedication to your thesis and quietness were substantial contributions to the peaceful working environment of our office. Thanks a lot for your tolerance with me and Facu while we were (shamelessly) talking in Spanish in our office :-)

Boris, I will bring along several memorable occasions shared with you, such as the crazy weekend in Paris and your birthday party at the student house, where I tried for the first time the “Bulgarian salad”, which I continue making at home (although lacking the proper rakea). I appreciate very much the sacrifice you made to lend me such a valuable piece of art that you treasure so much, mostly during those private and peaceful moments in the toilet...“The hitchhicker’s guide to the galaxy” book ... I never thought that I would be able to be faster than you in carting, but without even realizing, I am now less than half a second to make it!! :D ... You are such an enthusiastic and pleasant person to share time with and to enjoy several topics of conversations, despite your clear preference for cars... I hope that you will not let the external dark energies (emitted by irrelevant ones) drag you down and loose your enthusiasm and interest for astronomy, and other inventions

and design businesses of yours. I will be looking forward for the day when I will have the pleasure to see one of your prototypes ;-)

Matthijs & Beatrijs, thanks a lot for taking care of the translation of the summary of my thesis. I hope you win the University price to the best summary :-)

Kalle, I am grateful to you for being a cool (not cold!) Swedish friend, and for hosting me at your cozy house in Leiden during my first years of the PhD...

Giamba, I greatly enjoyed passing you the ball so you could show off your natural striker skills during all the football games we played together. And I also enjoyed damning you when you played for the opponent team :P ... Many thanks for keeping us entertained playing guitar during those poker nights :D

Andrea, I am very grateful for the exciting and exhausting squash matches at ACLO that triggered and raised my long time buried competitive spirit. Many thanks for the “pasta with bottarga” and all the other Italian dishes we shared at your place, even if some times they were just Domino’s pizzas ordered during our Nintendo FIFA games :P ... I enjoyed very much the last two years celebrating our birthdays together ...

Yang-Shyang, thank you very much for those long and lovely evenings playing piano, and the mutual encouragement for learning more about music in general, and for your persistent interest in showing me your favorite British music :P ... I very much enjoyed the exotic, light and healthy Taiwanese food, and all the experimental dishes that many times you prepared. I am truly grateful to you for being one of those active parts of the Earth that never stopped revolving during the last months of my PhD, despite of my (at times) discouraging grumpiness, and for inducing me to remain at least a bit sociable. Your sharp mind and positive criticism helped me to rediscover my own sharp edges and to realize that I was still full of foolish pride. But as A. Einstein said: ”once we accept our limits, we go beyond them” ... I will always be grateful to you for being a loyal and tender mate, and for being such a cute oriental girl ^_^

Peter, many thanks for being one of the few Dutch persons I managed to get close to. I greatly appreciate all the efforts you made during these years to get along with the gang of foreigners that must have seem estrange to you. And I hope you also appreciate the tremendous effort I made by attending and supporting your “peculiar” concerts with *No Consent* ;-)

Aycin, during the last two years we became closer friends, enduring the missfortunes of the Institute, but also enjoying the most exciting and fun moments, having fancy and delicious dinners at your place, and travelling to Brazil. You are such an enthusiastic Salsa partner, and every time we went to dance was an enlivening experience. The skills you show playing football, and your perseverance for improving your tennis game, motivated me to become more sportive and less lazy :D ... I highly appreciate all the deep discussions about science, people and life that we had during the sunny days in down town Groningen. Many thanks also for checking the last unnoticed typos in my thesis :-) ... I hope you will never loose your courage and determination for pursuing your own interests and ideas, even if that means to go against the main social streams in your home country and elsewhere...

Stephanie, you are the coolest and craziest mom I have ever met!! You manage to be very successful in science at the same time you rise two (maybe three? ;)) kids!! ... I am very impressed because I do not think I would be able to do the same. You took the lead when I was away for holidays and pushed a bitter and ungrateful enterprise, facing along with Aycin all the demagoguery of the moment. Thanks to your conviction and perseverance we all managed to accomplish the main underlying goal: to let people know that not everyone is submissive to the unwise and unfair decisions of few. You deserve the admiration and respect of everyone, and you certainly have mine. And do not worry, we will keep writing proposals until we manage to go to Hawaii together!! :D ... I will be longing to share with you more of those long party nights, and if one day you decide to open a bar in a tropical island, I will be glad to be your bartender *ad honorem* :D

Facu, we were lucky enough to start and finish this long journey at about the same time. I must admit that I was cooled down after two years living in Sweden (and not just because of the weather!), but the strong and warm passion that you always show for your roots helped me to rise and keep alive my South American spirit during these four years. I enjoyed very much all the time we spent sharing the office, complaining in complicity and cursing (mostly in Spanish :D) about all the annoying issues we encountered... I will be longing for all those indoor and outdoor football games, and for the long nights enjoying wine, movies and watching football on your big-screen tv, that added the spices to improve the taste and warm up life in the cold Dutch weather... I am sure that in the end you will realize that all the trouble we went through these years was not in vain ;-)

Anto, we also spent most of our PhD period together and we had the chance to share many special moments and fun times. I have never tried more delicious cakes than the ones you make! I think you should consider opening a small bakery as a hobby, since you will have for sure many loyal clients ;) ... It was also very funny to see how you lost all your “money” due to your incontrollable impulse to go *all in* (many times!) during those long poker nights ... but I hope you do not behave the same in real life :D ... It was always pleasant and entertaining to spend time with you, cooking and sharing recipes of different foods, and comparing the Chilean and Argentinian versions of many dishes. And I realize that they are basically the same, just like the idiosyncrasy of our countries ;-) ... Thanks a lot for being such a nice, easy going, and pleasant person to be with. I truly admire you for the huge patience and tolerance that you must have to cope with someone like Facu :P

In brief, Facu & Anto, many thanks for the friendship we developed during all these years, which should remain despite of the distance...

Paolo & Mirjam, you are one of the best examples I know to probe that couples between people of two different countries and cultural backgrounds can match very well, and that such a cute and lovely baby as Sofie can be the result of a beautiful marriage. You encourage me to try the same, since I will be away from my home country for a long while! :D ... Although, I think I am not yet ready for children, which may be the reason why I never volunteer myself as baby-sitter ;-) ... Paolo, I wish we can buy that sailing boat and travel through the canals in the Netherlands

all the way down to Sardinia! Mirjam, I hope in the future we will be able to dance tango again, if Paolo does not mind :P ... I will be looking forward to see how fast Sofie grows and hoping that she will remember me :D

Beike, many thanks for all the Italian style coffee you shared with many of us after lunch, taking care of the preparations so we can just sit and enjoy (as lazy bastards :D) your nice coffee, always accompanied with a pleasant chat. I greatly appreciate the efforts you made, before and during the dinners and fun parties organized at your place, and specially for all the energy and unconditional help and dedication you brought to the various events I organized at my place...

Christophe, you are such a nice fellow with so much talent and enthusiasm for playing several musical instruments. You are a nice inspiration for trying to do the same from now on, and I wish we could have spent more time playing some music together...

To the female Italian mafia: Giuliana, Linda and Estefania, I am glad that I had the chance to share many fun times with such enthusiastic, happy, energetic and easy going persons. Many thanks for bringing the shining and warm Latin blood to all the events I shared with you...

To the Turkish army: Elif, Aycin, Burcu and Esra, you all have very sweet spirits, and I am glad I met you all and to have the luck of being enriched with your culture and personal experiences just by spending time with you.

Burcu, many thanks for all the special coffee that you prepared after lunch, which was a fair competition of Beike's coffee ;-) ... It was always nice to have you around in dinners and parties, and is a good bet to invite you for dinner, since you always appreciate the food that other people prepare :-)

Sara, as the lottery that some times life is, you fortunately arrived to share the house with me, bringing to my life new tasty recipes from the Italian cuisine, as well as the pleasant energy and enthusiasm of a young, sweet and clever girl. I will keep in my heart all the fun and happy days that we shared during those three months. And I will always be grateful to you for awakening once again my own interest and enthusiasm about neuroscience, and for helping me to reconnect with my deepest thoughts and feelings regarding people, life, and death...

My deepest and biggest gratitude is for the main source of unconditional love and comfort: my parents, my brother and uncle. You have always supported me in many ways during all these six years I have been abroad, and you have being coping very well with the deep empty space I created with my departure.

I am grateful to all these years living abroad, which taught me that an open communication, and the will for mutual listening and understanding, are needed to reduce the barriers between different persons and cultural backgrounds...

I still have few lines to fill in this page, so, to all the people & organizations that I may have forgotten to acknowledge, or left out because of the lack of time, I just can say ...

... "So long ... and thanks for all the fish".
(The hitchhicker's guide to the galaxy)